All-electrical Quantum Sensing with Silicon Carbide Devices

Christopher Tao-Kuan Lew
(ORCID:0000-0001-6432-4520)

Submitted in total fulfilment of requirements for the degree of

Doctor of Philosophy

June, 2022

School of Physics
University of Melbourne

Abstract

Silicon carbide (SiC) is a complimentary metal-oxide-semiconductor (CMOS) compatible wide bandgap semiconductor most notably used in high power electronics. Furthermore, SiC is a promising quantum materials platform able to host a wide variety of spin defects exhibiting long spin decoherence times. To leverage the full potential of SiC electronics for future quantum technologies, this thesis conducts a series of detailed investigations on electrically active spin defects in SiC with a particular emphasis on utilising these spin defects for quantum sensing applications measured using the electrically detected magnetic resonance (EDMR) technique. EDMR is a highly sensitive spectroscopic technique able to readout a small ensemble of electron spins in a fully fabricated electronic device by utilising the spin-dependent recombination (SDR) mechanism.

The magnetic field sensitivity of a processing-induced spin defect in a SiC diode device was first explored. Instead of utilising the spin resonance response, the electromagnetic irradiation-free hyperfine-induced spin-mixing response situated at zero magnetic field is used for magnetometry. It is shown that the magnetic field sensitivity can be enhanced by at least an order of magnitude by employing a balanced detection scheme for common-mode rejection and above bandgap optical illumination for photogeneration of electron-hole pairs. These two methods are not limited to the processing-induced spin defect studied here and may be applied to other spin defects utilising the EDMR technique.

Taking advantage of the wide selection of existing commercial SiC devices available, we then investigated the temperature dependence of the hyperfine-induced spin-mixing response in a commercial SiC power transistor device. As SiC electronics are typically operated under extreme environmental conditions, it is important to understand how the spin-mixing response changes with temperature and how changes in the device response can affect the spin-mixing response. Although a complex temperature dependence was observed for the spin-mixing response convoluted with changes in the de-

vice characteristics, a linear change in the signal linewidth with temperature was observed, which may have further implications for quantum sensing of temperature fluctuations.

Lastly, we have developed a multi-stage lock-in modulation pulsed EDMR (pEDMR) measurement scheme to study the spin dynamics of processing-induced spin defects in SiC. This alleviates some of the stringent experimental constraints associated with the pEDMR technique and allowed us to characterise the spin dephasing and decoherence times, which form the basis of more complex sensing protocols of DC and AC magnetic fields, respectively. The relatively long room temperature spin decoherence time on the order of $\sim \mu$s demonstrates that SiC is indeed a suitable quantum materials platform for quantum sensing applications.

The series of studies presented in this thesis shed new insight on several different aspects of quantum sensing utilising electrically detected spin defects and provides the first steps toward the realisation of an all-electrical SiC quantum sensor.

Acknowledgements

The completion of this thesis would not have been possible without the assistance and guidance from my supervisors, collaborators, and colleagues, as well as support and encouragement from my friends and family. First, I would like to thank my supervisors Jeffrey McCallum and Brett Johnson for giving me the opportunity to continue my studies in the world of condensed matter physics under your co-supervision and your unwavering support in pursuing areas of research well outside your usual comfort zones. I am forever grateful for this once in a lifetime experience and for helping me develop as a well-rounded and independent researcher. In thanking my supervisors, I would like to extend my gratitude to David Jamieson and Ann Roberts on my PhD candidature advisory committee. Thank you both for providing me feedback from a fresh perspective and making sure I did not fall behind on any administrative deadlines and paperwork.

Next, I wish to thank my collaborators who were directly involved with the results presented in this thesis. In no particular order, I would like to thank Daniel Creedon, Stephen Gregory, and Steve Yanni for their technical assistance and support in setting up the EDMR spectrometers outlined in Chapter 4, Takeshi Ohshima and Naoya Iwamoto at the National Institutes for Quantum and Radiological Science and Technology (QST) in Japan for providing me the sample studied in Chapter 5 and Chapter 7, and Vikas Sewani for the countless hours of insightful and fruitful discussions we have had over the years on a whole range of topics.

Throughout my PhD candidature, I had the unique opportunity to work on a wide range of research topics outside the scope of this thesis with both local and international collaborators. In no paricular order, I would like to thank Nikolai Dontschuk, David Broadway, Jean-Philippe Tetienne, David Simpson, and Lloyd Hollenberg from the quantum sensing group for their incredible generosity in sharing their lab equipment and quantum sensing expertise with me, as well as the opportunity to work on H-terminated diamond with incorporated nitrogen-vacancy centres, Qi Lim and Jim Williams for introduc-

ing me to the exciting field of hyperdoped silicon photodetectors, and Alistair Rowe from École Polytechnique for introducing me to the fascinating field of piezoimepedance in silicon.

The past four years would not have been as successful if it were not for the people who have aided me along the way in my endeavours. I would like to thank all the post-docs, lab technicians, administrators, and fellow students both past and present in the ECMP group scattered across the basement, level 1, and level 2 of the physics building. Outside of University, I would like to thank my friends for their friendship and support over the years and their constant reminders to come out of the basement laboratory to enjoy life outside of research. Last but not least, I must thank my family, particularly my mom, dad, sister, and extended family back in Taiwan that have been cheering me on from the very beginning. Without them, I would not be where I am today.

Statement of Originality

This is to certify that

1. The work presented in this thesis is the author's original work except where indicated in the preface.
2. Acknowledgement has been made in the text to all other material used.
3. This thesis is under the 100,000 work limit, exclusive of tables, maps, bibliography, and appendices.

Christopher Tao-Kuan Lew, June 2022

Preface

The device studied in Chapter 5 and Chapter 7 of this thesis was fabricated by our collaborators at the National Institutes for Quantum and Radiological Science and Technology (QST) in Japan.

This work was funded by the Australian Research Council Centre of Excellence for Quantum Computation and Communication Technology (No. CE110001027). Furthermore, I would like to acknowledge the Australian Government for the Research Training Program Scholarship.

List of Publications

In addition to the work presented in this thesis, I have contributed to other works outside the scope of this thesis that have been published in peer-reviewed journals. The papers are listed below chronologically:

C. T.-K. Lew, B. C. Johnson, and J. C. McCallum, *Deep level transient spectroscopy study of heavy ion implantation induced defects in silicon.* **Journal of Applied Physics**, 124.12 (2018), p. 125701.

D. A. Broadway, N. Dontschuk, A. Tsai, S. E. Lillie, C. T.-K. Lew, J. C. McCallum, B. C. Johnson, M. W. Doherty, A. Stacey, L. C. L. Hollenberg, and J.-P. Tetienne, *Spatial mapping of band bending in semiconductor devices using in situ quantum sensors.* **Nature Electronics**, 1.9 (2018), p. 502.

H. Li, C. T.-K. Lew, B. C. Johnson, J. C. McCallum, S. Arscott, and A. C. H. Rowe, *Giant, Anomalous Piezoimpedance in Silicon-on-insulator.* **Physical Review Applied**, 11.4 (2019), p. 044010.

B. C. Johnson, J. Wörle, D. Haasmann, C. T.-K. Lew, R. A. Parker, H. Knowles, B. Pingault, M. Atature, A. Gali, S. Dimitrijev, M. Camarda, and J. C. McCallum, *Optically Active Defects at the SiC/SiO_2 Interface.* **Physical Review Applied**, 12.4 (2019), p. 044024.

S. Q. Lim, C. T.-K. Lew, P. K. Chow, J. M. Warrender, J. S. Williams, B. C. Johnson, *Process-induced defects in Au-hyperdoped Si photodiodes.* **Journal of Applied Physics**, 126.22 (2019), p. 224502

S. Q. Lim, C. T.-K. Lew, P. K. Chow, J. M. Warrender, J. S. Williams, B. C. Johnson, *Toward understanding and optimizing Au-hyperdoped Si infrared photodetectors* **Applied Physics Letters Materials**, 8.6 (2020), p. 061109

C. T.-K. Lew, N. Dontschuk, D. A. Broadway, J.-P. Tetienne, J. C. McCallum,

L. C. L. Hollenberg, B. C. Johnson, *Investigation of charge carrier trapping in H-terminated diamond devices.* **Applied Physics Letters**, 117.14 (2020), p. 143507

H. Li, A. Thayil, C. T.-K. Lew, M. Filoche, B. C. Johnson, J. C. McCallum, S. Arscott, A. C. H. Rowe, *Piezoresistance in Defect-Engineered Silicon.* **Physical Review Applied**, 15.1 (2021), p. 014046.

R. A. Parker, N. Dontschuk, S.-I. Sato, C. T.-K. Lew, P. Reineck, A. Nadarajah, T. Ohshima, B. C. Gibson, S. Castelletto, J. C. McCallum, B. C. Johnson, *Infrared erbium photoluminescence enhancement in silicon carbide nanopillars.* **Journal of Applied Physics**, 130.14 (2021), p. 145101.

M. Bathen, C. T.-K. Lew, C. Dorfer, J. Woerle, S. Castelletto, U. Grossner, B. C. Johnson, *Characterization methods for defects and devices in silicon carbide.* **Journal of Applied Physics**, 131.14 (2022), p. 140903.

Contents

List of Figures

List of Tables

Introduction 1

1.1 Introduction

Quantum information processing (QIP) makes use of the fundamental laws of quantum mechanics to encode, process, and transmit quantum information with applications in quantum computing [1, 2], quantum communication [3], and quantum sensing [4]. Emerging QIP technologies will enable new capabilities and opportunities in a range of existing industries, leading to improved productivity and economic growth in the coming decades [5]. Two promising platforms for implementing QIP technologies are trapped ions and solid-state devices. Solid-state QIP technologies are particularly promising as they make use of the well-established commercial fabrication techniques employed in the semiconductor industry to develop scalable quantum devices. However, the delicate interaction of an electron spin, the physical implementation of an individual quantum bit of information (i.e., qubit), with its solid-state environment can lead to spin decoherence and the decay of quantum information, placing stringent requirements on the solid-state host material and the operating conditions.

Silicon carbide (SiC) is a complimentary metal-oxide-semiconductor (CMOS) compatible wide bandgap semiconductor widely used in high power electronics as it is able to effectively dissipate heat generated, tolerate radiation-harsh environments, and handle high voltages at high frequencies [6, 7]. Due to its weak spin-orbit coupling and low background magnetic noise, a wide range of intrinsic defects can naturally form or be created in SiC [8] well isolated from environmental perturbations. These atom-like defect systems, analogous to an electron bound to the nucleus of an atom in vacuum, have the unique advantage of exhibiting exceptional spin coherence properties while offering the potential for large-scale integration and coupling. The electron spin state is then typically projected onto other degrees of freedom, such as charge, photon, or phonon, which is easily accessed via standard

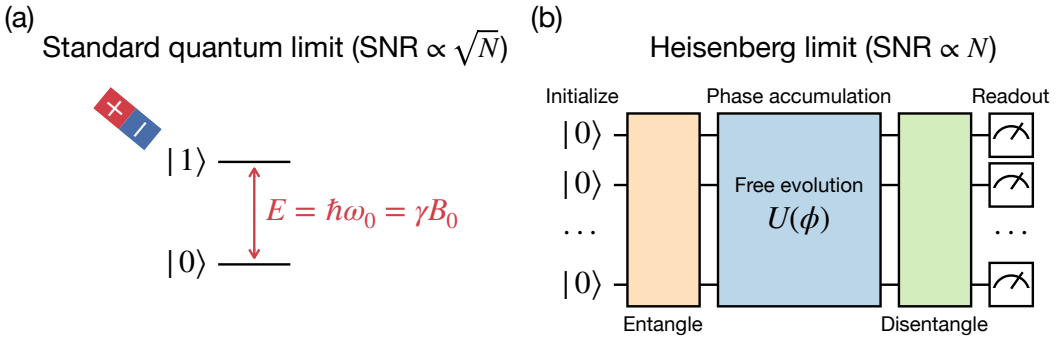

Fig. 1.1.: Illustration of quantum sensing in (a) the standard quantum limit and (b) the Heisenberg limit. In the standard quantum limit, the energy splitting of a two level quantum system in the presence of an external magnetic field is related by the coupling parameter, γ, and the SNR scales $\propto \sqrt{N}$ number of spins interrogated. In the Heisenberg limit, an ensemble of quantum sensors are brought into an entangled state for the Ramsey sensing protocol as an example in which the phase accumulated during free evolution is related to the Larmor transition frequency, ω_0. The sensitivity approaches the ultimate limit allowed by quantum mechanics and the measurement SNR scales $\propto N$.

measurement techniques. This work will make use of the spin-to-charge interface to address spin defects, also known as paramagnetic defects, in SiC for quantum sensing applications, particularly magnetometry.

The ability to accurately sense magnetic fields is crucial for a broad range of applications, ranging from planetary field mapping [9, 10], to monitoring current flow through electronic devices [11], to mapping magnetic fields within biological samples [12]. Quantum sensing involves the measurement of a quantum system observable that interacts with an external variable of interest; in our case a magnetic field, but can be also applied to electric field or temperature. The simplest implementation utilises a two-level quantum system in which interaction with an external magnetic field leads to a splitting in its energy levels and the transition energy between the two energy states is proportional to the external variable through a coupling parameter, γ, as shown in Fig. 1.1(a). This class of quantum sensing is deemed semi-classical as the sensitivity is limited by the standard quantum limit governed by shot noise (e.g., random fluctuations due to the discrete nature of electrons and photons) and spin projection noise (e.g., loss of information due to imperfect spin readout) [13]. To achieve full quantum advantage over its classical counterpart, quantum sensing that make use of quantum effects

such as coherence, entanglement, or squeeze states can reach the ultimate sensitivity allowed by quantum mechanics, defined by the Heisenberg limit. An example of Heisenberg-limited quantum sensing is shown in 1.1(b) using entangled states for the Ramsey sensing protocol in which the signal-to-noise ratio (SNR) scales proportional to N number of spins addressed, whereas sensing protocols operating at the standard quantum limit scales proportional to $\sqrt{N}$ [4]. Reaching the Heisenberg limit is an outstanding goal for quantum sensing.

Much of the recent success in solid-state spin defect-based quantum sensing have been demonstrated with the nitrogen-vacancy (NV) centre in diamond [14–17]. This prototypical quantum system has excellent sensitivity in the pT/$\sqrt{\text{Hz}}$ regime at room temperature [18] and can operate over a wide range of conditions. However, there is considerable effort in searching for alternative defects and materials that could improve upon or compliment the NV centre in diamond. The silicon vacancy (V_{Si}) defect in SiC for example exhibits excellent spin coherence and its emission wavelength operating in the near-infrared significantly reduces attenuation when integrated into existing telecommunication infrastructure [19, 20]. While significant achievements have already been demonstrated with optically detected quantum sensing, there remains significant interest and motivation to explore electrical detection. This is a result of the potential reduction in the supporting detection infrastructure and integration with existing Si and SiC electronics. Electrical readout of paramagnetic defects in SiC for remote magnetometry was first proposed by Cochrane et al. [9] and demonstrated using a SiC junction diode device with a sensitivity of 440 nT/$\sqrt{\text{Hz}}$, several orders of magnitude less sensitive than the NV centre in diamond. Initial calculations have shown that a sensitivity in the several 100's pT/$\sqrt{\text{Hz}}$ regime should be easily attainable [9], suggesting that significant improvements are yet to be made.

The fundamental objective of this thesis is to create a transformative platform based on SiC electronic devices for quantum sensing applications. To achieve this, a comprehensive understanding of the atom-like spin defects and the corresponding measurement protocols must be developed. As a result, a wide variety of fundamental questions must be answered, including: What are the sensitivity limits possible with SiC devices? What are the key properties and stability of these devices? What physical mechanisms

govern spin-to-charge processes in SiC? Can methods be developed to address the spin coherence in a SiC device? How might standard SiC devices be appropriate for quantum sensing applications? Each of the three experimental chapters are described below together with a description of the structure of this thesis.

1.2 Work reported in this thesis

This thesis reports on a series of studies on electrical readout of spin defects in SiC via spin-dependent recombination (SDR). In the SDR process, the spin symmetry of an intermediate spin-pair formed between an electron (or hole) and a paramagnetic defect obeying spin selection rules is manipulated with resonant EM excitation and magnetic resonance is readout via a change in the device conductivity [21]. A compact and cost-effective low field electrically detected magnetic resonance (EDMR) spectrometer was designed and constructed to carry out these measurements. Three specific aspects of SDR in SiC with the overarching theme of magnetometry were investigated and form the basis of the three main experimental chapters, as detailed below. The results from each study provides new understanding and insight on the SDR process in SiC and how it may be leveraged for quantum sensing.

1.2.1 Absolute magnetometry based on spin defects in SiC

Sub-nT/$\sqrt{\text{Hz}}$ magnetic field sensitivity is crucial for a wide range of high sensitivity applications detecting field strengths much smaller than the Earth's magnetic field. This has not been achieved yet with EDMR in SiC and to the best of our knowledge, the highest sensitivity achieved so far is 50 nT/$\sqrt{\text{Hz}}$ with an organic thin-film diode device [22]. As such, the fundamental sensitivity limit of EDMR-based magnetometers is currently unknown and is explored using a standard SiC pn junction diode fabricated by collaborators at QST. Instead of using the spin resonance response that requires resonant EM excitation typically used for magnetometry, the spin-mixing response between degenerate singlet and triplet states at zero magnetic field due

to the hyperfine interaction is used. This EM radiation free effect was first reported in SiC by Cochrane et al. [23] and is typically much larger in amplitude than the spin resonance response. A similar spin-mixing response in organic semiconductors is well documented and is also known as organic magnetoresistance (OMAR) [24–27].

The investigation begins with conducting a comprehensive continuous-wave EDMR (cwEDMR) study on the SDR response arising from a processing-induced paramagnetic defect in the SiC junction diode device at low magnetic fields. Fine structure in the EDMR spectrum corresponding to hyperfine (electron-nuclear) interaction and dipolar (electron-electron) interaction were observed. The strength of the spin-mixing response was electrically tunable and once optimised, the magnetic field sensitivity of the device was characterised. Several approaches in benchmarking the device sensitivity were considered and their applicability are discussed. Experimental methods in further enhancing the magnetic field sensitivity were then demonstrated and analysed.

1.2.2 Hyperfine-induced spin-mixing response

Following the experimental demonstration of a EDMR-based SiC magnetometer, the hyperfine-induced spin-mixing response was explored in more detail. For semiconductor materials such as SiC consisting of naturally abundant isotopes of ^{29}Si (3.68%) and ^{13}C (1.07%) both with nuclear spin $I = 1/2$, the nuclear magnetic field strength from each nuclear spin experienced by each electron spin in the spin-pair can lead to a complex lineshape in the spin-mixing response. This is in stark contrast to the OMAR response in disordered organic semiconductors where the nuclear magnetic field is averaged over a distribution of randomly orientated H nuclear spins [24–27]. Spin-spin interaction may also contribute to the lineshape of the spin-mixing response at ultrasmall magnetic fields as the singlet and triplet state degeneracy is lifted [23].

While SiC electronics is known to be operational at elevated temperatures, the temperature dependence of the spin-mixing response is not known. Furthermore, changes in the device characteristics at elevated temperatures may affect the spin-mixing response, which must be well documented

and understood for future applications. Thus, we make use of an existing commercially available SiC power metal-oxide-semiconductor field-effect-transistor (MOSFET) device and investigate the temperature dependence of the spin-mixing response. A modified charge pumping (CP) biasing scheme compatible with the vertically diffused MOS (VDMOS) device structure measured was implemented to dynamically induce SDR through spin defects at the SiC/SiO_2 interface. The spin-mixing response strongly varied with temperature and was well described with a simple empirical model consisting of a sum of Lorentzians. An unexpected linear dependence on temperature was observed for the linewidth of one of the Lorentzian components over a broad temperature range, which may be utilised for quantum sensing of external temperature variations.

1.2.3 Coherent spin initialization and readout

Coherent control and spin readout in the time-domain achieved with a short resonant pulse excitation is an important criteria for many advanced quantum protocols, but also provides a wealth of new information on the spin system interrogated previously not accessible in the adiabatic regime in cwEDMR. Historically, electrical detection of coherent spin propagation after a short resonant pulse excitation with pulsed EDMR (pEDMR) was not experimentally demonstrated until the turn of the century [28], decades after pulsed electron spin resonance (pESR) and pulsed optically detected magnetic resonance (pODMR) have been developed. Many technical challenges have contributed to this significant delay, including the introduction of a large spin-independent current background greater than the spin-dependent signal of interest due to the absorption of high power pulsed EM excitation by the metallic conductive contacts on the semiconductor device surface [29]. This has limited the applicability of pEDMR to a select few spin systems in highly optimised devices and experimental conditions with large enough SNR.

To study the coherent spin dynamics of the processing-induced spin defect in SiC at room temperature, a pEDMR lock-in measurement protocol was developed and implemented on our spectrometer. A substantial SNR enhancement achieved compared to typical measurements in the time-domain allowed us to explore a wide range of pulse techniques previously developed

for pESR. New insight on the exchange and dipolar interaction were revealed and measurements utilising multi-pulse sequences to characterise the spin dephasing and decoherence of the spin system were performed. These multi-pulse sequences are integral to DC and AC magnetometry protocols previously developed, respectively [13, 30]. The relatively long room temperature coherence time measured demonstrates that SiC is indeed a suitable quantum materials platform and these measurements in the context of DC and AC magnetometry were evaluated.

1.3 Thesis outline

This thesis consists of seven further chapters structured as follows:

Chapter 2 provides an overview of the structural and electronic properties of SiC. The properties of the SiC/SiO_2 interface, rich in spin defects, are also introduced. Lastly, the properties of known spin defects found in the SiC bulk and at the SiC/SiO_2 interface are then summarised.

Chapter 3 introduces the theoretical framework and relevant spin mechanisms involved in ESR and EDMR. Starting with a semi-classical picture describing the time evolution of an ensemble of electron spins using the Bloch equations, the allowed energy transitions are then considered using the spin Hamiltonian. The spin Hamiltonian is then expanded to describe an intermediate spin-pair in the SDR process and its equation of motion is then presented using the stochastic Liouville equation expressed in density matrix formalism.

Chapter 4 details the design and implementation of the EDMR spectrometers used in this thesis. The working principles of lock-in detection and the post acquisition data processing steps implemented will also be summarised. Lastly, the technical aspects and implementation of pEDMR with lock-in detection will be described and compared with conventional time-domain measurements.

Chapter 5 is the first experimental chapter of this thesis and begins with a comprehensive EDMR study of a typical SiC pn junction diode fabricated by

collaborators at QST. Once the spin-mixing and device response were characterised and optimised, magnetometry is demonstrated and benchmarked. Methods to further enhance the sensitivity, including common-mode rejection and above bandgap photoillumination are then explored, remarkably increasing the sensitivity by a factor of around 24.

Chapter 6 investigates the spin-mixing response in more detail in a commercial SiC power MOSFET device under CP conditions. The lineshape and linewidth of the spin-mixing response, characterised by a sum of Lorentzians are mapped out as a function of CP voltage, CP frequency, and temperature. A complex temperature dependence was observed as a result of both the intrinsic spin-mixing response and the device characteristics. The linewidth of one of the Lorentzian components used to describe the spin-mixing response is linear over a wide temperature range, which may offer a simplistic constant of proportionality for sensing temperature fluctuations.

Chapter 7 demonstrates coherent control and readout of spin defects at room temperature with pEDMR via lock-in detection. pEDMR results agree well and are consistent with cwEDMR measurements performed in Chapter 5. It is revealed that the two electron spins in the intermediate spin-pair are weakly coupled and their Larmor separation is small, leading to non-selective excitation and Rabi spin beating at twice the Rabi frequency. Spin dephasing and spin decoherence at room temperature were found to be comparably long and were considered for DC and AC magnetometry protocols, respectively.

Chapter 8 summarizes the main results from each experimental chapter. Potential future works and possible research directions based on unresolved or lingering questions from this thesis will be discussed.

Background

2

SiC is a rapidly-adopted semiconductor material used in a wide range of high power, high temperature, and high frequency applications. Furthermore, SiC is a suitable solid-state quantum materials platform to fabricate quantum devices. The structural and electronic properties of SiC, the semiconductor material of choice studied in this thesis, are introduced in this chapter. A brief overview of spin defects in SiC previously observed with ESR and EDMR will also be summarised.

2.1 Silicon carbide

SiC is a wide bandgap compound semiconductor composed of the stoichiometric ratio of Si and C. Each Si atom is covalently bonded to four neighbouring C atoms and vice versa to form a single bilayer. These extremely strong tetrahedral sp^3 hybridised bonds with a bond energy of 4.6 eV [31] give SiC its impressive structural properties. As such, historically one of the first large-scale industrial applications was utilising SiC as an abrasive [32].

As a semiconductor, SiC shares many of the outstanding properties of diamond, such as having a wide bandgap and large breakdown voltage, while being a material compatible with existing industry complimentary metal-oxide-semiconductor (CMOS) processes and more amenable to electrical device fabrication, similar to Si. The wide bandgap and low intrinsic carrier concentration ($n_i = 5 \times 10^{-9}$ cm^{-3} for 4H$-$SiC [33]) of SiC means that SiC can maintain its semiconducting property at elevated temperatures. SiC devices operating at temperatures above 500°C have been demonstrated for a wide range of devices and are touted to replace existing Si electronics in high-temperature circuitry commonly found in aerospace applications [34]. Due to its high breakdown voltage and high thermal conductivity, SiC devices can be operated at large biases and high switching frequencies, ideal for applications such as in automotive battery chargers and locomotive motors [35]. In addition, the high carrier saturation velocity ($\sim 2 \times 10^7$ cm/s [31]) of

SiC is able to support high power millimeter-wave and microwave devices, despite its poor carrier mobility [36].

As a quantum material, SiC exhibits low spin-orbit coupling and low magnetic background noise (i.e., low paramagnetic defect impurity, and nuclear spin concentration), making it a suitable host material for spin defects with long spin coherence times. Several promising spin defects have been discovered and identified exhibiting room temperature spin-dependent fluorescence at wavelengths in the near-infrared, including the negatively charged silicon vacancy (V_{Si}^{-}) [37–39] and the neutral divacancy (VV^{0}) [40, 41], making them more amenable to frequency up-conversion to telecommunication wavelengths for quantum communication applications [20]. By utilising the mature and CMOS-compatible nano-fabrication techniques established for SiC, the integration of optical defects into fabricated nanophotonic and cavity structures provides a straightforward pathway to enhance fluorescent emission due to the Purcell effect [42] and spatial wave-guiding [43]. Other deep level defects that do not possess the spin degree of freedom can still be used in quantum applications acting, for example, as single photon sources (SPSs) with each individual photon representing the basic unit of information for the quantum key distribution protocol and may be integrated into existing electronic devices for electrical control [44–46].

2.1.1 Polymorphism

Depending on the Si−C bilayer stacking sequence, SiC can form a wide variety of polytypes with slightly different structural, mechanical, optical, and electrical properties. To date, over 250 different SiC polytypes have been reported [47]. The three most extensively used polytypes are the cubic 3C−, hexagonal 4H−, and hexagonal 6H−SiC polytypes mainly because they are commercially available on the wafer scale. Devices fabricated on 4H− and 6H−SiC will be considered in this work. Table 2.1 summarizes some of the relevant properties of the 3C−, 4H−, and 6H−SiC polytype in comparison with silicon and diamond.

The Ramsdell notation [51] is used to unambiguously differentiate between SiC polytypes based on the Si−C bilayer stacking sequence along the [0001] crystallographic $c-$axis direction. For a given polytype, the polytype can be

	Si	C	4H-SiC	6H-SiC	3C-SiC
Stacking sequence	---	---	ABAC	ABCACB	ABC
Band gap (eV)	1.12	5.47	3.26	3.02	2.36
Breakdown voltage (MV/cm)	0.3	5.7	⊥ c-axis: 2.2 ∥ c-axis: 2.8	⊥ c-axis: 1.7 ∥ c-axis: 3.0	1.4
Thermal conductivity ($Wcm^{-1}K^{-1}$)	1.5	20	3.3-4.9	3.3-4.9	3.3-4.9
Donor ionization energy (meV)	P: 45 As: 54	P: 600 N: 1700	N: 61 (h), 126 (k) P: 60 (h), 120 (k)	N: 85 (h), 140 (k) P: 80 (h), 130 (k)	N: 55
Acceptor ionization energy (meV)	B: 45 Al: 72	B: 370	B: 280 Al: 198 (h), 201 (k)	B: 350 Al: 240	B: 350 Al: 250
Electron mobility ($cm^2V^{-1}s^{-1}$)	1400	2200	⊥ c-axis: 1020 ∥ c-axis: 1200	⊥ c-axis: 450 ∥ c-axis: 100	1000
Hole mobility ($cm^2V^{-1}s^{-1}$)	450	1800	120	100	100
Melting point (°C)	1420	4000	2830	2830	2830

Tab. 2.1.: Some relevant electrical properties of 3C−, 4H−, and 6H−SiC in comparison with Si and C sampled from Refs. [31, 33, 47–50]. (h) and (k) denote whether the dopant occupies the quasi-hexagonal or quasi-cubic lattice site, respectively. Values may slightly vary depending on references used.

uniquely defined by a number in combination with a letter, where the number denotes the number of Si−C bilayers required to uniquely define the SiC unit cell and the letter denotes the unit cell crystal symmetry. Only the 3C− polytype displays cubic (C) symmetry, whereas all other SiC polytypes exhibit either hexagonal (H) or rhombohedral (R) symmetry. To further illustrate the polymorphism of SiC, Fig. 2.1 compares the stacking sequence of 3C−, 4H−, and 6H− SiC. For every three consecutive Si−C bilayers, each bilayer is labelled with either 'A', 'B', or 'C'. Using this notation, the stacking sequence within the unit cell can be uniquely defined for each polytype. Note that depending on where the 'A' label starts in the bilayer, the stacking sequence notation may vary. For example, in some references, the stacking sequence 'ABAC' may be used to describe 4H−SiC, but is equivalent to the 'ABCB' notation presented here. At the end of the bilayer stacking sequence along the crystallographic $c-$axis direction, the choice of where the surface layer is terminated will result in a SiC surface either rich in Si (Si−face) or C atoms (C−face), as schematically shown in Fig. 2.1 for the 4H−SiC polytype. When oxidised, the surface layer termination can have profound effects on

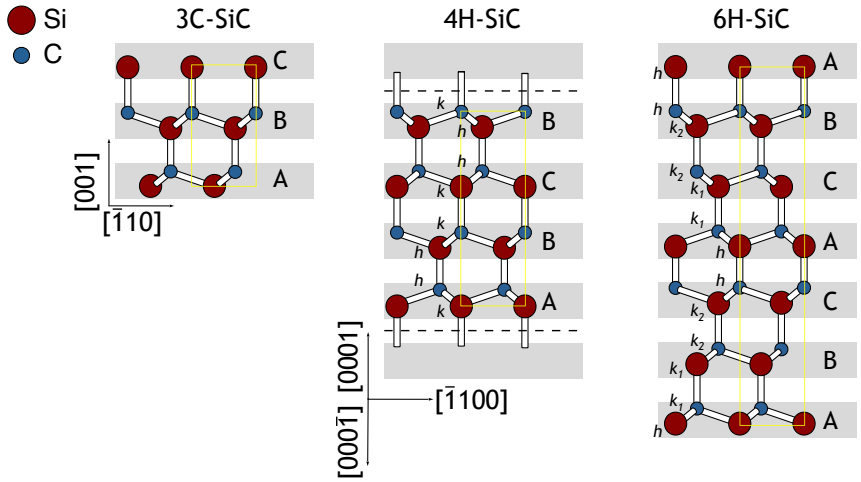

Fig. 2.1.: Illustration of the 3C−, 4H−, and 6H− SiC polytype stacking sequence along the [0001] crystallographic c−axis. For the 4H−SiC polytype, the termination along the [0001] direction results in a surface layer rich of C atoms (C−face), whereas the termination along the [000$\bar{1}$] direction results in a surface layer rich of Si atoms (Si−face). Quasi-hexagonal (h) and quasi-cubic (k) inequivalent sites are also denoted where relevant. Figure adapted from original artwork of Brett Johnson.

the SiC/SiO_2 interface properties, as will be seen in Sec. 2.2 where different types of spin defects can form exclusively at the oxide interface formed on the Si−face and the C−face.

A Si or C atom in the bilayer can be further distinguished using (h) or (k) to denote whether the local environment to the second-nearest neighbour around the lattice site occupied is quasi-hexagonal or quasi-cubic, respectively. The presence of inequivalent quasi-hexagonal and quasi-cubic sites results in the so-called site-effect [52], where dopant and defect energy levels are site dependent. As an example, two different ionization energies are provided in Table 2.1 for the N donor in 4H−SiC dependent on which lattice site is occupied. Note that the number of inequivalent (h) and (k) sites is different for each polytype, where atoms in the 3C−polytype only exist in the quasi-cubic site, while atoms in the 4H−polytype can exist either in the quasi-hexagonal or quasi-cubic site. For the 6H− polytype, there exists two non-equivalent quasi-cubic sites further denoted using (k_1) and (k_2).

The spin properties of defects situated on inequivalent lattice sites are also site-dependent, where substantially different coherence times have been previously reported for the c−axis (kk) and basally (kh) oriented divacancy

due to the different hyperfine fields the divacancy experiences from nearby nuclear spins [40]. Similarly, spin parameters such as the g−factor and hyperfine interaction strength summarised in Table 2.2 for a particular spin defect will also be site-dependent. Thus, angular dependent magnetic resonance measurements with the magnetic field parallel and perpendicular to the $c-$axis are particularly important for SiC in resolving all the possible site-dependent atomic configurations.

2.1.2 Doping

For the spin-dependent recombination readout process considered for this work, both majority and minority charge carriers are required, which can be introduced by doping. Incorporation of dopants into SiC epitaxial layers can be achieved by the introduction of N_2 or $AlCl_3$ from a gaseous source during the chemical vapour deposition (CVD) epitaxial growth process for n-type and p-type doping, respectively. N preferentially incorporates itself into the SiC lattice site usually occupied by a C atom, whereas Al preferentially incorporates itself into the SiC lattice site usually occupied by a Si atom [53]. For selective doping, ion implantation at elevated temperatures is required. The low dopant diffusion coefficients in SiC even at elevated temperatures [54] mean that doping through a diffusion process is not practical. Ion implantation is usually carried out between $\sim 500 - 800°$C to simultaneously minimise defect formation and avoid amorphization [44]. A subsequent high temperature ($\sim 1200 - 1800°$C) activation anneal is carried out to achieve maximum dopant activation. Hot implants have been shown to be crucial in achieving high quality Ohmic contact in SiC with low contact resistance [55, 56]. At elevated temperatures, the SiC surface morphology is known to severely degrade due to sublimation of Si atoms from the SiC surface [57]. Thus, prior to ion implantation a thin carbon film is usually grown on the SiC surface to avoid degradation of the surface morphology [44].

Commonly used dopants in SiC all have a non-zero nuclear spin and may contribute to the hyperfine interaction. For n-type doping, ^{31}P (100%) has a nuclear spin of $I = 1/2$, whereas N has two stable isotopes with ^{14}N (99.63%) and ^{15}N (0.37%) having a nuclear spin of $I = 1$ and $I = 1/2$, respectively. For p-type doping, ^{27}Al (100%) has a nuclear spin of $I = 5/2$, whereas B

has two stable isotopes with ^{10}B (19.9%) and ^{11}B (80.1%) having a nuclear spin of $I = 3$ and $I = 3/2$, respectively. During the ion implantation process, a 90° magnet is used to mass select which isotope is to implant into the SiC sample, with the isotope having the highest natural abundance typically chosen.

The smaller dopant ionization energy and larger carrier mobility found in 4H$-$SiC compared to 6H$-$SiC make it the more suitable polytype for electronic device fabrication, as summarized in Table 2.1. Due to the large acceptor ionization energy in comparison with the donor ionization energy regardless of polytype, the acceptor state is not completely ionised even at room temperature. This contributes to higher contact resistance in p$-$type SiC devices [55, 56]. Furthermore, complete carrier freeze-out can occur at around $150 - 200$ K in p$-$type SiC devices at moderate doping concentrations [58]. Similarly, complete carrier freeze-out for n$-$type SiC devices can occur at slightly lower temperatures due to its smaller ionization energy compared to acceptor dopants. As such, SiC electronics are generally not suitable for low temperature operation unless it is highly doped or optical carrier injection are utilised. Carrier freeze-out effects will be experimentally observed in Chapter 6.

2.1.3 SiC/SiO_2 interface

Like Si, SiC can form a stable insulating SiO_2 oxide layer on its surface when exposed to O atmosphere, enabling a straightforward method to fabricate CMOS devices, unlike diamond and other wide bandgap semiconductors. However, defects residing within the oxide layer and at the SiC/SiO_2 interface can have profound effects on the oxide quality and device performance. Additionally, the additional C atom in the stoichiometric composition of SiC compared to Si introduces an additional degree of complexity, resulting in a much higher defect density at and near the SiC/SiO_2 interface compared to the Si/SiO_2 interface as more defect bonding configurations are possible [46]. Thus, significant effort has been devoted to improving the SiC/SiO_2 interface quality as high interface defect density is closely linked to poor channel mobility and the voltage shift instability phenomenon in SiC metal-oxide-semiconductor field-effect transistor (MOSFET) devices [33, 59, 60].

The carbon cluster model proposed by Afanasev et al. [61] is generally widely accepted as the most complete model so far describing the density of states at the SiC/SiO_2 interface. In this model, the SiC/SiO_2 interface consists of incomplete paramagnetic Si and C dangling bonds, graphitic-like and sp^2 $\pi-$bonded carbon clusters, and near interfacial oxide traps (NIOTs). Only the sp^2 $\pi-$bonded carbon clusters and the NIOTs are thought to have a significant contribution to the interface density of states in the SiC bandgap. Thus, electrical characterisation techniques of the SiC/SiO_2 interface, such as capacitance-voltage (CV), impedance spectroscopy, deep level transient spectroscopy (DLTS), and EDMR are only sensitive to these types of defects. Furthermore, the long time constants of interface defects in the wide bandgap of SiC means that only interface traps situated $0.6 - 0.7$ eV away from the

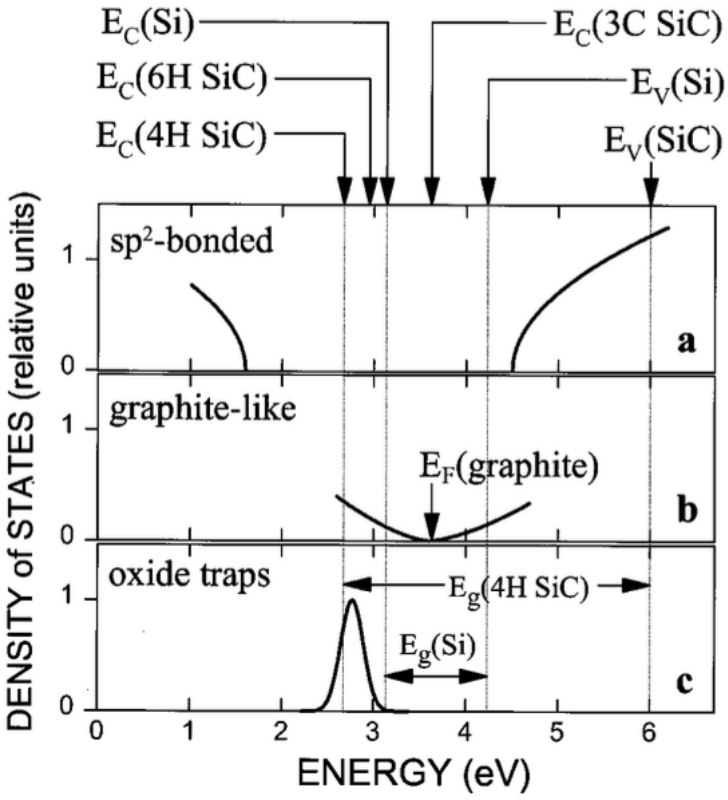

Fig. 2.2.: Illustration of the various contributions to the density of states at the SiC/SiO_2 interface described using the carbon cluster model for various SiC polytypes in comparison with Si. All energies are referenced with respect to the conduction band minimum of SiO_2 situated at 6 eV. The figure is reproduced from Ref. [61].

band edge are detectable at room temperature and elevated temperatures above $350°$C are required to detect midgap states [62]. A schematic of the various sources contributing to the interface density of states for different SiC polytypes in comparison with Si is shown in Fig. 2.2. All energies are referenced with respect to the conduction band minimum of SiO_2 situated at 6 eV. Unlike Si dangling bonds that play an integral role in the Si/SiO_2 interface density of states, the Si and C dangling bonds theoretically calculated to be situated in the bottom half of the bandgap in SiC are thought to play a minor role in the interface density of states and are therefore not included in Fig. 2.2. However more recently, the carbon dangling bond has been measured with EDMR, suggesting the carbon dangling bond has a larger contribution to the interface density of states than previously anticipated by the carbon cluster model. This will be discussed in more detail in Sec. 2.2.1.

From Fig. 2.2, the SiC/SiO_2 interface density of states is asymmetric and skewed toward the valence band edge, where interface state densities are typically on the order of 10^{13} cm^{-2} [61]. This is in stark contrast to the Si/SiO_2 interface in which the interface density of states consists only of a broad 'U-shaped' continuum of states due to band-tail states and two broad peaks associated with the Si dangling bond [63–65]. The two broad peaks are amphoteric in nature and are situated in the bottom and top half of the bandgap at around $E_V + 0.3$ eV and $E_V + 0.8$ eV, respectively, corresponding to the $0 \leftrightarrow 1$ and $1 \leftrightarrow 2$ electron transitions. As the Fermi level is near the valence band edge, the Si dangling bond is able to trap holes, whereas the Si dangling bond traps electrons when the Fermi level is near the conduction band edge. In the carbon cluster model for SiC, the interface state density is directly proportional to the C concentration at the interface. Thus, the interface density of states is higher at the $C-$face SiC/SiO_2 interface compared to the $Si-$face. While the exact atomic structure of the different types of C clusters are unknown and somewhat controversial, it is thought that the graphitic-like C clusters are larger in size and also amphoteric in nature.

In $4H-$ and $6H-$SiC, the NIOTs give rise to a high density of states near the conduction band edge and are also thought to be responsible for the voltage shift instability phenomena [59, 60]. These NIOTs have a binding energy of around 2.77 eV relative to the SiO_2 valence band edge [61] and hence are

situated near the conduction band edge in 4H− and 6H− SiC. Conversely, NIOTs are not detected in the smaller bandgap 3C−SiC. Spatially, these defects are situated within the SiO_2 matrix sufficiently close enough ($\sim 1.5-2.0$ nm) to the SiC/SiO_2 interface to electrically communicate with the substrate through both a tunnelling mechanism and a carrier capture/emission process [66]. Early reports suggest that these defects may be related to oxygen vacancies generated during the oxidation process [61]. Subsequent theoretical studies proposed alternative atomic configurations, including interstitial Si atoms and doubly bonded C−C dimers [67] or a Si_2−C−O defect complex [68]. Further experimental evidence suggests that NIOTs encompass a whole family of defects with different atomic origins [67, 69, 70]. Their identification and quantification remains an active area of research and understanding the SiC/SiO_2 interface is key to unlocking the full potential of SiC electronic devices.

2.1.4 Defect formation

In addition to oxidation, defects can arise during crystal growth, device fabrication, and even during device operation, especially in the radiation-harsh and high temperature environments SiC devices are typically operated under. All can have profound effects on the device properties, however, spin defects that behave like isolated atomic qubits are particularly promising for quantum applications. Here, we will summarise some of the processes that can result in the formation of defects in SiC.

Significant progress in SiC crystal growth over the past decades primarily driven by the high power SiC electronics industry have resulted in the production of high quality wafers essentially free of large macroscopic defects, including stacking faults, micropipes, and carrots [71]. However, intrinsic point defects consisting of vacancies (V_{Si} and V_C), antisites (Si_C and C_{Si}), interstitials (Si_i and C_i), and defect-pairs, such as the divacancy ($V_{Si}V_C$) can still exist. At elevated temperatures, these point defects can go on to form new defect complexes and secondary extended defects.

Standard fabrication processing steps, including oxidation, surface passivation, selective doping via ion implantation, and contact formation can all unintentionally further generate point defects. As an example, excess C

atoms are injected into the SiC bulk as interstitials during oxidation and can go on to form C clusters and a graphitic-like transitional layer between the oxide and the SiC bulk, creating a C-rich environment near the SiC/SiO_2 interface, as proposed by the carbon cluster model [61] in Sec. 2.1.3. Conversely, high energy particle [72], $\gamma-$ray [73, 74], and laser [75] irradiation are commonly used to intentionally break bonds and displace atoms off their lattice site such that vacancy-related spin defects are selectively created locally for quantum applications. Subsequent annealing strategies may be applied to repair some of the irradiation-induced damage and improve the spin coherence properties.

During device operation, it has been previously reported that the threshold voltage of SiC transistor devices experiences instability over time, which is particularly pronounced when a large negative bias is applied to the gate contact at elevated temperatures. This phenomenon is called negative bias temperature instability (NBTI), a significant transistor reliability issue in SiC, and is understood in terms of a combination of hole trapping by interface defects and the generation of interface traps [76]. This can be partially reversible by the de-trapping of the captured holes. The ability to selectively control defect formation with high spatial resolution while reducing undesired background residual defects will be crucial for fabricating future quantum technology devices.

2.2 A brief spin defect survey

We now turn our attention to the different types of spin defects that can be formed in SiC, specifically the ones that have been previously measured with the EDMR technique. Prior to the development of the EDMR technique, an extensive ESR literature dating back as early as the 1990's on intrinsic spin defects in SiC formed by particle irradiation and ion implantation have helped identify several technologically important spin defects, including the negatively charged silicon vacancy [39, 77, 78] and the neutral divacancy [79], which also turn out to be optically active. Extrinsic paramagnetic impurities in SiC have also been studied in detail, particularly transition metal impurities (e.g., V, Mo, and Ti [80, 81]) and dopant-defect complexes like the $N_C V_{Si}$ defect centre [82–85] (the SiC counterpart of the NV centre in diamond).

Center	Label	Site	$g_{\parallel}$	$g_{\perp}$	$A_{\parallel}$ (MHz)	$A_{\perp}$ (MHz)	D_1 (MHz)	D_2 (MHz)	Comments	Ref.
V_{Si} (-) (S=3/2)	T_{V1a}	h	2.0029		---		2.5	---	- V_{Si} becomes mobile at 700°C to form other defect complexes - Optically addressable with 808 nm photoexcitation	ESR: [39], [77], [78], [92]
					^{13}C: 80.2	^{13}C: 32.9				
	T_{V2a}	k			^{29}Si: 8.7		35	---		
					^{13}C: 80.0	^{13}C: 34.5				
	---	Interface	2.0030		---		---		- Observed in BJT, MOSFET, and pn junction devices	EDMR: [9], [10], [86], [87], [95]
					^{13}C: 78.5	^{13}C: 36.4				
$V_{Si}V_C$ (0) (S=1)	P6b	hh	2.0030		See Ref. [87]		1340	---	- Thermally stable up to 1500°C - Optically addressable with 795 nm photoexcitation	ESR: [79]
	P6'b	kk					1307	---		
	P7b	kh					1340	270		
	P7'b	hk					1223	30		
	P8a P8b	Interface	---	---	---		1400 1200	≤ 28	- Observed only at C-face SiC/SiO_2 interface formed by wet oxidation	EDMR: [99]
P_{bC} (S=1/2)	---	Porous SiC/SiO_2	2.0023	2.0032	---		---		- No paramagnetic Si dangling bonds are observed with ESR	ESR: [98]
					^{13}C: 219	^{13}C: 105				
	---	SiC (0001)/SiO_2	2.0029	2.0032	^{29}Si: 185				- Observed only at Si-face SiC/SiO_2 interface formed by dry oxidation	EDMR: [89], [91]
					^{13}C: 664	^{13}C: 451				
$C_{Si}V_C$ (+) (S=1/2)	HEI9a	hh	2.0023	2.0041	^{29}Si: 47.6-81.3		---		- Electron irradiated p-type SiC - Thermally stable up to 1100°C - Can exist in the (2+), (+), (0), (-), (2-), and (3-) charge state with the (2-) charge state unstable	ESR: [102], [103]
					^{13}C: 231	^{13}C: 64				
	HEI9b	kk	2.0020	2.0038	^{29}Si: 47.6-81.3					
					^{13}C: 279	^{13}C: 104				
	HEI10a	kh	2.0023	g_{xx}: 2.0035 g_{yy}: 2.0026	^{29}Si: 47.6-81.3					
					^{13}C: 245	$^{13}C_{xx}$: 73 $^{13}C_{yy}$: 74				
	HEI10b	hk	2.0026	g_{xx}: 2.0040 g_{yy}: 2.0035	^{29}Si: 47.6-81.3					
					^{13}C: 237	$^{13}C_{xx}$: 65 $^{13}C_{yy}$: 69				
	C-face defect	Interface	2.0018	2.0027	^{1}H: 31				- Observed only at C-face SiC/SiO_2 interface formed by wet oxidation	EDMR: [73], [99], [100], [101]
					^{13}C: 224	^{13}C: 59				
N_CV_{Si} (-) (S=1)	---	hh	2.0029	2.0035	^{14}N: 1.23 ^{29}Si: 10.3		1313	---	- Optically addressable with 980 nm photoexcitation - Thermally stable up to 1500°C - Accessible in the (0), (-), and (2-) charge state	ESR: [82], [83], [84], [85]
					^{13}C: 133.3	$^{13}C_{xx}$: 63.2 $^{13}C_{yy}$: 62.4				
	---	kk	2.0029	2.0036	^{14}N: 1.12 ^{29}Si: 11		1270	---		
					^{13}C: 126.2	$^{13}C_{xx}$: 56.4 $^{13}C_{yy}$: 55.6				
	---	(0) charge state	2.0054	2.0006	^{14}N: 36.4 ^{13}C: 117.7		---		- Observed in SiC pn junctions formed by N ion implantation	EDMR: [108], [109]

Tab. 2.2.: Spin parameters of previously assigned spin defects in 4H−SiC with ESR and EDMR. Values may slightly vary depending on references used. The principle axis ($\parallel$) is aligned with the c−axis ($[0001]$).

The spin properties and schematics of their different atomic configurations in the 4H−SiC polytype considered in this section are summarised in Table 2.2 and Fig. 2.3, respectively. Note that the spin properties summarised in Table 2.2, including the g−factor, hyperfine coupling strength, and dipolar coupling strength will be formally defined in Chapter 3, but in short these values are unique for each spin defect and are commonly used for defect identification. Due to the limited amount of research groups worldwide able

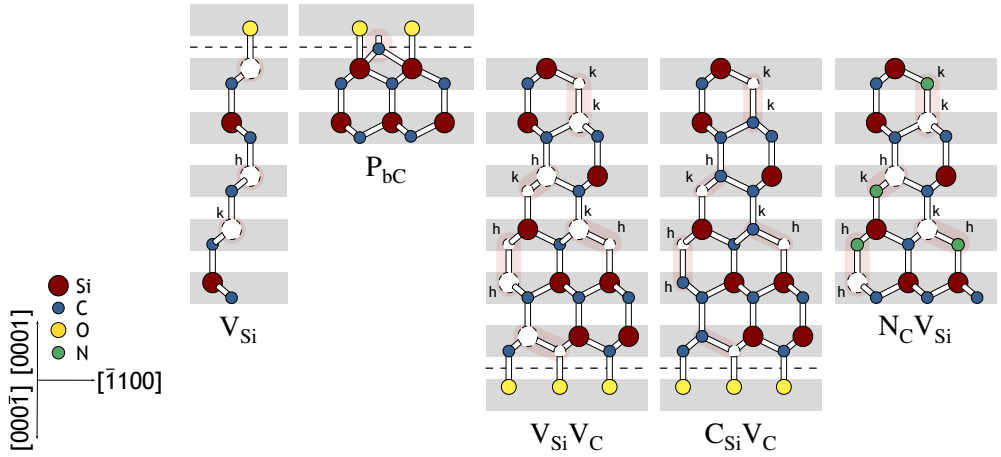

Fig. 2.3.: Atomic structure of previously identified spin defects in 4H−SiC summarised in Table 2.2 and their possible bonding configurations. Quasi-hexagonal (h) and quasi-cubic (k) inequivalent sites are also denoted where relevant.

to perform such EDMR measurements and the complicated nature of the spin-pair recombination readout mechanism, SiC spin defects that have been unambiguously identified with the EDMR technique remains elusive and these assignments heavily borrow upon the spin parameters previously measured with ESR instead. For reference, these ESR values are also summarised in Table 2.2. The types of spin defects that have been previously observed with EDMR can be generally grouped into three categories: spin defects situated at the SiC/SiO_2 interface formed on the Si−face, interface defects formed on the C−face, and spin defects in the SiC bulk. Each category will be explored in more detail below. We note that while this thesis does not directly address the identification of spin defects measured in the experimental chapters, it is still beneficial to understand how the EDMR technique can be applied to SiC and what has been already measured previously in the literature.

2.2.1 Si−face SiC/SiO_2 interface defects

An EDMR signal response can be readily measured from the SiC/SiO_2 interface formed by dry oxidation on the Si−face. Currently, the silicon vacancy and the carbon dangling bond are two candidates proposed by the Lenahan [10, 86–88] and Umeda group [89–91], respectively, as the

electrically active spin defect responsible for the interfacial EDMR response. Below, we will first review the silicon vacancy, which has also been studied extensively with ESR.

The negatively charged silicon vacancy in the SiC bulk was first detected in particle irradiated 3C$-$SiC crystals with ESR, exhibiting a ground state spin manifold of $S = 3/2$ [92]. In the 4H$-$ polytype, the silicon vacancy can occupy either the (h) or (k) lattice site, labelled $\mathrm{T_{v1a}}$ and $\mathrm{T_{v2a}}$, respectively. A characteristic of the high spin manifold is the presence of zero-field splitting (ZFS $= |2D_1|$) between the $m_s = \pm 1/2$ and $m_s = \pm 3/2$ spin states. For the silicon vacancy, ZFS is observable only in the SiC polytypes with hexagonal symmetry. Optically, the V1 and V2 photoluminescence (PL) lines at 868 and 917 nm in 4H$-$SiC are correlated to $\mathrm{T_{v1a}}$ and $\mathrm{T_{v2a}}$, respectively, which can be detected with ODMR under resonant excitation [93]. More recently, Niethammer et al. [94] demonstrated a hybrid approach in which the silicon vacancy was initialised optically and detected electrically using a spin-dependent photoionisation readout process.

Extensive EDMR studies from the Lenahan group [10, 86, 87, 95] have identified $\mathrm{V_{Si}}$ situated near or at the SiC/$\mathrm{SiO_2}$ interface as the main electrically active defect species at the interface, which extends well into the SiC bulk in a wide range of devices, including SiC MOSFETs, bipolar junction transistors (BJTs), and pn junctions. In all the devices measured, an isotropic g$-$factor between $2.0026-2.0031$ have been reported [9, 86, 87]. The assignment of $\mathrm{V_{Si}}$ comes about from comparing the measured EDMR hyperfine spectrum with the averaged ESR anisotropic hyperfine splitting values for ^{13}C previously measured in Ref. [39]. No ZFS has been observed for $\mathrm{V_{Si}}$ with EDMR as it is suggested the EDMR response corresponds to the $m_s = \pm 1/2$ to $m_s = \mp 1/2$ spin transition that is degenerate at zero magnetic field [87]. It is unclear why the $m_s = \pm 1/2$ to $m_s = \mp 1/2$ spin transition is preferentially detected electrically and whether $m_s = \pm 1/2$ to $m_s = \pm 3/2$ transitions are also detectable with EDMR. While silicon vacancies become mobile at 700°C and gradually anneals out at 1200°C [78], the even higher thermal budget employed for SiC device fabrication typically above 1500°C for oxidation and dopant activation suggests the unintentional creation of $\mathrm{V_{Si}}$ from ion implantation for the formation of n-type and p-type regions, for example, is unlikely to survive post-fabrication.

The alternative candidate for the dominate electrically active defect species at the SiC/SiO_2 interface is the P_{bC} center proposed by the Umeda group [89–91] with a spin manifold of $S = 1/2$. It was first previously measured with ESR by Cantin et al. [98] in oxidised porous SiC samples. The discrepancies between the anisotropic g−factor and hyperfine parameters measured with ESR and EDMR summarised in Table 2.2 are attributed to the atomic structural differences in the P_{bC} center residing either in the porous or interfacial environment, respectively. It was previously shown that by utilising various post-oxidation annealing (POA) strategies, a decrease in the P_{bC} density was correlated to an increase in the transistor channel field-effect mobility μ_{FE} [91]. It is speculated that P_{bC} centres can trap mobile electrons in the channel and act as a scattering center, negatively impacting μ_{FE}. Thus, a direct correlation between the spin density of the P_{bC} centre and the channel mobility is established. This result may suggest that the carbon dangling bond may play a non-negligible and larger role in the SiC/SiO_2 interface state density than previously anticipated in the carbon cluster model [61]. Given its close correspondence to the P_b centre at the Si/SiO_2 interface, it is expected that the P_{bC} centre at the SiC/SiO_2 interface is also amphoteric in nature and located near the midgap [89].

The assignment of V_{Si} as the dominant electrically active defect at the SiC/SiO_2 interface remains highly debated. Works by Gruber et al. [96] and Cottom et al. [97] from the same research group have both pointed out several inconsistencies and discrepancies within the works of the Lenahan group in terms of the wide range of g−factors quoted and the somewhat different hyperfine spectrum reported dependent on the device measured and experimental conditions used. Instead, Gruber et al. [96] have demonstrated using the hyperfine parameters of the carbon dangling bond (P_{bC}) taken from the ESR literature that it is a better candidate to explain the measured EDMR spectrum. This is subsequently followed up by the work of Cottom et al. [97] in which experimental EDMR spectra and hyperfine parameters were compared with ab initio calculations. It was demonstrated that the EDMR spectrum can be reasonably explained by a combination of the carbon dangling bond and the dual carbon dangling bond defect (i.e., two adjacent weakly correlated P_{bC} defects), although small concentrations of V_{Si} was not entirely ruled out.

The assignment of the P_{bC} center has been previously challenged by Anders et al., [95] from the Lenahan group in which they argue that the P_{bC} center does not play a significant role in the interface state density since the ESR P_{bC} g−factor for oxidised porous SiC does not match up with the resonant field of the EDMR spectrum measured under charge pumping conditions, where the majority of the bandgap was sampled at K-band (~ 16 GHz) frequencies. Instead, a broad resonance response centred about the resonant field corresponding to an isotropic g$= 2.0030$ was measured which they assign to the V_{Si}. This interpretation was then refuted by Cottom et al. [97] and the discrepancy was attributed to the different amounts of spectral broadening from the local strain at the interface (proportional to the interfacial quality) between the different SiC devices studied by the various research groups. Different experimental setups and operating modes, including fast passage [86], charge pumping [87, 95], and conventional EDMR may also give rise to this discrepancy in the literature.

It is currently not possible to completely rule out one defect candidate over the other as the dominant electrically active defect at the SiC/SiO_2 interface and further work is required. Defect identification based on comparison of g−factor and hyperfine parameters with known ESR values may not be adequate, which is further complicated by the disordered nature of the SiC/SiO_2 interface that may introduce spectral broadening. Correlation with alternative techniques, such as pEDMR may provide new insight on the atomic origin of the paramagnetic interface defect previously not accessible with standard cwEDMR and the use of isotopically enriched SiC samples may help resolve weak hyperfine structure.

2.2.2 C−face SiC/SiO_2 interface defects

At the SiC/SiO_2 interface formed on the C−face by wet (i.e., water vapour-rich H_2O environment) oxidation instead of the Si−face interface formed by thermal oxidation described above, a different type of interfacial defect, also known as the C−face defect, has been reported [99–101]. The dominant EDMR signal was assigned to an interfacial carbon antisite carbon vacancy complex ($C_{Si}V_C$) in the positive charge state based on its hyperfine parameters being similar to values previously measured for $C_{Si}V_C$ in the SiC bulk with

ESR [102]. In ESR, the positively charged carbon antisite carbon vacancy complex, previously labelled as HEI9a/b and HEI9a/b, can form four possible bonding configurations in p−type 4H−SiC (see Table 2.2). The apparent inconsistency in the anisotropic g−factors measured with EDMR and ESR is attributed to the disordered nature at the SiC/SiO_2 interface compared to the SiC bulk [99]. In the negative charge state, the $C_{Si}V_C$ complex is also spin active and has been previously assigned to the SI5 center [103]. In the neutral charge state, the $C_{Si}V_C$ complex, although spin inactive, photoluminesces at emission wavelengths between $648.5 - 676.4$ nm, labelled the AB lines [104].

To observe the C−face defect with EDMR, a large negative gate bias is required by supplying holes to the interface to bring the defect complex from its neutral charge state with $S = 1$ spin manifold into its positively charged state with $S = 1/2$ spin manifold. In its neutral charge state, the doubly occupied $C_{Si}V_C$ does not capture mobile electrons in the channel region and negatively impact the channel mobility. This is consistent with the observation of SiC transistors fabricated on the C−face boasting a higher channel mobility, despite the presence of C−face defects at moderate concentrations. The unpaired electron on the C_{Si} atom can be H−passivated, significantly reducing the $C_{Si}V_C$ concentration. Conversely, a depassivation process can be achieved by γ−irradiation, breaking H−passivation at the oxide interface [73]. These two fabrication processes offer a potential simple method to precisely control the C−face defect concentration.

A weaker set of interface defects were also observed along with the $C_{Si}V_C$ defect center at the SiC/SiO_2 interface formed by wet oxidation on the C−face, labelled the $P8a$ and $P8b$ center [99]. These defect centres were tentatively assigned to interfacial divacancies $V_{Si}V_C$ in the basal (hk and kh) configuration based on their dipolar coupling parameters arising from their high $S = 1$ spin manifold being similar to values measured for $V_{Si}V_C$ using ESR in the SiC bulk [79]. In the SiC bulk, $V_{Si}V_C$ can form four possible bonding configurations, labelled $P6b/P6b'$ (c−axis) and $P7b/P7b'$ (basal). Similar to the $C_{Si}V_C$ defect complex, a large negative gate bias is required to tune the charged state of $V_{Si}V_C$ to observe its EDMR response.

In the SiC bulk, the four bonding configurations of the divacancy correspond to the four UD−2 photoluminescence lines situated between $1077 - 1132$

nm [105]. Both $C_{Si}V_C$ [106] and $V_{Si}V_C$ [105] are well known SPSs in the SiC bulk and more recently SPSs in wet-oxidized C−face MOSFETs have been observed [107]. Conversely, no SPSs were observed in MOSFETs fabricated on the Si−face or with dry oxidation. The higher channel mobility in wet oxidized C−face MOSFETs along with the existence of multiple spin defects that may act as SPSs highlight the significant differences in surface chemistry and its importance for future SiC devices compared to the more established dry oxidized Si−face SiC/SiO_2 interface.

2.2.3 Spin defects in the SiC bulk

While the majority of the literature focuses on defects at the SiC/SiO_2 interface that are directly correlated with the SiC transistor device performance, EDMR studies on spin defects in the SiC bulk is limited. An extrinsic spin defect formed as a result of N implantation has been consistently observed in 4H−SiC pn junction devices, which may have a non-negligible effect on the quality of the n−type doping. This N−related defect has an anisotropic g−factor of $g_{||} = 2.0048$ and $g_{\perp} = 2.0005$, as reported by Aichinger et al., [108]. A similar anisotropic g−factor of $g_{||} = 2.0054 \pm 0.0004$ and $g_{\perp} = 2.0006 \pm 0.0004$ was reported by Cottom et al., [109]. Within experimental uncertainty, both reports are likely observing the same N-related defect complex. Density functional theory (DFT) calculations suggest the nitrogen silicon vacancy complex N_CV_{Si} in its neutral charged state with $S = 1/2$ spin manifold best describes the experimentally measured EDMR spectrum. Further work is required to unambiguously confirm this tentative assignment. While the neutrally charged NV center in 6H−SiC has been previously observed with ESR [82], a direct correlation with results from EDMR measurements has not yet been established. Instead, the negatively charged NV center in SiC, has been extensively studied with ESR. It exhibits a $S = 1$ spin manifold and was found to photoluminescence at 1252 and 1291 nm in the axial configuration (hh and kk) [83–85, 110].

2.3 Summary

The relevant properties of SiC are introduced in this chapter from both an electronic device and quantum materials platform perspective. A brief survey of previously identified spin defects in SiC with EDMR was then summarised. These spin defects can act as recombination centres and affect the electrical properties of the measured device, while offering unique spin properties for future quantum technologies. Definitive identification of their atomic structure remains an elusive and challenging pursuit, however, these spin defects will more than likely play a significant role in future SiC quantum devices.

3 Principles of magnetic resonance

This thesis focuses on utilising the spin properties of paramagnetic defects in SiC for quantum sensing applications measured using the EDMR technique. As such, the theory behind the SDR mechanism is reviewed in this chapter, thereby laying the fundamental basis for the later experimental chapters. Starting with an introduction on ESR for a spin ensemble, the theoretical framework is then extended to describe a spin-pair ensemble involved in the SDR process for EDMR. Lastly, the coherent spin dynamics of the spin-pair in the time-domain are then reviewed, which will be required to interpret the experimental results in Chapter 7.

3.1 Electron spin resonance

In the presence of an external magnetic field ($\mathbf{B} = B_0\,\hat{\mathbf{z}}$), a free electron with a magnetic moment and spin $S = 1/2$ acts like a compass and aligns itself either parallel ($m_s = -1/2$) or anti-parallel ($m_s = +1/2$) with the external magnetic field. As the quantum mechanical property spin is quantised, the energy splitting between the two spin states is

$$\Delta E = g\mu_B B_0 \Delta m_s \,, \tag{3.1}$$

where g is the Landé g$-$factor, μ_B the Bohr magneton, and $\Delta m_s = \pm 1$ is the allowed spin state transition. This is called the Zeeman effect and was first observed in 1896 for the splitting of atomic spectral lines into multiple components in the presence of a static external magnetic field [111]. In the absence of a magnetic field, the two spin states are energetically degenerate and the introduction of a magnetic field lifts this degeneracy. Spin transitions

can be induced by introducing electromagnetic (EM) radiation of frequency ν matching the energy level splitting

$$\Delta E = g\mu_B B_0 = h\nu \,, \tag{3.2}$$

where h is the Planck constant. For a non-interacting and isolated free electron, $g_e \approx 2.002319$ [112]. Experimental values that deviate from g_e in a solid-state environment, for example, contain information about the magnetic environment around the unpaired electron and serve as a fingerprint for that paramagnetic state. This will be discussed in more detail in Sec. 3.3.1.

In a continuous-wave (cw) measurement, ESR is performed by fixing the frequency and power of the EM radiation and sweeping the magnetic field through the resonance condition in Eq. 3.2, while the power of the EM radiation is monitored. In most commercial ESR spectrometer setups, a sample is placed inside a rectangular TE_{102} cavity resonator operated at X-band microwave (MW) frequencies ($\nu \approx 9.8$ GHz), corresponding to a resonant field at $B_0 \approx 350$ mT. At the resonance condition, the reflected MW power from the cavity resonator is reduced as the sample absorbs $h\nu$ amount of photon energy to induce spin transitions. The ESR signal intensity is then proportional to the spin population difference in the spin down and spin up state, $\Delta N = N_\downarrow - N_\uparrow$, which can be calibrated against a known sample with a well-defined spin concentration. In thermal equilibrium, this is governed by Boltzmann statistics

$$\Delta N = N_\downarrow - N_\uparrow = 1 - \exp(-\Delta E/k_B T) \,, \tag{3.3}$$

where k_B is the Boltzmann constant and T the temperature. The relative population difference, $\Delta N/N_0 = (N_\downarrow - N_\uparrow)/(N_\downarrow + N_\uparrow)$, also known as the spin polarization, is dependent on the temperature and the Zeeman energy splitting, ΔE, which in turn is dependent on the EM radiation frequency. Under typical experimental conditions employed for a commercial ESR spectrometer at room temperature ($T = 298$ K), a spin polarization of only 0.079% is achieved. This places a lower limit on the sensitivity and the total number of spins, N_0, that can be detected with ESR, which is typically around 10^{11} spins/mT linewidth for a commercial X-band ESR spectrometer [113].

In the following section, the equations of motion of a spin ensemble will be considered using classical mechanics, which will reveal how the net magnetization of a spin ensemble, proportional to the spin concentration, is related to the MW absorption measured in an ESR experiment.

3.2 Bloch equations

In classical mechanics, an electron can be modelled as a magnetic dipole with a magnetic moment, $\boldsymbol{\mu}$. When placed inside an external magnetic field, $\mathbf{B_0}$, the electron experiences a torque

$$\boldsymbol{\tau} = \frac{d\mathbf{J}}{dt} = \boldsymbol{\mu} \times \mathbf{B_0} \,, \tag{3.4}$$

with $\mathbf{J}$ the angular momentum vector. The magnetic moment and angular momentum are related by the gyromagnetic ratio

$$\gamma = \frac{\boldsymbol{\mu}}{\mathbf{J}} = \frac{q}{2m_e} \,, \tag{3.5}$$

where q is the electronic charge and m_e is the electron mass. Assuming the external magnetic field points solely in the $\hat{\mathbf{z}}$ direction for simplicity, the three Cartesian components of the torque are

$$\frac{d\mu_x}{dt} = \gamma \mu_y B_0 \tag{3.6a}$$

$$\frac{d\mu_y}{dt} = -\gamma \mu_x B_0 \tag{3.6b}$$

$$\frac{d\mu_z}{dt} = 0 \,. \tag{3.6c}$$

Eqs. 3.6(a)−3.6(c) are a set of coupled first order ordinary differential equations (ODEs) that can be solved trivially. Its solution takes on the form

$$\mu(t) = \mu(0) e^{-i\omega_0 t} = \mu(0)[\cos(\omega_0 t) - i \sin(\omega_0 t)] \,, \tag{3.7}$$

where $\omega_0 = \gamma B_0$ is the Larmor frequency. The $\hat{\mathbf{x}}$ and $\hat{\mathbf{y}}$ components of the magnetic moment can be retrieved from the real and imaginary parts of Eq. 3.7, respectively, and the $\hat{\mathbf{z}}$ component of the magnetic moment is equal to a constant

$$\mu_x(t) = \mu(0)\cos(\omega_0 t) \tag{3.8a}$$
$$\mu_y(t) = -\mu(0)\sin(\omega_0 t) \tag{3.8b}$$
$$\mu_z(t) = const\,. \tag{3.8c}$$

Physically, Eqs. 3.8(a)−3.8(c) describe the transverse components of the electron spin magnetic moment precessing around the $\hat{\mathbf{z}}$ axis at the Larmor frequency, while the longitudinal magnetization remains constant as a function of time in a static magnetic field from the perspective of a stationary observer in the laboratory frame of reference.

For an ensemble of spins in a solid-state host, the magnetization of a material is defined as the sum of the net magnetic moments

$$\mathbf{M} = \sum_i \boldsymbol{\mu_i}\,. \tag{3.9}$$

The magnetization vector will also experience a torque when placed inside an external magnetic field

$$\boldsymbol{\tau} = \frac{d\mathbf{M}}{dt} = \gamma(\mathbf{M} \times \mathbf{B_0})\,. \tag{3.10}$$

As the spins in the ensemble can now interact with its surrounding, the net magnetization can decay over time. In 1946, Felix Bloch [114] introduced two phenomenological time constant terms, T_1 and T_2, to describe the net magnetisation decay due to spin-lattice and spin-spin interaction within the ensemble of spins, respectively, and the equations of motion for magnetization in Eq. 3.10 now become

$$\frac{dM_x}{dt} = \gamma(M_y B_z - M_z B_y) - \frac{M_x}{T_2} \tag{3.11a}$$

$$\frac{dM_y}{dt} = -\gamma(M_x B_z - M_z B_x) - \frac{M_y}{T_2} \tag{3.11b}$$

$$\frac{dM_z}{dt} = \gamma(M_x B_y - M_y B_x) - \frac{(M_z - M_0)}{T_1}\,, \tag{3.11c}$$

where M_0 is the thermal equilibrium magnetization. This set of equations is known as the Bloch equations. When spin-relaxation is negligible ($T_{1,2} \to \infty$), the solution to Eqs. 3.11(a)−3.11(c) take on the same form as the solution found in Eqs. 3.8(a)−3.8(c) except that the magnetic moment is replaced by the net magnetization. The net thermal equilibrium magnetization is related to the total number of spins by

$$M_0 = -N_0 \frac{g\mu_B B_0}{2k_b T}\,. \tag{3.12}$$

In the presence of EM excitation used to drive spin transitions, the magnetic component can be expressed as an oscillating magnetic field

$$\mathbf{B_1}(t) = 2B_1 \cos(\omega t)\,\hat{\mathbf{x}}\,, \tag{3.13}$$

where B_1 and $\omega = 2\pi\nu$ are the amplitude and angular frequency of the oscillating magnetic field, respectively. While Eq. 3.13 describes a linearly polarized oscillating magnetic field, which is typically used experimentally, it is mathematically easier to work with circularly polarized fields. Eq. 3.13 can be decomposed into left and right circularly polarized fields

$$\mathbf{B_{1,R}}(t) = B_1[\cos(\omega t)\,\hat{\mathbf{x}} + \sin(\omega t)\,\hat{\mathbf{y}}] \tag{3.14a}$$

$$\mathbf{B_{1,L}}(t) = B_1[\cos(\omega t)\,\hat{\mathbf{x}} - \sin(\omega t)\,\hat{\mathbf{y}}]\,. \tag{3.14b}$$

For simplicity and without the loss of generality, the effective total magnetic field using a left circularly polarized oscillating magnetic field becomes

$$\mathbf{B} = \mathbf{B_0} + \mathbf{B_1}(t) = [B_1 \cos(\omega t)\, \hat{\mathbf{x}} - B_1 \sin(\omega t)\, \hat{\mathbf{y}} + B_0\, \hat{\mathbf{z}}]\,. \tag{3.15}$$

The magnetization vector now follows a non-trivial nutation trajectory due to the introduction of the $\mathbf{B_1}(t)$ field and its equations of motion are then

$$\frac{dM_x}{dt} = \gamma[M_y B_0 + M_z B_1 \sin(\omega t)] - \frac{M_x}{T_2} \tag{3.16a}$$

$$\frac{dM_y}{dt} = \gamma[M_z B_1 \cos(\omega t) - M_x B_0] + \frac{M_y}{T_2} \tag{3.16b}$$

$$\frac{dM_z}{dt} = -\gamma[M_x B_1 \sin(\omega t) - M_y B_1 \sin(\omega t)] - \frac{M_z - M_0}{T_1}\,. \tag{3.16c}$$

Instead of a simple precession where the magnetization vector rotates about the fixed $\hat{\mathbf{z}}$ axis due to $\mathbf{B_0}$, nutation describes a change in the angle between the magnetization vector and the $\hat{\mathbf{z}}$ axis due to $\mathbf{B_1}(t)$, similar to a wobbling spinning top. Mathematically, precession and nutation corresponds to a change in the first (α) and second (β) Euler angle, respectively.

To simplify the problem, we introduce a rotating frame of reference where the stationary observer in the laboratory frame now rotates about the $\hat{\mathbf{z}}$ axis at frequency ω such that $\mathbf{B_1}(t)$ becomes time-independent. The transformation is mathematically achieved using the following relations

$$M_x^{'} = M_x \cos(\omega t) - M_y \sin(\omega t) \tag{3.17a}$$

$$M_y^{'} = M_x \sin(\omega t) + M_y \cos(\omega t) \tag{3.17b}$$

$$M_z^{'} = M_z\,. \tag{3.17c}$$

In this new rotating reference frame, the magnetization equation of motion now becomes

$$\begin{aligned}\frac{d\mathbf{M}'}{dt} &= \frac{d\mathbf{M}}{dt} - \boldsymbol{\omega} \times \mathbf{M} \\ &= (\boldsymbol{\omega_0} - \boldsymbol{\omega} + \gamma \mathbf{B_1}) \times \mathbf{M}\,,\end{aligned} \tag{3.18}$$

which describes spin nutation about an effective magnetic field

$$\begin{aligned}\mathbf{B_{eff}} &= \mathbf{B_0} - \frac{\boldsymbol{\omega}}{\gamma} + \mathbf{B_1} \\ &= B_1\,\hat{\mathbf{x}}' + \left(B_0 - \frac{\omega}{\gamma}\right)\hat{\mathbf{z}}'\,,\end{aligned} \tag{3.19}$$

tilted about the $\hat{\mathbf{z}}'$ axis by angle

$$\varphi = -\arctan\left(\frac{\omega_1}{\omega - \omega_0}\right), \tag{3.20}$$

at the Rabi nutation frequency

$$\Omega = \sqrt{\gamma^2 B_1^2 + (\omega - \omega_0)^2}\,, \tag{3.21}$$

where $\omega_1 = \gamma B_1$. Eq. 3.21 simplifies to $\Omega = \omega_1 = \gamma B_1$ when in resonance ($\omega - \omega_0 = 0$). The Rabi frequency in resonance describes the frequency at which the spin ensemble population described here by the magnetization vector oscillates between the spin up and spin down eigenstates.

An illustration of the magnetization vector in the stationary laboratory and rotating frame of reference is shown in Fig. 3.1. When expanded out, the magnetization components in the rotating frame in Eq. 3.18 are

$$\frac{dM_x^{'}}{dt} = (\omega - \omega_0)M_y^{'} - \frac{M_x^{'}}{T_2} \tag{3.22a}$$

$$\frac{dM_y^{'}}{dt} = -(\omega - \omega_0)M_x^{'} - \omega_1 M_z^{'} - \frac{M_y^{'}}{T_2} \tag{3.22b}$$

$$\frac{dM_z^{'}}{dt} = \omega_1 M_y^{'} - \frac{M_z^{'} - M_0}{T_1}\,. \tag{3.22c}$$

In the steady-state, the solution to Eqs. 3.22(a)–3.22(c) can be readily solved by setting the left hand side of the equations to zero

$$M_x^{'} = M_0 \frac{\omega_1 T_2^2(\omega_0 - \omega)}{1 + \omega_1^2 T_1 T_2 + ((\omega_0 - \omega)T_2)^2} \tag{3.23a}$$

$$M_y^{'} = M_0 \frac{\omega_1 T_2}{1 + \omega_1^2 T_1 T_2 + ((\omega_0 - \omega)T_2)^2} \tag{3.23b}$$

$$M_z^{'} = M_0 \frac{1 + ((\omega_0 - \omega)T_2)^2}{1 + \omega_1^2 T_1 T_2 + ((\omega_0 - \omega)T_2)^2}\,. \tag{3.23c}$$

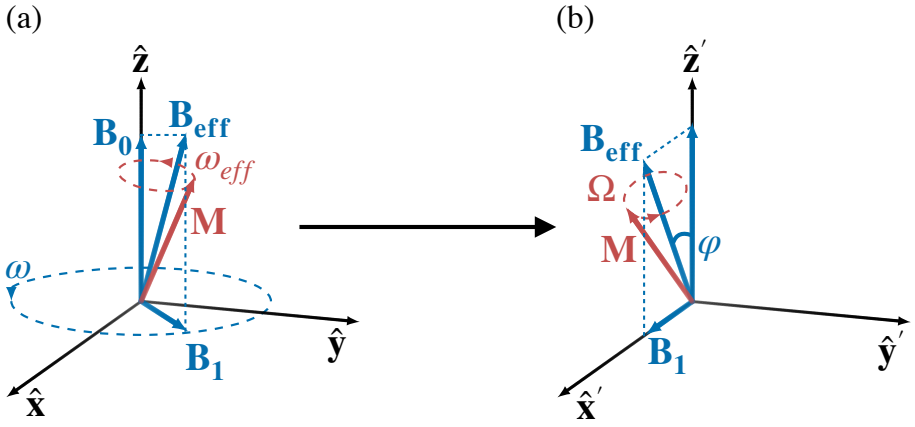

Fig. 3.1.: Illustration of the magnetization vector, $\mathbf{M}$, under a static magnetic field, $\mathbf{B_0}$, and a circularly polarized oscillating EM field, $\mathbf{B_1}(t)$, in the (a) laboratory and (b) rotating frame of reference. In the laboratory frame in (a), the nutation of $\mathbf{M}$ is a sum of the precession around $\mathbf{B_{eff}}$ at frequency $\omega_{eff} = \sqrt{\omega_0^2 + \omega_1^2}$ and the precession around $\mathbf{B_1}(t)$ at frequency ω. In the rotating frame in (b), $\mathbf{B_1}$ becomes time-invariant and $\mathbf{M}$ precesses around $\mathbf{B_{eff}}$, tilted from the $\hat{\mathbf{z}}'$ axis by angle φ, at the Rabi frequency Ω.

The transverse magnetization components in the rotating frame are related to the complex susceptibility by [115]

$$\chi = \chi' + i\chi'' = \frac{M_x'}{B_1} - i\frac{M_y'}{B_1}\,, \tag{3.24}$$

where the in-phase dispersion and the out-of-phase absorption components are experimentally detected in an cw-ESR measurement using homodyne detection with a lock-in amplifier. The EM power, P, absorbed by the sample in spin resonance is related to the quadrature absorption [116]

$$P = \frac{\partial}{\partial t}(-\mathbf{M}\cdot\mathbf{B}) = \omega\chi'' B_1^2\,. \tag{3.25}$$

Two extreme limits can be considered to simplify Eqs. 3.23(a)–3.23(c). First, in the weak field limit ($\omega_1^2 T_1 T_2 << 1$),

$$M_x' = M_0 \frac{\omega_1 T_2^2(\omega_0-\omega)}{1+((\omega_0-\omega)T_2)^2} \tag{3.26a}$$

$$M_y' = M_0 \frac{\omega_1 T_2}{1+((\omega_0-\omega)T_2)^2} \tag{3.26b}$$

$$M_z' = M_0\,. \tag{3.26c}$$

In resonance ($\omega_0 - \omega$), Eqs. 3.26(a)–3.26(c) further simplifies to

$$M_x' = 0 \tag{3.27a}$$

$$M_y' = M_0\omega_1 T_2 \tag{3.27b}$$

$$M_z' = M_0\,. \tag{3.27c}$$

This weak field limit is sometimes also known as the linear regime in an ESR measurement as the detected voltage signal is proportional to the square root of the absorbed microwave power, which in turn is proportional to B_1 (i.e., $V_{Signal} \propto \sqrt{P} \propto B_1$).

In the strong saturation limit where $\omega_1^2 T_1 T_2 >> 1$, the steady-state magnetization vanishes and no ESR is observed ($\mathbf{M}' = 0$). This saturation occurs when the rate of spin flipping due to the oscillating B_1 field is faster than the T_1 relaxation rate between the spin up and spin down state, thereby reducing the spin polarization between the two levels [113]. While the Bloch equations are derived using a semi-classical treatment of magnetization, as we will see in Sec. 3.5 using a quantum mechanical treatment with density matrix formalism, the Bloch equations are able to describe most of the main features of the spin evolution in an oscillating B_1 magnetic field.

3.3 Spin Hamiltonian

The Bloch description presented in the previous section considers only the magnetic interaction of a free electron solely with an external magnetic field due to the Zeeman interaction. For paramagnetic species in the solid-state, such as spin defects in SiC, high order magnetic interactions with the local environment consisting of other electron spin species (spin-spin) and with nearby nuclear spins (hyperfine) need to be considered. These interactions were briefly introduced in Sec. 2.2 and can lead to further energy splitting, resulting in additional ESR allowed transitions. To understand these additional energy transitions, the time-independent spin Hamiltonian is considered in the following.

Ignoring purely nuclear interactions, such as the nuclear Zeeman and nuclear quadrupole interaction, the spin Hamiltonian for an electron spin is given by

$$\hat{\mathcal{H}}_0 = \hat{\mathcal{H}}_Z + \hat{\mathcal{H}}_{HF} + \hat{\mathcal{H}}_{SS} \,, \tag{3.28}$$

where $\hat{\mathcal{H}}_Z$ is the electron Zeeman interaction, $\hat{\mathcal{H}}_{HF}$ the hyperfine interaction, and $\hat{\mathcal{H}}_{SS}$ the spin-spin interaction Hamiltonian. Each term in the Hamiltonian will be addressed individually below.

3.3.1 Zeeman interaction

In Sec. 3.2, we have seen that a classical description of the magnetic moment of an electron is related to its angular momentum and the gyromagnetic ratio ($\boldsymbol{\mu} = \gamma \mathbf{J}$). In quantum field theory, the gyromagnetic ratio derived from the magnetic moment of an electron can be shown to be larger by a factor g due to quantum electrodynamics effects [117]

$$\boldsymbol{\mu} = \gamma \mathbf{S} = g \frac{-q}{2m_e} \mathbf{S} = -\frac{g\mu_B}{\hbar} \mathbf{S} \,, \tag{3.29}$$

where $\hbar = h/2\pi$ is the reduced Planck constant. The electron Zeeman Hamiltonian describing the potential energy of the magnetic moment in a magnetic field is

$$\hat{\boldsymbol{\mathcal{H}}}_{\boldsymbol{Z}} = -\boldsymbol{\mu} \cdot \mathbf{B_0} = \frac{g\mu_B}{\hbar} \, \mathbf{S} \cdot \mathbf{B_0} = g\mu_B B_0 \hat{S}_z = m_s g \mu_B B_0 \,, \tag{3.30}$$

where $\hat{S}_z$ is the electron spin operator in the $\hat{\mathbf{z}}$ direction and the energy difference between the corresponding energy eigenstates between the spin up $|\uparrow\rangle$ and spin down $|\downarrow\rangle$ state was previously introduced in Eq. 3.1. We note that we have defined the spin operator in dimensionless units of $\hbar = 1$.

To generalise the spin Hamiltonian to paramagnetic states in a solid-state crystalline host that may have a well-defined symmetry, the g$-$factor is replaced by a generalised 3×3 g$-$tensor to account for any anisotropies

$$\hat{\boldsymbol{\mathcal{H}}}_{\boldsymbol{Z}} = \mu_B \, \mathbf{S} \cdot \mathbf{g} \cdot \mathbf{B_0} \,. \tag{3.31}$$

The g$-$tensor is usually symmetric and can be diagonalisable via a rotational transform such that the coordinate system is now with respect to the sample's principal axis

$$\mathbf{g_{diag}} = \mathbf{R}^T(\alpha, \beta, \gamma) \cdot \mathbf{g} \cdot \mathbf{R}(\alpha, \beta, \gamma) = \begin{pmatrix} g_x & 0 & 0 \\ 0 & g_y & 0 \\ 0 & 0 & g_z \end{pmatrix} \,, \tag{3.32}$$

where α, β, and γ are the Euler angles. Thus, the g$-$tensor can be uniquely defined using six independent variables given by the g$-$factor along the principle axis (g_x, g_y, g_z) and the three Euler angles describing the orientation of the principle axis. Eq. 3.32 is sometimes expressed in terms of a Δg shift from the isotropic free-electron g$-$factor

$$\mathbf{g_{diag}} = g_e\,\mathbb{I} + \Delta\mathbf{g} = \begin{pmatrix} g_e & 0 & 0 \\ 0 & g_e & 0 \\ 0 & 0 & g_e \end{pmatrix} + \begin{pmatrix} \Delta g_1 & 0 & 0 \\ 0 & \Delta g_2 & 0 \\ 0 & 0 & \Delta g_3 \end{pmatrix}, \tag{3.33}$$

where $\mathbb{I}$ is the identity matrix.

To determine the orientation of $\mathbf{B_0}$ with respect to the sample principle axis, $\mathbf{B_0} = B_0\sin(\theta)\cos(\phi)\,\hat{x} + B_0\sin(\theta)\sin(\phi)\,\hat{y} + B_0\cos(\theta)\,\hat{z}$ is expressed in terms of two polar angles, θ and ϕ, such that the observed effective g$-$factor for any orientation is

$$g(\theta,\phi) = \sqrt{(g_x\sin(\theta)\cos(\phi))^2 + (g_y\sin(\theta)\sin(\phi))^2 + (g_z\cos(\theta))^2}\,. \tag{3.34}$$

The anisotropy of the g$-$tensor is commonly described by three types of symmetries. For cubic symmetry, $g = g_x = g_y = g_z$ is isotropic and the measured ESR spectrum is the same for all orientations (see V_{Si}^{-} and $V_C V_{Si}$ in Table 2.2 for example). For axial symmetry, the observed effective g$-$factor is $g(\theta) = \sqrt{(g_\perp\sin(\theta))^2 + (g_{||}\cos(\theta))^2}$ when the orientation of $\mathbf{B_0}$ with respect to the symmetry axis is such that $g_\perp = g_x = g_y$ and $g_{||} = g_z$ (see P_{bC} and $N_C V_{Si}$ in Table 2.2 for example). For rhombic symmetry, $g_x \neq g_y \neq g_z$ and the observed effective g$-$factor is described by Eq. 3.34. In crystalline samples where the spin defects are all aligned in the same orientation, the g$-$factor anisotropy can be mapped out by rotating the sample with respect to the applied magnetic field as a function of θ and ϕ.

Deviations from the free-electron g$-$factor found in the solid-state is a consequence of spin-orbit coupling due to relativistic interaction between the spin angular momentum of an electron with its orbital angular momentum

as it is bound by the electrostatic field of a positively charge nucleus. This relativistic effect is described by the spin-orbit coupling Hamiltonian

$$\hat{\boldsymbol{\mathcal{H}}}_{\boldsymbol{SO}} = \lambda\, \hat{\mathbf{L}} \cdot \hat{\mathbf{S}}\,, \tag{3.35}$$

where λ is the spin-orbit coupling constant, $\hat{\mathbf{L}}$ is the orbital angular momentum operator and $\hat{\mathbf{S}}$ is the spin orbital angular momentum operator. Using second-order perturbation theory, the g$-$tensor can be calculated using [118]

$$g_{ij} = g_e \delta_{ij} + 2\lambda \Lambda_{ij}\,, \tag{3.36}$$

where δ_{ij} is the Kronecker delta and

$$\Lambda_{ij} = \sum_n \frac{\langle \psi_0 |\, L_i \,| \psi_n \rangle \langle \psi_n |\, L_j \,| \psi_0 \rangle}{E_0 - E_n}\,, \tag{3.37}$$

with ψ_0 and ψ_n the ground state and n^{th} excited state wavefunction of the paramagnetic center, respectively, and E_0 and E_n their corresponding energies. For spin systems in solids with small spin-orbit coupling such as SiC [119], the second-order correction term in Eq. 3.36 is negligibly small such that $g \sim 2$, as indicated by the various g$-$factor values summarised in Table 2.2.

3.3.2 Hyperfine interaction

In the presence of a non-zero nuclear magnetic dipole moment, an electron experiences a local magnetic field arising from the nuclei, $\mathbf{B_I}$, causing further splitting in the allowed energy spin states. This is called the hyperfine interaction. From the electron's reference frame, the electron experiences a total magnetic field strength, $\mathbf{B_{tot}} = \mathbf{B_0} \pm \mathbf{B_I}$, depending on whether the nuclear magnetic moment is aligned with or against $\mathbf{B_0}$, respectively.

The hyperfine interaction Hamiltonian is expressed as

$$\hat{\boldsymbol{\mathcal{H}}}_{\boldsymbol{HF}} = \hat{\mathbf{S}} \cdot \mathbf{A} \cdot \hat{\mathbf{I}}\,, \tag{3.38}$$

where $\mathbf{A}$ denotes the hyperfine coupling tensor and $\hat{\mathbf{I}}$ is the nuclear spin operator. Eq. 3.38 can be further divided into the Fermi-contact and the electron-nuclear dipolar interaction term

$$\mathbf{A} = a_{iso}\,\mathbb{I} + \mathbf{T}\,, \tag{3.39}$$

where a_{iso} is the isotropic hyperfine coupling constant, and $\mathbf{T}$ is the electron-nuclear dipole-dipole coupling tensor. The isotropic hyperfine coupling constant is also known as the Fermi contact term and is a result of the s-orbital electron interacting with the atomic nucleus [120, 121]

$$a_{iso} = \frac{2}{3}\mu_0 g_e \mu_B g_N \mu_N |\psi_0(0)|^2\,, \tag{3.40}$$

where μ_0 is the vacuum permeability, g_N the nuclear Landé g$-$factor, μ_N the nuclear magneton, and $|\psi_0(0)|^2$ is the finite electron spin density at the nucleus when $r = 0$. On the other hand, the electron-nuclear dipolar coupling tensor is a 3×3 traceless and symmetric matrix with matrix elements [120]

$$T_{ij} = \frac{\mu_0}{4\pi} g_e \mu_B g_N \mu_N \left\langle \psi_0 \middle| \frac{3 r_i r_j - \delta_{ij} r^2}{r^5} \middle| \psi_0 \right\rangle\,, \tag{3.41}$$

where r is the distance between the electron and nucleus. Similar to the Landé g$-$tensor in Eq. 3.32, the electron-nuclear dipolar coupling tensor is also diagonalisable via a rotational transformation along its principle axis

$$\begin{aligned} \mathbf{T}_{\mathbf{diag}} &= \mathbf{R}^T(\alpha,\beta,\gamma)\cdot\mathbf{T}\cdot\mathbf{R}(\alpha,\beta,\gamma) \\ &= \begin{pmatrix} T_x & 0 & 0 \\ 0 & T_y & 0 \\ 0 & 0 & T_z \end{pmatrix} = T \begin{pmatrix} -(1-\rho) & 0 & 0 \\ 0 & -(1+\rho) & 0 \\ 0 & 0 & 2 \end{pmatrix}\,, \end{aligned} \tag{3.42}$$

where $T = T_z/2$ is the axial component and $\rho = (T_x - T_y)/2$ is the rhombic component. When there are more than one magnetic nuclei species present, such as in SiC with naturally abundant isotopes of ^{29}Si (3.68%) and ^{13}C

(1.07%) both with nuclear spin $I = 1/2$, a summation is introduced in the hyperfine interaction Hamiltonian

$$\hat{\mathcal{H}}_{\boldsymbol{HF}} = \sum_j \hat{\mathbf{S}} \cdot \mathbf{A}_j \cdot \hat{\mathbf{I}}_j \,, \tag{3.43}$$

where the index denotes the j^{th} inequivalent nucleus.

3.3.3 Spin-spin interaction

Spin-spin interactions arising from interactions with nearby electron spin can be further differentiated into dipole-dipole and exchange interaction

$$\hat{\mathcal{H}}_{\boldsymbol{SS}} = \hat{\mathcal{H}}_{\boldsymbol{DD,ee}} + \hat{\mathcal{H}}_{\boldsymbol{EX}} \,. \tag{3.44}$$

Dipole-dipole interactions entail the mutual interaction between the magnetic moments of unpaired electrons in spin systems with $S > 1/2$. As a result, the degeneracy at zero magnetic field is lifted, which was previously observed in Sec. 2.2.2 for the divacancy spin defect in SiC. The dipole-dipole interaction Hamiltonian, also sometimes known as the zero-field splitting (ZFS) Hamiltonian, $\hat{\mathcal{H}}_{\boldsymbol{ZFS}}$, is given by

$$\hat{\mathcal{H}}_{\boldsymbol{DD,ee}} = \hat{\mathbf{S}} \cdot \mathbf{D} \cdot \hat{\mathbf{S}} \,, \tag{3.45}$$

where $\mathbf{D}$ is the dipolar coupling tensor.

Similar to $\mathbf{g}$ and $\mathbf{A}$, $\mathbf{D}$ is symmetric, traceless, and can be diagonalisable via a rotational transformation along its principle axis

$$\mathbf{D}_{\mathbf{diag}} = \begin{pmatrix} D_x & 0 & 0 \\ 0 & D_y & 0 \\ 0 & 0 & D_z \end{pmatrix} = \begin{pmatrix} -\frac{D_1}{3} + D_2 & 0 & 0 \\ 0 & -\frac{D_1}{3} - D_2 & 0 \\ 0 & 0 & \frac{2}{3}D_1 \end{pmatrix} \,, \tag{3.46}$$

where $D_1 = 3D_z/2$ and $D_2 = (D_x - D_y)/2$ are the axial and rhombic dipolar coupling constants, respectively. Notice that $\mathbf{D_{diag}}$ takes on the exact same form as $\mathbf{T_{diag}}$, but describes the dipole-dipole interaction between two electron spins instead

$$D_{ij} = \frac{\mu_0}{4\pi} g_a g_b \mu_B^2 \left\langle \psi_0 \left| \frac{3r_i r_j - \delta_{ij} r^2}{r^5} \right| \psi_0 \right\rangle . \tag{3.47}$$

The dipole-dipole interaction is a purely spatial phenomena and highly dependent on the symmetry of the system, where $D_1 = D_2 = 0$ for cubic symmetry, $D_1 \neq 0$ and $D_2 = 0$ for axial symmetry, and $D_1 \neq 0$ and $D_2 \neq 0$ for rhombic symmetry. Dipole-dipole interaction may arise between the two electron spins in the effective $S = 1$ intermediate spin-pair involved in the SDR mechanism subject to the symmetry of the spin system. This will be discussed in more detail in Sec. 3.4.2.

When two identical particles are in close proximity with one another, the wavefunctions of the indistinguishable particles overlap and are subject to spatial exchange. The exchange interaction Hamiltonian is expressed as

$$\hat{\boldsymbol{\mathcal{H}}}_{\boldsymbol{EX}} = \hat{\mathbf{S}}_\mathbf{a} \cdot \mathbf{J} \cdot \hat{\mathbf{S}}_\mathbf{b} , \tag{3.48}$$

where $\mathbf{J}$ is the exchange coupling matrix proportional to the degree of overlap between the wavefunctions. Typically, exchange coupling becomes dominant when the separation between two unpaired electrons is less than a few nanometers [122]. For simplicity, the exchange coupling is assumed to be isotropic such that Eq. 3.48 can be simplified to

$$\hat{\boldsymbol{\mathcal{H}}}_{\boldsymbol{EX}} = -J\, \hat{\mathbf{S}}_\mathbf{a} \cdot \hat{\mathbf{S}}_\mathbf{b} . \tag{3.49}$$

We note that several conflicting conventions are used for the isotropic exchange coupling, with other sources denoting J to be positive or with an additional factor of 2. Nonetheless, with the convention adopted in Eq. 3.49, the exchange interaction is responsible for ferromagnetism ($J > 0$) and antiferromagnetism ($J < 0$) in solids, where the sign of the exchange coupling constant governs whether nearby electrons spins are aligned either parallel

($J > 0$) or anti-parallel ($J < 0$) with each other. The exchange interaction can also lift the degeneracy at zero magnetic field, which will be explored in more detail in Sec. 3.4.2.

3.4 Spin-pair model

A major shortcoming of the ESR technique is its spin polarization limited spin sensitivity ($\sim 10^{11}$ spins/mT linewidth [113]) and its incompatibility with fully-fabricated semiconductor devices as metallic contacts can absorb and distort the B_1 modes of the cavity resonator. EDMR offers an alternative detection approach by monitoring only paramagnetic species participating in spin-dependent charge transport processes rather than the reflected EM irradiation power in conventional ESR measurements. This leads to a substantial spin sensitivity enhancement by many orders of magnitude over conventional ESR and even toward the single spin level [123, 124]. Since its first demonstration in 1966 by Schmidt and Solomon [125] in which a resonant photoconductivity change in Si was observed due to spin-dependent scattering off neutral impurities, EDMR has been successfully applied to study a wide variety of semiconductor devices and various spin-dependent transport mechanisms. These spin-dependent charge transport mechanisms include recombination [9, 126], tunnelling [124, 127], charge trapping [128, 129], scattering [130, 131], and hopping [132, 133]. The spin-dependent transport mechanisms listed above all involve a spin-pair formed between two interacting spins in which the spin selection rules are obeyed and the symmetry of the spin-pair directly influences the charge transport process. This can be detected as a change in the device conductivity. Only the spin-dependent recombination process is relevant to this work, which will be described in the following section.

3.4.1 Spin-dependent recombination

Electrical detection of the SDR process was first experimentally observed in Si by Lépine in 1972 [134]. In Lépine's original work, SDR was explained in terms of an increase in capture cross-section due to a change in the spin

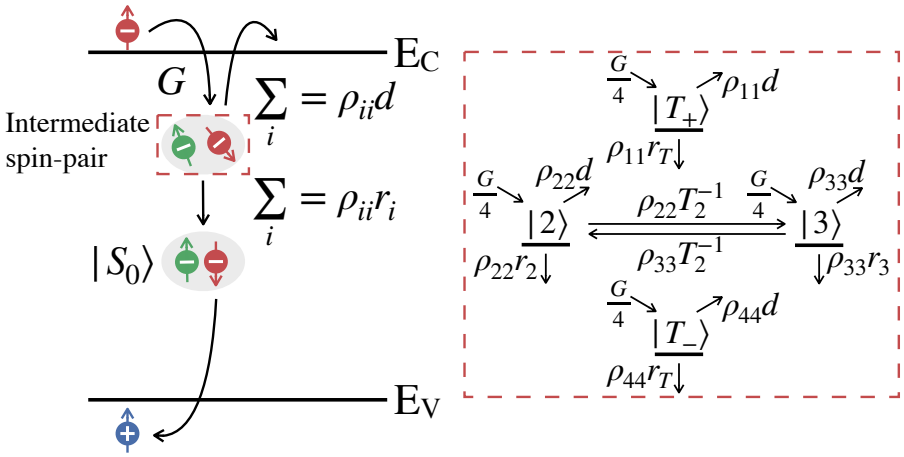

Fig. 3.2.: Illustration of the spin-dependent recombination mechanism through a deep level defect state. Prior to recombination, an intermediate spin-pair formed between a conduction band electron and a paramagnetic defect can exist in any of its four energy eigenstates and only the singlet state can complete the recombination process. The inset shown in the red dashed box indicates the various pathways each energy eigenstate can be either spontaneously created or annihilated.

polarization governed by the Boltzmann distribution described in Eq. 3.3. However, the polarization model proposed by Lépine was not able to explain the large signal intensity of the observed spin dependent photoconductivity as well as temperature and magnetic field dependencies. It was not until 1978 when a model proposed by Kaplan, Solomon, and Mott (KSM) [21] based on the formation of an intermediate spin-pair prior to recombination was able to correctly describe the experimentally observed results.

A visual interpretation of the KSM spin-pair model is shown in Fig. 3.2. Under the KSM spin-pair framework, an intermediate spin-pair is formed between an electron in close spatial proximity to a deep level paramagnetic state with four possible spin eigenstates prior to recombination. As the electron-hole pair is annihilated in the recombination event, this process requires the total angular momentum of the system to be conserved ($\Delta \mathbf{J} = \Delta \mathbf{S} + \Delta \mathbf{L} = 0$). In crystalline semiconductor structures where spin-orbit coupling is negligibly small like SiC, only the conservation of the spin angular momentum is required. As a result, only spin-pairs in the singlet state configuration ($S = 0$) are able to recombine, whereas spin-pairs in the triplet state ($S = 1$) disassociate. The singlet-to-triplet state ratio can be modified by introducing an ESR spin transition. As a result, a reduction in the number of free charge carriers is observed due

to an enhancement in the number of recombination events in resonance, which is observed as a decrease in the overall device conductivity.

In the following, we first extend the spin Hamiltonian formalism introduced in Sec. 3.3 for an intermediate spin-pair. Then, the time dependence of the SDR process visually expressed in the red dashed box of Fig. 3.2 based on electronic transition rates between each eigenstate will be described in Sec. 3.5.

3.4.2 Spin-pair Hamiltonian

For a spin-pair system consisting of two electron spins ($S_a = S_b = 1/2$), the time-independent spin-pair Hamiltonian is given by

$$\begin{aligned}\hat{\mathcal{H}}_{\mathbf{0}} &= \hat{\mathcal{H}}_{\boldsymbol{Z}} + \hat{\mathcal{H}}_{\boldsymbol{HF}} + \hat{\mathcal{H}}_{\boldsymbol{EX}} + \hat{\mathcal{H}}_{\boldsymbol{DD,ee}} \\ &= \mu_B(g_a\,\hat{\mathbf{S}}_{\mathbf{a}}\cdot\mathbf{B_0} + g_b\,\hat{\mathbf{S}}_{\mathbf{b}}\cdot\mathbf{B_0}) + \sum_{i=a,b}\sum_{j}\hat{\mathbf{S}}_{\mathbf{i}}\cdot\mathbf{A_{ij}}\cdot\hat{\mathbf{I}}_{\mathbf{j}} \\ &\quad - J\,\hat{\mathbf{S}}_{\mathbf{a}}\cdot\hat{\mathbf{S}}_{\mathbf{b}} - \hat{\mathbf{S}}_{\mathbf{a}}\cdot\mathbf{D}\cdot\hat{\mathbf{S}}_{\mathbf{b}}\,.\end{aligned} \tag{3.50}$$

Each term in the spin-pair Hamiltonian has been briefly introduced in Sec. 3.3, except now the Zeeman and hyperfine Hamiltonian includes a second term and an additional summation, respectively, to take into account the additional electron spin $S_b = 1/2$ in the spin-pair. The complex Hamiltonian in Eq. 3.50 is not diagonal in the simple Zeeman basis $|\psi\rangle = |m_s\rangle_a \otimes |m_s\rangle_b = (|\uparrow\uparrow\rangle, |\uparrow\downarrow\rangle, |\downarrow\uparrow\rangle, |\downarrow\downarrow\rangle)$ due to the presence of spin-spin interactions. Instead, it is typically easier to work in the basis state described by the total spin angular momentum and the total spin projection angular momentum of the intermediate spin-pair ($|s, m_s\rangle = |s, m_s\rangle_a \otimes |s, m_s\rangle_b$) such that

$$|T_+\rangle = |\uparrow\uparrow\rangle \tag{3.51a}$$
$$|S_0\rangle = (|\uparrow\downarrow\rangle - |\downarrow\uparrow\rangle)/\sqrt{2} \tag{3.51b}$$
$$|T_0\rangle = (|\downarrow\uparrow\rangle + |\uparrow\downarrow\rangle)/\sqrt{2} \tag{3.51c}$$
$$|T_-\rangle = |\downarrow\downarrow\rangle\ , \tag{3.51d}$$

becomes

$$|T_+\rangle = |+1,+1\rangle \tag{3.52a}$$
$$|S_0\rangle = |0,0\rangle \tag{3.52b}$$
$$|T_0\rangle = |+1,0\rangle \tag{3.52c}$$
$$|T_-\rangle = |+1,-1\rangle \ . \tag{3.52d}$$

We note that the $1/\sqrt{2}$ normalisation factor in Eqs. 3.51(b)$-$3.51(c) holds only for the case of purely singlet and triplet states, respectively, which occurs in the presence of strong spin-spin coupling between the two spins in the spin-pair. This will be discussed in more detail in Sec. 3.5 and generalised for any arbitrary spin-spin coupling strength. For the following, we will assume purely singlet and triplet states and each term in the spin-pair Hamiltonian will be considered individually.

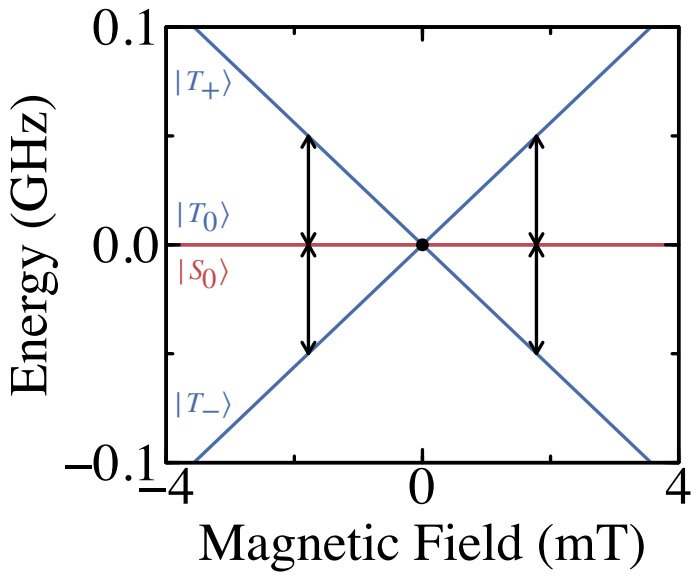

Fig. 3.3.: Simulation of the energy eigenvalues for the spin-pair Hamiltonian due to the Zeeman interaction, with the corresponding eigenstates indicated. Vertical arrows indicate $\Delta m_s = \pm 1$ spin transitions at an arbitrary chosen frequency of $\nu = 50$ MHz and the black dot indicates the degeneracy between triplet and singlet states.

For the simplest case where only the Zeeman interaction of the spin-pair is considered, we have seen from Sec. 3.3.1 for an individual spin that the energy eigenvalues are determined by the $\hat{S}_z$ operator when the external magnetic field is pointing solely in the $\hat{\mathbf{z}}$ direction. Thus,

$$\hat{\boldsymbol{\mathcal{H}}}_{\boldsymbol{Z}} |T_+\rangle = g\mu_B B_0 |+1,+1\rangle \tag{3.53a}$$
$$\hat{\boldsymbol{\mathcal{H}}}_{\boldsymbol{Z}} |S_0\rangle = 0 |0,0\rangle \tag{3.53b}$$
$$\hat{\boldsymbol{\mathcal{H}}}_{\boldsymbol{Z}} |T_0\rangle = 0 |+1,0\rangle \tag{3.53c}$$
$$\hat{\boldsymbol{\mathcal{H}}}_{\boldsymbol{Z}} |T_-\rangle = -g\mu_B B_0 |+1,-1\rangle \ , \tag{3.53d}$$

where $\hat{S}_z |s,m_s\rangle = \hbar m_s |s,m_s\rangle$ and for simplicity we have assumed that $g_a = g_b = g$. The energy eigenvalues in Eqs. 3.53(a)– 3.53(d) are plotted as a function of magnetic field in Fig. 3.3. We note that energy is expressed as a multiple of h and in units of GHz. Spin resonance transitions indicated by the vertical arrows between $T_\pm$ to T_0 spin-pair states due to an arbitrary chosen $\nu = 50$ MHz EM excitation corresponds to a resonance field at $B_0 \approx \pm 1.78$ mT. At precisely zero magnetic field, all four eigenstates are degenerate and the triplet states are able to spin-mix with the singlet state. This is also sometimes referred to as intersystem crossing (ISC) and as a result, recombination can take place even in the absence of EM irradiation. This zero-field spin-mixing phenomena is quenched by lifting the degeneracy on application of an increasing external magnetic field in which only T_0 and S_0 remain degenerate. The degeneracy can be further lifted with the introduction of exchange, dipolar, and hyperfine interaction, leading to peculiar features in the zero-field response, as will be shown in the following here. Next, we will consider the effects of exchange interaction on the allowed energy eigenvalues of the intermediate spin-pair.

The exchange interaction spin-pair Hamiltonian involves the dot product between the spin operator of each individual spin within the spin-pair, where it can be shown that

$$(\hat{\mathbf{S}}_\mathbf{a} \cdot \hat{\mathbf{S}}_\mathbf{b}) |s,m_s\rangle = \frac{s(s+1) - 3/2}{2} |s,m_s\rangle \ , \tag{3.54}$$

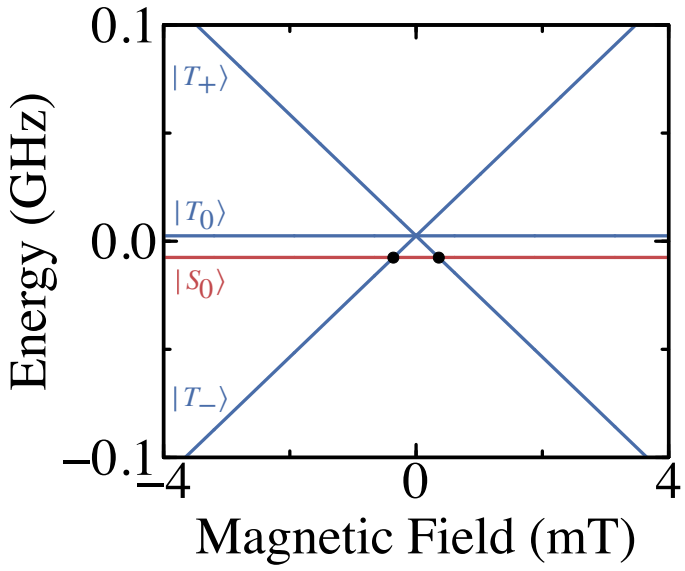

Fig. 3.4.: Simulation of the energy eigenvalues for the spin-pair Hamiltonian due to Zeeman and exchange interaction, with the corresponding eigenstates indicated. An exchange coupling strength of $J = -10$ MHz was arbitrarily chosen.

knowing that $\hat{\mathbf{S}}^{\mathbf{2}} = \hat{\mathbf{S}}_{\mathbf{a}}^{\mathbf{2}} + \hat{\mathbf{S}}_{\mathbf{a}} \cdot \hat{\mathbf{S}}_{\mathbf{b}} + \hat{\mathbf{S}}_{\mathbf{b}}^{\mathbf{2}}$ and $\hat{\mathbf{S}}^{\mathbf{2}} |s, m_s\rangle = \hbar^2 s(s+1) |s, m_s\rangle$. Thus, the corresponding energy eigenvalues of the spin-pair Hamiltonian due to Zeeman and exchange interaction are

$$(\hat{\boldsymbol{\mathcal{H}}}_{\boldsymbol{Z}} + \hat{\boldsymbol{\mathcal{H}}}_{\boldsymbol{EX}}) |T_+\rangle = g\mu_B B_0 - \frac{J}{4} |+1, +1\rangle \tag{3.55a}$$

$$(\hat{\boldsymbol{\mathcal{H}}}_{\boldsymbol{Z}} + \hat{\boldsymbol{\mathcal{H}}}_{\boldsymbol{EX}}) |S_0\rangle = \frac{3J}{4} |0, 0\rangle \tag{3.55b}$$

$$(\hat{\boldsymbol{\mathcal{H}}}_{\boldsymbol{Z}} + \hat{\boldsymbol{\mathcal{H}}}_{\boldsymbol{EX}}) |T_0\rangle = -\frac{J}{4} |+1, 0\rangle \tag{3.55c}$$

$$(\hat{\boldsymbol{\mathcal{H}}}_{\boldsymbol{Z}} + \hat{\boldsymbol{\mathcal{H}}}_{\boldsymbol{EX}}) |T_-\rangle = -g\mu_B B_0 - \frac{J}{4} |+1, -1\rangle \ . \tag{3.55d}$$

Eqs. 3.55(a)−3.55(d) describe a shift in the triplet eigenstates relative to zero by $J/4$ amount of energy. Furthermore, at zero magnetic field, the triplet states are separated by J amount of energy relative to the singlet state, as illustrated in Fig. 3.4 for $J = -10$ MHz. The zero-field degeneracy observed in Fig. 3.3 is lifted and the ISCs between triplet and singlet states occur

at small magnetic fields away from zero indicated by the black symbols in Fig. 3.4.

In the presence of dipole-dipole interaction, the dipolar interaction spin-pair Hamiltonian can be computed by first expanding out the dipole-dipole coupling tensor in Eq. 3.46

$$\begin{aligned}\hat{\boldsymbol{\mathcal{H}}}_{\boldsymbol{DD,ee}} &= \hat{\mathbf{S}}_{\mathbf{a}} \cdot \mathbf{D} \cdot \hat{\mathbf{S}}_{\mathbf{b}} \\ &= \Big(-\frac{D_1}{3} + D_2 \Big) \hat{S}_x^2 - \Big(\frac{D_1}{3} + D_2 \Big) \hat{S}_y^2 + \frac{2}{3} D_1 \hat{S}_z^2 \\ &= D_1 \Big(\hat{S}_z^2 - \frac{1}{3} (\hat{S}_x^2 + \hat{S}_y^2 + \hat{S}_z^2) \Big) + D_2 (\hat{S}_x^2 - \hat{S}_y^2) \,,\end{aligned} \tag{3.56}$$

with the Cartesian spin operators in the transverse direction related to the raising and lowering operators given by [135]

$$\begin{aligned}\hat{S}_+ \left| s, m_s \right\rangle &= \frac{1}{2} (\hat{S}_x + i \hat{S}_y) \left| s, m_s \right\rangle && \text{(3.57a)} \\ &= \sqrt{(s(s+1) - m_s(m_s+1))} \left| s, m_s + 1 \right\rangle \\ \hat{S}_- \left| s, m_s \right\rangle &= \frac{1}{2} (\hat{S}_x - i \hat{S}_y) \left| s, m_s \right\rangle && \text{(3.57b)} \\ &= \sqrt{(s(s+1) - m_s(m_s-1))} \left| s, m_s - 1 \right\rangle \,.\end{aligned}$$

By rearranging Eqs. 3.57(a)–3.57(b) in terms of the Cartesian spin operators, it can be shown that

$$\hat{S}_x = \frac{1}{2} (\hat{S}_+ + \hat{S}_-) \tag{3.58a}$$

$$\hat{S}_y = \frac{1}{2i} (\hat{S}_+ - \hat{S}_-) \tag{3.58b}$$

$$\hat{S}_x^2 + \hat{S}_y^2 = \hat{S}_x^2 - \hat{S}_y^2 = \frac{1}{2} (\hat{S}_+^2 + \hat{S}_-^2) \,, \tag{3.58c}$$

and a general expression describing how the dipole-dipole interaction spin-pair Hamiltonian acts on eigenstate $|s, m_s\rangle$ can be written as

$$\begin{aligned}\hat{\boldsymbol{\mathcal{H}}}_{\boldsymbol{DD,ee}}\,|s,m_s\rangle = D_1 m_s^2\,|s,m_s\rangle - \frac{D_1}{3}(s(s+1))\,|s,m_s\rangle \\ + \frac{D_2}{2}(s(s+1) - m_s(m_s+1))\,|s,m_s+2\rangle \\ + \frac{D_2}{2}(s(s+1) - m_s(m_s-1))\,|s,m_s-2\rangle\ .\end{aligned} \tag{3.59}$$

Thus, the spin-pair Hamiltonian in the presence of Zeeman, hyperfine, and dipole-dipole interaction is then

$$\begin{aligned}(\hat{\boldsymbol{\mathcal{H}}}_{\boldsymbol{Z}} + \hat{\boldsymbol{\mathcal{H}}}_{\boldsymbol{EX}} + \hat{\boldsymbol{\mathcal{H}}}_{\boldsymbol{DD,ee}})\,|T_+\rangle &= \left(g\mu_B B_0 - \frac{J}{4} + \frac{D_1}{3}\right)|+1,+1\rangle \\ &\quad + D_2\,|+1,-1\rangle \end{aligned} \tag{3.60a}$$

$$(\hat{\boldsymbol{\mathcal{H}}}_{\boldsymbol{Z}} + \hat{\boldsymbol{\mathcal{H}}}_{\boldsymbol{EX}} + \hat{\boldsymbol{\mathcal{H}}}_{\boldsymbol{DD,ee}})\,|S_0\rangle = \frac{3J}{4}\,|0,0\rangle \tag{3.60b}$$

$$(\hat{\boldsymbol{\mathcal{H}}}_{\boldsymbol{Z}} + \hat{\boldsymbol{\mathcal{H}}}_{\boldsymbol{EX}} + \hat{\boldsymbol{\mathcal{H}}}_{\boldsymbol{DD,ee}})\,|T_0\rangle = -\left(\frac{J}{4} + \frac{2}{3}D_1\right)|+1,0\rangle \tag{3.60c}$$

$$\begin{aligned}(\hat{\boldsymbol{\mathcal{H}}}_{\boldsymbol{Z}} + \hat{\boldsymbol{\mathcal{H}}}_{\boldsymbol{EX}} + \hat{\boldsymbol{\mathcal{H}}}_{\boldsymbol{DD,ee}})\,|T_-\rangle &= -\left(g\mu_B B_0 + \frac{J}{4} - \frac{D_1}{3}\right)|+1,-1\rangle \\ &\quad + D_2\,|+1,+1\rangle\ .\end{aligned} \tag{3.60d}$$

From Eq. 3.60(a) and Eq. 3.60(d), it can be seen that the dipolar interaction spin-pair Hamiltonian is not diagonal in the chosen basis state. As a consequence, the off-diagonal matrix elements imply forbidden $\Delta m_s = \pm 2$ transitions between $|T_+\rangle$ and $|T_-\rangle$ are now weakly allowed. These forbidden transitions will be observed experimentally in Chapter 5 and their locations can be used to directly measure D_1 and D_2. To determine the corresponding energy eigenvalues for the chosen basis state, the characteristic equation $\det\left(\hat{\boldsymbol{\mathcal{H}}}_{\boldsymbol{0}} - E\mathbb{I}\right) = 0$ is computed to yield

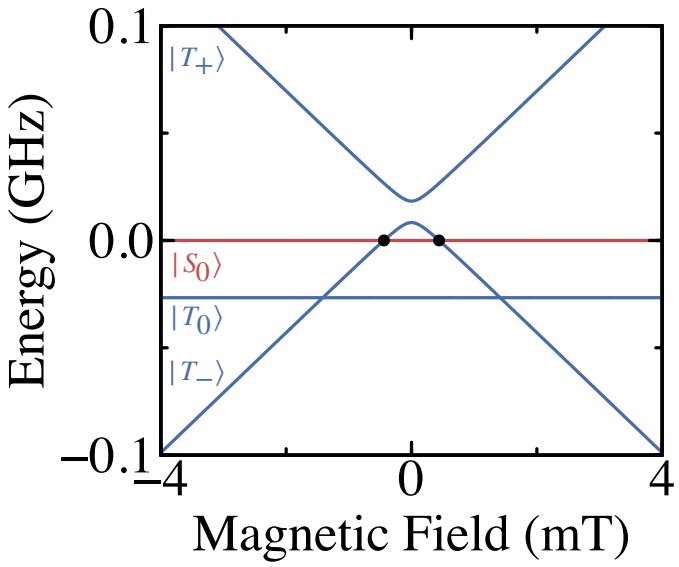

Fig. 3.5.: Simulation of the energy eigenvalues for the spin-pair Hamiltonian due to the Zeeman and dipole-dipole interaction, with the corresponding eigenstates indicated. D_1 and D_2 were arbitrarily chosen to be equal to 40 and 5 MHz, respectively.

$$E_{T_+} = -\frac{J}{4} - \frac{D_1}{3} + \sqrt{(g\mu_B B_0)^2 + D_2^2} \tag{3.61a}$$

$$E_{S_0} = -\frac{3J}{4} \tag{3.61b}$$

$$E_{T_0} = -\frac{J}{4} - \frac{2D_1}{3} \tag{3.61c}$$

$$E_{T_-} = -\frac{J}{4} - \frac{D_1}{3} - \sqrt{(g\mu_B B_0)^2 + D_2^2}\,. \tag{3.61d}$$

In the absence of exchange interaction where only the Zeeman and dipole-dipole interaction are considered, Eqs. 3.61(a)−3.61(d) also describe a lift in the degeneracy between the triplet states at zero magnetic field. As illustrated in Fig. 3.5, E_{T_0} is only dependent on D_1 and $E_{T_\pm}$ are separated by energy $2D_2$. For this simulation, D_1 and D_2 were arbitrarily chosen to be equal to 40 and 5 MHz, respectively. At zero magnetic field, the degeneracy between $|T_\pm\rangle$ and $|S_0\rangle$ is lifted and now the ISCs are separated by $2D_1/3$ in units of magnetic field.

Lastly, we will now consider the hyperfine interaction spin-pair Hamiltonian for the simplest case where a nearby isotropic nuclear spin of $I = 1/2$ is present. For the following, the $|m_s\rangle_a \otimes |m_s\rangle_b \otimes |m_I\rangle$ basis state is considered to describe the three particle system. The hyperfine interaction spin-pair Hamiltonian when expanded out is

$$\hat{\boldsymbol{\mathcal{H}}}_{\boldsymbol{HF}} = \hat{\mathbf{S}}_{\mathbf{a}} \cdot \mathbf{A}_{\mathbf{a}} \cdot \hat{\mathbf{I}} + \hat{\mathbf{S}}_{\mathbf{b}} \cdot \mathbf{A}_{\mathbf{b}} \cdot \hat{\mathbf{I}}\,, \tag{3.62}$$

where we have dropped the summation over j as we are only dealing with one nuclear spin species. From Eqs. 3.58(a)−3.58(b), the Cartesian spin operators were shown to be the sum or difference of the raising or lowering operators. This similarly holds true for the Cartesian nuclear spin operators when operating on the nuclear spin. As an example, the hyperfine interaction spin-pair Hamiltonian acts on state $|\uparrow,\uparrow,\Uparrow\rangle$ in the following way

$$\begin{aligned}\hat{\boldsymbol{\mathcal{H}}}_{\boldsymbol{HF}} |\uparrow,\uparrow,\Uparrow\rangle = &\frac{A_{ax}}{4} |\downarrow,\uparrow,\Downarrow\rangle + \frac{A_{bx}}{4} |\uparrow,\downarrow,\Downarrow\rangle \\ &- \frac{A_{ay}}{4} |\downarrow,\uparrow,\Downarrow\rangle - \frac{A_{by}}{4} |\uparrow,\downarrow,\Downarrow\rangle \\ &+ \frac{A_{az}}{4} |\uparrow,\uparrow,\Uparrow\rangle + \frac{A_{bz}}{4} |\uparrow,\uparrow,\Uparrow\rangle\ .\end{aligned} \tag{3.63}$$

In the $|s, m_s\rangle \otimes |m_I\rangle$ basis state, using the following transformation

$$|\uparrow,\uparrow\rangle = |T_+\rangle \tag{3.64a}$$
$$|\uparrow,\downarrow\rangle = (|T_0\rangle - |S_0\rangle)/\sqrt{2} \tag{3.64b}$$
$$|\downarrow,\uparrow\rangle = (|T_0\rangle + |S_0\rangle)/\sqrt{2} \tag{3.64c}$$
$$|\downarrow,\downarrow\rangle = |T_-\rangle\ , \tag{3.64d}$$

Eq. 3.63 becomes

$$\begin{aligned}\hat{\boldsymbol{\mathcal{H}}}_{\boldsymbol{HF}}\left|T_{+},\Uparrow\right\rangle = &\frac{(A_{ax}+A_{bx})}{4\sqrt{2}}\left|T_{0},\Downarrow\right\rangle + \frac{(A_{ax}-A_{bx})}{4\sqrt{2}}\left|S_{0},\Downarrow\right\rangle \\ &- \frac{(A_{ay}+A_{by})}{4\sqrt{2}}\left|T_{0},\Downarrow\right\rangle - \frac{(A_{ay}-A_{by})}{4\sqrt{2}}\left|S_{0},\Downarrow\right\rangle \\ &+ \frac{(A_{az}+A_{bz})}{4}\left|T_{+},\Uparrow\right\rangle \ .\end{aligned} \tag{3.65}$$

Completing the derivation for the seven remaining spin-pair eigenstate configurations and including the effects of Zeeman, exchange, and dipole-dipole interaction found in Eqs. 3.60(a)−3.60(d), the full spin-pair Hamiltonian is then

$$\hat{\boldsymbol{\mathcal{H}}}_{\mathbf{0}} \left| T_+, \pm\frac{1}{2} \right\rangle = \left\{ g\mu_B B_0 \pm \left(\frac{A_{az} + A_{bz}}{4} \right) + \frac{D_1}{3} + \frac{J}{4} \right\} \left| T_+, \pm\frac{1}{2} \right\rangle + \left(\frac{\pm\left(A_{ax} - A_{bx}\right) \mp \left(A_{ay} - A_{by}\right)}{4\sqrt{2}} \right) \left| S_0, \mp\frac{1}{2} \right\rangle + \left(\frac{\pm\left(A_{ax} + A_{bx}\right) \mp \left(A_{ay} + A_{by}\right)}{4\sqrt{2}} \right) \left| T_0, \mp\frac{1}{2} \right\rangle + D_2 \left| T_-, \pm\frac{1}{2} \right\rangle \tag{3.66a}$$

$$\hat{\boldsymbol{\mathcal{H}}}_{\mathbf{0}} \left| S_0, \pm\frac{1}{2} \right\rangle = \left(\frac{\mp\left(A_{ax} - A_{bx}\right) \pm \left(A_{ay} - A_{by}\right)}{4\sqrt{2}} \right) \left| T_+, \mp\frac{1}{2} \right\rangle - \frac{3J}{4} \left| S_0, \pm\frac{1}{2} \right\rangle \mp \left(\frac{A_{az} - A_{bz}}{4} \right) \left| T_0, \pm\frac{1}{2} \right\rangle + \left(\frac{\pm\left(A_{ax} - A_{bx}\right) \mp \left(A_{ay} - A_{by}\right)}{4\sqrt{2}} \right) \left| T_-, \mp\frac{1}{2} \right\rangle \tag{3.66b}$$

$$\hat{\boldsymbol{\mathcal{H}}}_{\mathbf{0}} \left| T_0, \pm\frac{1}{2} \right\rangle = \left(\frac{\mp\left(A_{ax} + A_{bx}\right) \pm \left(A_{ay} + A_{by}\right)}{4\sqrt{2}} \right) \left| T_+, \mp\frac{1}{2} \right\rangle \pm \left(\frac{A_{az} - A_{bz}}{4} \right) \left| S_0, \pm\frac{1}{2} \right\rangle + \left\{ -\frac{2}{3} D_1 + \frac{J}{4} \right\} \left| T_0, \pm\frac{1}{2} \right\rangle + \left(\frac{\pm\left(A_{ax} + A_{bx}\right) \mp \left(A_{ay} + A_{by}\right)}{4\sqrt{2}} \right) \left| T_-, \mp\frac{1}{2} \right\rangle \tag{3.66c}$$

$$\hat{\boldsymbol{\mathcal{H}}}_{\mathbf{0}} \left| T_-, \pm\frac{1}{2} \right\rangle = D_2 \left| T_+, \pm\frac{1}{2} \right\rangle + \left(\frac{\pm\left(A_{ax} - A_{bx}\right) \mp \left(A_{ay} - A_{by}\right)}{4\sqrt{2}} \right) \left| S_0, \mp\frac{1}{2} \right\rangle + \left(\frac{\pm\left(A_{ax} + A_{bx}\right) \mp \left(A_{ay} + A_{by}\right)}{4\sqrt{2}} \right) \left| T_0, \mp\frac{1}{2} \right\rangle + \left\{ -g\mu_B B_0 \pm \left(\frac{A_{az} + A_{bz}}{4} \right) + \frac{D_1}{3} + \frac{J}{4} \right\} \left| T_-, \pm\frac{1}{2} \right\rangle . \tag{3.66d}$$

Eqs 3.66(a)–3.66(d) form a 8×8 matrix with multiple non-diagonal matrix elements. Spin-mixing can occur between $T_\pm$ and S_0 through the transverse hyperfine coupling interaction (A_{ix}, A_{iy}), whereas spin-mixing between T_0

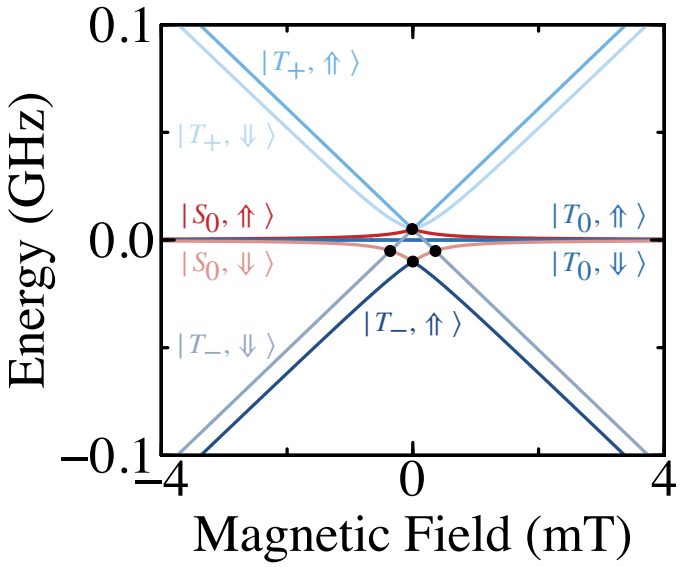

Fig. 3.6.: Simulation of the energy eigenvalues for the spin-pair Hamiltonian due to the Zeeman and hyperfine interaction, with the corresponding eigenstates indicated. It is assumed that the hyperfine interaction is isotropic and acts equally on both spins in the spin-pair at a coupling strength of 10 MHz.

and S_0 occurs through the longitudinal hyperfine coupling interaction (A_{iz}), as indicated by the non-zero off-diagonal matrix elements. To calculate the corresponding energy eigenvalues, the characteristic equation is computed numerically, as shown in Fig. 3.6 ignoring spin-spin interaction. For this simulation, an isotropic hyperfine interaction is considered and both electron spins in the spin-pair experience the same interaction strength ($A_{ix} = A_{iy} = A_{iz} = 10$ MHz). Spin-mixing between degenerate singlet and triplet states (black symbols in Fig. 3.6) can occur at small magnetic fields away from zero as the spin-pair experiences a local magnetic field equal to the sum and difference between the external and nuclear magnetic field. Thus, the location of the ISCs can be directly correlated to the hyperfine coupling constant without the requirement of EM irradiation.

A more rigorous and computational demanding simulation is required to describe the hyperfine interaction in semiconductor materials like SiC with two or more nuclear spin species. In such a case, the basis state $|s, m_s\rangle \otimes |m_I\rangle_1 \otimes |m_I\rangle_2$ is required to solve for a 16×16 spin-pair Hamiltonian. With the aid of the EasySpin MATLAB toolbox [136], an example simulation of the energy eigenvalues is shown in Fig. 3.7 for $\mathbf{A_{i1}} = 20$ MHz and $\mathbf{A_{i2}} = 16$

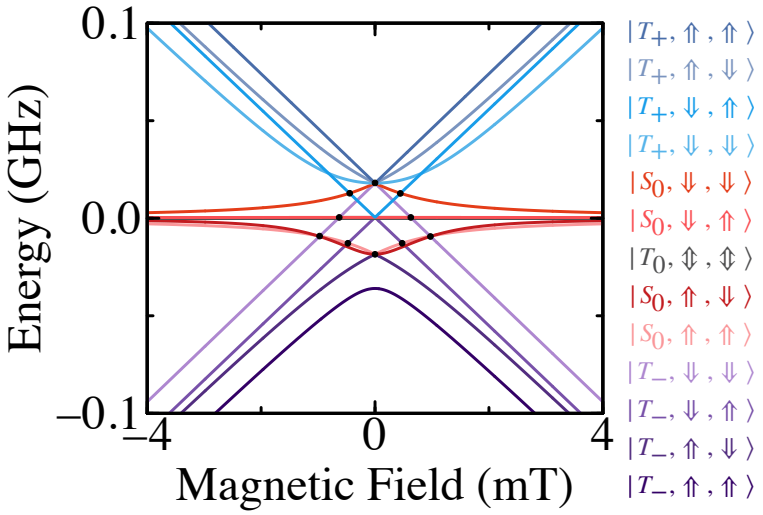

Fig. 3.7.: Simulation of the energy eigenvalues for the spin-pair Hamiltonian due to the Zeeman and hyperfine interaction in the presence of two nuclear spins $I_1 = I_2 = 1/2$, with the corresponding eigenstates indicated. It is assumed that the hyperfine interaction for each nuclear spin is isotropic and acts equally on both spins in the spin-pair. The hyperfine coupling constant for nuclear spin I_1 and I_2 are 20 and 16 MHz, respectively.

MHz, clearly highlighting the complexity of the problem even for just a four particle spin system.

In summary, the individual terms in the spin-pair Hamiltonian are introduced in this section, complimented by idealised simulations to help visualise how each type of spin interaction affects the energy eigenvalues of the four spin-pair eigenstates near zero magnetic field. These terms will have profound effects on the experimentally measured zero-field response in Chapter 5 and Chapter 6, revealing new insight and offering an alternative approach to probe the spin properties of the paramagnetic species measured without EM excitation.

3.5 Pulsed EDMR

The description of the spin-pair up to this point has not taken into account any time-dependencies during the resonant excitation of the spin-pair. While this description is perfectly valid for cwEDMR operation, it will not be able

to describe pulsed EDMR (pEDMR) operation employed in Chapter 7. As such, a general time-dependent theory of SDR is introduced below, closely following the original work by Boehme and Lips [137]. This time-domain formalism is consistent with and simplifies to the time-independent description given in Sec. 3.4 when t $\rightarrow \infty$. The time-domain theory of SDR is based on electronic transition rates illustrated in Fig. 3.2 between the intermediate spin-pair eigenstates prior to singlet state recombination, which provides a direct link between the measured device conductivity and the recombination rates, similar to the relationship found between the measurable EM absorption and the spin magnetization for ESR in Sec. 3.2. Thus, the current transient in response to a resonant pulse excitation is directly proportional to the time evolution of the spin population in the singlet and triplet state.

3.5.1 Electronic transition rates

Here, we will first reconsider the time-independent spin-pair Hamiltonian, ignoring the effects of nuclear spin and g−tensor anisotropy

$$\hat{\mathcal{H}}_{\mathbf{0}} = \mu_B(g_a\,\hat{\mathbf{S}}_{\mathbf{a}}\cdot\mathbf{B_0} + g_b\,\hat{\mathbf{S}}_{\mathbf{b}}\cdot\mathbf{B_0}) - J\,\hat{\mathbf{S}}_{\mathbf{a}}\cdot\hat{\mathbf{S}}_{\mathbf{b}} - D^d[3\hat{S}_a^z\hat{S}_b^z - \hat{\mathbf{S}}_{\mathbf{a}}\cdot\hat{\mathbf{S}}_{\mathbf{b}}]\,, \quad (3.67)$$

with D^d related to the axial dipolar coupling constant and equal to $-D_1/3$. We note that the dipole-dipole interaction term takes on a different form from when it was first introduced in Eq. 3.50, where here we have taken the high field approximation. In this high field limit, $|D_{ij}| \ll |g_i\mu_B B_0|$ and D_2 vanishes in Eq. 3.46 such that the dipole interaction Hamiltonian simplifies to Eq. 3.67. In the product basis state $|m_s\rangle_a \otimes |m_s\rangle_b = (|\uparrow\uparrow\rangle, |\uparrow\downarrow\rangle, |\downarrow\uparrow\rangle, |\downarrow\downarrow\rangle)$, the time-independent spin-pair Hamiltonian in Eq. 3.67 is a non-diagonal matrix that can be diagonalized by applying a unitary transformation

$$\hat{\boldsymbol{U}} = \begin{pmatrix} 1 & 0 & 0 & 0 \\ 0 & \cos(\phi) & \sin(\phi) & 0 \\ 0 & -\sin(\phi) & \cos(\phi) & 0 \\ 0 & 0 & 0 & 1 \end{pmatrix}, \quad (3.68)$$

where ϕ is the spin-mixing angle

$$\phi = \frac{1}{2}\arcsin\left(\frac{J + D^d}{\hbar\omega_\Delta}\right). \tag{3.69}$$

Once the spin-pair Hamiltonian in Eq. 3.67 is diagonalised following a unitary transform, the energy eigenvalues in the new spin basis are then

$$\hat{\boldsymbol{\mathcal{H}}}_{\mathbf{0}} = \begin{pmatrix} \frac{\hbar\Sigma\omega}{2} - J + D^d & 0 & 0 & 0 \\ 0 & -D^d + \hbar\omega_\Delta & 0 & 0 \\ 0 & 0 & -D^d - \hbar\omega_\Delta & 0 \\ 0 & 0 & 0 & -\frac{\hbar\Sigma\omega}{2} - J + D^d \end{pmatrix}, \tag{3.70}$$

and the corresponding eigenstates are

$$|\psi\rangle = \begin{pmatrix} |1\rangle \\ |2\rangle \\ |3\rangle \\ |4\rangle \end{pmatrix} = \begin{pmatrix} |\uparrow\uparrow\rangle \\ \cos(\phi)\,|\uparrow\downarrow\rangle - \sin(\phi)\,|\downarrow\uparrow\rangle \\ \sin(\phi)\,|\uparrow\downarrow\rangle + \cos(\phi)\,|\downarrow\uparrow\rangle \\ |\downarrow\downarrow\rangle \end{pmatrix}, \tag{3.71}$$

where ω_Δ is half the frequency separation between state $|2\rangle$ and $|3\rangle$

$$\omega_\Delta = \sqrt{\frac{(J + D^d)^2}{\hbar} + \frac{\Delta\omega^2}{4}}, \tag{3.72}$$

with $\Sigma\omega = \omega_a + \omega_b$ and $\Delta\omega = \omega_a - \omega_b$ the sum and difference of the Larmor frequencies of each individual spin in the spin-pair, respectively. Under the transformation, the two eigenstates $|T_+\rangle = |1\rangle$ and $|T_-\rangle = |4\rangle$ remain unchanged, whereas eigenstates $|2\rangle$ and $|3\rangle$ are mixed with both singlet and triplet content dependent on the amplitudes of J and D^d at intermediate coupling strengths. In the weak coupling limit such that $|J + D^d| \ll \hbar\omega_\Delta$, the spin-mixing angle approaches zero. Thus, $|2\rangle$ and $|3\rangle$ become $|\uparrow\downarrow\rangle$ and

$|\downarrow\uparrow\rangle$, respectively. In the strong coupling limit where $|J + D^d| \gg \hbar\omega_\Delta$, the spin-mixing angle approaches $\pi/4$ and the mixed states $|2\rangle$ and $|3\rangle$ simplify to purely singlet $|S_0\rangle = (|\uparrow\downarrow\rangle - |\downarrow\uparrow\rangle)/\sqrt{2}$ and triplet $|T_0\rangle = (|\uparrow\downarrow\rangle + |\downarrow\uparrow\rangle)/\sqrt{2}$ states, respectively, as we have previously seen in Eqs. 3.51(b)−3.51(c).

In the KSM model, it is assumed that recombination occurs at different transition rates, r_S and r_T, dependent on whether the intermediate spin-pair is in a purely singlet (antisymmetric permutation) or purely triplet (symmetric permutation) state, respectively. Furthermore, the singlet state recombination rate is assumed to be significantly faster than the triplet state recombination rate ($r_S \gg r_T$). The basis change due to spin-spin interaction implies that eigenstates $|2\rangle$ and $|3\rangle$ will have different amounts of purely singlet and triplet state content, resulting in different recombination probabilities

$$r_i = r_S |\langle i|S_0\rangle|^2 + r_T |\langle i|T_0\rangle|^2 \qquad i = 2, 3\,. \tag{3.73}$$

Thus, the recombination probabilities for each eigenstate are

$$r_1 = r_T \tag{3.74a}$$

$$r_2 = \frac{r_S}{2}\left[1 - \frac{J + D^d}{\hbar\omega_\Delta}\right] + \frac{r_T}{2}\left[1 + \frac{J + D^d}{\hbar\omega_\Delta}\right] \tag{3.74b}$$

$$r_3 = \frac{r_S}{2}\left[1 + \frac{J + D^d}{\hbar\omega_\Delta}\right] + \frac{r_T}{2}\left[1 - \frac{J + D^d}{\hbar\omega_\Delta}\right] \tag{3.74c}$$

$$r_4 = r_T\,. \tag{3.74d}$$

The recombination rate for each eigenstate in Eqs. 3.74(a)−3.74(d) is plotted as a function of the spin-spin interaction strength ($\frac{J+D^d}{\hbar\omega_\Delta}$) in Fig. 3.8. Both $|1\rangle$ and $|4\rangle$ have recombination rates equal to the triplet state recombination rate regardless of the spin-spin interaction strength. In the weak coupling limit ($|J + D^d| \ll \hbar\omega_\Delta$), both $|2\rangle$ and $|3\rangle$ have recombination rates equal to $\frac{r_S+r_T}{2}$. On the contrary in the strong coupling limit ($|J + D^d| \gg \hbar\omega_\Delta$), the recombination rate for state $|2\rangle$ approaches r_T, whereas the recombination rate for state $|3\rangle$ approaches r_S.

To extend our description to an ensemble of spin-pairs, the spin state of the spin-pair ensemble can be represented by a density matrix, $\boldsymbol{\rho}$, where its diagonal matrix elements, $\rho_{ii} = c_i \left|i\right\rangle \left\langle i\right|$, describes the probability c_i of finding the spin-pair ensemble in state $\left|i\right\rangle$. It is assumed that all off-diagonal matrix elements of the density matrix related to the coherence of the transition between state $\left|i\right\rangle$ and $\left|j\right\rangle$ are equal to zero. The dynamics of the ensemble spin-pair density is then governed by the stochastic Liouville equation analogous to the time-dependent Schrödinger equation

$$\frac{\partial \boldsymbol{\rho}(t)}{\partial t} = -\frac{i}{\hbar}[\hat{\boldsymbol{\mathcal{H}}}, \boldsymbol{\rho}] + \boldsymbol{\mathcal{S}}[\boldsymbol{\rho}(t)] + \boldsymbol{\mathcal{R}}[\boldsymbol{\rho}(t) - \boldsymbol{\rho}^0] \,, \tag{3.75}$$

where $\boldsymbol{\mathcal{S}} = \boldsymbol{\mathcal{S}}_{cr} + \boldsymbol{\mathcal{S}}_{an}$ is the stochastic operator consisting of a spin-pair creation and annihilation term, respectively, $\boldsymbol{\mathcal{R}}$ the Redfield operator that describes spin decoherence due to spin relaxation, and $\boldsymbol{\rho}^0$ the steady-state equilibrium ensemble spin-pair density. Historically, Haberkorn and Dietz [138] first developed the theoretical framework to apply the stochastic Liouville equation to recombining spin-pairs and Barabanov et al. [139] extended it to the general case where spin relaxation is no longer negligible by in-

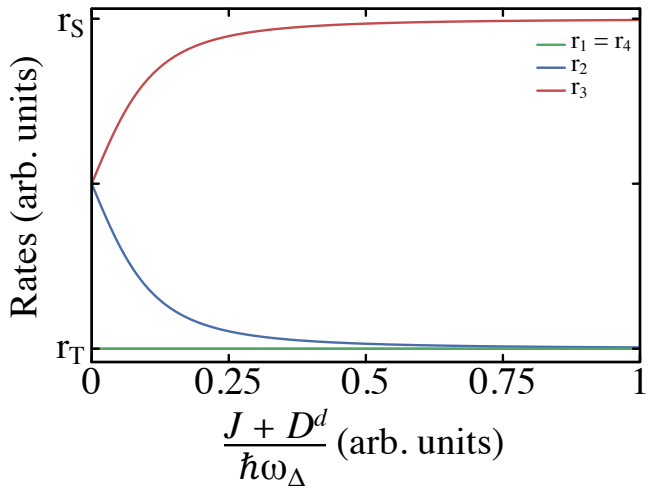

Fig. 3.8.: Simulation of the recombination rate for each eigenstate as a function of increasing spin-spin interaction strength. Both r_1 and r_4 remain unchanged with increasing spin-spin interaction strength and are equal to r_T. Instead, r_2 approaches r_T and r_3 approaches r_S as the spin-spin interaction strength increases.

troducing the Redfield operator based on Redfield's quantum mechanical theory of spin relaxation [140]. The Redfield operator takes into account spin-spin interactions of individual spin-pairs with the surrounding ensemble characterised by the T_2 time. Once the time-dependent solution to Eq. 3.75 is solved for $\boldsymbol{\rho}(t)$, it can be related to the total spin-pair recombination rate, which is just the sum of all singlet and triplet state transitions

$$R(t) = r_S \operatorname{Tr}[|S_0\rangle \langle S_0| \boldsymbol{\rho}(t)] + r_T \sum_{i=-1}^{1} \operatorname{Tr}[|T_i\rangle \langle T_i| \boldsymbol{\rho}(t)] \,, \tag{3.76}$$

which simplifies to

$$R(t) = \sum_{i=1}^{4} r_i \rho_{ii} \,. \tag{3.77}$$

Experimentally, the change in the total recombination rate due to spin resonance is measurable as a change in the sample conductivity

$$\Delta\sigma(t) = q[\Delta n_e(t)\mu_e + \Delta n_h(t)\mu_h] \,, \tag{3.78}$$

where $n_{e,h}(t)$ and $\mu_{e,h}$ are the electron and hole densities and mobilities, respectively. Assuming the mobilities are constant, the change in conductivity is only dependent on the electron and hole densities, which in turn are dependent on the generation, recombination, and dissociation rates of the intermediate spin-pair. It is assumed a constant source of charge carriers is supplied to the system such that the generation rate of spin-pairs, G, is also constant. Furthermore, the dissociation of spin-pairs is assumed to be spin-independent such that the dissociation rate, $D(t) = d \operatorname{Tr}[\boldsymbol{\rho}(t)]$, depends only on the dissociation probability and spin-pair density. Thus, the change in the electron and hole densities can be written in terms of the dissociation and recombination of the ensemble spin-pair

$$\Delta n_e(t) = \tau_L \Delta D(t) = \tau_L [D(t) - D_{ss}] = \tau_L d \sum_{i=1}^{4} \Delta \rho_{ii}(t) \tag{3.79a}$$

$$\Delta n_h(t) = -\tau_L \Delta R(t) = -\tau_L [R(t) - R_{ss}] = -\tau_L \sum_{i=1}^{4} r_i \Delta \rho_{ii}(t) \,, \tag{3.79b}$$

where D_{ss} and R_{ss} are the steady-state dissociation and recombination rates, respectively, τ_L the carrier lifetime, assumed here to be equal for both electrons and holes, and $\Delta \rho_{ii}(t) = \rho_{ii}(t) - \rho_{ii}^{ss}$ the change in the ensemble spin-pair density from steady-state. From Eqs. 3.79(a)−3.79(b), the change in sample conductivity induced by resonant EM irradiation can be expressed as

$$\Delta \sigma(t) = q \tau_L d \mu_e \sum_{i=1}^{4} \Delta \rho_{ii}(t) \left(1 - \frac{r_i}{d} \frac{\mu_h}{\mu_e}\right) . \tag{3.80}$$

Eq. 3.80 suggests that the measured change in device conductivity can either be positive or negative depending on the electron and hole densities. Furthermore, Eq. 3.80 provides a direct link between an experimentally measurable parameter in the device conductivity and the underlying spin-dependent recombination rates and energy eigenstates of the ensemble spin-pair.

In the basis state chosen, the annihilation component of the stochastic operator in Eq. 3.75 simplifies to [138]

$$[\mathcal{S}_{an}]_{ii} = (r_i + d) \rho_{ii} \,, \tag{3.81}$$

and the four spin-pair states are equally populated by a quarter of the generation rate described by the creation component of the stochastic operator ($[\mathcal{S}_{cr}]_{ii} = G\, \mathbb{I}/4$). The stochastic Liouville equation in Eq. 3.75 reduces to a relatively straightforward set of rate equations, assuming spin-spin relaxation defined by T_2 only occurs between eigenstates $|2\rangle$ and $|3\rangle$ according to

Redfield's relaxation theory [140]. An illustration of the rate model is shown in Fig. 3.2 and the set of rate equations is

$$\frac{\partial}{\partial t}\begin{pmatrix}\rho_{11}\\ \rho_{22}\\ \rho_{33}\\ \rho_{44}\end{pmatrix} = \begin{pmatrix}-d-r_T & 0 & 0 & 0\\ 0 & -d-r_2-\frac{1}{T_2} & \frac{1}{T_2} & 0\\ 0 & \frac{1}{T_2} & -d-r_3-\frac{1}{T_2} & 0\\ 0 & 0 & 0 & -d-r_T\end{pmatrix}\begin{pmatrix}\rho_{11}\\ \rho_{22}\\ \rho_{33}\\ \rho_{44}\end{pmatrix} + \frac{G}{4}\begin{pmatrix}1\\ 1\\ 1\\ 1\end{pmatrix}. \tag{3.82}$$

Upon closer inspection, the rate equations are a set of linear, autonomous, first order linear ODEs of the form $\dot{y} + ay = b$. The corresponding solution is just the sum of the homogeneous and steady-state solution ($y = y_H + y_{ss}$). The steady-state solution ($\partial\rho_{ii}/\partial t = 0$) is

$$\rho^{ss}_{11,44} = \frac{G}{4}\frac{1}{d+r_T} \tag{3.83a}$$

$$\rho^{ss}_{22,33} = \frac{G}{4}\frac{\frac{2}{T^2}+d+r_{3,2}}{d^2+r_2 d+\frac{2d}{T_2}+r_3 d+r_2 r_3+\frac{r_3}{T_2}+\frac{r_2}{T_2}}. \tag{3.83b}$$

On the other hand, the solution to the homogeneous component ($\dot{y} + ay = 0$) of the ODE takes on the form of an exponential decay function $y_H(t) = Ce^{-t/\tau}$ with the constant coefficient matrix calculated from the eigenvectors

$$\tilde{C} = \begin{pmatrix}1 & 0 & 0 & 0\\ 0 & \frac{T_2}{2}(r_3-r_2+\xi) & 1 & 0\\ 0 & 1 & \frac{T_2}{2}(r_3-r_2-\xi) & 0\\ 0 & 0 & 0 & 1\end{pmatrix}, \tag{3.84}$$

and the decay time constants are determined from the eigenvalues

$$\tau_1 = -(d + r_T) \tag{3.85a}$$

$$\tau_2 = -\frac{1}{T_2} - d - \frac{r_2}{2} - \frac{r_3}{2} + \frac{\xi}{2} \tag{3.85b}$$

$$\tau_3 = -\frac{1}{T_2} - d - \frac{r_2}{2} - \frac{r_3}{2} - \frac{\xi}{2} \tag{3.85c}$$

$$\tau_4 = -(d + r_T)\,, \tag{3.85d}$$

where $\xi = \sqrt{\frac{4}{T_2^2} + (r_3 - r_2)^2}$. From Eqs. 3.85(a)−3.85(d), the solution to Eq. 3.82 can be computed, which follows a multiexponential decay function characterised by three time constants ($\tau_1 = \tau_4$, τ_2, τ_3) operating on different timescales.

To illustrate the recombination behaviour of the ensemble spin-pair after a short coherent resonant pulse of length τ, again we assume that the singlet state recombination rate, related to r_2 and r_3, is much faster than the triplet recombination rate and dissociation rate (i.e., $r_3 \gg 1/T_2 \approx r_2 > r_T \gg d$). In equilibrium prior to resonant pulsed excitation, under the assumptions made above, the initial steady-state ensemble spin-pair density in Eqs. 3.83(a)−3.83(b) simplifies to

$$\rho^{ss}_{11,44} = \frac{G}{4r_T} = \rho^{ss} \tag{3.86a}$$

$$\rho^{ss}_{22,33} = 0\,, \tag{3.86b}$$

which describes that the ensemble spin-pair are initially populated in the triplet spin state. Assuming that spin-pair generation, recombination, and dissociation are negligible during the short EM irradiation pulse such that the absolute number of spin-pairs remains constant, we can define the relative density change in terms of $\rho_{11,44}$ and $\rho_{22,33}$ as

$$-\Delta(\tau) := \frac{\rho_{11,44} - \rho^{ss}_{11,44}}{\mathrm{Tr}[\rho^{ss}]} \tag{3.87a}$$

$$\frac{\rho_{22,33} - \rho^{ss}_{22,33}}{\mathrm{Tr}[\rho^{ss}]} = \Big(1 \pm \frac{J + D^d}{\hbar\omega_\Delta}\Big)\Delta(\tau)\,, \tag{3.87b}$$

with $\Delta\omega \ll \gamma B_1$. The origin and derivation of Eqs. 3.87(a)-3.87(b) will appear in Sec. 3.5.2 when the dynamics of the ensemble spin-pair during the resonant EM excitation is considered. With the aforementioned assumptions considered and the definition for the relative density change $\Delta(\tau)$ defined, the conductivity change after pulsed resonant excitation in Eq. 3.80 becomes

$$\begin{aligned}\Delta\sigma(t) = \frac{q\tau_L d\mu_e G}{2r_T}\Big[2\Big(\frac{r_T}{d}\frac{\mu_h}{\mu_e} - 1\Big)e^{-(r_T+d)t} - \Big(\frac{r_2}{d}\frac{\mu_h}{\mu_e} - 1\Big) \\ \Big(1 + \frac{J + D^d}{\hbar\omega_\Delta}\Big)e^{-\left(d + \frac{1}{T_2} + \frac{r_2}{2}\right)t} - \frac{r_3}{d}\frac{\mu_h}{\mu_e}\Big(1 - \frac{J + D^d}{\hbar\omega_\Delta}\Big)e^{-r_3 t}\Big]\Delta(\tau)\,.\end{aligned} \tag{3.88}$$

Eq. 3.88 consists of three exponential decays occurring on three different timescales based on the time constants in Eqs. 3.85(a)−3.85(b) labelled $\tau_{slow} = \tau_1 = \tau_2 = (r_T + d)$, $\tau_{med.} = (d + 1/T_2 + r_2/2) \approx \tau_2$ and $\tau_{fast} = r_S = r_3 \approx \tau_3$. Furthermore, the prefactor of each individual exponential decay in Eq. 3.88 can either be positive (recombination enhancement) or negative (recombination quenching) in value relative to the steady-state conductivity dependant on r_2 and r_3 that are proportional to the spin-spin interaction strength from Eqs. 3.74(b)−3.74(c). An example simulation of Eq. 3.88 is plotted as a function of time in Fig. 3.9, demonstrating that the exponential decays corresponding to τ_{slow} and $\tau_{med.}$ are positive and negative in value, respectively, for $(J + D^d)/\hbar\omega_\Delta = 0.98$. Furthermore, the exponential decay corresponding to τ_{fast} quickly decays back to zero.

From Eq. 3.88, the conductivity transient at any arbitrary time is directly proportional to the relative spin state density change ($\Delta\sigma(t,\tau) \propto \Delta(\tau)$). As such, the conductivity change at any arbitrary time after the end of the resonant pulse excitation allows direct access to the recombination rates during the resonant pulse excitation typically occurring on the nanosecond timescale

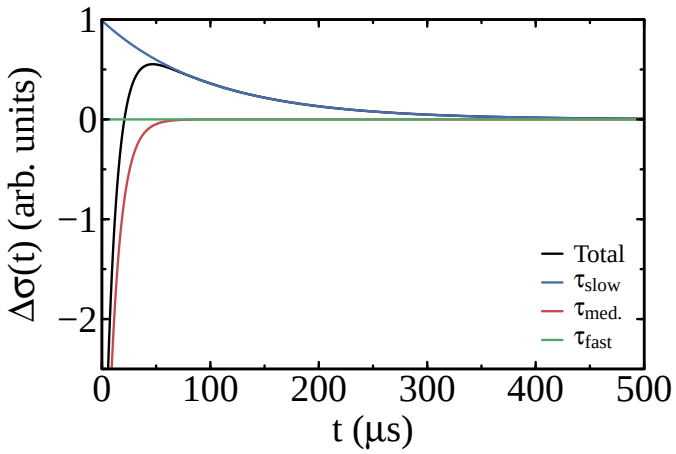

Fig. 3.9.: Simulation of the conductivity transient and its individual exponential decay components in response to a resonant excitation pulse based on Eq. 3.88. For this simulation, values of $r_T = 10^4$ s^{-1}, $r_S = 10^7$ s^{-1}, $d = 10^2$ s^{-1}, $T_2 = 15\ \mu$s, and $(J + D^d)/\hbar\omega_\Delta = 0.98$ were chosen, demonstrating that both a positive and negative transient component can exist.

not accessible with existing detection electronics and transimpedance preamplifiers. This result suggests electrically detection of coherent spin dynamics is possible, where resonant spin dynamics can be indirectly accessed and reconstructed at more favourable timescales as the conductivity transient decays back to equilibrium. An experimental conductivity transient in response to a resonant excitation pulse will be seen in Fig. 7.4(b) and subsequent pEDMR measurements utilising lock-in detection effectively integrates over the time interval as the conductivity transient decays back to equilibrium.

During resonant pulse excitation, we have previously seen in Sec. 3.2 that a spin ensemble undergoes Rabi oscillations. For an ensemble spin-pair with arbitrary spin-spin coupling strength, a phenomenon called spin-beating can occur in the Rabi oscillations, which will be explored below.

3.5.2 Rabi oscillations

Mathematically, it is easier to work in the rotating frame of reference using the Bloch sphere representation introduced in Sec. 3.2, which removes the time dependency of $\mathbf{B_1}(t)$. The corresponding spin-pair Hamiltonian also becomes time-independent

$$\hat{\boldsymbol{\mathcal{H}}}_{\mathbf{1}} = \mu_B(g_a \hat{\mathbf{S}}_{\mathbf{a}} \cdot \mathbf{B_1} + g_b \hat{\mathbf{S}}_{\mathbf{b}} \cdot \mathbf{B_1}) \,. \tag{3.89}$$

Therefore, the total spin-pair ensemble Hamiltonian is the sum of the time-independent Hamiltonian and the time-dependent Hamiltonian due to EM irradiation in the rotating frame ($\hat{\boldsymbol{\mathcal{H}}} = \hat{\boldsymbol{\mathcal{H}}}_{\mathbf{0}} + \hat{\boldsymbol{\mathcal{H}}}_{\mathbf{1}}$), where $\hat{\boldsymbol{\mathcal{H}}}_{\mathbf{1}}$ is treated as a perturbation to the quantum system. Instead of trying to solve for the stochastic Liouville equation in 3.75 by substituting in the total spin-pair ensemble Hamiltonian, which will result in multiple off-diagonal non-zero elements that substantially complicates the calculations, an alternative approach utilising rotation operators to describe the spin propagation of the ensemble spin-pair during pulsed resonant excitation is used. This approach is made possible as it is assumed that incoherent processes, such as spin-spin interactions and spin relaxation during pulsed resonant excitation is negligible, which usually holds true under experimental conditions where spin-spin interaction is much weaker than the Zeeman interaction ($(D^d + J) \ll \omega_{a,b}$)) and the B_1 field used ($(D^d + J) \ll \hbar\gamma B_1$). In addition, spin relaxation times found in semiconductor hosts with weak spin-orbit coupling ($\sim 10^{-6} - 10^{-3}$ s) [37, 41, 124] are negligible during the short ($< 10^{-7}$ s) pulsed resonant excitation ($\tau \ll T_1, T_2$).

Similar to the spin precession described semi-classically using Bloch equations in Sec. 3.2, an electron spin precesses around an effective magnetic field in the rotating frame of reference

$$\mathbf{B_{eff}} = B_1 \, \hat{\mathbf{x}} + \big(B_0 - \frac{\omega\hbar}{g\mu_B}\big) \, \hat{\mathbf{z}} \,, \tag{3.90}$$

that is pointed along vector

$$\hat{\mathbf{n}} = \frac{\gamma B_1}{\omega} \, \hat{\mathbf{x}}' + \big(\frac{\omega - \omega_i}{\Omega}\big) \, \hat{\mathbf{z}}' \,. \tag{3.91}$$

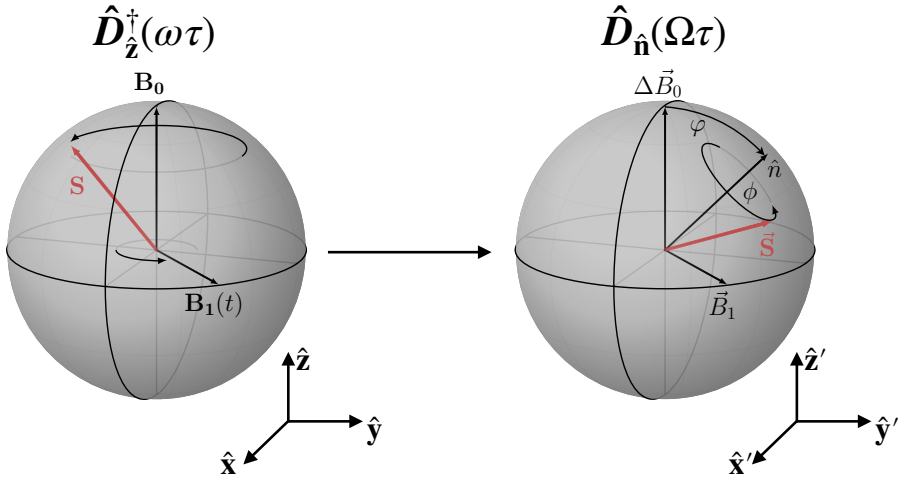

Fig. 3.10.: (a) Illustration of the complex spin nutation trajectory on the Bloch sphere in the stationary laboratory frame of reference. (b) Illustration of the same spin nutation trajectory on the Bloch sphere in the rotating frame of reference where $\mathbf{B_1}$ becomes time-invariant and the spin vector precesses around vector $\hat{\mathbf{n}}$.

The spin precession about axis $\hat{\mathbf{n}}$ can be expressed with the following rotation operator

$$\begin{aligned}\hat{\boldsymbol{\mathcal{D}}}_{\hat{\mathbf{n}}}(\phi) &= \exp\Big(-\frac{i}{\hbar}\mathbf{S}\cdot\hat{\mathbf{n}}\,\phi\Big)\\ &= \mathbb{I}\cos\Big(\frac{\phi}{2}\Big) - i\boldsymbol{\sigma}\cdot\hat{\mathbf{n}}\sin\Big(\frac{\phi}{2}\Big)\,,\end{aligned} \tag{3.92}$$

where $\boldsymbol{\sigma}$ represents the Pauli matrices. As a result, the spin dynamics due to pulsed resonant excitation of length τ and frequency ω on a spin with Larmor frequency ω_i can be written as a rotation operator

$$\hat{\boldsymbol{\mathcal{D}}}(\tau,\omega,\omega_i) = \hat{\boldsymbol{\mathcal{D}}}_{\hat{\mathbf{z}}}(\omega\tau)\hat{\boldsymbol{\mathcal{D}}}_{\hat{\mathbf{n}}}(\Omega\tau)\hat{\boldsymbol{\mathcal{D}}}^{\dagger}_{\hat{\mathbf{z}}}(\omega\tau)\,, \tag{3.93}$$

consisting of three rotations in and out of the rotating reference frame with the Rabi precession in between the middle. An illustration of spin $S = 1/2$ subject to $\mathbf{B} = \mathbf{B_0} + \mathbf{B_1}$ in the stationary observer and rotating frame of reference on the Bloch sphere is shown in Fig. 3.10. For a spin-pair with two

different Larmor frequencies, ω_a and ω_b, the rotation operator is simply the Kronecker product of the rotation operator for each individual spin

$$\hat{\boldsymbol{\mathcal{D}}}(\tau,\omega,\omega_a,\omega_b) = \hat{\boldsymbol{\mathcal{D}}}_a(\tau,\omega,\omega_a) \otimes \hat{\boldsymbol{\mathcal{D}}}_b(\tau,\omega,\omega_b)\ , \tag{3.94}$$

where $\hat{\boldsymbol{\mathcal{D}}}(\tau,\omega,\omega_a,\omega_b)$ is a 4×4 matrix of the following form

$$\hat{\boldsymbol{\mathcal{D}}}(\tau,\omega,\omega_a,\omega_b) = \begin{pmatrix} \xi^a\xi^b & -\xi^a\zeta^b & -\zeta^a\xi^b & \zeta^a\zeta^b \\ \xi^a\bar{\zeta^b} & \xi^a\bar{\xi^b} & -\zeta^a\bar{\zeta^b} & -\zeta^a\bar{\xi^b} \\ \bar{\zeta^a}\xi^b & -\zeta^a\bar{\zeta^b} & \bar{\xi^a}\xi^b & -\xi^a\bar{\zeta^b} \\ \bar{\zeta^a}\bar{\zeta^b} & \bar{\zeta^a}\bar{\xi^b} & \bar{\xi^a}\bar{\zeta^b} & \bar{\xi^a}\bar{\xi^b} \end{pmatrix}\ , \tag{3.95}$$

with

$$\xi^{a,b} = \cos\left(\frac{\Omega_{a,b}\tau}{2}\right) + i\sin\left(\frac{\Omega_{a,b}\tau}{2}\right)\cos(\varphi_{a,b}) \tag{3.96a}$$

$$\zeta^{a,b} = \sin\left(\frac{\Omega_{a,b}\tau}{2}\right)e^{-i\omega\tau}\sin(\varphi_{a,b}) \tag{3.96b}$$

$$\cos(\varphi_{a,b}) = \frac{\omega-\omega_{a,b}}{\Omega_{a,b}} \tag{3.96c}$$

$$\sin(\varphi_{a,b}) = \frac{\gamma B_1}{\Omega_{a,b}}\ . \tag{3.96d}$$

Given that the rotation operator in Eq. 3.94 describes the spin precession of the spin-pair during pulsed resonant excitation, the time-evolution of the ensemble spin-pair density from the steady-state is given by the following transformation

$$\boldsymbol{\rho}(\tau) = \hat{\boldsymbol{\mathcal{D}}}^{\dagger}\boldsymbol{\rho}^{ss}\hat{\boldsymbol{\mathcal{D}}}\ . \tag{3.97}$$

Eq. 3.97 can be solved by substituting in Eqs. 3.87(a)−3.87(b) and Eq. 3.95

$$\boldsymbol{\rho}(\tau) = \rho^{ss} \begin{pmatrix} |\xi^a\xi^b|^2 + |\zeta^a\zeta^b|^2 & \xi^b\zeta^b(|\xi^a|^2 - |\zeta^a|^2) & \xi^a\zeta^a(|\xi^b|^2 - |\zeta^b|^2) & 2\xi^a\xi^b\zeta^a\zeta^b \\ \bar{\xi^b}\bar{\zeta^b}(|\xi^a|^2 - |\zeta^a|^2) & |\xi^a\zeta^b|^2 + |\zeta^a\xi^b|^2 & 2\xi^a\bar{\xi^b}\zeta^a\bar{\zeta^b} & \xi^b\zeta^b(|\zeta^a|^2 - |\xi^a|^2) \\ \bar{\xi^a}\bar{\zeta^a}(|\xi^b|^2 - |\zeta^b|^2) & 2\bar{\xi^a}\xi^b\bar{\zeta^a}\zeta^b & |\xi^a\zeta^b|^2 + |\zeta^a\xi^b|^2 & \bar{\xi^b}\bar{\zeta^b}(|\zeta^a|^2 - |\xi^a|^2) \\ 2\bar{\xi^a}\bar{\xi^b}\bar{\zeta^a}\bar{\zeta^b} & \bar{\xi^a}\bar{\zeta^a}(|\zeta^b|^2 - |\xi^b|^2) & \bar{\xi^b}\bar{\zeta^b}(|\zeta^a|^2 - |\xi^a|^2) & |\xi^a\xi^b|^2 + |\zeta^a\zeta^b|^2 \end{pmatrix} . \tag{3.98}$$

Note that Eq. 3.98 describes the coherent spin dynamics of an ensemble spin-pair during resonant pulsed excitation and is derived from the initial steady-state ensemble spin-pair density (see Eqs. 3.86(a)−3.86(b)) following a rotation transform in the absence of any spin-spin interaction. Thus, the following transformation is used to transform out into the incoherent time-domain after pulsed resonant excitation in which spin-spin interaction is taken into account

$$\tilde{\boldsymbol{\rho}}^E(\tau) = \hat{\boldsymbol{U}}(\phi)\boldsymbol{\rho}(\tau)\hat{\boldsymbol{U}}^\dagger(\phi) \, . \tag{3.99}$$

Using Eqs. 3.68−3.69 and Eq. 3.98, the transformation in Eq. 3.99 yields the following diagonal matrix elements

$$\rho^E_{11,44} = \rho^{ss}\Delta^u(\tau) \tag{3.100a}$$

$$\rho^E_{22,33} = \rho^{ss}\Delta^v(\tau) \pm \rho^{ss}\frac{J + D^d}{\hbar\omega_\Delta}\Delta^\omega(\tau) \, , \tag{3.100b}$$

where

$$\Delta^u(\tau) = |\xi^a\xi^b|^2 + |\zeta^a\zeta^b|^2 \tag{3.101a}$$
$$= \left[\cos^2\left(\frac{\Omega_a\tau}{2}\right) + \sin^2\left(\frac{\Omega_a\tau}{2}\right)\cos^2(\varphi_a)\right]\left[\cos^2\left(\frac{\Omega_b\tau}{2}\right) + \sin^2\left(\frac{\Omega_b\tau}{2}\right)\cos^2(\varphi_b)\right] + \sin^2\left(\frac{\Omega_b\tau}{2}\right)\sin^2\left(\frac{\Omega_a\tau}{2}\right)\sin^2(\varphi_a)\sin^2(\varphi_b)$$
$$\Delta^v(\tau) = |\xi^a\zeta^b|^2 + |\zeta^a\xi^b|^2 \tag{3.101b}$$
$$= \left[\cos^2\left(\frac{\Omega_a\tau}{2}\right) + \sin^2\left(\frac{\Omega_a\tau}{2}\right)\cos^2(\varphi_a)\right]\sin^2\left(\frac{\Omega_b\tau}{2}\right)\sin^2(\varphi_b) + \left[\cos^2\left(\frac{\Omega_b\tau}{2}\right) + \sin^2\left(\frac{\Omega_b\tau}{2}\right)\cos^2(\varphi_b)\right] + \sin^2\left(\frac{\Omega_a\tau}{2}\right)\sin^2(\varphi_a)$$
$$\Delta^w(\tau) = 2\,\mathrm{Re}(2\xi^a\bar{\xi^b}\zeta^a\bar{\zeta^b}) \tag{3.101c}$$
$$= 2\sin\left(\frac{\Omega_a\tau}{2}\right)\sin\left(\frac{\Omega_b\tau}{2}\right)\cos\left(\frac{\Omega_a\tau}{2}\right)\cos\left(\frac{\Omega_b\tau}{2}\right)\sin(\varphi_a)\sin(\varphi_b) + 2\sin^2\left(\frac{\Omega_a\tau}{2}\right)\sin^2\left(\frac{\Omega_b\tau}{2}\right)\cos(\varphi_a)\cos(\varphi_b)\sin(\varphi_a)\sin(\varphi_b)\,.$$

The changes in the spin-pair energy eigenstates due to Rabi oscillations is directly affected by spin-spin interaction, as evident by the second term in Eq. 3.100(b).

Two limiting cases are considered to further simplify Eqs. 3.101(a)–3.101(c). First, for the case where the Larmor separation between the two spins is small ($\omega_a - \omega_b \ll \gamma B_1$), the Larmor frequencies approach a common value, ω_L. Therefore, the excitation of each individual spin is impossible (i.e., non-selective). In this regime,

$$\cos(\varphi_a) \approx \cos(\varphi_b) \approx \frac{\omega - \omega_L}{\Omega_L} \tag{3.102a}$$
$$\sin(\varphi_a) \approx \sin(\varphi_b) \approx \frac{\gamma B_1}{\Omega_L}\,, \tag{3.102b}$$

where $\Omega_L = \sqrt{\gamma^2 B_1^2 + (\omega - \omega_L)^2}$ and Eqs. 3.101(a)–3.101(b) simplify to

$$\Delta^u(\tau) = 1 - \Delta^{v,w}(\tau) =: 1 - \Delta(\tau) \tag{3.103a}$$

$$\Delta^v(\tau) = \sin^2(\Omega_L\tau)\frac{\gamma^2 B_1^2}{\Omega_L^2} + 2\sin^4(\Omega_L\tau)\frac{\gamma^2 B_1^2(\omega-\omega_L)^2}{\Omega_L^4} \tag{3.103b}$$

$$\Delta^w(\tau) = \Delta^v(\tau) =: \Delta(\tau)\,. \tag{3.103c}$$

Substituting Eqs. 3.103(a)–3.103(c) back into Eqs. 3.100(a)–3.100(b) yields

$$\frac{\rho_{11,44} - \rho^{ss}_{11,44}}{\mathrm{Tr}[\rho^{ss}]} = -\Delta(\tau) \tag{3.104a}$$

$$\frac{\rho_{22,33} - \rho^{ss}_{22,33}}{\mathrm{Tr}[\rho^{ss}]} = \Big(1 \pm \frac{J + D^d}{\hbar\omega_\Delta}\Big)\Delta(\tau)\,, \tag{3.104b}$$

which was first introduced and defined in Eqs. 3.87(a)–3.87(b). In the vicinity of spin resonance ($\omega - \omega_L \ll \gamma B_1$), the relative density change simplifies to

$$\Delta(\tau) = \frac{1}{2}\frac{\gamma^2 B_1^2}{\Omega_L^2}[1 - \cos(2\Omega_L\tau)]\,, \tag{3.105}$$

and oscillates at twice the Rabi frequency. As a result, both spins within the spin-pair oscillate simultaneous.

For the case where the Larmor separation is large ($\omega - \omega_L \gg \gamma B_1$), the individual spins in the spin pair can be selectively excited under spin resonance. As a result, spin S_b will be off resonance when spin S_a is resonantly excited (and vice versa) such that $\omega - \omega_b \gg \gamma B_1$. In this regime,

$$\Omega_b = \omega - \omega_b \tag{3.106a}$$

$$\cos(\varphi_b) = 1 \tag{3.106b}$$

$$\sin(\varphi_b) = 0\,, \tag{3.106c}$$

and Eqs. 3.101(a)−3.101(c) simplifies to

$$\Delta^u(\tau) = 1 - \frac{\gamma^2 B_1^2}{\Omega_a^2} \sin^2\left(\frac{\Omega_a \tau}{2}\right) =: 1 - \Delta(\tau) \tag{3.107a}$$

$$\Delta^v(\tau) = \frac{\gamma^2 B_1^2}{\Omega_a^2} \sin^2\left(\frac{\Omega_a \tau}{2}\right) =: \Delta(\tau) \tag{3.107b}$$

$$\Delta^w(\tau) = 0\,. \tag{3.107c}$$

Substituting Eqs. 3.107(a)−3.107(c) back into Eqs. 3.100(a)−3.100(b) yields

$$\frac{\rho_{11,44} - \rho_{11,44}^{ss}}{\mathrm{Tr}[\tilde{\rho}^{ss}]} = -\,\Delta(\tau) \tag{3.108a}$$

$$\frac{\rho_{22,33} - \rho_{22,33}^{ss}}{\mathrm{Tr}[\tilde{\rho}^{ss}]} = \Delta(\tau)\,. \tag{3.108b}$$

Notice that the state density change of eigenstate $|2\rangle$ and $|3\rangle$ no longer depends on spin-spin interaction as compared to Eq. 3.104(b). In the vicinity of spin resonance, ($\omega - \omega_i \ll \gamma B_1$), the relative density change simplifies to

$$\Delta(\tau) = \frac{1}{2}\frac{\gamma^2 B_1^2}{\Omega_i^2}[1 - \cos(\Omega_i \tau)]\,, \tag{3.109}$$

and only one of the electron spins in the spin-pair precesses about B_1, while the other electron spin in the spin-pair is off resonance. In comparison with the non-selective strong spin-spin coupling regime, Eq. 3.109 oscillates at the Rabi frequency Ω_i, as expected for a single spin $S = 1/2$.

From Eq. 3.88, the measurable conductivity change is proportional to the relative density change in which the lineshape of the pulsed EDMR signal can be determined. In either case of small or large Larmor separation, the expression for the relative density change in Eq. 3.105 and Eq. 3.109, consists of a Lorentzian-shaped prefactor $\gamma B_1/\Omega$ with linewidth B_1. In practice, an ensemble spin-pair in a solid-state host best resembles a distribution of Larmor

frequencies, $\Phi_i(\omega_i)$, due to Landé g−factor inhomogeneity. Mathematically, this is described using a double integration

$$\boldsymbol{\rho}^{\boldsymbol{net}}(t) = \int_{-\infty}^{\infty}\int_{-\infty}^{\infty} d\omega_a d\omega_b \, \Phi_a(\omega_a)\Phi_b(\omega_b)\hat{\boldsymbol{\mathcal{D}}}^{\dagger}(\tau,\omega,\omega_a,\omega_b)\boldsymbol{\rho}^{\boldsymbol{ss}}\hat{\boldsymbol{\mathcal{D}}}(\tau,\omega,\omega_a,\omega_b) \, . \tag{3.110}$$

When the Larmor separation between the two electron spins in the spin-pair is large, the distribution of Larmor frequencies far off resonance integrates to one. In contrast, two cases must be considered when the Larmor separation between the two electron spins in the spin-pair is small. For the case where the Larmor distribution is smaller than the oscillating magnetic field ($\omega - \omega_L \ll \gamma B_1$), the lineshape of the pulsed EDMR signal is dominated by the B_1-induced Lorentz broadening as Landé g−factor inhomogeneity is negligible. On the other hand, when the Larmor distribution is larger than the oscillating magnetic field ($\omega - \omega_L \gg \gamma B_1$) and the Larmor separation ($\omega - \omega_L \gg \omega_a - \omega_b$), the spin-pair can be described using just one distribution. Effectively, in all cases described above, the double integral in Eq. 3.110 reduces down to a single integral and the effective relative density change is then

$$\Delta^{eff}(\tau) = \int_{-\infty}^{\infty} d\omega_L \, \Phi(\omega_L)\frac{\gamma^2 B_1^2}{\gamma^2 B_1^2 + (\omega - \omega_L^2)}\sin^2(\kappa\sqrt{\gamma^2 B_1^2 + (\omega - \omega_L)^2}\tau) \, , \tag{3.111}$$

where $\kappa = 1/2$ and $\kappa = 1$ for large and small Larmor separation, respectively. Eq. 3.111 can be further simplified in the case where $\Phi(\omega_L)$ is assumed constant and smooth within the range of B_1 such that

$$\Delta^{eff}(\tau) = \gamma B_1 \Phi(\omega) T(\alpha) \, , \tag{3.112}$$

with the inhomogeneous distribution now centred about the resonant excitation frequency, ω, and $T(\alpha)$ is the general transient function

$$T(\alpha) = \int_{-\infty}^{\infty} \frac{\sin^2(\alpha\sqrt{1+x^2})}{1+x^2} dx \,, \tag{3.113}$$

in which $x = (\omega - \omega_L)/\gamma B_1$ and $\alpha = \kappa\gamma B_1 \tau$ is the turning angle. The transient function can also be expressed in terms of the Bessel function of the first kind

$$T(\alpha) = \pi \int_0^{\alpha} J_0(2x) dx \,, \tag{3.114}$$

which reflects the Rabi oscillation of the spin-pair ensemble during pulsed resonant excitation. Both Eq. 3.113 and Eq. 3.114 cannot be integrated analytically and must be solved numerically. The transient function will be later used in Chapter 7 to fit experimentally measured Rabi oscillations.

3.6 Summary

In this chapter, a detailed description of the theory behind SDR has been introduced, thereby laying the theoretical foundation for interpreting the EDMR measurements in the later experimental chapters. In particular, the SDR process that gives rise to a change in conductivity measured with EDMR was established. Furthermore, the direct link between the measured conductivity change and coherent spin dynamics in the time-domain was presented. This will be particularly important for Chapter 7 in which various pulse sequences are explored and employed with the pEDMR technique on paramagnetic defects in SiC.

Experimental Methods 4

This chapter details the design and implementation of the EDMR spectrometers used in this thesis. Hardware configurations required to implement continuous-wave and pulsed EDMR operation at different magnetic field strengths will be outlined. Simulations of the oscillating EM field, the theory of operation behind lock-in detection, and post acquisition data processing steps implemented will also be presented. Other characterisation techniques, such as random telegraph signal (RTS), electroluminescence (EL), and deep level transient spectroscopy (DLTS) were also used, but the details and results will be provided in the Appendix.

4.1 Design and implementation of EDMR spectrometers

Within this thesis, we present results measured either on a custom-built low-field ($\nu = 263$ MHz) EDMR spectrometer, a temperature controllable ($80 - 500$ K) intermediate-field spectrometer, or a high-field ($\nu = 8.08$ GHz) EDMR spectrometer for continuous-wave operation. The low-field spectrometer was adapted for pulsed-EDMR (pEDMR) measurements. Generally, the hardware required for an EDMR measurement can be grouped into three categories: hardware for delivering resonant EM excitation, hardware for producing a linear changing and oscillating magnetic field, and hardware for measuring small changes in the device current. All three spectrometers effectively share the same detection electronics and differ in the magnetic field source. Key features and limitations of each custom-built EDMR spectrometer will be detailed below.

4.1.1 Low-field EDMR spectrometer

A block diagram of the low-field EDMR spectrometer implemented is shown in Fig 4.1. The majority of the results presented in this thesis were measured

using this spectrometer. To produce a uniform static magnetic field, a set of coils was wound using enamelled copper wire of diameter 1.02 mm (American wire gauge 18). Windings of 395 turns ($R = 1.8\,\Omega$ each) were used on a set of custom-designed 3D-printed enclosures in a Helmholtz configuration, where the magnetic field produced along the axis crossing the center of the coils is well-defined by the Biot-Savart law

$$B_0 = \left(\frac{4}{5}\right)^{3/2} \frac{\mu_0 n I}{r}\,, \tag{4.1}$$

where μ_0 is the permeability constant and equal to $4\pi \times 10^{-7}$ T·m/A, n the total number of turns, I the current, and r the radius of the coil. A Kepco bipolar BOP power supply operating in voltage amplifier mode is used in

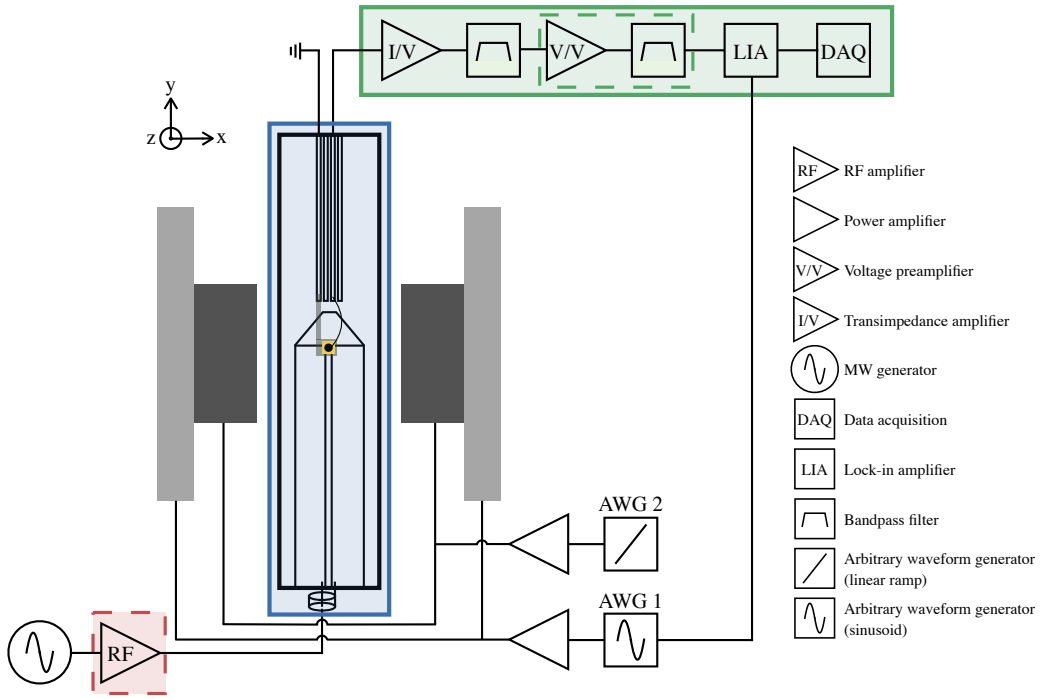

Fig. 4.1.: Block diagram of the low-field EDMR setup. The sample is attached to a custom-designed PCB and situated at the centre of a set of Helmholtz coils. In this configuration, the sample orientation can be rotated about the $\hat{\mathbf{y}}$ axis. The inner set of Helmholtz coils are used to generate a linear changing magnetic field, whereas the outer set of Helmholtz coils are used to generate an oscillating magnetic field for lock-in detection when required. Optional hardware used only for certain instances are indicated by the dashed colour boxes. Refer to main text for more detail.

conjunction with a Rigol DG4162 arbitrary waveform generator (AWG) to generate a linear magnetic field sweep. At its maximum, the magnetic field reaches approximately ± 13 mT at the center of the coils, which were equally spaced apart. The power supply was operated in constant voltage mode as the output noise is substantially smaller than when operating in constant current mode as per the specifications of the power supply. Changes in the coil resistance due to heating effects when operating in constant voltage mode were taken into account post-processing by using a linear interpolation algorithm to align each individual magnetic field sweep. The coil temperature was kept below 50°C by limiting the current through the coils connected in series to ± 2.5 A. No special cooling system was used to regulate the temperature of the coils.

A second set of coils ($n = 90, R = 0.6\ \Omega$ each) spaced further apart was used to produce a small oscillating magnetic field for lock-in detection, in combination with a second Kepco BOP power supply in voltage amplifier mode and the internal sinusoidal reference of a lock-in amplifier (SR830). As the impedance of a purely inductive load increases with frequency (i.e., $Z_L = i\omega L$), the amplitude of the modulating magnetic field diminishes with the modulation frequency. For the modulation frequency of $f_{mod} = 177.53$ Hz typically chosen in our measurements, the maximum peak-to-peak modulation amplitude was approximately 0.25 mT. The magnetic field strength was measured using a commercial hall effect sensor (DRV5055) situated at one end of the Helmholtz coils. Offsets in the magnetic field with respect to the sample position is calculated by measuring a calibration curve in which the hall effect sensor is placed at the sample position.

Samples are mounted onto a custom-designed printed circuit board (PCB) with an embedded antenna situated below the solder mask for resonant EM excitation (see Fig. 4.5(a)). Additional details about the PCB design are provided in Sec. 4.1.2. The PCB can be rotated about the $\hat{\mathbf{y}}$ axis in $10^\circ \pm 2^\circ$ increments, where measurements are typically performed with the magnetic field either parallel or perpendicular to the sample surface. Electrical contact to the device is provided using wire bonds to the four available exposed copper traces situated far away from the embedded antenna to minimise undesired EM crosstalk. Devices with a back metallic contact were contacted to one of the copper traces using silver conductive paste. At the end of

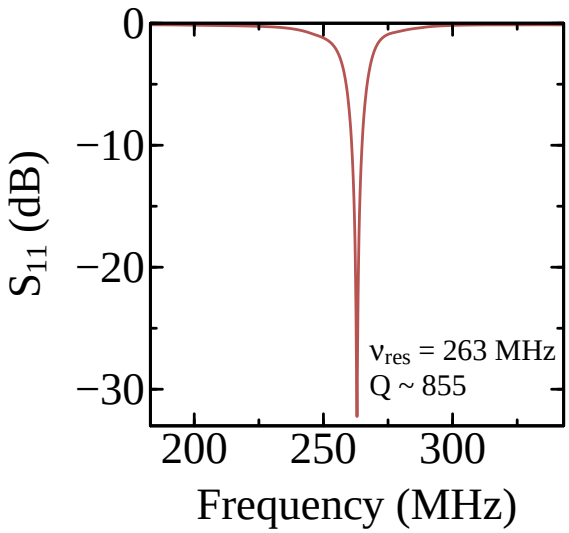

Fig. 4.2.: Reflection coefficient, S_{11}, of the embedded PCB antenna connected to a short circuit stub with a sample loaded on top of the PCB, exhibiting maximum power radiated at approximately 263 MHz with a Q-factor of 855.

the PCB, the copper traces are soldered to a male USB connector, which plugs into a female USB receiver connected to a breakout box with wires terminated into female BNC connectors for easy assess for the detection electronics. The other end of the PCB with two exposed copper pads at the end of the embedded antenna is terminated and soldered with a female SMA connector.

Resonant EM excitation was generated using an Agilent E8257C signal generator in line with an optional Mini-circuits ZHL-50W-52+ high power amplifier when powers above 1 W were required. Initially, radio frequency (RF) delivery to the sample was envisioned using a separate surface coil typically used for nuclear magnetic resonance (NMR) measurements, whereas the embedded PCB antenna in Fig. 4.5(a) was designed to operate at X-band MW frequencies. Spin resonance was not measurable using the proposed surface coil RF delivery and instead, a direct short circuit stub terminator connected right next to the PCB antenna using a tee connector was implemented. In this configuration, the short circuit stub behaves as a reactive element with either purely capacitive or inductive load that fortuitously impedance matches and minimises the amount of signal reflections within the transmission path at approximately 263 MHz. This is shown in Fig 4.2 with a sample loaded on top

of the PCB. The reflection coefficient, S_{11}, measures the amount of power reflected from the embedded antenna and is measured as a function of RF frequency using a Rohde & Schwarz ZNB20 vector network analyser (VNA). Assuming paramagnetic defects with $g \sim 2$, the spin resonance condition will occur at approximately ± 9.4 mT, well within the operational magnetic field range.

An external bias can be applied across the device using either an AWG or the internal voltage source of the transimpedance amplifier (SR570). To measure normalised resonant changes in the device conductivity typically on the order of $10^{-6}-10^{-2}$ due to a large background current on the order of $10^{-7}-10^{-5}$ A, it is essential to compensate and suppress unwanted DC background currents with the transimpedance amplifier prior to amplification. This allows for a high gain setting typically in the range of 10^{9} A/V to be selected. Note that the gain setting will be fundamentally limited by the gain-bandwidth product of the transimpedance amplifier and the modulation frequency chosen for the lock-in amplifier. For the SR570 transimpedance amplifier on the 10^{9} A/V gain setting, the bandwidth, defined by the cut-off frequency where the signal is attenuated by a half (i.e., -3 dB) is 200 Hz on the high bandwidth setting. Further signal conditioning is performed with the internal two stage RC bandpass filters of the transimpedance amplifier to remove DC current drifts and high frequency noise. For weaker signals, additional amplification and signal conditioning with a SR560 voltage preamplifier is used. The amplified modulating signal is then demodulated using a lock-in amplifier. Successful detection of small hyperfine and spin-spin interaction features in the EDMR spectrum is only made possible with lock-in detection. As such, the theory of operation of lock-in amplification is explored in more detail in Sec. 4.2.1. Raw data from the output of channel X and Y from the lock-in amplifier are then digitized using a NI DAQ 6269.

4.1.2 High-field EDMR spectrometer

The high-field EDMR spectrometer shares the majority of the same components as the low-field setup, but replaces the Helmholtz coil with a benchtop electromagnet ($R = 2.2\,\mathrm{k}\Omega$) with its own set of modulation coils, as shown in Fig. 4.3. To drive the electromagnet, a Kepco ATE 325-0.8 M unipolar

power supply is used in voltage amplifier mode in conjunction with an AWG to produce a linear magnetic field sweep. At the maximum rating of the power supply, the magnetic field reaches approximately 320 mT measured using a Lakeshore F41 teslameter situated at the center between the electromagnet poles. This imposes an upper limit on the MW frequency to approximately 8.96 GHz.

The embedded antenna was inspired by the design used in Ref. [141]. Finite element method (FEM) simulations using the software package COMSOL were implemented to determine the antenna resonant frequency and its B_1 distribution. Initial simulations using a microstrip coupled to a ring resonator [142] with a well-defined analytical solution were performed to ensure solutions computed from the FEM modelling were realistic. A parametric sweep of the antenna geometry and characteristics was then simulated as a function of frequency. The simulated reflection coefficient is shown in Fig. 4.4 (black curve), where a fundamental frequency of approximately $f_0 = 2$ GHz and harmonics situated at $f_n = (n+1)f_0$ with $n = 1, 2, 3, ...$ were found and indicated in the figure on the upper scale.

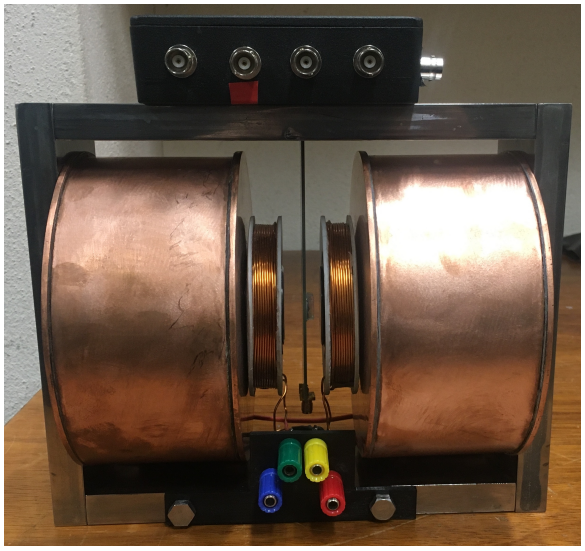

Fig. 4.3.: Photograph of the benchtop electromagnet used in the high-field EDMR setup with a sample attached to the custom-designed PCB situated at the centre between the poles of the electromagnet. Electrical contacts to the device are accessible via the four available female BNC connectors mounted on the breakout box.

Considering the maximum operational magnetic field strength, the 4^{th} harmonic situated at $f_4 = 7.97$ GHz is used for high-field EDMR measurements, which corresponds to a resonant field at approximately 286 mT assuming $g \sim 2$. Once optimised, the PCB design was then transferred to Autodesk EAGLE for commercial fabrication. The measured reflection coefficient is compared with simulated results in Fig. 4.4 for the case where the sample was (red curve) and was not (blue curve) mounted on the PCB. Relatively good agreement between the simulated and measured harmonics in the reflection coefficient was observed above the 3^{rd} harmonic with the unloaded harmonics occurring systematically at lower frequencies than the simulated response. This may be a result of the frequency-dependent permittivity of the FR4 fibreglass material used for the PCB [143], where the FEM modelling assumes a constant frequency-independent permittivity. In addition, the manufacturing tolerances of the PCB may also contribute to this discrepancy. A systematic shift toward higher frequencies was observed when the sample was mounted on the PCB. Note that the resonant frequency of the antenna will be slightly different for each device measured depending on the geometry and the amount of metallic contact surfaces that perturb the EM field. As such, S_{11} measurements were performed prior to each measurement to optimise the antenna response. The origin of the vastly different antenna reflection response measured at low frequencies below the 4^{th} harmonic in comparison to the simulated results is currently unknown, although it does not affect the normal operation of EDMR at high magnetic fields.

For the given experimental setup where the sample surface is parallel to B_0 pointed along the $\hat{\mathbf{x}}$ axis, B_1 orientated either along the $\hat{\mathbf{y}}$ or $\hat{\mathbf{z}}$ axis is required to induce spin resonance. Similarly, B_1 orientated either along the $\hat{\mathbf{x}}$ or $\hat{\mathbf{y}}$ axis is required to induce spin resonance when the sample surface is perpendicular to B_0 for the configuration shown in Fig. 4.3. The simulated Cartesian components of the magnetic and electric field distribution along the xy plane placed approximately $50\ \mu\mathrm{m}$ above the PCB for $\nu = 7.97$ GHz and $P = 250$ mW is shown Fig. 4.5(b)$-$(c). In the simulations, a 1×1 mm^2 square sample indicated at the center of the simulated image plots was treated as a perfect aluminium conductor. The addition of the conducting sample did not have any significant impact on the simulated field distributions. Furthermore, there exists a node in the electric field distribution within the 1×1 mm^2 sample

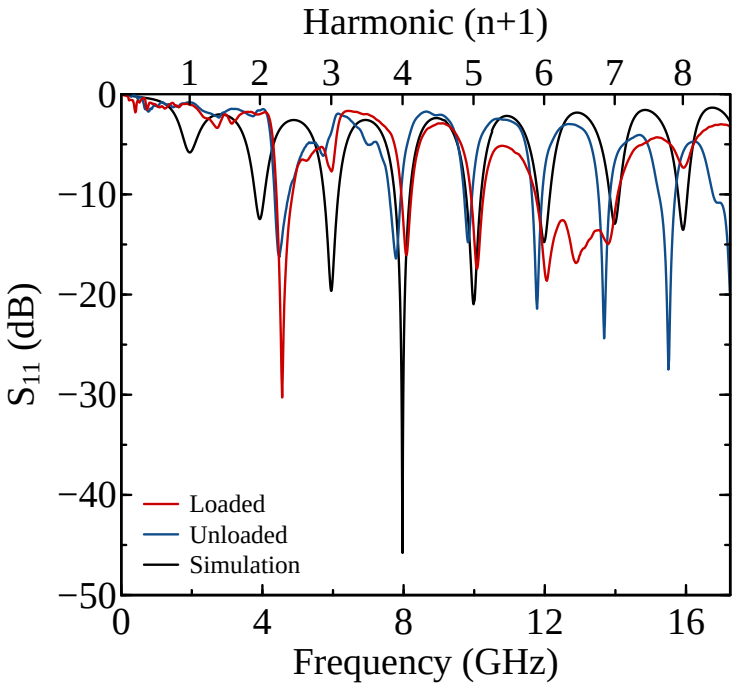

Fig. 4.4.: Reflection coefficient of the embedded PCB antenna simulated with FEM modelling (black curve) in comparison with experimental results with (red curve) and without (blue curve) a sample placed on top of the embedded antenna. The simulated fundamental frequency at approximately $f_0 = 2$ GHz and harmonics situated at $f_n = (n+1)f_0$ with $n = 1, 2, 3, ...$ were found and marked on the upper scale.

area, as shown in Fig. 4.5(c). This helps minimise undesired electric field perturbation effects on the sample [141].

4.1.3 Intermediate-field spectrometer

Results presented in Chapter 6 were primarily measured using an intermediate-field spectrometer with temperature controllable capabilities, whereas the low-field and high-field spectrometers described above are only operational at room temperature. In this setup, the device was measured in a cryostat under vacuum (Janis ST-100H) and placed at the center of an electromagnet ($R = 54.7\,\Omega$) driven using a Kepco BOP power supply in conjunction with an AWG. Sample temperature between $80 - 400$ K was achievable with liquid nitrogen transfer to the cryostat and an internal cryostat heater controlled using a Lakeshore 331 temperature controller. In its current configuration,

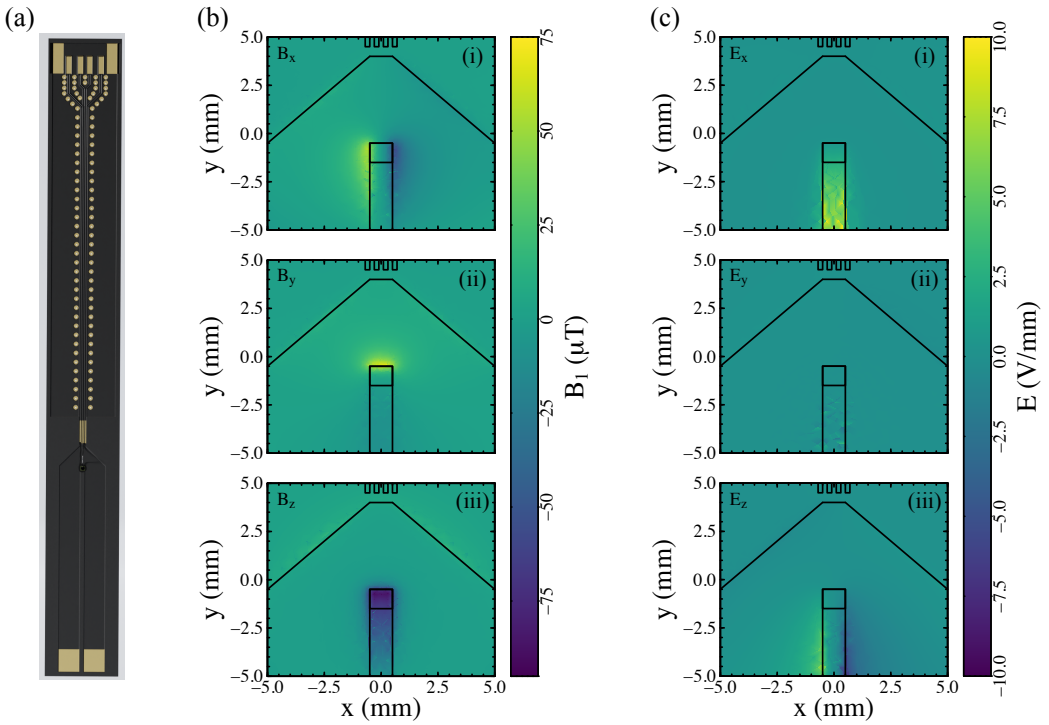

Fig. 4.5.: (a) Rendered image of the PCB design implemented with a 1×1 mm^2 device electrically bonded to the four available exposed copper traces. (b)-(c) Simulated magnetic and electric field distribution along the xy plane placed $50\ \mu$m above the PCB for $\nu = 7.97$ GHz and $P = 250$ mW.

the lack of dedicated cryogenic high frequency coaxial cables down the cryostat meant that delivery of resonant EM excitation to the sample was not possible. Instead, only the zero-field spin-mixing response was considered in Chapter 6. At the maximum rating of the power supply, the magnetic field reaches approximately ± 55 mT. Similar to the low-field EDMR setup, a calibration curve was measured to calculate the offset in magnetic field strength using a hall effect sensor (AH49H) attached outside the cryostat with respect to the sample position.

4.2 Data acquisition and signal processing

To observe small spin resonant-induced signals, careful consideration and attenuation of noise sources present in an EDMR measurement is required. Typically, lock-in amplification and signal averaging are two effective noise

reduction methods implemented. Below, we discuss these two methods in detail.

4.2.1 Lock-in amplification

Due to the random nature of charge carrier capture and emission involved in the recombination process, random fluctuations in the number of free charge carriers during charge transport appears, leading to measurable current noise. This type of noise is called flicker noise and has a spectral density proportional to $1/f$, which is particularly problematic for EDMR measurements where the desired signal is effectively situated at DC. On a single trapping and detrapping event level, this process is known as random telegraph signal (RTS) noise [144], where $1/f$ noise is just the summation over RTS noise due to a distribution of traps each with its own unique time constant. To effectively attenuate $1/f$ noise, lock-in amplification is used. In short, the desired DC signal of interest is encoded and measured at some modulation frequency far away from the dominant low frequency noise source and then demodulated back down to DC. Thus, an enhancement in the sensitivity is achieved as lock-in detection is only sensitive to frequency components at the modulation frequency oscillating in-phase with the reference modulation source.

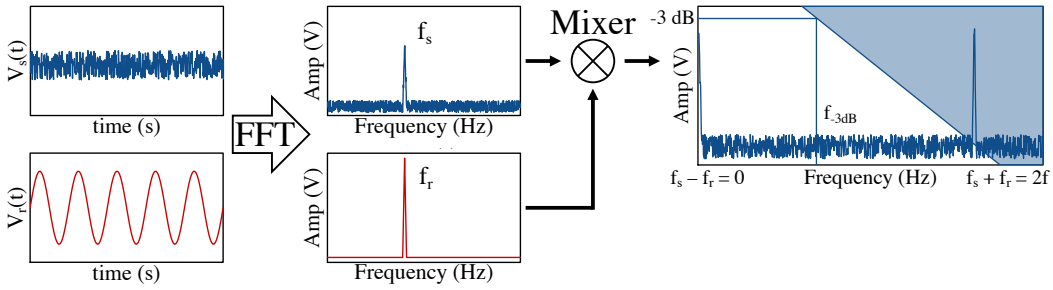

Fig. 4.6.: Schematic of the working principle of lock-in amplification. A fast Fourier transform (FFT) is utilised to convert the signal from the time-domain into the frequency-domain. In the frequency domain, the desired signal and the reference signal are multiplied through a mixer, where only the sum and the difference of their frequency components are non-zero. When the reference and signal frequency are equal, the signal is demodulated at DC (0 Hz) and the 2f component is removed using a low-pass filter.

The basic working principle of lock-in detection is schematically illustrated in Fig. 4.6, where a homodyne detector is followed by a low-pass filter. For the simplest case, the DC signal of interest is superimposed with frequency-independent white noise. Mathematically, the desired signal and a reference modulation source can be expressed as two arbitrary sinusoidal voltage waveforms

$$V_s(t) = V_s \sin(2\pi f_s t + \theta_s) \tag{4.2a}$$
$$V_r(t) = V_r \sin(2\pi f_r t + \theta_r)\,, \tag{4.2b}$$

where V_s and V_r, f_s and f_r, and θ_s and θ_r are the amplitude, frequency, and phase of the desired signal and reference modulation source, respectively. The frequency mixer multiplies the reference voltage waveform with the signal voltage waveform such that

$$V_{mix}(t) = V_s V_r \sin(2\pi f_s t + \theta_s) \sin(2\pi f_r t + \theta_r)\,, \tag{4.3}$$

which can be rewritten as

$$\begin{aligned} V_{mix}(t) = {} & V_s V_r \cos(2\pi(f_s - f_r)t + (\theta_r - \theta_s))/2 \\ & - V_s V_r \cos(2\pi(f_s + f_r)t + (\theta_r + \theta_s))/2\,. \end{aligned} \tag{4.4}$$

When the reference and desired signal frequency are equal ($f = f_r = f_s$), only the sum and the difference of the frequency components occurring at $2f$ and 0 Hz are observed as non-zero components in the frequency-domain, respectively,

$$V_{mix}(t) = V_s V_r \cos(\theta)/2 - V_s V_r \cos(4\pi f t + (\theta_r + \theta_s))/2\,, \tag{4.5}$$

with $\theta = \theta_r - \theta_s$. A low-pass filter is then used to remove the second harmonic $2f$ component such that the original DC signal is retrieved

$$V_{mix}(t) = V_s V_r \cos(\theta)/2\,. \tag{4.6}$$

From Eq. 4.6, V_{mix} is maximized when $\theta = \theta_r - \theta_s = 0°$ or minimised when $\theta = 90°$. The arbitrary choice of θ is known as phase-sensitive detection (PSD) and most lock-in amplifiers implement a second channel with the modulating reference source phase shifted by $90°$ such that

$$\begin{aligned} V_r(t) &= V_r \sin(2\pi f_r t + \theta_r + 90°) \\ &= V_r \cos(2\pi f_r t + \theta_r)\,. \end{aligned} \tag{4.7}$$

Similarly, it can be shown that the output voltage signal of the second channel becomes

$$V_{mix}(t) = V_s V_r \sin(\theta)/2\,. \tag{4.8}$$

Eq. 4.6 and Eq. 4.8 are proportional to channel X (in-phase) and channel Y (quadrature) of the lock-in amplifier, respectively, and the vector magnitude of the desired signal can be computed independent of the phase

$$X = V_s \cos(\theta) \tag{4.9a}$$
$$Y = V_s \sin(\theta) \tag{4.9b}$$
$$R = V_s = \sqrt{X^2 + Y^2} \tag{4.9c}$$
$$\theta = \arctan(Y/X)\,. \tag{4.9d}$$

When the desired signal is superimposed with a noise source containing multiple discrete frequency components, frequency components arising from noise-reference mixing will appear in the frequency spectrum. The choice in low-pass filter settings, including the filter time constant and filter

slope, is crucial in effectively removing these non-zero noise-reference mixed components. The time constant, τ, of the low-pass filter is defined as

$$\tau = \frac{1}{2\pi f_c} , \tag{4.10}$$

where f_c is the cut-off frequency occurring at the -3 dB point in which the signal amplitude is attenuated by a half. Beyond the -3 dB point, the low-pass filter attenuation is defined by the filter slope in which a filter with a larger slope approaches an ideal step function defined by a brickwall filter. Thus, a similar attenuation factor using a low-pass filter with a long time constant and a shallower slope can be achieved using a low-pass filter with a shorter time constant and sharper slope. Together, the filter time constant and filter slope are related to the equivalent noise bandwidth (ENBW), which in turn is related to the wait time required for the lock-in amplifier to settle to its final value in response to changes in the measured signal. These settings will fundamentally limit how fast a magnetic field sweep can be performed without any unintentional signal attenuation.

Typically, a small modulating magnetic field on top of the linear magnetic field sweep is used for lock-in detection in EDMR. This brings the system in and out of resonance as the resonant condition is swept through. If the modulation amplitude, B_{mod}, is small compared to the natural Lorentzian linewidth of the resonance signal, then the lock-in output is approximately the derivative of the Lorentzian signal with respect to the magnetic field. Distortion and Gaussian broadening to the lock-in output can occur when B_{mod} is large in comparison to natural linewidth. A general rule of thumb is to set B_{mod} to one-tenth of the natural linewidth of the spin resonance signal of interest to avoid Gaussian broadening, although larger modulation amplitudes may be required when the signal-to-noise ratio (SNR) is poor [113]. Spurious signals not related to SDR in the quadrature component of the lock-in output may arise due to stray capacitance in parallel with the device under test (DUT) that make up the measurement circuit [145]. These undesired signals are strongly dependent on the phase of the reference modulation source. Hence, it is important prior to each EDMR scan to maximise the signal amplitude in channel X and minimise the signal amplitude in channel Y of the lock-in amplifier by adjusting the phase of the reference modulation source.

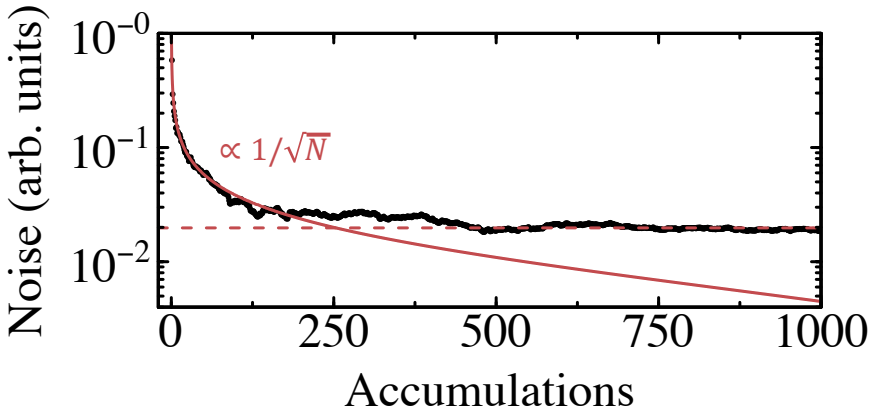

Fig. 4.7.: Measured noise reduction as a function of the number of accumulations for a set of experimental data, initially following a $1/\sqrt{N}$ dependence expected for shot noise before deviating and saturating for large number of accumulations.

4.2.2 Signal averaging

Prior to signal averaging, the raw data output digitized from channel X and channel Y of the lock-in amplifier is processed the following way. A custom code implemented in Labview is used to define the start of the triggering of each magnetic field sweep and data acquisition. Typically, 2.5×10^5 samples are taken for each individual sweep with the sampling rate adjusted to match the period of the magnetic field sweep. A linear interpolation algorithm is then applied in the programming language R post-processing to align each sweep and account for any drifts in the magnetic field based on the magnetic field strength measured with a Hall effect sensor or a Teslameter. Once aligned, a running average algorithm is then implemented to reduce the number of data points and increase the SNR. Each individual reduced scan is then averaged. As the dominant noise source from the measurement arises from shot noise due to the discrete nature of electric charge in the measured current, the noise distribution is governed by Poisson statistics and reduces $\propto 1/\sqrt{N}$, with N the number of accumulations. This is shown in Fig. 4.7 for an example experimental data set. The noise, defined as the standard deviation of the raw data collected from the lock-in output, roughly follows a $1/\sqrt{N}$ dependence initially, but appears to deviate and saturate (red dotted line) as the number of accumulations increases. This suggests that other noise sources are also present. For this particular experimental data set,

at least 500 individual scans are required for signal averaging, which takes approximately 14 hours when each magnetic field scan takes 100 s.

Ultimately, the total acquisition time of an EDMR measurement relies upon an adequate SNR to resolve small features of interest. As such, signal processing of noisy data remains an active field of research. Beyond the straightforward running average and signal averaging implemented in this work, adaptive signal averaging based on an exponentially weighted recursive least-squares (EWRLS) algorithm has been previously demonstrated to achieve a higher SNR within a shorter acquisition time [146, 147]. However, this result was not able to be replicated by Brinton and Hirsh [148] in which they suggested that the effectiveness of the EWRLS algorithm is sensitive to the type of noise source present in the measured EDMR spectrum. We were also not able to observe any significant difference in the SNR between the averaged EDMR spectrum processed through our running average and signal averaging algorithm and the EWRLS algorithm found in the EasySpin MATLAB toolbox [136] applied on some experimental data measured on our EDMR spectrometer (not shown). Therefore, the EWRLS algorithm was not implemented as it may also introduce artefacts to the averaged spectrum when using inappropriate initial parameter settings for the algorithm.

4.3 Pulsed EDMR operation

The experimental constraints imposed on pEDMR are significantly more stringent than cwEDMR as high power pulsed EM excitation is required for detecting small changes in the device current on short timescales. Below, we will detail the hardware requirements to successfully implement pEDMR measurements. Particularly, the time-domain and lock-in pEDMR approach are presented and discussed. The different pulse sequences employed are later introduced in detail in Chapter 7.

4.3.1 Time-domain pEDMR

A block diagram of the low-field EDMR setup first previously introduced in Sec. 4.1.1 adapted for time-domain pEDMR is shown in Fig. 4.8. In this

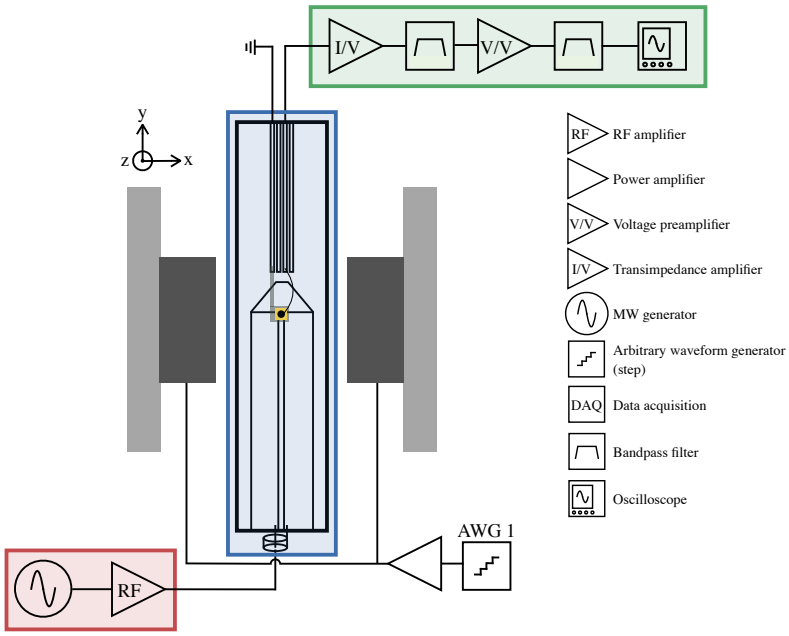

Fig. 4.8.: Block diagram of the low-field EDMR setup adapted for pulsed operation measured in the time-domain. The main hardware change is the removal of the lock-in amplifier and the data acquisition is now performed using an oscilloscope. Refer to main text for more detail.

configuration, the RF pulse is defined internally with the Agilent E8257C analog signal generator (10 ns resolution) and amplified using a Mini-circuits ZHL-50W-52+ high power amplifier. In the time-domain, the gain-bandwidth product of the transimpedance amplifier must be preserved for optimum time resolution, while maintaining high gain to detect resonant-induced small changes in the device current. The device current is measured using a Femto-DLPCA-200 transimpedance amplifier, whose bandwidth is larger on any gain setting than the SR570, but significantly worse at compensating for offset currents. Further amplification and signal conditioning is provided using a SR560 voltage preamplifier. High-pass filtering was utilised to remove the DC component of the device current as only the AC transient response is of interest. A Tektronix TDS 3052B 500 MHz oscilloscope was used to digitize the transient response.

The sample design and geometry are also critical factors that ensure the successful implementation of a pEDMR measurement. In particular, the sample resistance must be minimised to maximise sample currents, which

in turn also maximises the time resolution of the transimpedance amplifier [149]. As such, a lateral interdigitated contact design is often utilised, where each set of fingers separated by some distance is effectively connected up in parallel as part of the whole interdigitated design, thereby reducing the overall sample resistance. Second, any metallic surfaces in the vicinity of the B_1 field can distort the eigenmodes of the magnetic field distribution, leading to B_1 inhomogeneity and a rapid artificial dephasing of the spins during resonant pulse excitation [149]. Thus, the Rabi spin nutation may not be detectable as the artificial spin dephasing occurs on a shorter timescale than the Rabi oscillation. To minimise this issue, the thickness of the metallic contacts should be less than the penetration skin depth of the RF irradiation, which is around $5\ \mu\mathrm{m}$ for Al at 263 MHz. Standard lithographically-defined contact pads and metallization fabrication processes are able to readily meet the above criteria. However, wire bonds for electrical contacting the device with diameters comparable to the skin depth will lead to B_1 inhomogeneity and must be minimised.

Non-resonant currents due to high power pulsed RF irradiation exasperated by B_1 inhomogeneity appear as background current signals superimposed with the resonant transient response. These background signals are usually large in amplitude and require careful baseline correction to reveal the resonant transient response of interest. Furthermore, the amplitude of the background signals increases linearly with increasing pulse width and radiation power. Thus, a balance between high SNR, pulse width, and RF power must be experimentally determined, which may put a large constraint on the possible experimental settings that can be applied.

An example of the baseline correction procedure is shown in Fig. 4.9 subject to a $4\ \mu\mathrm{s}$ RF pulse (grey curve), where the raw transient response measured at the resonance condition (blue curve) is subtracted from the raw transient response measured far away from resonance (black curve). A sub-nA resonant current quenching transient response is revealed after the baseline correction (red curve), consistent with the framework presented in Sec. 3.5, where an enhancement in the recombination rate due to spin resonance corresponds to a decrease in free carrier density and device conductivity. The current transient can be integrated using a boxcar function over an integration interval, Δt, to determine the amount of charge, ΔQ, proportional

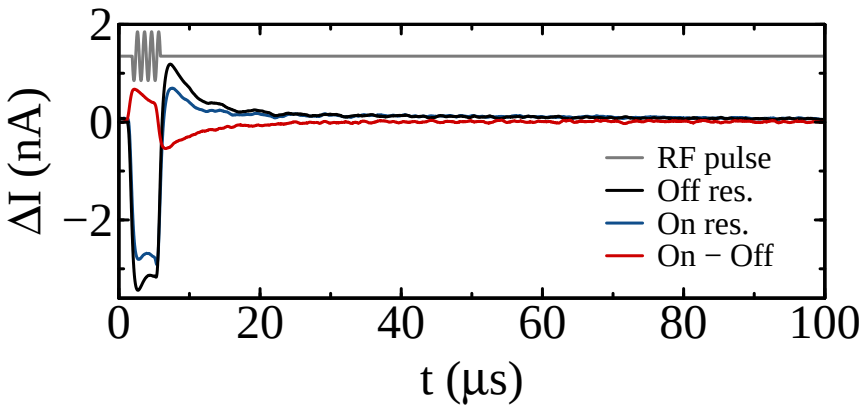

Fig. 4.9.: Averaged current transient response over $25,600$ transients after a $4\ \mu s$ RF pulse (grey curve) at $P = 950$ mW measured on (blue curve) and off (black curve) resonance. After the off resonance background subtraction, a small resonant current quenching transient response is revealed (red curve).

to the number of spins. An additional advantage of the numerical integration is the SNR enhancement as the boxcar integrator acts as a low pass filter suppressing noise sources with a frequency component above $1/\Delta t$. Note that the start of the current transient after the RF pulse may be attenuated by the rise/fall time of the transimpedance amplifier at the particular gain setting chosen.

The background correction procedure described above can lead to large errors when the non-resonant current transient background is dependent on the magnetic field. This occurs particularly at low magnetic fields when the zero-field spin-mixing response is present. As such, the background correction is usually performed by taking the average of the off resonant transient obtained above and below the resonant field, although this does not completely remove the non-resonant background, as will be seen in Chapter 7. The requirement to measure current transients far off resonance for background subtraction adds to the long acquisition times already required to obtain a high SNR. For example, the averaged transient shown in Fig. 4.9 on and off resonance was averaged over $25,600$ individual transients and took approximately 4 minutes in total to acquire each transient.

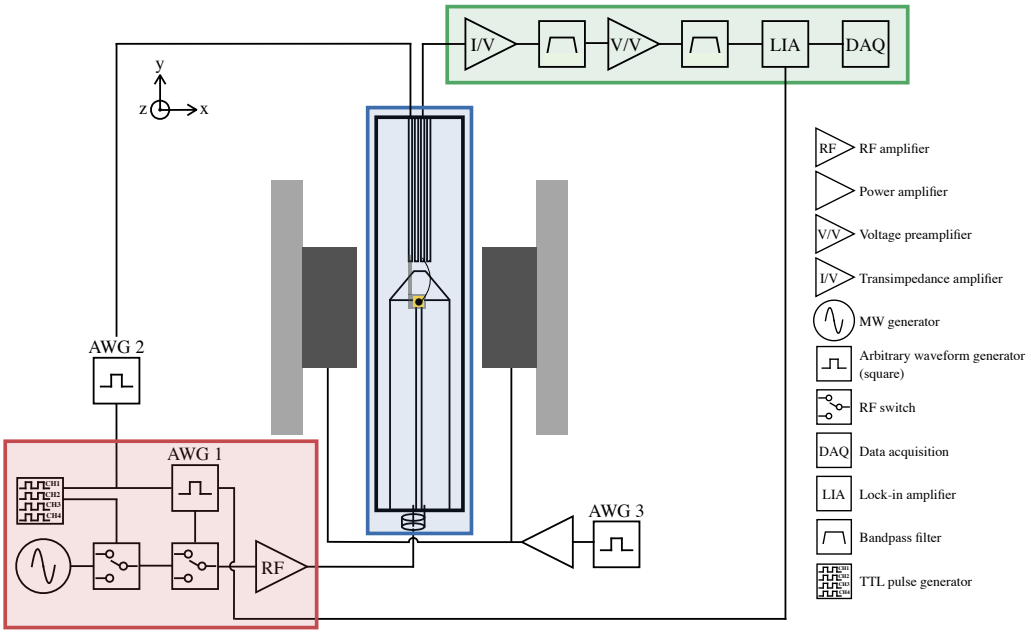

Fig. 4.10.: Block diagram of the low-field pEDMR setup for lock-in detection. A TTL pulse generator is used to synchronise the timing of the various hardware and define the RF pulse train with variable pulse lengths. Refer to main text for more detail.

4.3.2 Lock-in detection for pEDMR

The presence of a large non-resonant current background and limited time resolution associated with the pEDMR detection scheme in the time-domain has long been a significant limiting factor of the measurement technique and only a handful of idealised demonstrations of pEDMR have been reported, requiring significant optimisation of the sample design and detection hardware [126, 149, 150]. More recently, lock-in detection schemes for pulsed magnetic resonance measurements have been developed. These detection schemes have been found to be particularly effective for pODMR [151] and pulsed photoionization detected magnetic resonance measurements [94, 152] in which the MW pulsing sequence is modulated and encoded into a low frequency lock-in envelope. We apply the same working principle and adapt it for pEDMR operation. The working principle behind the lock-in pEDMR detection scheme is explained in more detail in Sec. 7.2.

A block diagram of the experimental setup for pEDMR with lock-in detection is shown in Fig. 4.10. At the heart of the measurement is the 4-channel programmable PulseBlaster ESR-PRO 500 TTL pulse generator (2 ns resolution) that controls and defines the timing of the multi-level pulsing sequence required for lock-in detection, while maintaining synchronicity across the test instruments. The cw RF output signal from the Agilent E8257C analog signal generator is shaped into the desired RF pulse train by switching on and off a Mini-Circuits ZASWA-2-50DR+ switch with a typical rise and fall time of $t_{r,f} = 5$ ns defined by channel 2 of the PulseBlaster. Then, the RF pulse train is modulated on and off using a second RF switch (ZX80-DR230+) at the lock-in modulation frequency, which effectively amplitude modulates (AM) the RF pulse train. The lock-in modulation envelope is defined with an AWG triggered off channel 1 of the PulseBlaster, which is also used to trigger the device voltage modulation defined by a second AWG.

4.4 Summary

This chapter provides a technical description of the three EDMR spectrometers constructed for this work, including their capabilities and limitations. The low-field EDMR spectrometer was adapted for pEDMR measurements and its operation in the time-domain and with lock-in detection are both outlined. Signal conditioning and processing considerations are also discussed, which is crucial for the successful detection of spin resonance with the EDMR technique.

5 Absolute magnetometry based on spin defects in SiC

This chapter presents EDMR results on a 6H−SiC n^+p junction diode, which forms the basis of an electrically-detected solid-state spin resonance magnetometer. A comprehensive cwEDMR study of a processing-induced spin defect involved in the SDR process is first performed. The device is then operated as a magnetometer and its sensitivity is benchmarked. Further sensitivity enhancement is demonstrated utilising common-mode rejection and above bandgap photoexcitation.

5.1 Introduction

Magnetic field sensing is an integral part of modern science, ranging from current sensing [11] to space exploration [9, 10] to detecting biological magnetic fields [12]. As a result of the diverse range of applications each with its own set of requirements, a plethora of magnetometer technologies have emerged over the past decades. Some of these technologies include superconducting quantum interference devices (SQUIDs) [153–155], Hall-effect sensors [156–159], vapour cells [160, 161], fluxgate magnetometers [162–164], and solid-state magnetic resonance-based sensors [9, 10, 14–16, 18, 19, 22, 165–171]. In particular, the latter have recently garnered widespread interest as they generally offer high sensitivity within a relatively small detection volume.

Magnetic resonance-based sensors exploit the Zeeman interaction to sense external magnetic fields by applying resonant EM radiation to drive spin transitions between two energy levels of an atomic system (see Sec. 3.3.1). The signal response is commonly detected optically with ODMR due to its highly efficient spin-to-photon readout mechanism and much of the initial success has been demonstrated with the NV centre in diamond [18, 172]. However, ODMR measurements usually require a bulky optical setup with

high power consumption and may not be compatible with magnetometry applications requiring low size, weight, and power (SWaP).

EDMR offers an alternative readout approach in which the supporting electrical detection infrastructure may be eventually integrated with the sensor itself within a single integrated circuit (IC) package. Furthermore, for applications where EM radiation may be prohibitively invasive to the measured field of interest, such as measurements in magnetically shielded environments, Cochrane et al. [9] have recently demonstrated an EM radiation-free magnetometer technology utilising the hyperfine-induced spin-mixing response situated at zero magnetic field in a SiC device. Currently, little is known about the viability of using this hyperfine-induced spin-mixing response as a sensor for wide-scale use, which ultimately hinges on the magnetic field sensitivity. In their original work, a sensitivity of $440\ \mathrm{nT}/\sqrt{\mathrm{Hz}}$ was demonstrated and a sub-nT/$\sqrt{\mathrm{Hz}}$ sensitivity was envisioned based on estimate calculations assuming devices with larger spin-mixing responses were possible, which is yet to be experimentally demonstrated.

In this experimental chapter, we conduct a comprehensive study on the spin resonance and spin-mixing response in a 6H$-$SiC junction diode device, which was then operated as a magnetometer and its sensitivity was thoroughly assessed. The paramagnetic defect species participating in the SDR process has an effective g$-$factor of 2.013 ± 0.0014 and is speculated to be a processing-induced defect situated near the junction in the SiC bulk. A set of overlapping superhyperfine features were observed at low magnetic fields and non-negligible dipolar coupling was present, as evident by the presence of half-field resonances. The device was then operated as a magnetometer and a baseline sensitivity of $730\ \mathrm{nT}/\sqrt{\mathrm{Hz}}$ was initially measured. By implementing a balanced detection scheme for common-mode rejection and optical injection of free charge carriers, an ultimate sensitivity of $30\ \mathrm{nT}/\sqrt{\mathrm{Hz}}$ was achieved. The experimental methods employed to enhance the sensitivity are not just applicable to this particular defect in SiC but can be applied to other spin systems utilising the SDR mechanism.

In the following section, a brief literature review on existing magnetometer technologies will be presented. This will be followed by a background theory section on the operation of a junction diode device in the context of an EDMR measurement and how its magnetic field sensitivity can be determined.

5.2 Literature review

Magnetic sensing exploits a wide range of physical phenomena from different fields of physics. Comprehensive reviews on different magnetometer technologies can be found elsewhere in Refs. [173, 174], however, neither reference has a dedicated section on solid-state magnetic resonance-based sensors, an area in which significant progress has recently been made. The following discussion will consider specified applications in which the sensor sensitivity and spatial separation is of utmost importance, which is where solid-state magnetic resonance-based sensors may have an advantage over other sensor technologies. Other relevant parameters of a sensor, such as size, weight, power consumption, frequency response, required operating conditions, and cost will not be directly compared between different magnetometer technologies below, but may still play a significant role in choosing one technology over another for a particular application.

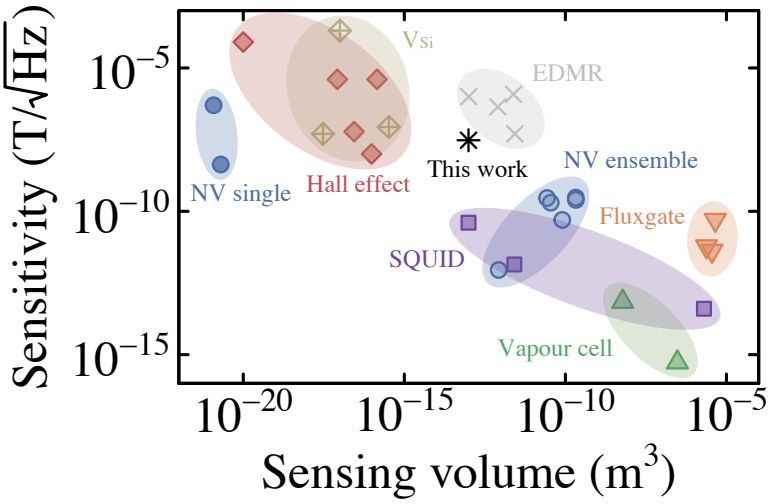

Fig. 5.1.: Sensitivity of some state of the art magnetometer technologies as a function of detection volume. Here, SQUIDs [153–155], Hall-effect sensors [156–159], vapour cells [160, 161], fluxgate magnetometers [162–164], quantum magnetometers based on NVs in diamond [14–16, 18, 165–168] and V_{Si}^{-} in SiC [19, 169, 170], and EDMR-based sensors [9, 10, 22, 171] are considered. For comparison, the performance of the magnetometer device studied in this chapter is also provided. In general, there is a trade-off between sensitivity and spatial resolution defined by the sensing volume with high sensitivity small sensing volume magnetometers (bottom left quadrant) the ultimate goal.

Figure 5.1 compares the sensitivity of various magnetometer technologies as a function of sensing volume. Here, the sensing volume is representative of the sensor spatial separation, where it is defined as the distance between the magnetic sensor and a magnetic source of interest modelled by a magnetic dipole that decays in strength by a distance r^{-3} from the source. We note that the supporting infrastructure for some magnetometer technologies can substantially increase the sensor spatial separation, such as the cryogenic cooling required for SQUIDs [175]. In the small volume low sensitivity limit, a single NV centre in a 30 nm nanocrystal diamond is able to detect the magnetic field emanated from an electron spin situated roughly ~ 10 nm away [16]. Higher sensitivity is achieved by considering a NV ensemble in which the sensing volume is increased, demonstrating a large degree of tunability. In the large volume high sensitivity limit, an optically pumped vapour of potassium atoms confined within a 0.3 cm^3 glass cell is able to reach unparalleled sub-fT/$\sqrt{\text{Hz}}$ sensitivity [161]. Existing EDMR-based magnetometers previously reported operate in the medium volume and sensitivity regime, but have the added advantage of the ability to reduce the device active area through nanofabrication and defect engineering. As EDMR-based sensors have only been considered recently, further demonstrations are required to define the ultimate sensor sensitivity and volume limits for this magnetometer technology. For reference, the ultimate sensitivity extrapolated for the device studied in this chapter is also indicated in Fig. 5.1 (black symbol).

Several semiconductor materials have been previously considered for fabricating EDMR-based sensors, including Si, organic thin films, and SiC. Historically, an EDMR-based magnetometer was first demonstrated using a commercial Si 1N4007 diode device with a sensitivity of $3\,\mu\text{T}/\sqrt{\text{Hz}}$ [171]. Earlier works have correlated the recombination center responsible for the spin resonance response in the 1N4007 diode to a Pt-related defect complex [176, 177]. A magnetic sensor based on polaron-pair recombination in an organic junction diode was then demonstrated by Baker et al. [22] with a sensitivity of $50\,\text{nT}/\sqrt{\text{Hz}}$. Generally, organic semiconductor devices can degrade over time upon exposure to atmosphere. While Baker et al. [22] have demonstrated that device degradation does not significantly impact the reproducibility of the resonance condition and hence the g$-$factor, the device may need periodic recalibration to take into account fluctuations in

the device conductivity and may not be suitable for harsher environments where operating conditions vary drastically over time.

Most recently, a magnetometer utilising the zero-field spin-mixing response in a SiC device was demonstrated by Cochrane et al. [9] with a sensitivity of $440\,\mathrm{nT}/\sqrt{\mathrm{Hz}}$. It has been touted to be suitable for aerospace applications in which remote calibration capabilities and radiation hardness are required [178]. Self-calibration can be achieved by introducing EM radiation and measuring the spin resonance response in a low-field EDMR measurement to determine the magnetic field offset using the Zeeman condition with respect to the zero-field response situated at true zero magnetic field (see Fig. 5.9). Alternatively, the hyperfine features imprinted on the zero-field response serves as constants of proportionality to convert into units of magnetic field (see Fig. 5.10(a)(ii)). A previous report from Cochrane et al. [10] has demonstrated that exposure to 2 MeV electron radiation at a fluence of 10^{14} cm^{-2} does not compromise the sensitivity of the magnetometer, although the device characteristics, particularly the built-in voltage, is reduced. As a result, the operating voltage in which the highest sensitivity is achieved changes, which may require periodic device tuning, but does not affect the general operation of the magnetometer.

5.3 Background

The SDR readout mechanism introduced in Sec. 3.4 requires a readily available source of free majority and minority charge carriers to participate in the recombination process in which the simplest device and the one investigated in this chapter is the pn junction. By operating the device under a small forward bias in which recombination current dominates, a SDR response can be measured under spin resonance. In the following, the basic operation of a pn junction diode is summarised in the context of tuning a diode device for an EDMR measurement. A comprehensive review of pn junction operation can be found elsewhere in Refs. [48, 179]. The second half of this section will then delve into different approaches in characterising the magnetic field sensitivity of an EDMR-based sensor.

5.3.1 pn junction device operation

A pn junction is a two-terminal device exhibiting rectifying behaviour in which electrical current can flow only in one direction. This junction is formed when a p-type semiconductor (hole majority carriers) is brought into contact with a n-type semiconductor (electron majority carriers), where the migration of charge carriers due to a large carrier concentration gradient results in a diffusion current, leaving behind a space charge region depleted of mobile charge carriers. The resulting electric field arising from the space charge region creates a drift current component opposing the diffusion current. Thermal equilibrium at the junction is established once no net current across the junction exist and the drift and diffusion currents for each type of charge carrier cancel out.

A schematic of a pn junction under forward bias is shown in Fig. 5.2(a) in which injected charge carriers diffuse to the other side of the junction and introduces an excess of minority charge carriers. For an ideal pn junction where no recombination exists inside the depletion width, W, the current−voltage (I−V) characteristics is dominated by diffusion current, as opposed to drift current in reverse bias. By introducing recombination within the depletion region through a single trap level situated at energy E_T near the middle of

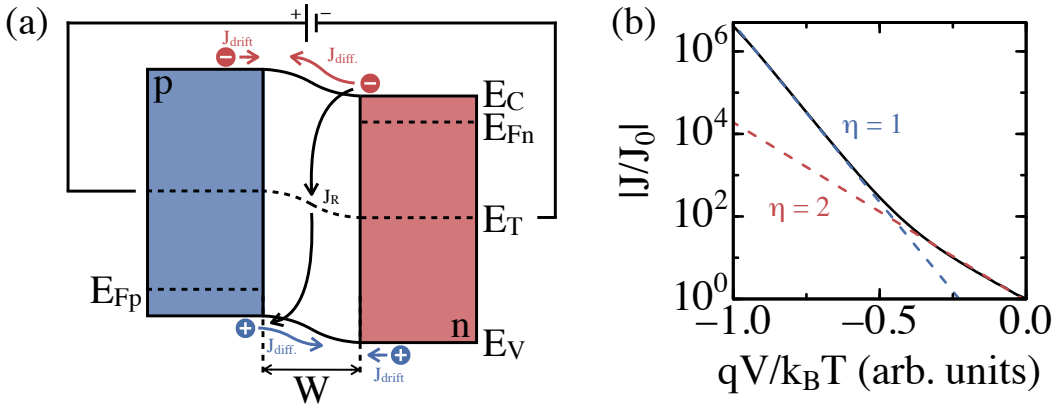

Fig. 5.2.: (a) Energy band diagram of a pn junction in forward bias. (b) I−V characteristics of a typical pn junction diode in forward bias. At small forward biases, recombination current dominates and $\eta = 2$ (red dotted line), whereas diffusion current dominates at large forward biases and $\eta = 1$ (blue dotted line) following Eq. 5.2.

the bandgap, the total current density for a forward biased pn junction is given by [48]

$$\begin{aligned} J &= J_{diff.} + J_R \\ &= J_{diff.,0} \exp\left(\frac{qV}{k_B T}\right) + J_{R,0} \exp\left(\frac{qV}{2k_B T}\right), \end{aligned} \tag{5.1}$$

with $J_{diff.,0}$ and $J_{R,0}$ the zero bias diffusion and recombination current density, respectively. A typical I−V curve of a pn junction diode is shown in Fig. 5.2(b) following Eq. 5.1. Experimentally, Eq. 5.1 can be simplified by the following empirical relation

$$J = J_0 \left\{ \exp\left(\frac{qV}{\eta k_B T}\right) - 1 \right\}, \tag{5.2}$$

where an ideality factor η is introduced and takes on a value between 1 and 2, with $\eta = 1$ when diffusion current dominates typically at larger forward biases (blue dotted line in Fig. 5.2(b)) and $\eta = 2$ when recombination current dominates generally at smaller forward biases (red dotted line in Fig. 5.2(b)). Prior to an EDMR measurement, the I−V characteristics of a pn junction device must be analysed to determine the appropriate biasing range in which $\eta = 2$ such that a SDR current under resonant excitation is measurable.

5.3.2 Sensitivity and noise spectral density

The magnetic field sensitivity of a magnetometer is generally expressed in terms of a magnetic noise amplitude spectral density in units of $\mathrm{T}/\sqrt{\mathrm{Hz}}$, or equivalently the square root of the magnetic noise power spectral density in units of T^2/Hz. Conceptually, the sensitivity is a measure of the minimum resolvable magnetic noise per square root unit of bandwidth. When expressed in this unit, sensitivity comparisons can be made regardless of experimental settings used and a smaller value corresponds to a more sensitive magnetometer. The origin of this definition comes about from the field of signal processing, where the noise level of a signal in the frequency-domain via a fast Fourier transform (FFT) is dependent on the bandwidth of the measurement. This in turn is dependent on the sampling rate and the number

of samples. Thus, the power spectrum is normalised per unit bandwidth of 1 Hz wide such that it becomes independent of the sampling rate and the number of samples [180]. As an example, a magnetometer with a sensitivity of $1\ \mathrm{nT_{rms}}/\sqrt{\mathrm{Hz}}$ is able to detect a $1\ \mathrm{nT_{rms}}$ magnetic field with a signal-to-noise ratio (SNR) of 2 after 2 seconds of averaging governed by the Nyquist theorem (bandwidth = $1/2\mathrm{t_{ave}}$) [181]. Further enhancement in the SNR is achieved by increasing the averaging time, as outlined in Sec. 4.2.2. For simplicity, we will now refer to the sensitivity, or equivalently the magnetic noise amplitude spectral density, as the noise spectral density (NSD).

For an EDMR measurement, lock-in detection is utilised to suppress $1/f$ noise that can overlap the desired spin resonance signal effectively measured at DC. Furthermore, the lock-in output of the spin resonance signal is approximately the first derivative of the Lorentzian or Gaussian broadened lineshape, which provides a linear response between the signal amplitude and magnetic field near resonance. As such, the sensitivity of an EDMR-based sensor is proportional to the signal linewidth and amplitude.

Figure 5.3 depicts three methods to determine the magnetic field sensitivity from an EDMR measurement. The method in Fig. 5.3(a) assumes that electrical shot-noise is the dominant noise source and the measured response takes on a Gaussian broadened lineshape situated at B_{res} [9, 22]

$$I(B) = \frac{\Delta I}{\sigma\sqrt{2\pi}} e^{-(B-B_{res})^2/2\sigma^2}\ , \tag{5.3}$$

where $\sigma/2$ and ΔI are the peak-to-peak linewidth and signal amplitude, respectively. The output from the lock-in amplifier (i.e., the demodulated current, I_D) is approximately the derivative lineshape when the modulation amplitude, B_{mod}, is much smaller than the peak-to-peak linewidth, as previously described in Sec. 4.2.1

$$I_D(B) \simeq \frac{\partial I(B)}{\partial B} B_{mod}\ . \tag{5.4}$$

The minimum resolvable external magnetic field, δB_{min}, is dependent on the slope of the lock-in output at the zero-crossing point and the measured current noise

$$\delta B_{min} = \frac{\Delta I_{noise}}{B_{mod}\left(\frac{\partial I_D(B)}{\partial B}\right)}\,, \tag{5.5}$$

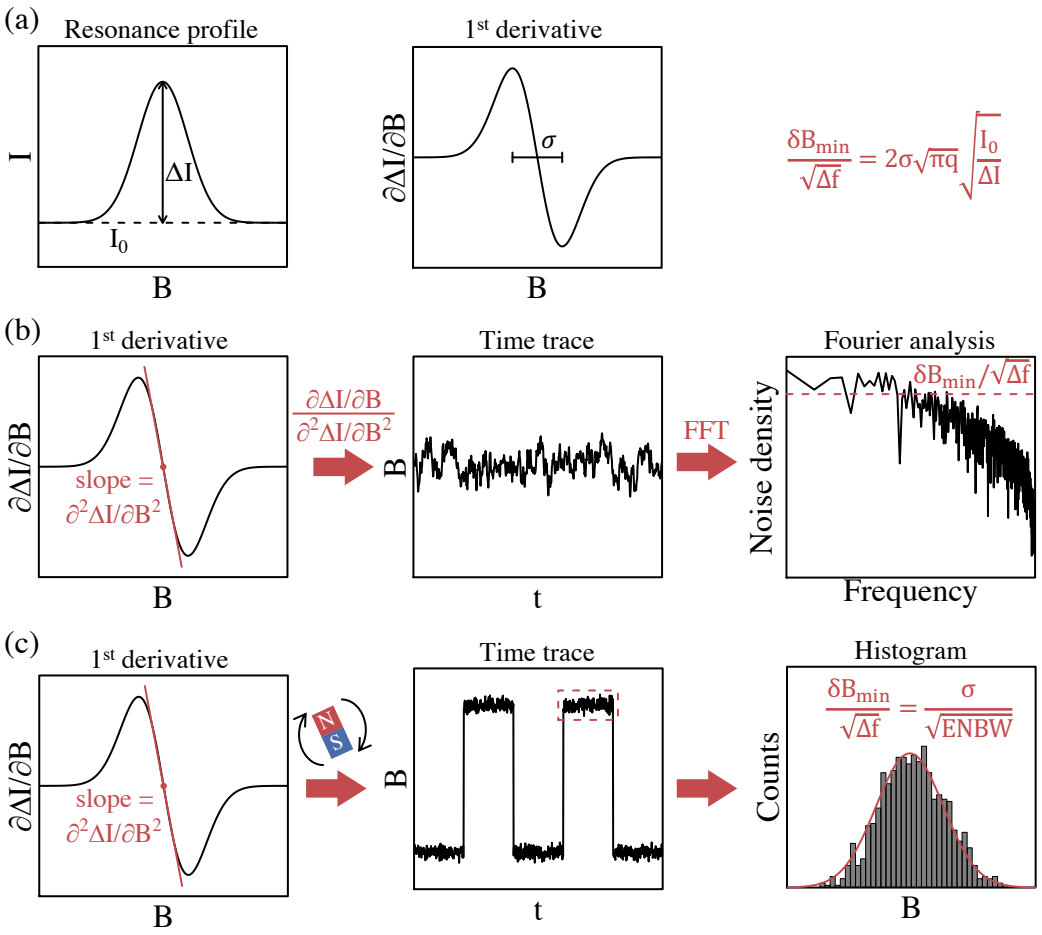

Fig. 5.3.: Schematic illustration of three different methods in calculating the magnetic field sensitivity of an EDMR-based magnetometer. The method depicted in (a) assumes an electrical shot-noise limited sensitivity, which can be simply calculated using Eq. 5.6 and the measured EDMR spectrum. The second method outlined in (b) performs a FFT on the time trace of the lock-in output at the zero-crossing point of the spin resonance response. Lastly, the method illustrated in (c) applies a square-wave modulated external magnetic field of alternating polarity and a histogram of the lock-in output time trace is used to determine the standard deviation to calculate the sensitivity.

where $\Delta I_{noise} = \sqrt{2qI_0\Delta f}$ is the root-mean-square (RMS) electrical shot noise with I_0 the spin-independent background current and Δf the bandwidth of the lock-in amplifier related to the the lock-in low-pass filter (see Eq. 4.10). Substituting Eqs. 5.3–5.4 into Eq. 5.5 and assuming the modulation amplitude is set equal to the linewidth ($B_{mod} = \sigma$), the magnetic noise spectral density is equal to

$$\frac{\delta B_{min}}{\sqrt{\Delta f}} = 2\sigma\sqrt{\pi q}\frac{\sqrt{I_0}}{\Delta I} \,. \tag{5.6}$$

While Eq. 5.6 provides a quick and simple method to calculate the sensitivity of a device, we found that Eq. 5.6 becomes invalid under certain experimental conditions. Particularly, the sensitivity approaches zero (i.e., infinite sensitivity) when I_0 approaches zero, which can occur experimentally when operating the device in a transition region where I_0 reverses in polarity for example. This will be explored in more detail in Sec. 5.5.4. In addition, other noise sources apart from electrical shot-noise are not considered in Eq. 5.6, which may have a significant contribution to the measured noise.

The approach outlined in Fig. 5.3(b) is based on the definition of the noise spectral density from signal processing and has been used extensively to characterise ODMR-based magnetometers. By taking a time trace of the lock-in output sitting at the zero-crossing point of the spin-dependent signal converted into units of magnetic field utilising the slope of the signal, the magnetic noise amplitude spectrum in units of $\mathrm{T_{rms}}$ is computed from the FFT. Note that the amplitude spectrum computed is a two-sided amplitude spectrum with half the peak amplitude mirrored against 0 Hz. A conversion to a single-sided amplitude spectrum is achieved by multiplying each frequency component other than 0 Hz by two and discarding the second half of the mirrored spectrum. The NSD is then determined by normalising the amplitude spectrum with respect to the square root of the equivalent noise bandwidth (ENBW), which is related to the lock-in amplifier low-pass filter slope and time constant found in the operating manual of the lock-in amplifier

$$\frac{\delta B_{min}}{\sqrt{\Delta f}} = \frac{\mathrm{Amplitude\ spectrum}}{\sqrt{\mathrm{ENBW}}} \,. \tag{5.7}$$

In this approach, no prior assumptions on the signal lineshape or noise source are required and the NSD frequency spectrum can be used spectroscopically to analyse the different magnetic noise sources present each with its own unique frequency response. For example, electrical noise from the mains outlet used to power the detection electronics will appear in the NSD frequency spectrum as discrete frequency components at twice the mains frequency (50 Hz in Australia) and its higher order harmonics as the magnetic flux density is strongest twice every cycle.

Lastly, the method summarised in Fig. 5.3(c) is a modified version of Eq. 5.7 sometimes used when demonstrating magnetometry in a real world scenario in which the lock-in output response at the zero-crossing point is monitored subject to a square-wave modulated external magnetic field of alternating polarity. The standard deviation determined from the histogram of the lock-in output time trace when the external magnetic field is either positive or negative in polarity replaces the amplitude spectrum term in Eq. 5.7 to calculate the magnetic field sensitivity. This method ideally requires a noiseless external magnetic field source of known magnetic field strength such that the measured standard deviation of the lock-in output time trace is solely from the performance of the magnetometer device rather than the external magnetic field source. All three methods in calculating the sensitivity introduced here will be applied to the measured data in Sec. 5.5.4.

5.4 Experimental methods

A range of 6H$-$SiC n^+p and complimentary p^+n diode devices were fabricated by our collaborators at the National Institutes for Quantum and Radiological Science and Technology (QST) in Japan. All 6H$-$SiC n^+p diode devices exhibited a SDR response, whereas no SDR response was observed for the p^+n diode devices. The 6H$-$SiC n^+p diode device with the strongest SDR response was used and all of the data presented in this chapter are from this device unless otherwise stated. Below, the processing steps for this particular device are outlined.

The diode device measured in this chapter shown in Fig. 5.4(a) was fabricated on a p$-$type epitaxial layer with a mean acceptor concentration of $2.3 \times$

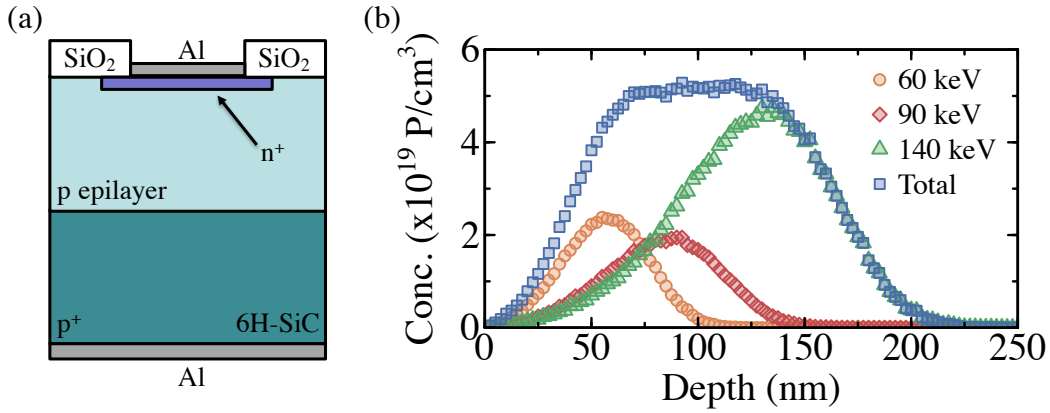

Fig. 5.4.: (a) Schematic of the n^+p 6H$-$SiC diode measured. (b) Monte carlo simulation using the SRIM package [182] of the threefold P implantation used to form the n^+ region. Refer to the main text for more detail on the implantation parameters.

10^{15} Al/cm^3 grown on a p$-$type wafer. The n^+ region was formed following a three-fold phosphorus implantation of energies and fluences of 60, 90, and 140 keV and 1.2×10^{14}, 1.3×10^{14}, and 4.2×10^{14} P/cm^2, respectively. This creates a relatively constant concentration profile of around 5×10^{19} P/cm^3 at the SiC surface, as indicated by the Monte Carlo simulation using the SRIM software package [182] in Fig. 5.4(b), assuming complete dopant activation. We note that the total doping profile is not abrupt at the junction as indicated by the tail end of the simulated P implantation profile in Fig. 5.4(b), resulting in a linearly graded junction. However, this non-ideal feature only occurs over a small transition region much thinner than the device layer such that it can to first order be approximated as an abrupt junction.

Fabrication processing steps utilising high temperatures involved addition of a protective thin layer of carbon film to prevent surface roughening, as previously outlined in Sec. 2.1.2. Subsequent removal of the carbon film was readily achieved using a dry oxidation process at 800°C [183]. Ion implantations were carrier out at 800°C to avoid amorphization [44]. Following implantation, an anneal at 1570°C for 10 minutes in an Ar atmosphere was used to simultaneously activate the implanted dopants and repair the implantation damage. A field oxide of approximately 100 nm was formed on the sample surface by pyrogenic oxidation at 1100°C (O_2 :$H_2 = 1 : 1$). This had the effect of bringing the SiC surface closer to the peak of the implantation

profile as 50 nm of SiC was consumed during the process. Front and back aluminium Ohmic contacts were deposited in vacuum with the front contact (1 mm diameter) undergoing an additional sintering at $500°$C for 5 minutes.

The EDMR results presented in this chapter were primarily performed on the low-field EDMR spectrometer described in Sec. 4.1.1 at room temperature with the external magnetic field parallel to the [0001] crystallographic direction (and perpendicular to the sample surface) unless otherwise stated. Magnetic field modulation was employed for lock-in detection at a modulation frequency of 177.53 Hz and a peak-to-peak modulation amplitude of $25\,\mu\mathrm{T_{pp}}$. Prior to lock-in detection, the measured device current underwent a two-stage amplification using a SR570 transimpedance preamplifier (2 nA/V gain, 200 Hz bandwidth, 6 dB $100-300$ Hz bandpass filter) and a SR560 voltage preamplifier ($\times 20$ gain, 6 dB $100-300$ Hz bandpass filter). For each measurement, the phase of the lock-in detector was tuned such that channel X was maximised, while channel Y was minimised. The raw voltage signal from both lock-in outputs were then processed following the steps outlined in Sec. 4.2.2.

In addition to the EDMR measurements presented in this chapter, a series of other measurement techniques were applied to the 6H$-$SiC n$^+$p diode to characterise its device properties. These results can be found in Appendix A$-$C and include random telegraph signal (RTS), electroluminescence (EL), and deep-level transient spectroscopy (DLTS) measurements, respectively. In short, RTS in the form of discrete jumps between two arbitrary current levels due to the capture and emission of a single charge carrier from a defect level was observed at large forward biases above -2.3 V. This coincided with the onset of EL from the D_1 centre associated with a Si antisite formed as a result of implantation-induced damage, surviving high temperature activation anneals. DLTS measurements also revealed a hole trap situated $E_V + E_T = 0.560$ eV within the bandgap at a concentration of approximately 1.5×10^{13} cm^{-3}. These additional measurements indicate the presence of at least three non-paramagnetic defects, which may act as competing recombination centres or trapping sites and may affect the SDR process in an EDMR measurement. However, the exact mechanisms involved and how these manifest themselves in the EDMR measurement are currently unknown. Further work will be required to understand the complex

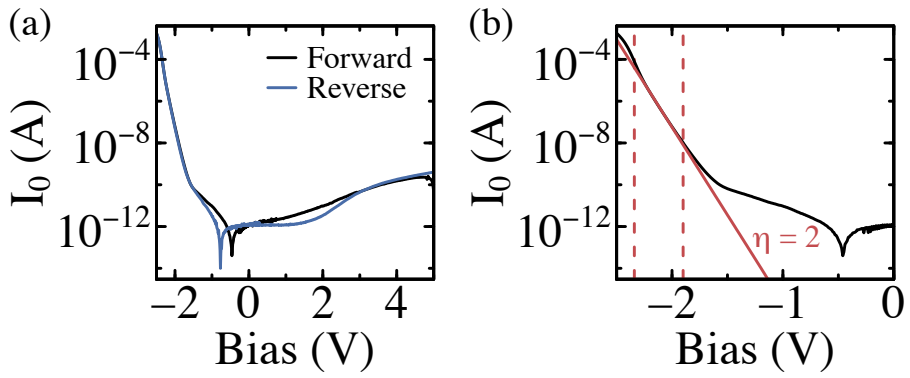

Fig. 5.5.: (a) I−V characteristics of the diode device, exhibiting the expected rectifying behaviour. Slight hysteresis in the measured current response was also observed, as indicated by the slightly different I−V characteristics between the voltage sweep in the forward (black curve) and reverse (blue curve) sweep direction. (b) Expanded plot of (a) at negative voltages superimposed with a theoretical curve following Eq. 5.2 for $\eta = 2$ (red solid line) where recombination current is expected to dominate between -1.9 and -2.3 V (dotted vertical lines).

interplay between these different defect species present. Eliminating these additional non-paramagnetic defects may be crucial in optimising future SiC magnetometer devices.

5.5 Results and discussion

A typical I−V curve of the device measured in the dark is shown in Fig. 5.5(a), exhibiting the expected rectifying behaviour of a n^+p diode with a reverse leakage current of around 5×10^{-8} A/cm^2 at 5 V. Slight hysteresis of around 0.31 V in the measured current response was also observed dependent on the voltage sweep direction. As previously outlined in Sec. 5.3.1, recombination within the depletion region dominates at small forward biases when $\eta = 2$ following Eq. 5.2. The expanded experimental I−V curve in Fig. 5.5(b) for negative voltages was overlaid with a theoretical curve following Eq. 5.2 for $\eta = 2$ (solid red line) and a regime in forward bias between -1.9 and -2.4 V where recombination current is expected to dominate (dotted vertical lines) was determined.

Operating the device at -2.2 V, DC traces of the device current as a function of the external magnetic field and RF frequency were recorded. The resulting two-dimensional map is shown in Fig. 5.6(a). A large zero-field response was observed with its peak amplitude and position independent of RF frequency. Two smaller features on either side of the zero-field response were observed and their peak positions linearly increased with increasing RF frequency following the Zeeman resonance condition. We note that the amplitudes of the resonance peaks may vary slightly with RF frequency which is a measurement artefact resulting from the frequency-dependent characteristics of the embedded PCB antenna. A cross-section of the two-dimensional map taken at 260 MHz (dashed horizontal line) is shown in Fig. 5.6(b). The quenching in the device conductivity is consistent with the reduction in free

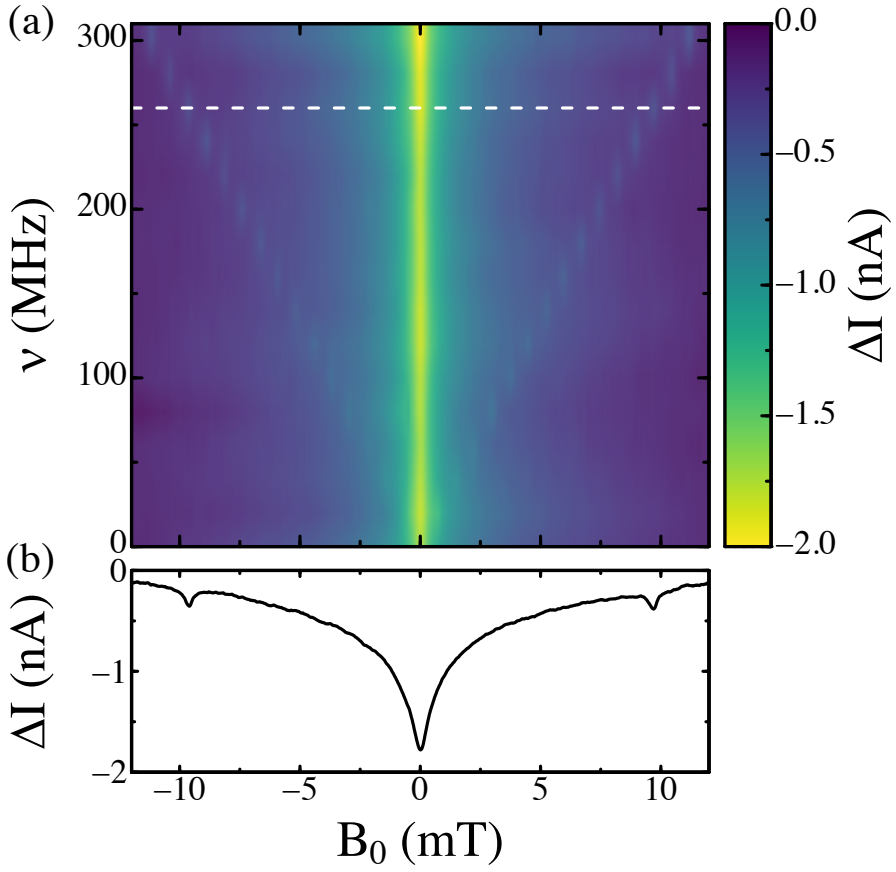

Fig. 5.6.: (a) Two-dimensional map of the SDR-induced change in device current as a function of RF frequency and magnetic field. (b) Slice of the two-dimensional map taken at $\nu = 260$ MHz indicated by the dotted white horizontal line in (a).

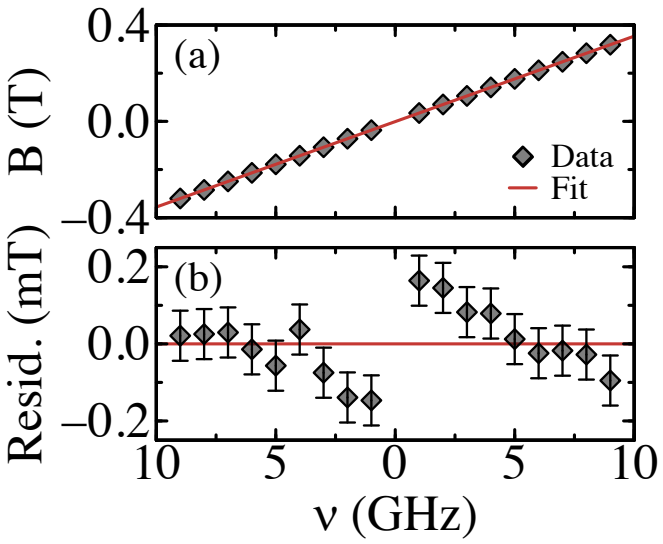

Fig. 5.7.: (a) Resonance fields measured as a function of MW frequency and a linear fit (red line) to the data used to extract an effective g-factor. Error bars are smaller than symbols and omitted for clarity. (b) Residual magnetic field from the linear fit to the data.

charge carriers as the recombination process is completed, as outlined in the spin-pair model in Sec. 3.4.

5.5.1 g−factor

The evolution of the spin resonance response with increasing resonant excitation frequency was extended into the GHz regime utilising our high-field EDMR spectrometer (described in Sec. 4.1.2) and the measured resonance peak position is plotted in Fig. 5.7(a). An effective g−factor of 2.0137 ± 0.0014 was extrapolated from the linear fit to the data according to $h\nu = g\mu_B B_{mea.} = g\mu_B(B_0 + B_{offset})$, which takes into account any constant magnetic field offset, B_{offset}, in the x-intercept [131]. For spin systems in SiC with weak spin-orbit coupling, the relatively large g-factor measured compared to the free electron g−factor is somewhat unexpected and vastly differs from literature values of common spin defects measured in similar SiC devices summarised in Table 2.2. While we do not directly attempt to determine the atomic origin of the spin defect measured here, we speculate and suggest the spin defect is a highly stable processing-induced defect residing near the diode junction

able to persist and survive the high temperature processing steps employed during fabrication.

To further investigate this unexpected g−factor value measured, the residual in the linear fit is plotted in Fig. 5.7(b). A systematic increase in the residual at lower magnetic fields is observed, which may suggest the presence of higher order terms in the spin-pair Hamiltonian that gradually becomes weaker as the Zeeman interaction dominates with increasing magnetic field. Thus, a simple linear fit following the Zeeman splitting relation in Eq. 3.2 may not be valid over the entire measurement range considered and higher MW frequencies beyond the capabilities our of experimental setup required for an accurate measurement of the g−factor utilising a linear fit. Alternatively, a relative g−factor measurement with respect to a well-characterised ESR calibration sample, such as 2,2-diphenyl-1-picrylhydrazyl (DPPH), may be considered. Unfortunately, this was currently beyond the reach of the resources available. Regardless, the following calculations and analysis will be carried out using the g−factor extrapolated from Fig. 5.7(a). This will have minimal impact in the context of magnetometry and potential alterations to the g−factor can be trivially corrected for with a multiplicative constant if required.

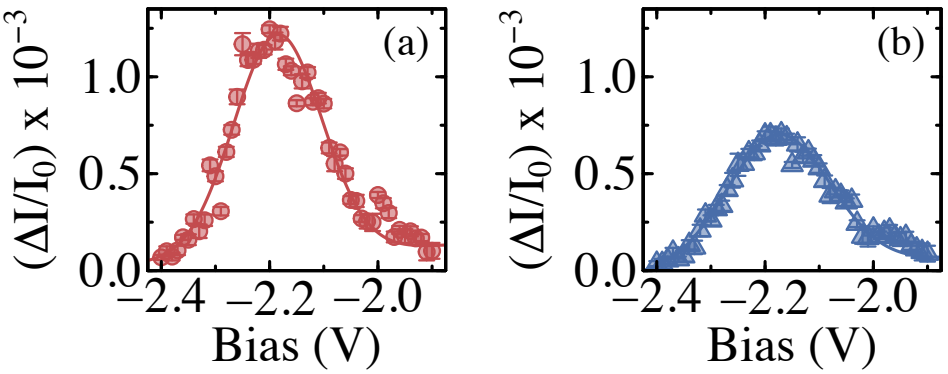

Fig. 5.8.: Normalised change in the SDR current for the (a) zero-field and (b) spin resonance signal as a function of applied forward bias. Gaussian curves (solid lines) are provided to guide the eye. Both signals reach a maximum at approximately -2.18 V.

5.5.2 Bias dependence

Figure 5.8 shows the normalised signal amplitude plotted against the applied bias for (a) the zero-field and (b) the spin resonance response, respectively. Solid lines are provided to guide the eye, which approximately follow Gaussian profiles both peaked around -2.18 V. The spin resonance response was measured with $P = 200$ mW and $\nu = 262.4$ MHz in which the embedded antenna operates most efficiently. A Gaussian bias dependence has been previously observed [23, 184] and is explained in terms of the balance between recombination current and diffusion current. In the low bias regime where diffusion current is negligible, the EDMR signal intensity increases proportionally with the recombination current component of the total forward bias current until it reaches a maximum. A sharp decrease then follows with the increase in diffusion current much larger than the recombination current. We note that this sharp decrease also coincides with the onset of RTS and EL (see Appendix A and B). The Gaussian bias dependence is a signature of a single energy level recombination center involved in the SDR process with the peak voltage related to the trap energy level in the bandgap [185].

The close correspondence between the zero-field and spin resonance response with applied forward bias unambiguously demonstrates that these two signals are both from the same physical recombination process. At its peak, the zero-field and spin resonance response reach normalised signal amplitudes of approximately 0.12% and 0.07%, respectively. These values are slightly smaller than values previously measured in 4H$-$SiC devices [9], but substantially larger than the signal contrasts measured in Si devices [186]. For the subsequent results presented, all measurements were conducted operating the device at -2.18 V unless otherwise stated.

5.5.3 Spin interactions

Utilising lock-in detection, higher order terms in the spin-pair Hamiltonian previously not observable in the DC spectrum in Fig. 5.6(b) are explored. The lock-in EDMR spectrum is plotted in Fig. 5.9 with the magnetic field (a) parallel and (b) perpendicular to the [0001] crystallographic direction, revealing a plethora of fine features. Magnifications of the main spectrum

by a factor of five are shown in the semi-transparent background. We note that qualitatively the resonant magnetic field is different when the magnetic field is parallel and perpendicular to the [0001] crystallographic direction, although no attempt was made to calculate the g−factor anisotropy as the spectral resolution at low magnetic fields is severely reduced, leading to inaccuracies.

At approximately half the resonant field indicated by the grey dotted lines, an extremely small feature was observed. As discussed in Sec. 3.4.2, these features are due to weakly allowed $\Delta m_s = \pm 2$ forbidden spin transitions from the spin-mixing between $|T_+\rangle$ and $|T_-\rangle$ states and are smaller than the spin resonance response by a factor of approximately 240. Thus, the presence of these weakly allowed transitions are indicators for the presence

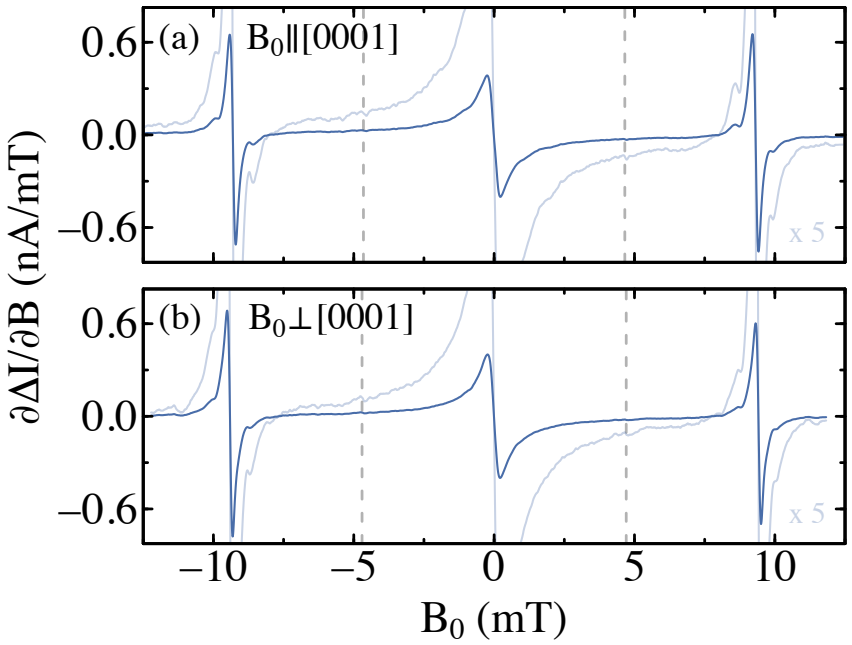

Fig. 5.9.: Optimised low-field EDMR spectrum with the magnetic field (a) parallel and (b) perpendicular to the sample surface in the [0001] crystallographic direction for $\nu = 262.4$ MHz and $P = 1$ W. The semi-transparent spectrum in the background are magnifications of the main spectrum by a factor of 5 to highlight smaller features due to hyperfine interactions and forbidden transitions.

of non-negligible dipole coupling. Theoretically, these transitions occur at [187]

$$\pm \mathrm{B}_{\mathrm{half}} = \pm \left(\frac{h\nu}{2g\mu_B} \sqrt{1 - \frac{4}{3}\left(\frac{D^\star}{\nu}\right)^2} \right), \tag{5.8}$$

with $D^\star = \sqrt{D_1^2 + D_2^2}$. When $\nu \gg D^\star$, the transition occurs precisely at half the resonant field and hence is sometimes also referred to as half-field transition. Upon closer inspection, the weakly allowed $\Delta m_s = \pm 2$ spin transitions for $\mathrm{B}_0 \parallel [0001]$ are situated at ± 4.672 mT (compared to half the resonant field at ± 4.655 mT), corresponding to $D^\star = 822 \pm 411$ kHz. This suggests that the dipolar interaction between the two electron spins in the

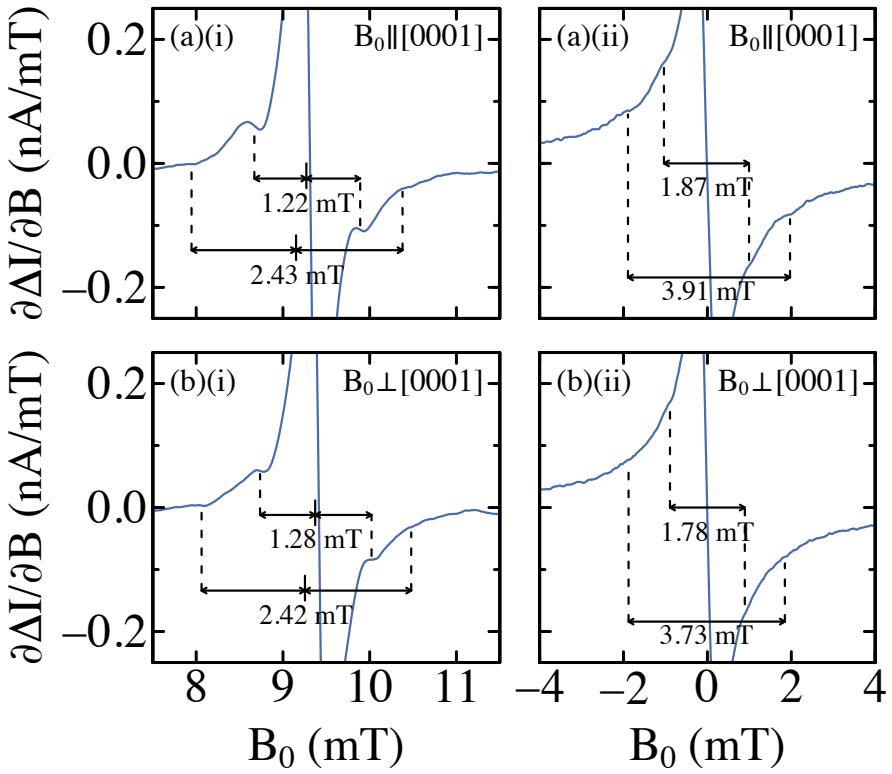

Fig. 5.10.: Magnification of the EDMR spectrum in Fig. 5.9 for the (a) spin resonance (at positive magnetic field) and (b) zero-field response when the magnetic field is (i) parallel and (ii) perpendicular to the sample surface. The separations between each set of hyperfine features are calculated from the local extrema in the (second) derivative spectrum.

spin-pair is effectively quite weak. We note that the large uncertainty value quoted reflects the loss in spectral resolution at low magnetic fields.

If D_2 is negligible (i.e., axially symmetric dipolar interaction tensor), Eq. 5.8 becomes a direct measure of D_1, which can be used to determine the zero-field splitting and spin-spin coupling distance between the two spins in the intermediate spin-pair using Eq. 3.47, assuming that point-dipole approximation is appropriate [187]. The spin-spin coupling distance has also been calculated using the peak-height ratios between the $\Delta m_s = \pm 1$ and $\Delta m_s = \pm 2$ spin transitions, although similar analysis will require a background spectrum subtraction without RF excitation to remove the large overlap of the zero-field response at low magnetic fields [188].

Referring back to the main features observed in Fig. 5.9, the fine structure associated with the spin resonance and zero-field response are related to the hyperfine interaction with more than one nearby nuclear spin species. This is also known as a superhyperfine interaction and the following analysis will focus only on the two sets of superhyperfine features closest to the zero-crossing point of the spin resonance and zero-field signal with the largest SNR. Additional sets of hyperfine peaks cannot be unambiguously resolved from the noise floor. A magnification of the EDMR spectrum is shown in Fig. 5.10 with the magnetic field (a) parallel and (b) perpendicular to the [0001] crystallographic direction for the (i) spin resonance (at positive magnetic fields) and (ii) zero-field spin-mixing response. The indicated hyperfine separations are calculated from determining the local extrema in the numerical second derivative spectrum, revealing an asymmetric hyperfine splitting shift toward smaller magnetic fields for the spin resonance signal. This is known as a Breit-Rabi shift [23, 189] and arises when the hyperfine splitting is comparable to the external magnetic field such that the eigenenergies of the spin-pair Hamiltonian is no longer linear with respect to the external magnetic field.

A summary of the hyperfine separations calculated are summarised in Table 5.1 with the orientation-dependent separations an indication of hyperfine anisotropy. The hyperfine features on the zero-field spin-mixing response are substantially broader than the hyperfine features on the spin resonance response by a factor ranging from $1.4 - 1.6$. This is consistent with previous findings and was attributed to the influence of the nuclear magnetic field

	$\Delta B_{\parallel}^{res}$ (mT)	$A_{\parallel}^{res}$ (MHz)	$\Delta B_{\perp}^{res}$ (mT)	$A_{\perp}^{res}$ (MHz)	$\Delta B_{\parallel}^{ZF}$ (mT)	$\Delta B_{\perp}^{ZF}$ (mT)
I_1	1.22	34.40	1.28	35.82	1.87	1.78
I_2	2.43	68.57	2.42	67.39	3.91	3.73

Tab. 5.1.: Summary of the hyperfine separation and interaction strength values calculated from Fig. 5.10. The nuclear spin I_1 refers to the first set of hyperfine features closest to the zero-crossing point, whereas the second nuclear spin I_2 refers to the outer set of hyperfine features. The hyperfine interaction strength is calculated using $A_{\parallel,\perp} = g\mu_B \Delta B_{\parallel,\perp}/h$.

relative to the applied external magnetic field [23]. Near zero magnetic field, the nuclear magnetic field influences the electron spins in the intermediate spin-pair, which in turn exerts its own magnetic field. As a result, the two electrons in the spin-pair align with this combination magnetic field. Conversely, in the presence of an external magnetic field, both the electron and nuclear spins align with the external magnetic field.

5.5.4 Magnetometry demonstration

We now seek to utilise the zero-field spin-mixing response to benchmark the device sensitivity to external magnetic fields. Each method introduced in Sec. 5.3.2 will be applied below. From Eq. 5.6, plugging in the appropriate values ($\Delta I = 1.67$ nA, $I_0 = 1.00\ \mu$A, and $\sigma = 1.14$ mT) yields an estimated shot-noise limited sensitivity of $\sim 970\ \mathrm{nT}/\sqrt{\mathrm{Hz}}$.

In comparison, utilising the second method outlined in Fig. 5.3(b), an average shot noise limited sensitivity of $\sim 730\ \mathrm{nT}/\sqrt{\mathrm{Hz}}$ was extrapolated at low frequencies near DC (see Fig. 5.12(b)(i) (green curve)). At higher frequencies, the steep roll-off in the NSD is a result of the lock-in low-pass filter settings used, with the cut-off frequency (-3 dB point) occurring at ~ 530 Hz following Eq. 4.10. For this measurement, a 10 s time trace of the lock-in output ($\tau = 300\ \mu$s, 24 dB/oct filter slope, ENBW $= 260$ Hz) at zero magnetic field is converted into units of magnetic field using the slope of the zero-field response shown in Fig. 5.15(b) (grey curve) and fast Fourier transformed. The sensitivity determined from the NSD is relatively consistent with the sensitivity determined above using Eq. 5.6, although slightly better by a factor of approximately 1.33.

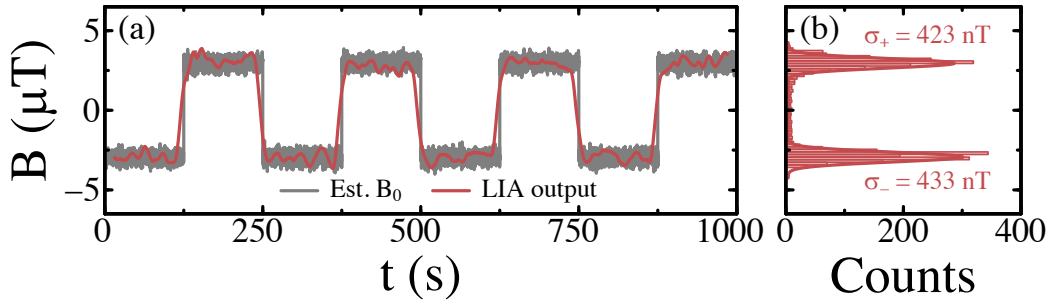

Fig. 5.11.: (a) Demonstration of magnetometry with the LIA output (red line) closely following a $\pm 2.96\ \mu\mathrm{T}$ square-wave modulated magnetic field (grey line). The noise associated with the generated magnetic field is estimated based on the electrical noise specifications of the power supply. (b) Histogram of the LIA output with a standard deviation of 423 and 433 nT when the generated magnetic field is positive and negative, respectively. This corresponds to a magnetic field sensitivity of $\sim 1.53\ \mu\mathrm{T}/\sqrt{\mathrm{Hz}}$.

Lastly, a square-wave modulated $\pm 2.96\ \mu\mathrm{T}$ magnetic field (period $= 250$ s) was generated using a set of Helmholtz coils and the lock-in response ($\tau = 3$ s and 24 dB/oct filter slope,) was recorded in Fig. 5.11(a). Estimation of the square-wave modulated magnetic field amplitude was carried out using the Helmholtz equation in Eq. 4.1 and similarly for its noise level, as per the current noise specifications of the Kepco power supply used. It is evident from Fig. 5.11(a) that the lock-in output response can accurately follow the slowly changing external magnetic field, explicitly demonstrating magnetometry in action. A histogram of the lock-in output was computed in Fig. 5.11(b) following a double-sided Gaussian distribution. Fits to the distribution revealed an average standard deviation of 428 nT, corresponding to a sensitivity of $\sim\ 1.53\ \mu\mathrm{T}/\sqrt{\mathrm{Hz}}$. This sensitivity is slightly larger than the values calculated above using the other two methods. It is speculated that this is mainly due to the magnetic noise associated with the square-wave modulated magnetic field rather than solely from the device response itself. As such, this method in characterising the sensitivity of the device is not suitable with the current experimental setup and a dedicated low noise magnetic source is required, such as a rotating permanent magnet.

5.5.5 Sensitivity enhancement

The magnetic field sensitivity calculated above for our SiC device was slightly underwhelming in comparison to other EDMR-based sensors reported in previous works ($440\,\mathrm{nT}/\sqrt{\mathrm{Hz}}$ for a SiC pn junction in Ref. [9] and $50\,\mathrm{nT}/\sqrt{\mathrm{Hz}}$ for an organic device in Ref. [22] for example). As such, different experimental procedures were explored with the aim of enhancing the magnetic field sensitivity of our measured SiC device. Two universal experimental procedures were found to greatly enhance the magnetic field sensitivity and are applicable to any other paramagnetic defect utilising the SDR mechanism. The first technique addresses the noise arising primarily from the detection electronics, which can be heavily suppressed by implementing a balanced detection scheme for common-mode rejection (CMR).

A block diagram of the balance detection scheme implemented is shown in Fig. 5.12(a). In this configuration, a second reference SiC diode device that underwent the same fabrication procedure is placed outside the Helmholtz coils and is measured using a second transimpedance preamplifier (SR570) under the same preamplifier settings and biasing conditions. Any identical noise (and signal) sources in the voltage waveform at the differential inputs of the lock-in amplifier from the two transimpedance preamplifiers will be effectively cancelled out. However, any imbalances, such as variations in the device response due to fabrication tolerances and variations in the performance of the two transimpedance preamplifiers will result in an imperfect cancellation, characterised by the common-mode rejection ratio (CMRR) [190]

$$\mathrm{CMRR} = 20\log(\mathrm{NSD}_0/\mathrm{NSD}_{\mathrm{CMR}})\,, \tag{5.9}$$

with NSD_0 and $\mathrm{NSD}_{\mathrm{CMR}}$ the noise spectral density without and with common-mode rejection, respectively. Utilising common-mode rejection, the NSD frequency spectrum is plotted in Fig. 5.12(b)(ii) (red curve) and a sensitivity of $\sim 130\,\mathrm{nT}/\sqrt{\mathrm{Hz}}$ was extrapolated at low frequencies near DC. More importantly, the NSD amplitude at twice the mains frequency (100 Hz) is heavily suppressed, demonstrating the successful cancellation of mains power noise common to both transimpedance preamplifiers, but diminishes

in effectiveness for the higher order harmonics. From Eq. 5.9, a CMRR of 15 dB is achieved at low frequencies, compared to a CMRR of 23 dB at 100 Hz. The front end input of the lock-in amplifier allows up to a CMRR of 100 dB, corresponding to a maximum sensitivity enhancement by a factor of 10^5, suggesting that other common-mode noise sources have yet to be identified and minimised.

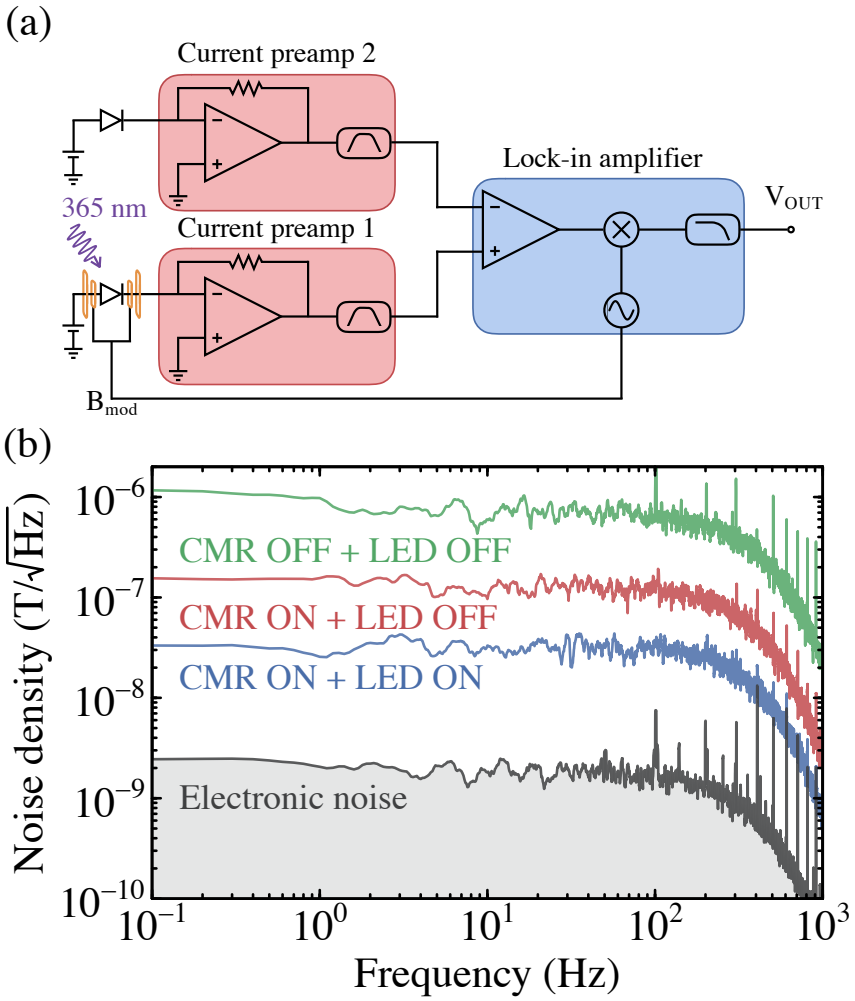

Fig. 5.12.: (a) Overview block diagram of the balanced detection scheme used to perform CMR. The output of a second matched diode situated outside the magnetic field is subtracted from the output of the main magnetometer device at the differential input of the lock-in amplifier. (b) Magnetic noise spectral density under the condition: (i) without CMR and photoexcitation, (ii) with CMR and without photoexcitation, and (iii) with CMR and photoexcitation. An electronic noise floor of ~ 2 nT/$\sqrt{\text{Hz}}$ for our current experimental setup was found.

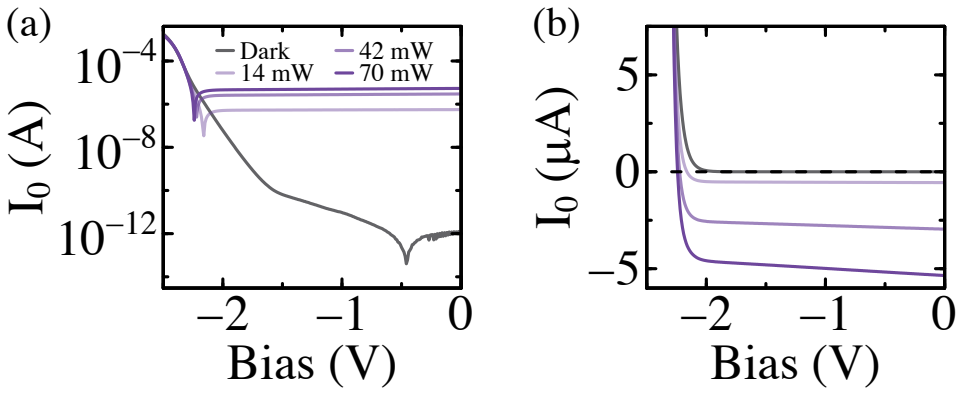

Fig. 5.13.: I−V characteristics of the diode device without and with 365 nm above bandgap photoexcitation at various powers on a (a) logarithmic and (b) linear scale. The above bandgap illumination introduces an additional generation current component to the total reverse bias current and shifts the overall I−V characteristics downwards.

The second sensitivity enhancement technique addresses the weak signal response of the zero-field spin-mixing feature by illuminating the device with above bandgap photoexcitation. Under optical illumination, an electron in the valence band is promoted into the conduction band by the absorption of a photon, leaving behind a hole. In other words, an electron-hole pair is generated. The photogenerated electron-hole pairs in the depletion region (or within a diffusion length) will be separated by the junction electric field as charge carriers drift across the depletion region, resulting in a photocurrent in the same direction as the drift current. This is also known as the short-circuit current of a photodiode when zero bias is applied [179]

$$\begin{aligned} J_{tot} &= J_{ther} - J_{ph} \\ &= J_0 \Big\{ \exp\left(\frac{qV}{\eta k_B T}\right) - 1 \Big\} - qG_{op}(L_p + W + L_n)\,, \end{aligned} \tag{5.10}$$

where J_{ther} was previously introduced in Eq. 5.2 without optical illumination and G_{op} the optical generation rate dependent on the photon collection efficiency, absorption coefficient, and photon flux.

A series of I−V curves measured with increasing illumination intensity is shown in Fig. 5.13 on a (a) logarithmic and (b) linear scale. The sample was illuminated using a Marktech MTE3650L4-UV-HP $\lambda = 365$ nm light-emitting

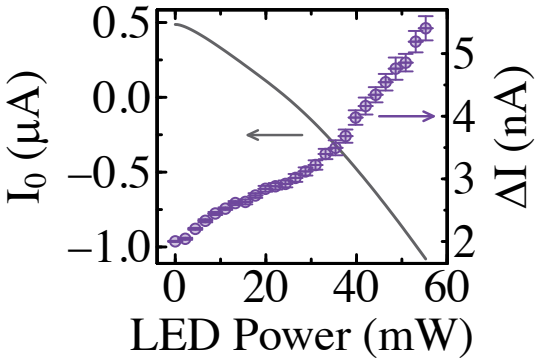

Fig. 5.14.: Amplitude of the zero-field signal (right axis) and the background current (left axis) as a function of the above bandgap photoexcitation illumination intensity at V $= -2.1$ V.

diode (LED) placed approximately 4 mm above the sample surface. Following Eq. 5.10, the I−V curve is shifted downward by a factor proportional to G_{op} with increasing illumination intensity, corresponding to an increase in reverse leakage current. At large forward biases, the exponential term in the diffusion current dominates when $\eta = 1$ and is much larger than J_{ph}. As such, above bandgap photoexcitation has negligible effect on the device response at large forward biases.

Figure 5.14 shows the spin-independent background current (grey curve) and the amplitude of the zero-field spin-mixing response (purple symbols) with increasing illumination intensity under a forward bias of -2.1 V. A monotonic increase in the amplitude of the zero-field response with increasing illumination intensity is observed. Charge carriers transiting through the depletion region under a forward bias have some probability of participating in a recombination event. The excess electron-hole pairs generated optically will thus increase the recombination rate and enhance the SDR response. We note that only a fraction of recombination events will be spin-dependent governed by the ratio between singlet state recombination rate and triplet state dissociation rate, as described by the KSM model, with a theoretical maximum contrast of 10% predicted [21].

The spin-independent background current in Fig. 5.14 is described by Eq. 5.10, where the second photocurrent term becomes larger than J_{ther} at approximately 24 mW. As a result, the overall current response becomes negative. We note that the electrical shot-noise limited sensitivity equation in Eq. 5.6

breaks down for 24 mW of optical excitation as I_0 approaches zero before becoming negative in value. While operating the device at high illumination intensities gave a larger zero-field response, the device suffered from long-term current drifts that periodically overloaded the gain setting on the transimpedance preamplifier. Experimentally, an illumination intensity of 42 mW was found to be a good trade-off between output stability and signal enhancement.

At a fixed illumination intensity of 42 mW, the bias dependence of the zero-field response is compared to the zero-field response measured in the dark in Fig. 5.15(a). Note that the zero-field response measured in the dark (grey symbols) is taken from Fig. 5.8(a) without the background current normalisation. Although ΔI measured in the dark is substantially larger at larger biases, the onset of RTS is not suitable for magnetometer operation (see Appendix A). This is reflected in the large error bars at high voltages with each data point measured from the EDMR spectrum averaged over 100 scans. In contrast, a vastly different voltage response is observed when optical illumination is introduced, peaking at a local maximum when V$=$ -2.2 V before substantially decreasing in amplitude. The non-trivial voltage dependence under optical illumination is not yet fully understood, however, we note that the sharp decrease in ΔI starts to occur above the open-circuit voltage of ~ -2.22 V when the overall current is approximately equal to zero. Furthermore, the broader voltage range under optical illumination over which the zero-field response is measurable in an EDMR measurement relaxes voltage tuning requirements.

The enhancement in the zero-field response is shown in Fig. 5.15(b) in comparison with the zero-field response measured in the dark for a single EDMR scan without signal averaging, revealing a sharper slope through the zero-crossing point by a factor of ~ 4.9 with negligible peak-to-peak linewidth broadening. We note that the slope fitted through the zero-crossing point starts to deviate from the zero-field response at magnetic field strengths close to the local signal maximum and minimum, which will introduce an error in the magnetic field reading under magnetometer mode. Here, we define the magnetic field sensing range as no more than 10% deviation between the slope fitted through the zero-crossing point and the zero-field response, which is approximately 0.44 mT in this case. This also implies that

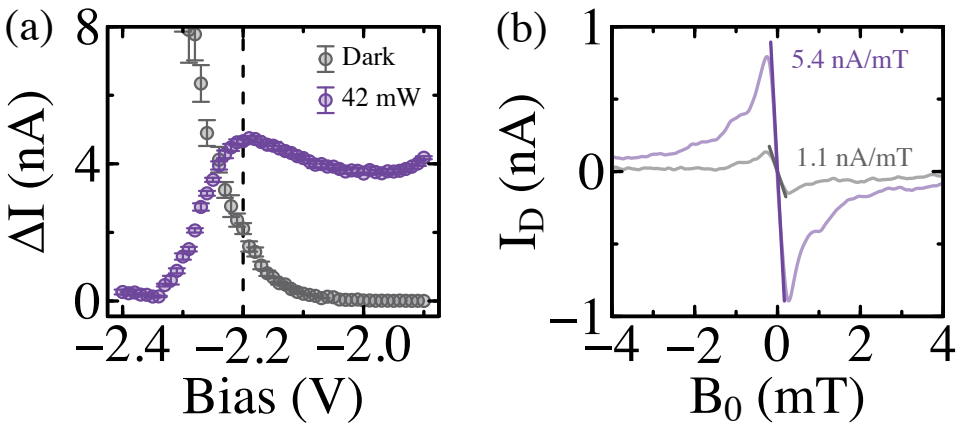

Fig. 5.15.: (a) EDMR signal amplitude of the zero-field feature as a function of applied bias without (grey symbols) and with 365 nm above bandgap photoexcitation at $P = 42$ mW (purple symbols). (b) Single EDMR scan of the zero-field feature taken at V $= -2.2$ V indicated by the vertical dotted line in (a). An enhancement in the slope of the zero-field signal by a factor of 4.9 is observed.

the peak-to-peak linewidth used in Eq. 5.6 underestimates the sensitivity dependent on the steepness of the slope fitted through the zero-crossing point.

Under optical illumination with CMR, the NSD frequency spectrum is calculated and shown in Fig. 5.12(b)(iii) (blue curve). A sensitivity of $\sim 30\,\mathrm{nT}/\sqrt{\mathrm{Hz}}$ was extrapolated, which is approximately an enhancement by a factor of 4.3 and 24.3 compared to the NSD with only CMR (red curve) and without CMR (green curve), respectively. We note that under our current experimental setup configuration, the reference device used in the balanced detection scheme was not simultaneously illuminated with above bandgap photoexcitation. As such, the balanced detection scheme implemented was not able to effectively eliminate common-mode noise from optical excitation and was only able to take into account common-mode mains power noise. A larger improvement in the CMRR is expected if both the sensor and reference device are illumination to approximately the same intensities.

The sensitivity limit imposed by the current experimental setup can be quantified by measuring the electronic NSD frequency spectrum arising from the detection electronics consisting of the current preamplifer, lock-in amplifier, and the analog-to-digital converter. The device response operated far away from zero magnetic field without CMR was recorded in Fig. 5.12(b)(iv) (black

curve) and an ultimate projected electronic noise floor of $\sim 2\,\mathrm{nT}/\sqrt{\mathrm{Hz}}$ was determined. In the context of demonstrating $\mathrm{sub}-\mathrm{nT}/\sqrt{\mathrm{Hz}}$ EDMR-based magnetometers, this result suggests that even without the enhancement methods outlined in this section, the sensitivity is currently limited by the detection electronics, which can be easily upgraded.

5.6 Summary and conclusion

A detailed EDMR study of a 6H-SiC junction diode device was conducted in this chapter. The measured EDMR response is due to a processing-induced paramagnetic spin defect with an effective g−factor of 2.0137 ± 0.0014. Several anisotropic superhyperfine features and half-field forbidden transitions corresponding to $D^{\star} = 822 \pm 411$ kHz were observed.

Different methods in calculating the magnetic field sensitivity of the zero-field response were then applied. A sensitivity of $730\,\mathrm{nT}/\sqrt{\mathrm{Hz}}$ was calculated from the NSD and the capabilities of the magnetometer was demonstrated subject to a square-wave modulated external magnetic field. To further enhance this magnetic field sensitivity, common-mode rejection and above bandgap photoexcitation were applied and an ultimate sensitivity of $30\,\mathrm{nT}/\sqrt{\mathrm{Hz}}$ was achieved. Both CMR and photoexcitation are general experimental techniques that can be applied to other spin systems to reduce experimental noise and enhance the recombination rate, respectively.

6 Hyperfine-induced spin-mixing response

In this chapter, the zero-field spin-mixing response in a commercial SiC power MOSFET is explored, particularly its electric field, charge pumping frequency, and temperature dependence. Due to the vertically diffused device structure typically employed in commercial high-power SiC transistors, a modified charge pumping biasing scheme is developed and applied to address paramagnetic defects at the oxide interface. The zero-field response exhibited a complex temperature dependence due to different competing mechanisms and any future applications utilising this zero-field response will have to take these effects into account. Furthermore, an intriguing linearly dependent linewidth was observed spanning across a wide temperature range, which may be utilised for temperature sensing.

6.1 Introduction

In the previous chapter, the hyperfine-induced spin-mixing response situated around zero magnetic field in a SiC junction diode was introduced and utilised for magnetometry. The zero-field response is a natural consequence of any spin-dependent transport mechanism involving a spin-pair and its hyperfine interaction with nearby nuclear spins. As a result, similar zero-field spin-mixing responses have been previously observed for a variety of other spin-dependent transport mechanisms, which will be reviewed in more detail in Sec. 6.2. The intricacies in the underlying mechanism involved in each type of spin-dependent transport can have a profound effect on the zero-field response, including its signal amplitude and linewidth, which are both important parameters for the magnetic field sensitivity.

The influence of external factors, such as temperature and electric field can also have a significant impact on the zero-field response. This can occur through intrinsic temperature dependent and electric field dependent terms in the spin-pair Hamiltonian in Eq. 3.50, although the exact mechanisms are

not yet fully understood. Alternatively, the device characteristics themselves may also have a strong dependence on both temperature and electric field and disentangling these effects from the spin-dependent effects may not be straightforward. It is evident that many of the intrinsic and extrinsic factors that govern the zero-field response requires further understanding and will be crucial for the development and optimisation of future SiC magnetometer devices utilising the zero-field response, but may also provide new insight on the role of spin-dependent recombination (SDR) in SiC.

In this experimental chapter, we take advantage of the wide selection of existing commercial SiC devices available and study the zero-field response of a commercial SiC power MOSFET device subject to different biasing conditions and operating temperatures, avoiding the requirement for device fabrication. Paramagnetic defects at the SiC/SiO_2 interface were addressed under a modified charge pumping (CP) biasing scheme, compatible with the vertically diffused MOS (VDMOS) device structure typically employed in commercial power transistors. The measured zero-field response contains three components that can be fitted and described by a sum of Lorentzian functions. Each component has a unique dependence on the applied bias and temperature due to different competing mechanisms and any future applications utilising this zero-field response will have to take these effects into account. The linewidth of one of the Lorentzian components exhibited a linear dependence on temperature over a wide temperature range and may have the potential to be utilised for thermometry. It is speculated that the underlying mechanism responsible for the observed dependence is due to the electron-nuclear dipolar interaction term in the hyperfine interaction, analogous to the electron-electron dipolar interaction responsible for the temperature-dependent zero-field splitting observed in some high spin manifold optical spin defects. A coupling coefficient of -1.452 ± 0.032 MHz/K was determined between $300 - 400$ K, corresponding to a temperature sensitivity of $\sim 1.614 \pm 0.035\ \mathrm{K}/\sqrt{\mathrm{Hz}}$ at room temperature.

In the following section, a brief literature review on the hyperfine-induced spin-mixing response in different spin and material systems will be summarised. This is followed by a background theory section on the CP technique and how it is used to induce SDR at the oxide interface in a transistor device.

6.2 Literature review

A magneto-response situated at zero magnetic field is commonly observed in disordered organic semiconductors with non-ferromagnetic contacts due to various spin-dependent transport mechanisms, including bipolaron formation, recombination of electron-hole pairs, and detrapping of charges by triplet excitons, and their hyperfine interaction with a local randomly orientated nuclear spin bath typically consisting of H atoms [26]. On a single electron level, the zero-field response has also been observed in double quantum dots at low temperatures [191, 192]. In the field of organic semiconductors, the zero-field response is also known as organic magnetoresistance (OMAR) and is typically large in value ($\geq 10\%$), requires small magnetic fields (< 10 mT), and measurable at room temperature [25, 26, 193], making it attractive for potential future spintronic applications, including read heads of magnetic hard drives [194] and magnetic field sensing [24].

While there exists strong similarities between the various spin-dependent transport mechanisms, the properties of the resulting OMAR often differs substantially, leading to ambiguity and confusion within the literature. In particular, both positive and negative OMAR responses have been previously reported, as well as the presence of additional features at ultra-small magnetic fields of opposite sign [24, 25, 27]. Furthermore, these peculiar features of the OMAR response can be tuned extrinsically with temperature and electric fields, where the OMAR response can change sign under certain experimental conditions. To address these ambiguities, there have been significant efforts toward modelling the spin system using a generalised master equation based on the stochastic Liouville equation introduced in Eq. 3.75 with the system Hamiltonian adapted for each specific spin-dependent mechanism [26, 195]. The steady-state solution to the stochastic Liouville equation in general can successfully capture the main features of the experimentally measured spin-mixing response. It has been demonstrated that the sign and amplitude of the OMAR response is dependent on a wide range of factors, but has a strong dependence on the ratio between the dissociation and recombination rate. On the other hand, the linewidth of the zero-field response is strongly dependent on the hyperfine coupling strength [26].

Naturally, the stochastic Liouville equation has also been applied to the zero-field response observed in Si and SiC with the spin Hamiltonian adapted for both SDR and spin-dependent trap-assisted tunnelling (SDTAT) [88, 196]. Relatively good fits are achieved by setting the hyperfine coupling, singlet recombination rate, and triplet dissociation rate as free parameters. While these fits provide a value for the singlet recombination and triplet dissociation rate for a given experimentally measured spectrum, these rates are not trivially accessible in a standard EDMR measurement. As such, comparisons with experimental values are currently lacking and limited physical insight can be inferred. Regardless, the stochastic Liouville equation has been successfully implemented for a wide range of quantum systems, demonstrating it is a versatile and invaluable theoretical tool to help compliment and shed new insight on experimental data.

The hyperfine interaction and thus the linewidth of the zero-field response can be tuned experimentally with careful isotope selection of the local nuclear environment. Previously, it has been demonstrated with an organic polymer device that replacing the hydrogen atoms with deuterium atoms, exhibiting a smaller hyperfine coupling strength, sharpens the zero-field magneto-electroluminscence response [27]. A similar narrowing effect in the linewidth of the zero-field response arising from the Si/SiO_2 interface has also been reported in a ^{29}Si depleted device by introducing an isotopically enriched ^{28}Si epitaxial layer [197, 198]. These observations are consistent with theoretical calculations from the stochastic Liouville equations. The ability to control the linewidth through isotopic engineering will be crucial in enhancing the magnetic field sensitivity of future magnetometer devices utilising the spin-mixing zero-field response.

In comparison to the disordered nature of organic semiconductors which gives rise to a randomly distributed hyperfine field, the crystalline structure of SiC yields a distinguishable superhyperfine spectrum corresponding to individual hyperfine interaction with each different nuclear spin species present [23]. As a result, the OMAR response is the average over a distribution of randomly orientated H nuclear spins, whereas resolvable features appear in the SiC zero-field response directly proportional to the hyperfine interaction strengths, as previously seen in Fig. 5.10(a)-(b)(ii). This may explain why OMAR responses are significantly larger in amplitude than the zero-field

responses found in SiC devices, however, the additional resolvable features that appear in the SiC zero-field response may be utilised for magnetic field calibration, as previously outlined in Sec. 5.2.

6.3 Background

Several biasing schemes have been developed to address paramagnetic defects at the oxide interface in a transistor device for an EDMR measurement, including the gate-diode [96], bipolar amplification effect (BAE) [199], and CP biasing configuration [200]. The CP biasing configuration was previously found to produce a large SDR response in SiC MOSFET devices in which interface defects situated within the majority of the SiC bandgap was addressed [200]. In this chapter, a modified version of CP [201–205] developed for power VDMOSFET devices without a dedicated substrate contact is applied in the context of an EDMR measurement. The more complex device structure results in peculiar that cannot be fully explained by standard CP theory and will be explored in more detail in Sec. 6.5.

6.3.1 Charge pumping theory

Charge pumping (CP) is a powerful defect spectroscopy technique first demonstrated in 1969 by Brugler and Jespers [206] that involves applying a voltage pulse to the gate contact and pumping the device between accumulation and inversion. A schematic of the device response at different stages of the gate pulse is shown in Fig. 6.1 for an n-channel MOSFET. When the gate voltage is below the flatband voltage, V_{FB}, (1), the device is in strong accumulation and a fraction of the holes accumulating at the surface are captured by interface states. As the gate pulse switches from accumulation to inversion (2), free mobile holes flow back to the substrate, while electrons supplied from the source and drain start to flow into the channel and recombine with the trapped holes when the gate bias is above the threshold voltage, V_{TH}. However, some of the trapped holes can be thermally emitted back into the valence band prior to the channel being flooded by electrons, provided the trap energy levels are sufficiently close to the band

edge. When the gate voltage is above the flatband and threshold voltages (3), the device is in strong inversion and a fraction of inversion layer electrons supplied from the source and drain are trapped by the interface states, thus becoming negatively charged. As the gate pulse switches from inversion to accumulation (4), inversion layer electrons flow back into the source and drain, while trapped electrons recombine with accumulated holes at the surface when the gate bias is below the flatband voltage. Similar to step (2), a fraction of trapped electrons with enough thermal energy will emit back into the conduction band instead of recombining with holes accumulated at the surface. The device now returns back into strong accumulation (5) and the whole process is repeated at the charge pumping frequency, f_{CP}. As a result, a DC substrate current, I_{CP}, flowing through the substrate contact due to carriers recombining at SiC/SiO_2 interface traps is directly related to the mean interface state density, $\overline{D_{it}}$

$$I_{CP} = q f_{CP} A_G \overline{D_{it}} \Delta E \,, \tag{6.1}$$

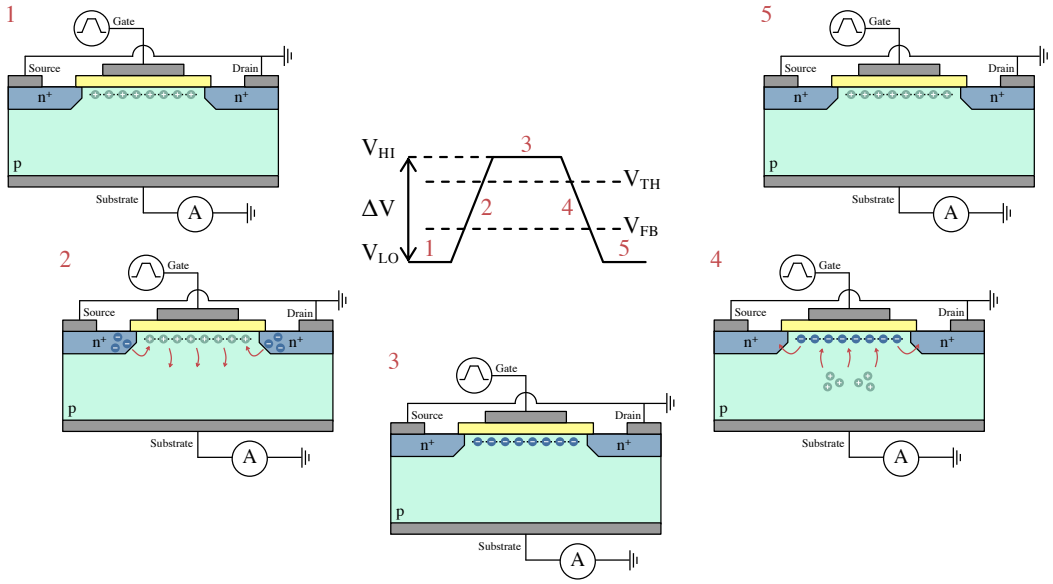

Fig. 6.1.: Charge pumping voltage waveform applied to the gate contact with the threshold and flatband voltage of an n-channel MOSFET indicated. The device response at five different stages of the gate pulse numbered between $1-5$ are also shown. Refer to the main text for more detail.

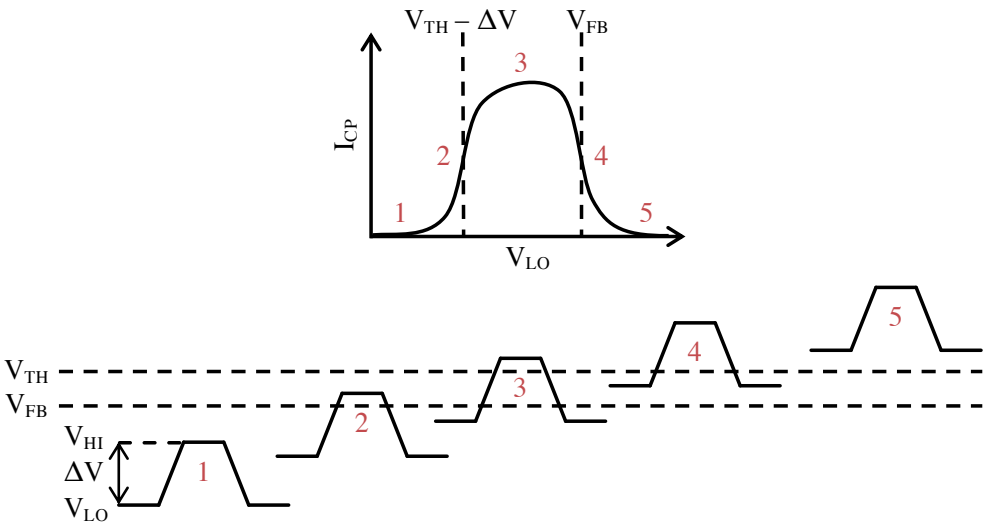

Fig. 6.2.: Illustration of the expected CP curve in the variable base mode, where the pulse amplitude, ΔV, is held constant, while the gate pulse low level, V_{LO}, is varied. Five distinct regions of operation on the CP curve are identified based on the position of the gate voltage waveform relative to the flatband and threshold voltage. Refer to the main text for more detail.

where A_G is the effective gate area and ΔE the total energy interval swept

$$\Delta E = 2k_B T \ln\left(\frac{|\Delta V|}{v_{th}\sigma_c n_i |V_{TH} - V_{FB}| t_{r,f}}\right), \tag{6.2}$$

with $\Delta V = V_{HI} - V_{LO}$ the gate pulse height, v_{th} the thermal velocity, σ_c the capture cross-section, n_i the intrinsic carrier concentration, V_{TH} the threshold voltage, V_{FB} the flatband voltage, and $t_{r,f}$ the rise and fall times of the gate pulse [207, 208]. It is assumed here for simplicity that the thermal velocity and the capture cross-section for both electrons and holes are equal.

In the variable base method, ΔV is held constant, while the gate pulse low level, V_{LO}, is swept from accumulation to inversion, as shown in Fig. 6.2, yielding a characteristic CP curve. Alternative CP methods include the variable pulse height method, where V_{LO} or V_{HI} is held constant in strong accumulation or inversion, while ΔV increases in amplitude toward strong inversion or accumulation, respectively. A maximum CP current is measured in region (3) in Fig. 6.2 when the device is driven between strong accumulation

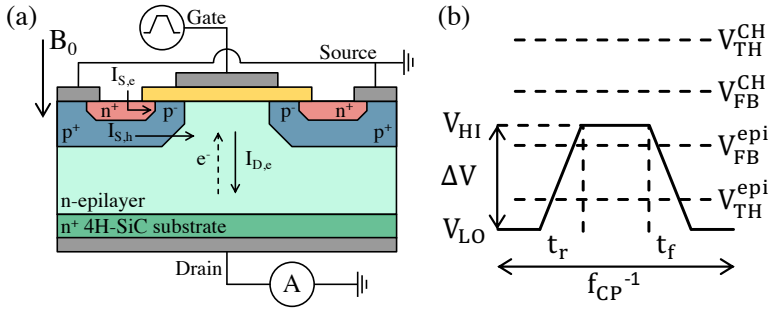

Fig. 6.3.: (a) Schematic of the CP technique modified for 3-terminal VDMOSFET structure, where the CP current is collected at the drain contact with the source contacts grounded. The device is placed inside a static magnetic field as indicated for the magneto-response measurements. (b) Definition of the trapezoidal gate pulse waveform applied to the gate contact. The flatband (FB) and threshold (TH) voltages at the epilayer/oxide (epi) and p^-/oxide (CH) interfaces are indicated.

($V_{LO} < V_{FB}$) and strong inversion ($V_{HI} > V_{TH}$) following Eq. 6.1. Conversely, negligible CP current is measured in regions (1) and (5) when the entire gate pulse is in strong accumulation below the flatband voltage and in strong inversion above the threshold voltage, respectively. In these regions, the measured substrate current is dominated by gate leakage current instead. A transitional phase occurs in regions (2) and (4) when the device is driven into weak inversion ($V_{FB} < V_{HI} < V_{TH}$) and weak accumulation ($V_{FB} < V_{LO} < V_{TH}$), respectively. From the left and right edges of the CP curve, estimates of the threshold and flatband voltages can thus be calculated, respectively.

6.4 Sample details and method

An unpackaged commercial 36 A/900 V n-channel 4H-SiC power MOSFET (CPM3-0900-0065B) purchased from Cree Inc. was studied in the research presented in this chapter. The device adopts a VDMOS structure where the source and substrate wells are directly shorted together by the source contact metallization, as shown schematically in Fig. 6.3(a). Since the VDMOS device structure lacks a dedicated substrate contact for standard CP, we employ a modified version [201–205] with the CP current measured from the drain contact, while grounding the source terminals. In this configuration, a 3-terminal n-channel VDMOSFET can be effectively treated as two back-

to-back conventional 4-terminal p-channel and n-channel MOSFETs under proper biasing conditions defined by the VDMOSFET n-epilayer/SiO_2 and p^-/SiO_2 interfaces, respectively. Thus, both the threshold and flatband voltages of the n-epilayer/SiO_2 interface, V_{TH}^{epi} and V_{FB}^{epi}, and the p^-/SiO_2 interface, V_{TH}^{CH} and V_{FB}^{CH}, have to be considered (see Fig. 6.3(b)).

All measurements presented in this chapter were performed using the temperature controllable spectrometer described in Sec. 4.1.3 without lock-in amplification. A trapezoidal gate pulse at a frequency and rise/fall time of $f_{CP} = 500$ kHz and $t_{r,f} = 50$ ns, respectively, was used unless otherwise stated (see definitions in Fig. 6.3(b)). The resulting CP current at the drain contact was measured using a SR570 transimpedance preamplifier with a band-pass filter ($0.03 - 10$ Hz) to minimise long term drifts and suppress undesired high frequency current transients occurring during the rise and fall times of the gate pulse [209]. Measurements of the zero-field response were performed in a static magnetic field perpendicular to the sample surface (see Fig. 6.3(a)) and averaged over 500 individual magnetic field scans to enhance the SNR, followed by a numerical derivative for spectral fitting.

6.5 Results and discussion

Figure 6.4(a) shows a typical CP curve with $\Delta V = 4$ V. The measured CP current is several orders of magnitude larger than the CP current typically measured in a conventional 4-terminal MOSFET. This is due to the fact that a power VDMOSFET device comprises of several hundred to thousand elementary cells that are all connected in parallel and contributing to the overall CP current [210], with a single elementary cell depicted in Fig. 6.3(a). Upon closer inspection in the region indicated by the red dashed box in Fig. 6.4(a), a positive-valued CP feature is observed in Fig. 6.4 (b). Due to the dynamic charging and discharging of the interface states, the threshold and flatband voltages are continuously shifting, resulting in broadened edges in the CP curve [208]. Approximate values of the ideal threshold and flatband voltages are estimated from the local extrema in the derivative, as indicated by the red dashed lines in Fig. 6.4(a)−(b). We note that the slight distortion in the CP curve characterised by the broadened edges and the lack of a flat response as I_{CP} reaches a maximum is a result of the small pulse amplitude

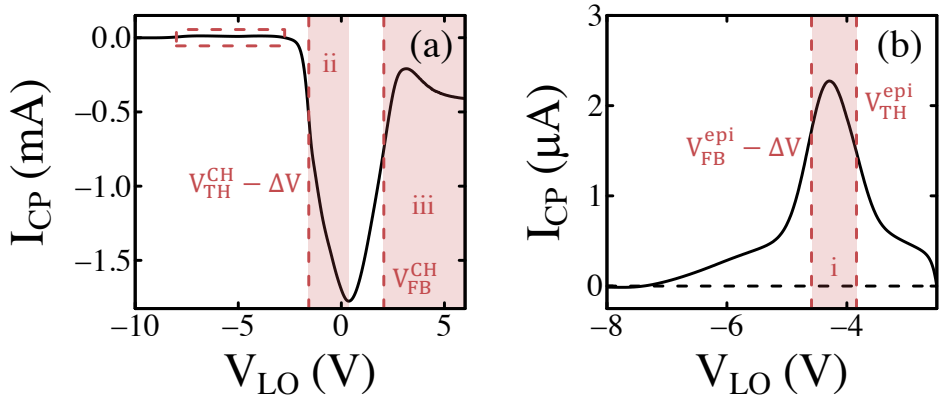

Fig. 6.4.: (a) CP current as a function of the low level gate voltage, V_{LO}, with $\Delta V = 4$ V. (b) Magnification of the region indicated by the red dashed box in (a), revealing a positive-valued peak. For region (i), $V_{LO} + \Delta V > V_{FB}^{epi}$ and $V_{LO} < V_{TH}^{epi}$. For region (ii), $V_{LO} + \Delta V > V_{TH}^{CH}$ and $V_{LO} > V_{FB}^{CH}$ for region (iii). Refer to the main text for more detail. Vertical dashed lines indicate estimates of the flatband and threshold voltages for the n-epilayer/SiO_2 and p^-/SiO_2 interface, respectively.

chosen limited by the voltage range of the arbitrary waveform generator used, although standard CP analysis remains valid. The appearance of both a positive-valued and negative-valued CP feature was first somewhat unexpected, but can be understood in terms of the device operating under different regimes relative to the threshold and flatband voltages at the two different interfaces as follows:

When $V_{LO} < V_{TH}^{epi}$, the measured DC drain current is just equal to the gate leakage current as the n-epilayer/SiO_2 interface remains in inversion. In region (i) where $V_{LO} + \Delta V > V_{FB}^{epi}$ and $V_{LO} < V_{TH}^{epi}$, the DC drain electron current, $I_{D,e}$, is equal to the net electron and hole recombination rate at the full n-epilayer/SiO_2 interface. The DC source electron current, $I_{S,e}$, is small due to the device being operated in the p-channel subthreshold regime, while the DC drain hole current, $I_{D,h}$, is negligible. Thus, the measured DC drain current is the CP current, as defined in Eq. 6.1 (i.e., $I_{CP} = I_D = I_{D,e}$) and is positive in value, adopting the convention shown in Fig. 6.3 (a). As V_{LO} further increases such that $V_{LO} + \Delta V \geq V_{FB}^{epi}$ and $V_{LO} > V_{TH}^{epi}$, the CP current decreases as the n-epilayer/SiO_2 interface becomes inactive due to insufficient hole capturing during the low level of the gate pulse. In region (ii) where $V_{LO} + \Delta V > V_{TH}^{CH}$, independent of the pulse amplitude, the channel starts to open and the

n^+ source regions become active. The measured drain current becomes $I_D = -I_S = I_{S,h} - I_{S,e}$ and can change sign when $|I_{S,e}| >> |I_{S,h}|$, although a characteristic CP curve is still observable as the drain-source voltage, $V_{DS} = 0$ V. In comparison to region (i) in Fig. 6.4(b), the measured drain current is larger by approximately six orders of magnitude due to the additional channel current and the larger effective gate area probed at the p^-/SiO_2 interface. The effective gate area at the p^-/SiO_2 interface, proportional to the gate-source capacitance, is larger than the gate-drain capacitance proportional to the effective gate area at the n-epilayer/SiO_2 interface, as provided by the device datasheet, although the exact dimensions of the device is not known nor provided by the manufacturer. As the device enters region (iii) where $V_{LO} > V_{FB}^{CH}$, a small increase in the magnitude of the CP current is observed. Here, the p^-/SiO_2 interface is permanently in inversion and the measured drain current is just the MOSFET I−V characteristics at $V_{DS} = 0$ V.

Inside an external magnetic field, the CP current is heavily suppressed when $|B_0| > 0$, as shown in Fig. 6.5(a) operating at $V_{LO} = -4.6$ V. The positive-

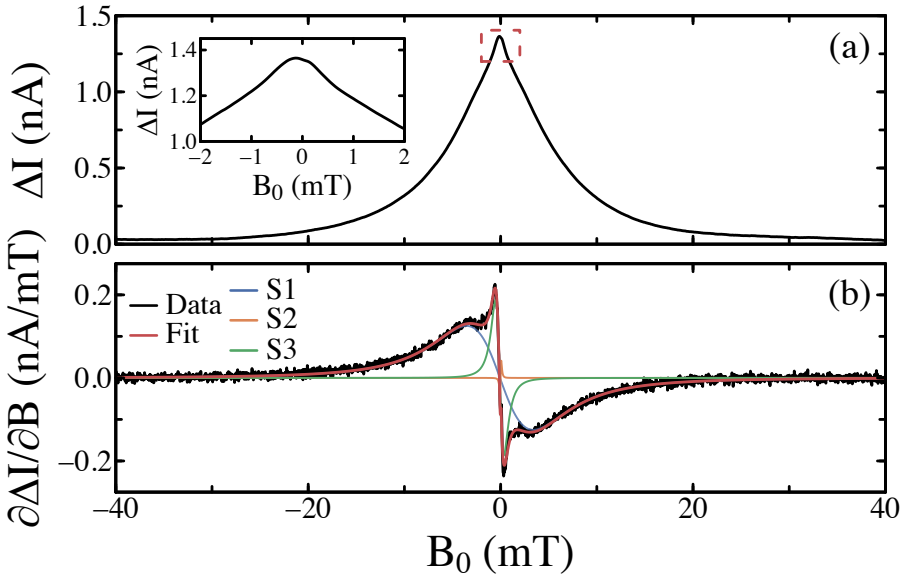

Fig. 6.5.: (a) Change in the CP current under an external magnetic field at room temperature with $V_{LO} = -4.6$ V. The inset magnifies the region indicated by the red dashed box, revealing a small dip in the CP current at precisely zero magnetic field. (b) Numerical derivative of (a) and the overall fit (red line) to the experimental data following the derivative of Eq. 6.3. The overall fit can be decomposed into three Lorentzians labelled S1-S3, with S2 negative in sign (orange line).

valued zero-field response indicates an enhancement in recombination, as opposed to a quenching in the device conductivity observed for the SiC junction diode in Chapter 5. We stress that the zero-field response was only observed when operating the device at voltages near the positive-value CP feature in Fig. 6.4(b). This voltage dependence will be explored in more detail below in Sec. 6.5.1. At extremely small magnetic fields below $|B_0| < 2$ mT shown in the inset of Fig. 6.5(a), an additional feature is visible, where the CP current slightly decreases at precisely zero magnetic field. We note that the slight linear asymmetry is an artefact of the measurement and is dependent on the direction of the magnetic field sweep, possibly due to the ferromagnetic Ni contact used for the drain metallization. We further note that the measured magneto-response is not due to ferromagnetic resonance-related effects as the zero-field response was only measurable under CP biasing conditions.

To better resolve the convoluted zero-field response, a numerical derivative is taken and displayed in Fig. 6.5(b). A generalised mathematical model consisting of a sum of Lorentzians without any a priori knowledge is considered and the overall zero-field response at room temperature can be adequately modelled by three Lorenztians based on the principle of parsimony with each component centred around zero magnetic field of the following form

$$\Delta I(B_0) = \Delta I_{CP}\left(\frac{\Delta B^2}{\Delta B^2 + B_0^2}\right), \tag{6.3}$$

where $\Delta B = \sigma_{\mathrm{FWHM}}/2$ and σ_{FWHM} is the full width at half maximum (FWHM) linewidth. Note that the FWHM of a Lorentzian function is related to its peak-to-peak derivative linewidth by a factor of $1/\sqrt{3}$. Each individual Lorentzian component labelled S1,S2, and S3 (blue, orange, and green curves) and the overall fit (red curve) are also included in Fig. 6.5(b).

The ultra-small magnetic field feature highlighted in the inset of Fig. 6.5(a) can be mathematically described by a negative-valued Lorentzian (orange line in Fig. 6.5(b)). Similar ultra-small magnetic field effects characterised by the presence of a non-monotonic W-shaped (or inverted W-shaped) feature in the zero-field response below $|B_0| < 1$ mT have been previously reported

in various organic semiconductor devices [24, 26, 27], although several different mechanisms can give rise to the same feature. Specifically, it can be reproduced intrinsically by the stochastic Liouville equation in both unipolar (bipolaron model) and bipolar (electron-hole pair model) devices by only considering the Zeeman and hyperfine interaction in the spin-pair Hamiltonian subject to the balance between spin-mixing and spin-pair formation rates. In contrast, spin-spin interaction (exchange and dipolar) can also give rise to the same feature, with the spin-mixing degeneracy between singlet and triplet states at zero magnetic field lifted [24, 26], as previously described in Sec. 3.4.2. The current mathematical model applied based on Eq. 6.3 does not confirm nor disprove which mechanism is responsible for this feature and the presence of spin-spin interaction may be observed in the Rabi nutation of a pEDMR measurement [211]. Instead, in the following section, the zero-field response and its dependence on different experimental conditions is explored, which may provide new insight on the underlying mechanism responsible for the observed features in the zero-field response.

6.5.1 Bias dependence

A set of zero-field responses were taken as a function of V_{LO} around the positive-valued CP peak in Fig. 6.4(b) and fitted using the derivative of Eq. 6.3. The extracted fitting parameters are summarized in Fig. 6.6(b)$-$(c) for each individual fit following the coloured symbols in Fig. 6.6(a). Some of the extracted parameters are multiplied by the indicated factors for comparative purposes. Note that Fig. 6.6(a) is a reproduction of Fig. 6.5(b) without the raw data. The amplitude of each Lorenztian fit and the overall amplitude closely follows the positive-valued CP peak (see Fig. 6.6 (d)), suggesting the paramagnetic defect responsible for the zero-field response is also the dominating recombination center in the CP process at the n-epilayer/SiO_2 interface. For this particular device, the maximum signal contrast reaches almost 0.1$\%$ at room temperature for $V_{LO} = -4.3$ V (see Fig. 6.6(e)), slightly smaller in magnitude than the zero-field response in the SiC junction diode studied in Chapter 5 ($\sim 0.125\%$).

Taking advantage of the spectroscopic capabilities of the CP technique, the mean number of interface traps participating in the recombination process

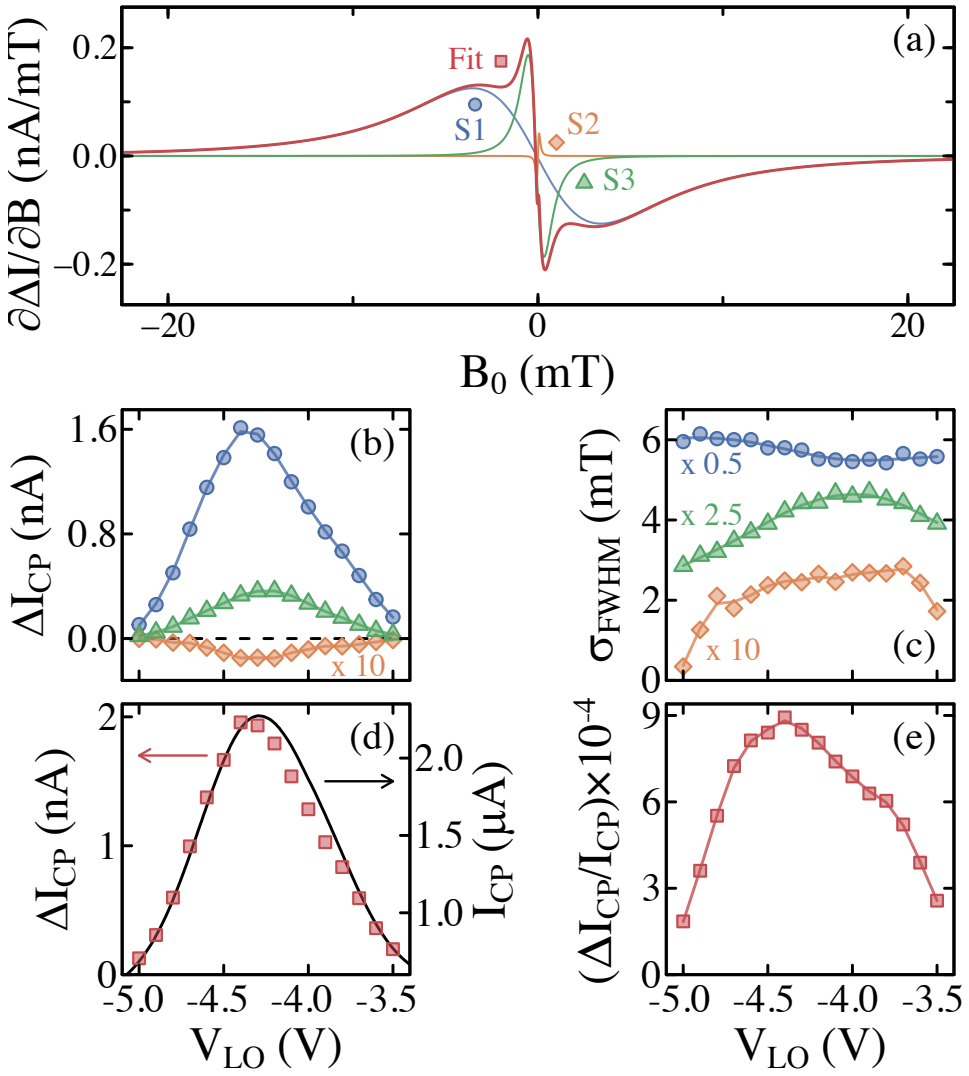

Fig. 6.6.: (a) Individual and overall fits to the experimental data reproduced from Fig. 6.5(b) and their corresponding symbols referred below in (b)-(e). (b) Signal amplitude, ΔI_{CP}, and (c) full width at half maximum, σ_{FWHM}, of each individual Lorentzian fit, as a function of V_{LO}. For comparative purposes, smaller values are multiplied by the factors indicated. (d) CP current reproduced from Fig. 6.4(c) (solid line) and the overall signal amplitude (symbols) calculated from the sum of the individual fits to the experimental data versus V_{LO}. (e) Relative change in CP current as a function of V_{LO}. The coloured solid lines are guides for the eye and errors bars are smaller than symbols.

(i.e., $\overline{N_{it}} = \overline{D_{it}} A_G = I_{CP}/(q f_{CP} \Delta E)$) is approximately 2.6×10^7 interface traps that lie within $\Delta E = 2.77$ eV of the bandgap referenced relative to the midgap. We note that the effective gate area is not known. From the signal contrast of the zero-field response summarised in Fig. 6.6(e), the number

of intermediate spin-pairs that undergoes the spin-mixing process can be estimated, equating to approximately 1.0×10^4 spin-pairs at $V_{LO} = -4.3$ V.

The zero-field response was only found to exist within a limited narrow bias range around the positive-valued CP feature in Fig. 6.4(b). When $V_{LO} > -2.5$ V and I_{CP} is negative, corresponding to the measured drain current equalling the sum of the CP current due to recombination at the p^-/SiO_2 interface and the drain-source current for $V_{DS} = 0$ V, the zero-field response was not measurable. Although it is expected that paramagnetic defects at the p^-/SiO_2 interface are also present, the large background drain current measured corresponding to a signal contrast of approximately $\Delta I/I_0 \sim 10^{-6}$ is well below the sensitivity limit of a standard EDMR measurement. As a result, the presence of paramagnetic defects at the p^-/SiO_2 interface cannot be entirely ruled out and spin information at this interface is not accessible for the VDMOSFET device structure studied here under CP conditions.

For each individual Lorentzian component, the fitted linewidth extracted has its own non-trivial and unique dependence on V_{LO}, as shown in Fig. 6.6(c). Interestingly, there seems to exist a local extrema near $V_{LO} = -4$ V, where S2 and S3 reaches a maximum, while S1 reaches a minimum. We note that this voltage is near the n-epilayer/SiO_2 interface threshold voltage, $V_{TH}^{epi} \sim -3.83$ V, however, it is currently unclear how and if the device turn-on response has an affect on the zero-field response. Variation in σ_{FWHM} for S1 can reach up to ~ 1.45 mT, whereas S2 and S3 can vary up to around 0.25 and 0.74 mT, respectively, within a 1.5 V voltage range. The large variation in σ_{FWHM} demonstrates a large degree of electrical tunability in the zero-field response, however, the exact dependence and mechanisms involved are not yet fully understood and warrants further investigation.

6.5.2 Time dependence

The dynamic recombination kinetics involved in a CP measurement introduces an extra temporal degree of freedom, as compared to a basic DC biasing scheme applied in Chapter 5 to a junction diode device, which may occur on the same time-scales as the spin-pair recombination and dissociation rates and affect the measured zero-field response. This additional temporal degree of freedom presents a unique opportunity to explore the spin

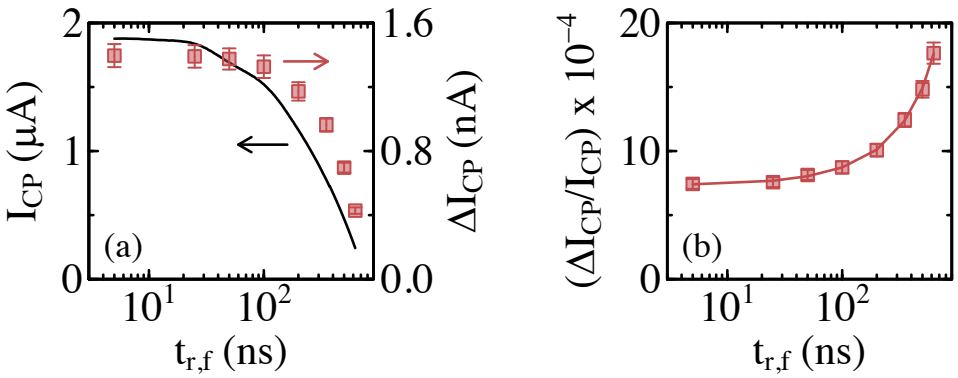

Fig. 6.7.: Background CP current (black line) and the change in CP current (shaded symbols) versus the rise and fall time of the gate pulse voltage. (b) Relative change in CP current as a function of the rise and fall time of the gate pulse voltage. The colored solid line is a guide for the eye.

and charge dynamics of an cwEDMR measurement under CP conditions. Here, we perform a tentative study on how $t_{r,f}$ and f_{CP} in the CP gate pulse can affect the amplitude of the CP current and the overall zero-field response. Note that only the overall zero-field response is considered here rather than each individual Lorentzian component.

Figure 6.7(a) shows the change in I_{CP} and ΔI_{CP} as a function of $t_{r,f}$. Measurements were performed holding V_{LO} andf_{CP} constant at -4.6 V and 500 kHz, respectively. Similar to Fig. 6.6(d), a close correspondence is observed between I_{CP} and ΔI_{CP} with changing $t_{r,f}$, again confirming that the paramagnetic defect responsible for the zero-field response also participates in the CP process. From standard CP theory, as the gate pulse rise and fall time is decreased, the CP detection energy window increases following Eq. 6.3, leading to an enhancement in I_{CP} until it reaches a saturation. Thus, only fast interface traps within ΔE are able to participate in the recombination process and contribute to the CP current.

Conversely, trapped charge carriers outside ΔE are almost immediately detrapped through the thermal emission process back into their respective energy bands, as depicted in steps (2) and (4) in Fig. 6.1. As a result, gate pulses with sufficiently long rise and fall times greater than the thermal emission rate will reduce the number of recombination events and the CP current. A rough estimate of the thermal emission rate can then be determined from when the CP current is substantially reduced as a function of increasing $t_{r,f}$,

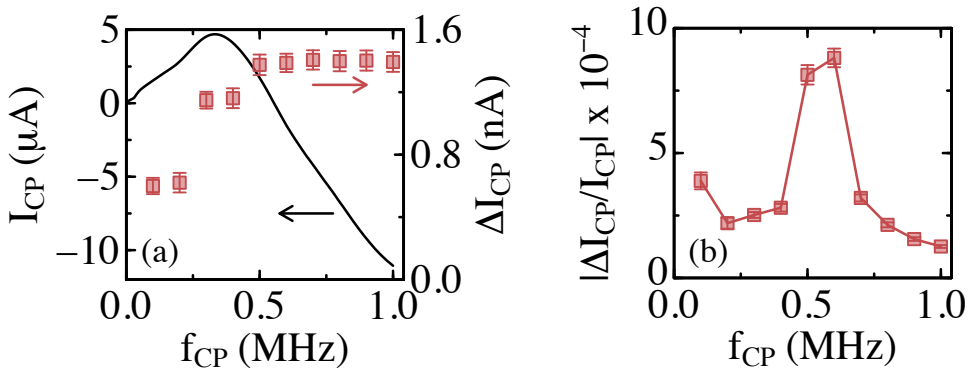

Fig. 6.8.: (a) Background CP current (black line) and the change in CP current (shaded symbols) versus the CP frequency. (b) Relative change in CP current as a function of the CP frequency. The coloured solid line is a guide for the eye.

taking into account the change in the CP energy window. From Fig. 6.7(a), a substantial decrease in the CP current starts to occur when $t_{r,f} > 30$ ns, indicating that the thermal emission time constant is approximately on the same time-scale.

We note that the amplitude of the zero-field response starts to decrease at slightly longer rise and fall times approximately above 100 ns, which may suggest that the spin-mixing process is limited by some other process occurring at longer time-scales instead of the thermal emission process, possibly related to the singlet recombination and triplet dissociation rates. Interestingly, the maximum normalised signal contrast is obtained at slower rise and fall times, as shown in Fig. 6.7(b) when both I_{CP} and ΔI_{CP} are at a minimum. However, experimentally I_{CP} can be partially compensated by the transimpedance preamplifier and a large ΔI_{CP} is generally preferred rather than $\Delta I_{CP}/I_{CP}$.

The other temporal parameter in the CP gate pulse is the CP frequency and its influence on the CP current and the amplitude of the overall zero-field response is shown in Fig. 6.8(a). Measurements were performed with V_{LO} and $t_{r,f}$ held constant at -4.6 V and 50 ns, respectively, such that the energy window probed is independent of f_{CP} following Eq. 6.3. The CP current increases monotonically with f_{CP} and reaches a maximum at approximately $f_{CP} = 350$ kHz, consistent with the expected theoretical linear dependence following Eq. 6.1. This is followed by a decrease in the CP current before the CP current changes sign at approximately $f_{CP} = 550$ kHz, deviating from

Eq. 6.1. To understand this anomalous CP frequency dependence at high frequencies, a CP curve at $f_{CP} = 1$ MHz was measured and is shown in Fig. 6.9. This closely resembles the CP curve measured at $f_{CP} = 500$ kHz, except the positive-valued peak in Fig. 6.4(b) has now disappeared and the CP current is always negative in value (see inset of Fig. 6.9). Thus, the change in sign of the CP current observed above approximately $f_{CP} = 550$ kHz in Fig. 6.8(a) corresponds to the disappearance of the positive-valued CP peak as the negative-valued CP response becomes larger in magnitude.

At high CP frequencies, the disappearance of the positive-valued CP peak may also be due to a thermal freeze-out effect, where the emission rate (strongly dependent on temperature) from the deep N donor state [212] becomes slower than the CP frequency. As a result, limited free charge carriers are supplied for the dynamic CP process. However, we note that a large zero-field response is still measurable (see Fig. 6.8(a)) even with the disappearance of the positive-valued CP peak. This suggests that recombination at the n-epilayer/SiO_2 interface is still present, which does not disappear until above approximately $f_{CP} = 2.5$ MHz where the zero-field response is no longer measurable (not shown). As the p-type source wells are highly doped with readily available charge carriers able to participate in the CP process, the dominant negative-valued CP peak corresponding to the p^-/SiO_2 interface persists even at high CP frequencies and does not suffer from freeze-out effects. This is later corroborated by low-temperature CP measurements in Fig. 6.12(a).

The amplitude of the zero-field response does not follow the background CP current dependence on f_{CP}, unlike the zero-field response dependence on V_{LO} and $t_{r,f}$ reported in Fig. 6.6(c) and Fig. 6.7(a), respectively. Instead, the amplitude of the zero-field response appears to saturate above $f_{CP} = 500$ kHz regardless of whether the positive-valued CP feature is present or not. A similar saturation behaviour has been previously reported for the zero-field response [88] and the spin resonance response [87, 88] under EM excitation. The saturation behaviour is explained in terms of the dynamic CP process occurring on a faster time-scale than the underlying spin dynamics involved. For the zero-field response, the CP frequency becomes faster than the spin-mixing rate of the spin-pair [88]. For the spin resonance response, the CP frequency becomes faster than the finite time required to induce a spin flip

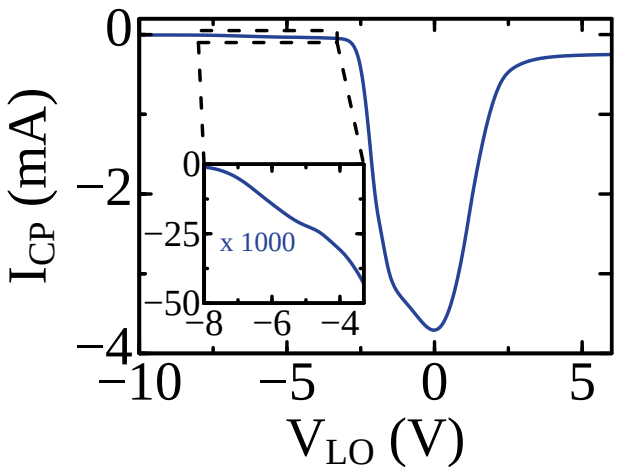

Fig. 6.9.: CP current as a function of the low level gate voltage, V_{LO}, measured at $f_{CP} = 1$ MHz. The inset shows a magnification of the region indicated by the dashed box, revealing the disappearance of the positive-valued peak observed in Fig. 6.4 and the CP current becomes negative in value.

transition governed by the Rabi frequency [87]. A rough estimate of the spin-mixing rate from Fig. 6.8(a) is on the order of $2\ \mu$s.

Finally, returning back to Fig. 6.8(b), we note that due to the sign change of I_{CP} at approximately $f_{CP} = 550$ kHz, an artificially-induced maximum normalised signal contrast is observed. Assuming a linearly dependent background CP current instead, the maximum normalised signal contrast will be achieved at lower CP frequencies, where both I_{CP} and ΔI_{CP} are at a minimum, similar to the $t_{r,f}$ dependence observed in Fig. 6.7(b).

6.5.3 Temperature dependence

Having demonstrated that the overall zero-field response can be adequately resolved into three distinct Lorentzians each with its own unique dependence on V_{LO} and observed that the temporal dependence of the CP process is closely related to temperature, we now investigate the zero-field response as a function of temperature. The temperature evolution at $V_{LO} = -4.6$ V is shown in Fig. 6.10 between T$= 210 - 400$ K. Each spectrum presented spans across $\partial\Delta I/\partial B = \pm 0.75$ nA/mT and $B_0 = \pm 40$ mT.

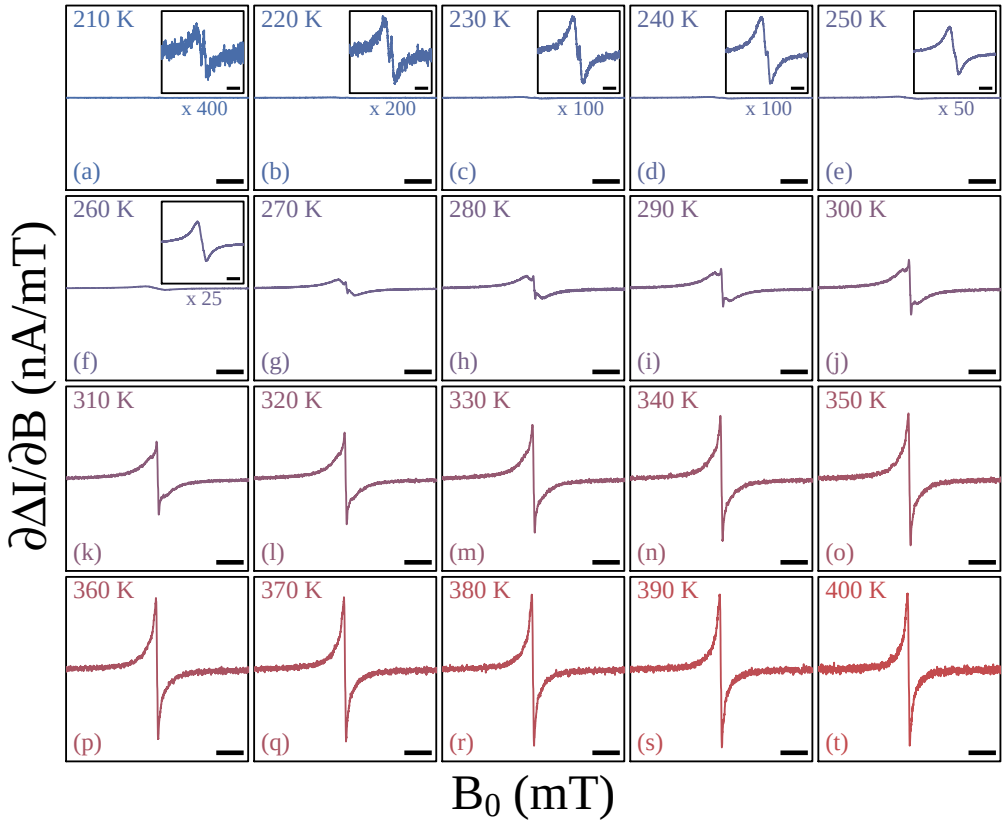

Fig. 6.10.: Numerical derivative of the zero-field magneto-response measured between $210 - 400$ K in increments of 10 K with the weaker signals measured at low temperatures enhanced in the inset by the factors indicated. Each scale bar corresponds to 10 mT.

At each temperature, the spectrum is fitted using the derivative of Eq. 6.3 and the fitted parameters are summarised in Fig. 6.11(b)−(c) for each individual fit following the coloured symbols in Fig. 6.11(a). We note that due to the poor SNR for the spectrum measured at T$= 210$ K, a spectral fit to the data was not possible and therefore omitted in this summary. Measurements above T$= 400$ K were avoided due to the deterioration of the electrical contacts to the device. Conversely, at T$= 200$ K and below, no zero-field response was measurable above the noise-floor of our current spectrometer setup.

For temperatures below 280 K, the overall zero-field response is best described using only two Lorentzians instead of the three Lorentzians previously applied in Fig. 6.5(b) at room temperature, corresponding to the disappearance of S3. Generally, the amplitudes of the individual Lorentzians fitted to

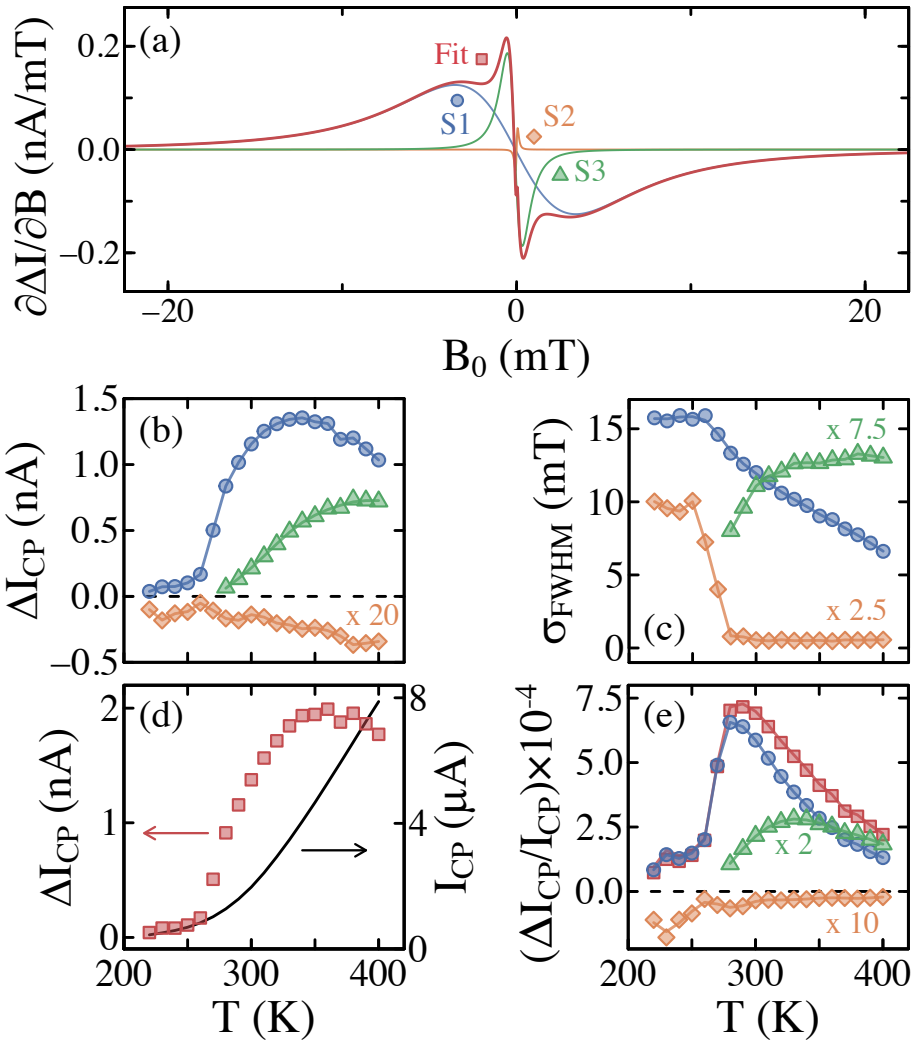

Fig. 6.11.: (a) Individual and overall fits to the experimental data reproduced from Fig. 6.5(b) and their corresponding symbols referred below in (b)-(e). (b) Signal amplitude, ΔI_{CP}, and (c) full width at half maximum, σ_{FWHM}, of each individual component extracted from the fits to the experimental data, as a function of temperature. (d) CP current measured at $V_{LO} = -4.6$ V (solid line) and the overall signal amplitude (symbols) calculated from the sum of each individual fit versus temperature. (e) Relative magnetoresistance of each individual component and overall fit as a function of temperature. The coloured solid lines are guides for the eye and errors bars are smaller than symbols. For comparative purposes, smaller values are multiplied by the factors indicated in (b)−(e).

the zero-field response increases with temperature and saturates at elevated temperatures. Upon saturation, only the amplitude for S1 appears to slightly decrease above T$= 350$ K, which contributes to a slight decrease in the

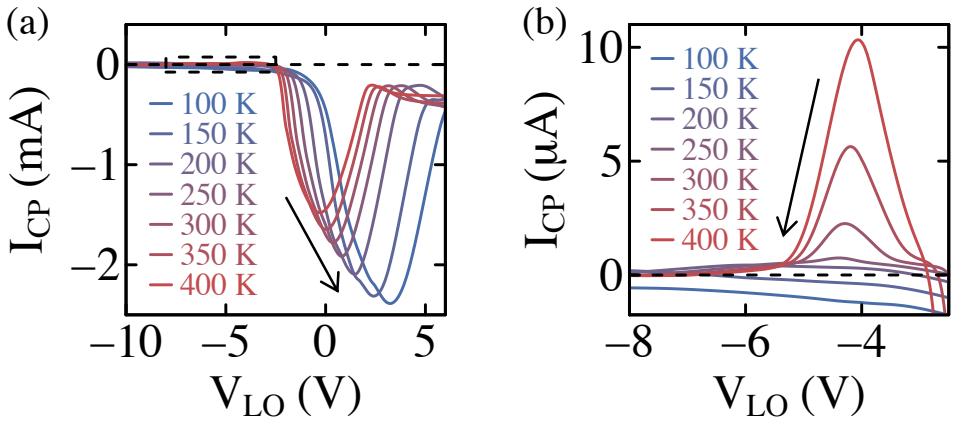

Fig. 6.12.: (a) Series of CP curves as a function of temperature in 50 K increments between $100 - 400$ K. In addition to an increase in the magnitude of the CP current, the CP curve shifts toward positive voltages with decreasing temperature. (b) Magnification of the region in (a) indicated by the black dashed box, revealing the positive CP feature decreases in amplitude and disappears completely below 200 K due to carrier freeze-out. Furthermore, the positive CP feature shifts toward negative voltages with decreasing temperature, opposite to the main CP curve in (a).

amplitude of the overall zero-field response in Fig. 6.11(d) as S1 has the largest contribution to the overall response. This saturation behaviour at elevated temperatures is not observed in the CP current (black curve in Fig. 6.11(d)) where the CP current monotonically increases with temperature. In the normalised signal contrast in Fig. 6.11(e), a heavy attenuation in the normalised signal contrast is observed for S1 and the overall zero-field response above T > 290 K, whereas the normalised signal contrast of S3 decreases at slightly higher temperatures above T > 350 K.

From standard CP theory, a decrease in temperature corresponds to an increase in the CP energy window following Eq. 6.2, with the thermal velocity and intrinsic carrier concentration in the denominator proportional to temperature. Furthermore, the thermal emission process is heavily suppressed at lower temperatures, further enhancing the CP current [207]. This standard CP dependence is not observed in Fig. 6.11(d) (black curve) and instead the opposite dependence is observed. To investigate this anomalous dependence in more detail, a series of CP curves was taken between $100 - 400$ K in 50 K increments and these are shown in Fig. 6.12. The standard CP temperature dependence is observed in Fig. 6.12(a) for the negative-valued CP peak corresponding to the p^-/SiO_2 interface, accompanied by a broadening

and shift to positive voltages with decreasing temperature. In contrast, the positive-valued CP feature in Fig. 6.12(b) reduces in amplitude, disappears, and becomes negative in value below approximately 200 K, corresponding to the disappearance of the zero-field response in Fig. 6.10. This reduction in the positive-valued CP feature is accompanied by a shift to negative voltages, in the opposite direction to the CP peak voltage shift observed in Fig. 6.12(a).

We speculate that this anomalous CP temperature response for the positive-valued peak is a consequence of the rapid decrease in free charge carrier concentration in the n-epilayer that are able to participate in the CP process with decreasing temperature until complete carrier freeze-out occurs at approximately 200 K [213]. This effect has a stronger dependence on temperature than the thermal emission process and the widening in the CP energy window in Eq. 6.2. As such, at the n-epilayer/SiO_2 interface, the observed temperature dependence of the positive-valued CP feature is dominated by carrier freeze-out effects rather than the temperature dependence of the CP process. In contrast, carrier freeze-out effects at the p^-/SiO_2 interface are negligible as the source wells are heavily doped such that standard CP characteristics are retained at low temperatures.

The voltage shift in the position of the positive-valued CP feature revealed in Fig. 6.12(b) indicates a change in the device characteristics at the n-epilayer/SiO_2 interface. Particularly, both V_{FB}^{epi} and V_{TH}^{epi} are shift toward negative voltages with decreasing temperature by approximately -0.5 V over the entire temperature range swept between $210 - 400$ K. We note that this dynamic voltage shift with temperature was not taken into account when tuning the device for the zero-field response measurements, which may have contributed to the observed heavy attenuation in the normalised zero-field response above T$= 300$ K in Fig. 6.11(e). Future measurements involving the zero-field response monitored over a large temperature range will have to take this dynamic change in the threshold and flatband voltages into account to determine whether this effect alone can fully account for the observed dependence in Fig. 6.11(e).

In the context of magnetometry, the large variability in the zero-field response with respect to temperature (and CP parameters) suggests a large degree of tunability. For example, the device sensitivity to magnetic fields, proportional

to the signal amplitude and inversely proportional to the linewidth, can be maximised when operating the device at approximately T$= 360$ K. However, this also suggests that the device sensitivity is not constant with temperature and any slight fluctuation in temperature will require appropriate adjustments to the device settings. Alternatively, a temperature controlled environment via a feedback loop, for example, may be implemented to stabilise the magnetic field sensitivity. We also note that due to the presence of the ultra-small magnetic field feature (S2), the slope of the overall zero-field response is not linear. Instead, the zero-field response exhibits a linear response within a reduced magnetic field range defined by the linewidth of the ultra-small magnetic field feature.

Similar to the bias dependence observed in Fig. 6.6(c), the linewidth of each Lorentzian component has its own unique dependence on temperature, as indicated in Fig. 6.11(c). Generally, the linewidths of both S1 and S2 appear to increase with decreasing temperature until they reach a saturation value below approximately 250 K, whereas the linewidth of S3 increases with increasing temperature and saturates above 330 K. Of particular interest is the S1 linewidth, which exhibits a near linear dependence on temperature between T$= 260 - 400$ K.

Similar dependences have been previously observed for the zero-field splitting of several optical spin defect systems, including the NV center in diamond [214, 215], an unidentified defect in SiC [216], and the boron vacancy in hexagonal boron nitride (hBN) [217], in which the peak position under zero magnetic field changes with temperature as the EM excitation frequency is scanned through resonance. The underlying mechanism responsible for the temperature-dependent zero-field splitting parameter is attributed to the local lattice expansion and compression of the host semiconductor crystal induced by variations in the temperature [215], which has a r^{-3} separation dependence between the substitutional N atom and the C vacancy that form the NV center in diamond for example, following Eq. 3.47. A similar r^{-3} separation dependence between the electron and nuclear spin is also present in the electron-nuclear dipolar interaction in Eq. 3.41 that forms part of the hyperfine interaction, which may help explain the observed linewidth dependence of S1 on temperature for the zero-field response, although theoretical calculations are required to confirm this interpretation.

Regardless of its origin, upon closer inspection within the temperature range between T$= 300 - 400$ K shown in Fig. 6.13(a), a linear fit to the data reveals a rate of change in the linewidth of dσ_{FWHM}/dT$= -51.85 \pm 1.13$ μT/K. In units of frequency, the rate of change in the linewidth, also known as the coupling coefficient β, is equal to -1.452 ± 0.032 MHz/K, assuming $g \sim 2$. We note that the linewidth starts to deviate from linearity below 300 K and thus this region was avoided in the linear fit procedure. Within the temperature range considered for the fitting procedure, the residual error between the linear fit and the measured data was maintained within $\sim \pm 0.2$ mT ($\sim \pm 5.6$ MHz), as shown in Fig. 6.13(b). The extracted coupling coefficient is comparable to the thermal shift determined for an unidentified optical spin defect previously discovered in SiC ($\beta = -1.1$ MHz/K [216]) and significantly larger than the thermal shift of the NV centre in diamond ($\beta = -74.2$ kHz/K [214]). Furthermore, the extracted coupling coefficient is slightly larger than the thermal shift of the boron vacancy in hBN ($\beta = -623$ MHz/K [217]).

The temperature sensitivity of the device can be calculated analogous to the magnetic field sensitivity introduced in Sec. 5.3.2 with the coupling coefficient

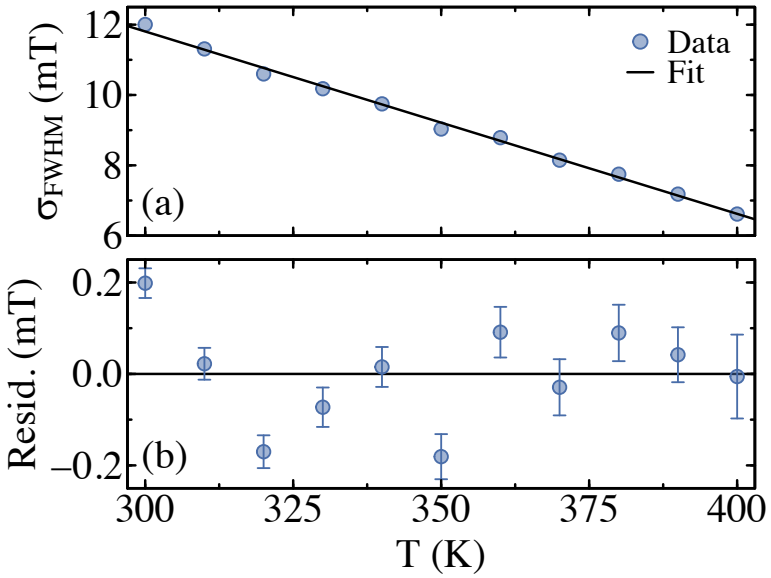

Fig. 6.13.: (a) Extracted FWHM linewidth of the S1 component fitted to the zero-field response as a function of temperature. The coupling coefficient is determined from a linear fit to the data and is equal to dσ_{FWHM}/dT = -51.85 $\pm$ 1.13 µT/K. (b) Residual error between the experimental data and the fit in (a).

providing a direct link between magnetic field and temperature. Thus, the temperature sensitivity utilising lock-in detection is

$$\frac{\delta T_{min}}{\sqrt{\Delta f}} = \frac{\sigma_{\mathrm{stddev}}}{\beta \delta \sqrt{\mathrm{ENBW}}}\,, \tag{6.4}$$

where σ_{stddev} is the standard deviation from the lock-in output and δ is the slope of the zero-field response. Plugging in the appropiate values ($\sigma_{\mathrm{stddev}} = 3.47$ pA/mT, $\delta = -0.064$ nA/mT^2, ENBW$= 0.417$ Hz) with the standard deviation and ENBW extracted from a separate lock-in measurement of the zero-field response (not shown), the temperature sensitivity at room temperature is approximately $\sim 1.614 \pm 0.035\ \mathrm{K}/\sqrt{\mathrm{Hz}}$. This value is comparable to the temperature sensitivity of the unidentified optical spin defect in SiC ($\sim 1\ \mathrm{K}/\sqrt{\mathrm{Hz}}$ [216]), slightly more sensitive than the boron vacancy in hBN ($\sim 3.82\ \mathrm{K}/\sqrt{\mathrm{Hz}}$ [217]), and much less sensitive than the NV center in diamond ($\sim 0.76\ \mathrm{mK}/\sqrt{\mathrm{Hz}}$ [218]). Despite having the smallest coupling coefficient, the NV center in diamond offers the best temperature sensitivity as a result of its superior signal contrast, which has been further optimised by utilising pulse protocols where the sensitivity far exceeds standard cw operation and approaches the spin projection noise limit. In order to fully leverage the vastly larger coupling coefficient of the measured device for high sensitivity temperature sensing, a much larger zero-field response is required.

6.6 Summary and conclusion

In this chapter, we were able to demonstrate that spin-dependent charge pumping is measurable in a commercial SiC power MOSFET adopting a VDMOS device structure. The subtle intricacies and differences in the CP response due to the more complex device structure compared to a conventional 4-terminal lateral transistor were outlined and explained in terms of standard CP theory. For VDMOS structures, standard CP theory is only valid over a limited voltage range probing the epilayer/SiO_2 interface, whereas analysis of the channel/SiO_2 interface is made difficult by the addition of a

large channel current as the transistor is switched on. As a result, analysis at this interface is generally avoided.

Paramagnetic defects at the n-epilayer/SiO_2 interface was then probed on application of an external magnetic field, where the hyperfine-induced spin-mixing response was interrogated, subject to changes in the CP settings and variations in temperature. The zero-field response was measurable within a large temperature range between $200 - 400$ K. Furthermore, the overall zero-field response was adequately modelled by a sum of three Lorentzians all centred around zero magnetic field above 280 K, with an ultra-small magnetic field feature described using a Lorentzian function negative in sign. At low temperatures below 280 K, the lineshape of the zero-field response drastically changes and is instead described by the sum of two Lorentzians functions.

A close correspondence between the zero-field response and the CP current was generally observed, confirming that the same paramagnetic defects contribute to both processes. However, at low temperatures and at CP high frequencies where effects due to the incomplete ionization of N donors in the n-epilayer become non-negligible, the close correspondence between the zero-field response and the CP current start to deviate. These effects will have to be taken into account for future applications utilising the zero-field response.

An intriguing linear response was observed between the linewidth of S1 and temperature. Analogous to the temperature-dependent zero-field splitting parameter seen in several $S > 1/2$ optical spin defects with a similar response due to changes in the dipole interaction distance from local lattice expansion and compression, we tentatively attribute the observed dependence to the electron-nuclear dipolar interaction in the hyperfine interaction Hamiltonian. A coupling coefficient of -1.452 ± 0.032 MHz/K was determined from a linear fit over a reduced temperature range between $300 - 400$ K, corresponding to a temperature sensitivity of $\sim 1.614 \pm 0.035\ \mathrm{K}/\sqrt{\mathrm{Hz}}$ at room temperature. These values are quite competitive to other optical spin defect systems, but further theoretical work is required to understand the origin of this effect to fully realise its potential.

Coherent Spin Manipulation and Detection

7

In this final experimental chapter, we present results on coherent spin dynamics of a small ensemble of intermediate spin-pairs in a SiC junction diode using pulsed-EDMR. A lock-in detection scheme based on a three stage modulation cycle is implemented, significantly enhancing the signal-to-noise ratio and reducing the measurement acquisition time. This allowed us to explore various pulse protocols previously developed for pulsed-ESR to characterise the fundamental spin dynamics of the spin-pair ensemble, including Rabi spin precession, spin dephasing, and spin decoherence. DC and AC magnetometry protocols based on spin dephasing and spin decoherence measurements, respectively, are evaluated.

7.1 Introduction

The ability to measure the spin state of a spin system and trace its coherent spin dynamics over time is a key prerequisite [2] for donor-based quantum computing [1]. In addition, the phase accumulated during the spin state evolution of the spin system due to non-uniform external magnetic fields forms the basis of both DC and AC magnetometry protocols based on the Ramsey and Hahn-echo pulse sequence, respectively [13, 30]. Existing pulsed-ESR (pESR) techniques typically employed to observe coherent spin motion are not feasible for the readout of a small ensemble of spins in a fully fabrication device encapsulated with metallic contacts. Instead in this final experimental chapter, we leverage the pulse protocols developed for pESR and the high sensitivity of EDMR to characterise the spin dynamics of the tentatively ascribed fabrication-induced paramagnetic defect measured in the SiC junction diode device introduced in Chapter 5 using pulsed-EDMR (pEDMR).

To successfully perform pEDMR on our spectrometer setup at room temperature, a multi-stage lock-in modulation measurement scheme is developed,

vastly improving the signal-to-noise ratio (SNR) and substantially reducing the acquisition time. In short, the measurement scheme modulates the magnetic field in and out of resonance, amplitude modulates the resonant excitation pulse sequence, and phase modulates the resonant excitation pulse in which the spin state rotation on the Bloch sphere is manipulated. The enhanced sensitivity of the lock-in detection scheme employed allowed us to study the coherent spin dynamics of a small ensemble of spin-pairs on the order of $10^2 - 10^3$ in the SiC junction diode at room temperature. At low magnetic fields where all measurements were carried out, Rabi oscillations exhibited an additional second harmonic spin-beating component in which the weakly coupled electron spins in the intermediate spin-pair are non-selectively excited simultaneously at resonance. Signs of exponential decay in the integrated charge were observed after applying the Ramsey and Hahn-echo pulse sequence, which was then used to determine the average spin dephasing time, $T_2^\star$, and the average transverse spin decoherence time, T_2, respectively, of the ensemble spin-pair. These rather surprisingly long characteristic time constants at room temperature suggest that the implementation of electrically detected Ramsey based DC and Hahn-echo based AC sensing protocols are feasible with SiC.

In the following section, a brief historical overview and literature review of the pEDMR technique will be presented. This will be followed by a background theory section on the different pulse sequences considered in this chapter and the spin state evolution at different stages of each pulse sequence is described using Bloch sphere representation.

7.2 Literature review

Currently, only a select few highly optimised quantum systems have been studied using pEDMR, including the ^{31}P$-$Pb spin-pair at cryogenic temperatures [29, 126, 150, 219–221], spin-pairs in microcrystalline Si [28, 222], and electron-hole exciton spin-pairs in organic semiconductors [22, 211, 223–228] at room temperature. To the best of our knowledge, intermediate spin-pairs involved in the SDR process have not yet been studied using pEDMR in SiC. Instead, individual colour centres in wide bandgap semiconductors like diamond and SiC have been studied extensively with pulsed-ODMR

(pODMR) [38, 41, 105, 151, 169, 229–231]. More recently, hybrid optical initialisation and electrical readout pulsed magnetic resonance measurements have also been demonstrated, although the spin readout mechanism relies on the spin-dependent photoionisation process instead [94, 119, 152, 232, 233]. This new hybrid approach is sometimes referred to as pulsed photoionisation detected magnetic resonance (pPDMR).

Historically, the pEDMR technique was not successfully implemented until the turn of the century [28] years after pESR and pODMR had already been established. Several reasons have contributed to this delay, mainly due to the many experimental challenges associated with delivering high power electromagnetic (EM) irradiation to the conductive, and therefore absorbing, semiconductor device and the limited time resolution of the transimpedance preamplifier used to detect small spin-dependent current transients ($\sim$pA$-$nA) on the $\mathrm{ns} - \mu\mathrm{s}$ timescale. The development of the time-domain theory of SDR by Boehme and Lips in 2003 [137] revealed that spin dynamics of the spin state occurring on the ns time-scale can be reconstructed from the incoherent current transient after resonant pulsed excitation occurring on the μs time-scale (see Sec. 3.5 for full derivation). Thus, it was realised that the pEDMR technique was experimentally possible despite the limited bandwidth far below the MHz range ($\sim \mu\mathrm{s}$) for nA/V sensitivity even with today's state of the art transimpedance preamplifiers. Furthermore, careful device structure design utilising interdigited contacts to maximise the amplitude of the current transient response [149] partially alleviated the gain-bandwidth trade-off.

While the spin dynamics are retrievable from the current transients, these measurements strongly suffer from large low frequency noise and non-resonant background signals induced by the applied high power pulsed EM irradiation. The amplitude often greatly exceeds the spin-dependent signal of interest, requiring additional off-resonant background measurement and subtraction to reveal the actual spin-dependent response (see Sec. 4.3.1). This effectively doubles the acquisition time and limits the SNR [29]. Furthermore, magnetoresistance effects in which the measured current response is dependent on the magnetic field may lead to errors in the offset correction, requiring the implementation of non-trivial field-dependent background corrections.

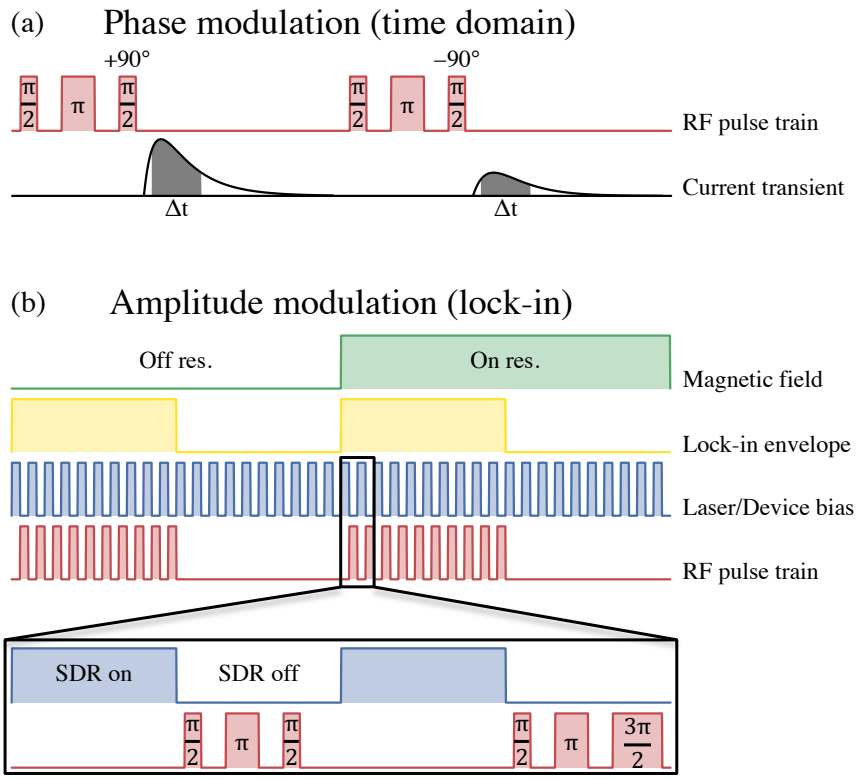

Fig. 7.1.: Illustration of (a) the phase cycling lock-in detection scheme in the time-domain introduced by Hoehne et al., [29] in comparison with the (b) modified amplitude modulated lock-in detection scheme used in this chapter for the spin-echo pulse sequence. The amplitude modulation of the pulse sequence with lock-in detection partially alleviates the temporal resolution required for transient measurements and the limited bandwidth of the transimpedance preamplifier, while alternating the spin projection pulse between $\pi/2$ and $3\pi/2$ achieves a similar phase cycling effect as a $180°$ phase shift in (a).

For pEDMR measurements utilising multi-pulse protocols, Hoehne et al. [29] demonstrated an effective lock-in detection scheme based on a two-step phase cycling previously developed for pESR, improving the SNR by one order of magnitude while cancelling out the non-resonant background signals. A visual representation of the technique is shown in Fig. 7.1(a) using a modified $\pi/2 - \tau_1 - \pi - \tau_2 - \pi/2$ spin echo pulse sequence as an example. The modified spin echo pulse sequence will be properly defined later in Sec. 7.3.2. We note that the modified spin echo pulse sequence introduces an additional $\pi/2-$pulse at the end of the pulse sequence for spin readout (see Sec. 7.3 for more details) compared to the standard spin echo pulse

sequence employed in pESR. The last $\pi/2$ spin projection pulse is alternated between $\pm 90°$, forming an effective overall $2\pi-$pulse for $+90°$ phase and an effective overall $\pi-$pulse for $-90°$ phase. By subtracting the integrated charge of the current transient over time interval $\Delta t = t_2 - t_1$ between the two traces of opposite phase (i.e., $\Delta Q = \frac{1}{q}\int_{t_1}^{t_2} \Delta I dt$), leading to an overall $+180°$ phase shift, and repeated over N repetitions, a lock-in amplification effect is achieved without using an actual lock-in amplifier. As will be seen in the following section, the phase modulation in the Bloch sphere representation corresponds to a spin state rotation in the opposite direction. The introduction of phase cycling and the enhanced SNR was crucial in fully realising the wide range of multi-pulse protocols previously developed with NMR and pESR for pEDMR, with more recent publications successfully demonstrating electrically-detected spin inversion recovery used to measure T_1 spin-lattice relaxation time [150], electron nuclear double resonance (ENDOR) [234], and double electron electron resonance (DEER) [235] for example.

Highly specialised test instruments are required to implement the phase-cycled pEDMR technique, including an in-phase and quadrature (IQ) modulator or a phase shifter for phase cycling, fast data acquisition card with ns time resolution for the boxcar integration of the captured current transient, and a ≥ 1 kW travelling wave tube (TWT) amplifier to generate high power $\pi-$pulses on the order of tens of ns. The majority of these instruments can be found in existing commercial pESR spectrometers operating at X-band frequencies, which can be modified for electrical detection. However, the additional increase in cost and complexity of the magnetic resonance setup in comparison to standard cwEDMR further reduces an already small handful of highly specialised laboratories globally that are able to perform such measurements. Some of these challenges can be circumvented by taking advantage of the fact that SDR is independent of spin polarisation such that pEDMR can be performed at low magnetic fields and at RF frequencies. As such, the TWT amplifier can be replaced with a more commercially available and budget friendly solid-state RF amplifier.

To overcome the requirement of a ns resolution fast data acquisition card and the limited bandwidth of the transimpedance preamplifier, we draw inspiration from a commonly used technique in pODMR and pPDMR utilising amplitude modulation of the EM excitation pulse sequence with a lock-in amplifier

and modify it for electrical spin readout. A schematic of the amplitude modulation lock-in detection scheme is shown in Fig. 7.1(b) again using the same modified spin-echo pulse sequence as an example. The pulse sequence is repeated and encoded within an envelope typically on the ms timescale within the bandwidth of the transimpedance preamplifier for lock-in detection, while the device bias is square-wave modulated between when recombination is maximised and minimised, analogous to pulsed illumination for spin ground state initialisation and spin readout in pODMR. Modulation of the device bias is well separated from the pulse sequence in the time-domain to avoid and remove EM irradiation-induced non-resonant current transient background response. Furthermore, the device bias in the on state after the pulse sequence defines the boxcar integration window such that the output of the lock-in amplifier is proportional to the change in integrated charge after resonant pulse excitation. Additional non-resonant background subtraction is performed by taking an extra off-resonant measurement for baseline offset correction. Lastly, for multi-pulse sequences, the final spin projection pulse is alternated between a $\pi/2$ and $3\pi/2$ pulse, creating a similar phase cycling effect seen in Fig. 7.1(a).

7.3 Background

The observation of Rabi oscillations that reflect the spin-pair population in either the triplet or singlet state is a key pre-requisite required to coherently drive the spin system, typically defined by the $\pi-$pulse length. In combination with the $\pi/2-$pulse length, these two pulse durations serve as fundamental building blocks for all multi-pulse protocols. Of particular interest for the application of magnetometry is the Ramsey and Hahn-echo pulsing sequence, which will be considered in this work. In this section, the spin state evolution in time at different stages of the Ramsey and Hahn-echo pulse sequence will be explored using Bloch sphere representation, which will demonstrate how these pulse sequences can be used for sensing external DC and AC magnetic fields, respectively.

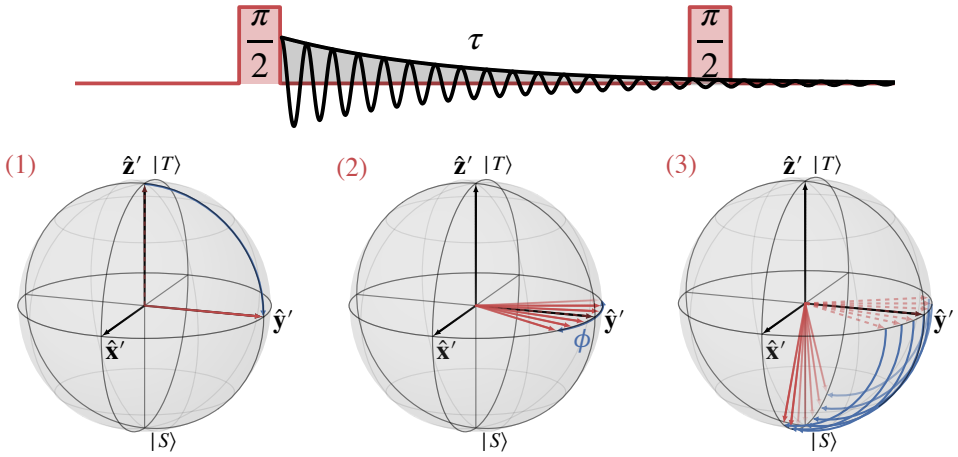

Fig. 7.2.: Schematic of the Ramsey pulse sequence and the spin-pair response at three different stages of the sequence on the Bloch sphere labelled between $(1) - (3)$. Refer to the main text for more detail.

7.3.1 Free induction decay

In classical magnetism, the Ramsey pulse sequence is equivalent to measuring the free induction decay (FID) of an ensemble of spins in which the transverse component of the electron or nuclear spin magnetization precesses about the longitudinal external magnetic field at the Larmor frequency. Due to inhomogeneity in the external magnetic field, the spin-pair ensemble precesses at different rates and undergoes an exponential decay characterised by the spin dephasing time constant, $T_2^\star$. As a result, the phase relationship within the spin-pair ensemble becomes unknown.

A schematic of the Ramsey pulse sequence is shown in Fig. 7.2. For an ensemble of spin-pairs, a $\pi/2-$pulse first rotates the spin-pair state vector by 90° on the Bloch sphere to the transverse $\hat{\mathbf{x}}' - \hat{\mathbf{y}}'$ plane to create a superposition of triplet and singlet states. During the free evolution time, τ, each spin-pair within the ensemble precesses about their own Larmor frequency as each spin-pair experiences a slightly different magnetic field strength with spin-pairs experiencing a larger external magnetic field precessing at a faster rate, resulting in a dephasing represented as a spreading of the state vector on the Bloch sphere in the transverse $\hat{\mathbf{x}}' - \hat{\mathbf{y}}'$ plane. This spreading can also

be thought as a phase accumulated proportional to the external magnetic field component parallel to the spin defect axis under consideration [30]

$$\phi = \gamma \int_0^\tau B_\parallel(t)dt \,. \tag{7.1}$$

As the SDR readout mechanism relies on the spin symmetry between the two spins in the spin-pair, a second $\pi/2-$pulse is required to project the spin-pair state back onto the $\hat{\mathbf{z}}'$ axis. The FID can then be reconstructed by measuring the signal response as a function of τ with the integrated charge proportional to the accumulated phase and hence the parallel external magnetic field component. When operating slightly detuned from the resonance condition, the FID response is superimposed with oscillations corresponding to the beating of the spin precession with the EM field. By taking the Fourier transform of the oscillating FID signal, the location of the Fourier frequency component will reveal the deviation from the resonant magnetic field.

For multi-pulse protocols utilising a $\pi/2$ spin projection pulse for spin readout, phase cycling can be implemented to enhance the SNR. The spin projection pulse is alternated between a $\pi/2$ and $3\pi/2$ pulse, which effectively forms an overall π and 2π pulse, respectively, for the Ramsey pulse sequence. Equivalently, the ensemble spin state initially in the triplet parallel configuration transitions into the singlet anti-parallel configuration after an overall $\pi-$pulse Ramsey sequence, whereas the initial spin state population in the triplet state remains unchanged after an overall $2\pi-$pulse Ramsey sequence. Subtraction of the two signals normalised yields a change in the integrated charge proportional to the fractional difference between spin-pairs in the anti-parallel and parallel configuration after the Ramsey pulse sequence ($\Delta Q \propto (n_{ap} - n_p)/(n_{ap} + n_p)$).

7.3.2 Spin-echo

The Hahn-echo pulse sequence is an extension of the Ramsey sequence by introducing a $\pi-$pulse between the first and second $\pi/2$ pulse. A schematic of the spin echo sequence is shown in Fig. 7.3. Again, the first $\pi/2-$pulse rotates the spin-pair state vector by $90°$ on the Bloch sphere to the transverse $\hat{\mathbf{x}}' - \hat{\mathbf{y}}'$ plane to create a superposition of triplet and singlet states

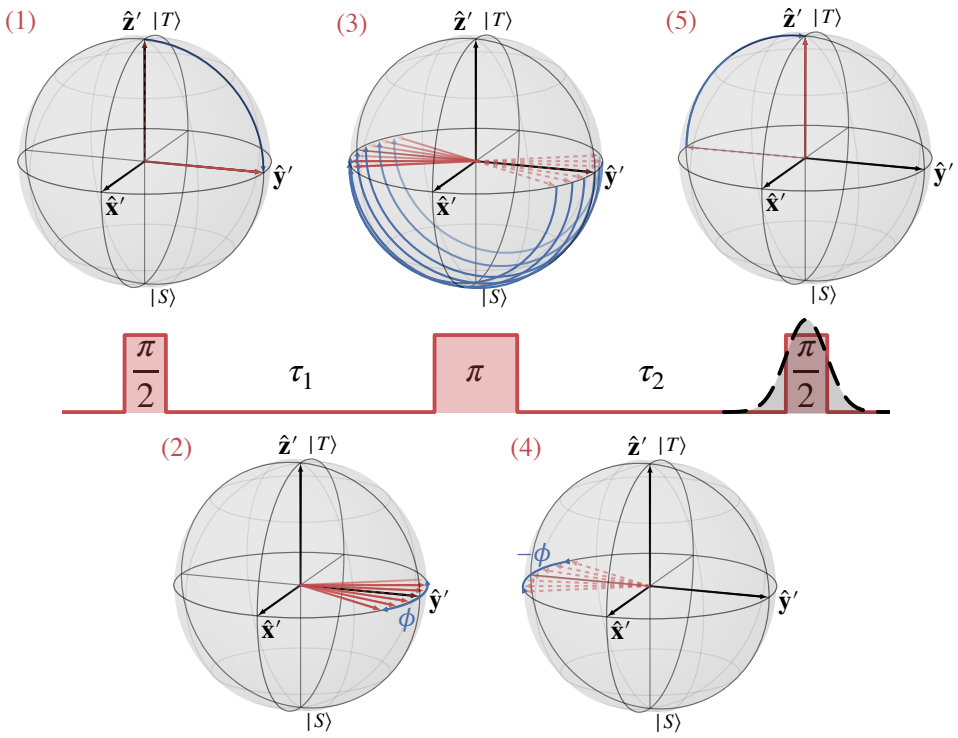

Fig. 7.3.: Schematic of the Hahn-echo pulse sequence and the spin-pair response at five different stages of the sequence on the Bloch sphere labelled between $(1)-(5)$. Refer to the main text for more detail.

in which phase is accumulated over a fixed arbitrarily free evolution time, τ_1. A $\pi-$pulse is then used to refocus and flip all spin-pairs by $180°$ about the $\hat{\mathbf{x}}'-$axis, inverting the phase acquired during τ_1. Now, spin-pairs in the ensemble experiencing a larger external magnetic field lag behind those experiencing a smaller external magnetic field. As a result, the relative phase accumulated cancels out when the free evolution time after the refocusing pulse is equal to the free evolution time before the refocusing pulse ($\tau_2 = \tau_1 = \tau$) and a spin-echo is formed [30]

$$\phi = \gamma \left[\int_0^{\tau_1} B_{\parallel}(t)dt - \int_{\tau_1}^{\tau_2} B_{\parallel}(t)dt \right]. \tag{7.2}$$

Only AC magnetic fields along the spin defect axis oscillating at an even multiple of the free evolution time ($\omega_{AC} = \pi/\tau$) are detected, whereas the phase accumulated during the two free precession times due to slow varying

DC magnetic fields are of opposite sign and are hence filtered out. Again, for electrical spin readout, a final $\pi/2-$pulse is required to project the spin-pair state back onto the $\hat{\mathbf{z}}$ axis and the spin projection pulse is alternated between $\pi/2$ and $3\pi/2$ to form an effective 2π and 3π pulse, respectively, for phase cycling. Subtraction of the signal measured from the effective $3\pi-$pulse from the effective $2\pi-$pulse yields a change in integrated charge proportional to the fractional difference between spin-pairs in the anti-parallel and parallel configuration after the spin-echo pulse sequence ($\Delta Q \propto (n_{ap} - n_p)/(n_{ap} + n_p)$).

The decay in the spin echo amplitude characterised by the spin-spin relaxation time constant, T_2, can be reconstructed by setting $\tau = \tau_1 = \tau_2$ and monitoring the echo amplitude decrease as a function of τ. Unlike the $T_2^\star$ time characterised by spin dephasing within the spin-pair ensemble, the decoupling $\pi-$pulse in the spin echo sequence filters out and leaves behind only irreversible dephasing effects that lead to pure spin decoherence. As such, $T_2^\star$ serves as a lower limit for T_2 and T_2 can exceed $T_2^\star$ by several orders of magnitude. By monitoring the integrated charge proportional to the phase accumulated due to AC magnetic fields at a fixed free evolution time, the AC magnetic field amplitude can be reconstructed. Ultimately, the DC and AC magnetometry sensitivity is limited by the $T_2^\star$ and T_2 time, respectively, of the quantum sensor used.

7.4 Methods

The results presented in this chapter have been carried out on the same 6H-SiC junction diode studied in Chapter 5 with a circular metallic front contact not optimal for pEDMR measurements. A summary of the device structure and characteristics can be found in Sec. 5.4. pEDMR measurements were conducted using the modified low-field spectrometer setup described in Sec. 4.3.

For the time-domain pEDMR measurements, a $\tau_p = 4\,\mu\text{s}$ and $P_{RF} = 950$ mW RF pulse was used. Estimation of the RF power takes into account the insertion loss of the SMA cables and RF switches used when appropriate. A long RF pulse was required to induce a large enough current transient

response detectable with the measurement setup and settings used as the SNR for the current transient in response to RF pulses on the ns timescale was too low even at higher powers. The current transients were recorded using a Femto-DLPCA-200 high-speed transimpedance preamplifier on the 10^7 V/A gain setting with a rise/fall response time of 7μs. Further amplification by a factor of 20 and high-pass filtering ($f_{-3dB} = 300$ Hz) was applied using a SR560 voltage preamplifier and a Tektronix TDS3052B oscilloscope was used to digitize 100 μs long transient responses at a 10^8 samples/sec acquisition rate (10 ns resolution). At each magnetic field increment, the transient was averaged over 2.56×10^4 accumulations, taking approximately four minutes to acquire and average.

For the pEDMR measurements using the modified lock-in detection scheme, the lock-in modulation frequency was set to ~ 178.57 Hz (period $= 5.6$ ms). Within the modulation envelope, the device bias modulation frequency was set to 50 kHz (period $= 20$ μs) and the RF pulse sequence was applied during the 10 μs off state of the square-wave modulated device bias where recombination current is negligible. A fixed constant delay of 800 ns was introduced between the end of the pulse sequence and the on state of the square-wave modulated device bias. This ensures that the total number of device bias modulation and RF pulses are constant within each half cycle of the lock-in envelope as the measurement variable is varied (i.e., τ_p in a Rabi measurement and τ in a Ramsey and Hahn-echo measurement) [151]. In this case, the device bias modulation and RF pulse sequence was repeated 280 times within each half cycle of the lock-in envelope with the signal strength directly proportional to N repetitions. SDR was switched on and off by square-wave modulating the device bias between -2.25 V and -1.50 V, respectively. As the device bias was now AC modulated, the biases were chosen to take into account the increase in the device impedance measured at 50 kHz using an LCR meter (HP4284A) such that the device current approximately matches the DC IV characteristics in Fig. 5.5(b). The lock-in output was recorded by alternating the magnetic field strength on and off resonance between $\mathrm{B}_0 = -9.31$ mT and $\mathrm{B}_0 = -3.22$ mT, respectively, and an additional set of data were recorded for multi-pulse measurements with the spin projection pulse alternated between $\pi/2$ and $3\pi/2$ for phase cycling. Subtraction of the phase-cycled and magnetic field modulated lock-in outputs were performed post-processing.

7.5 Results and discussion

Figure 7.4(a) displays a corrected two-dimensional map of the device current in response to a RF pulse as a function of time and magnetic field after non-resonant background correction. Here, $t = 0\ \mu s$ is defined $7\ \mu s$ after the RF pulse is switched off to account for the limited rise/fall response time of the transimpedance preamplifier for the particular gain setting used. A resonance is observed at $B_0 = -9.31$ mT and more clearly in Fig. 7.4(c) where a time slice of the two-dimensional plot is taken at $t = 5.5\ \mu s$. In addition, a small linear offset is observed due to the hyperfine-induced spin-mixing response.

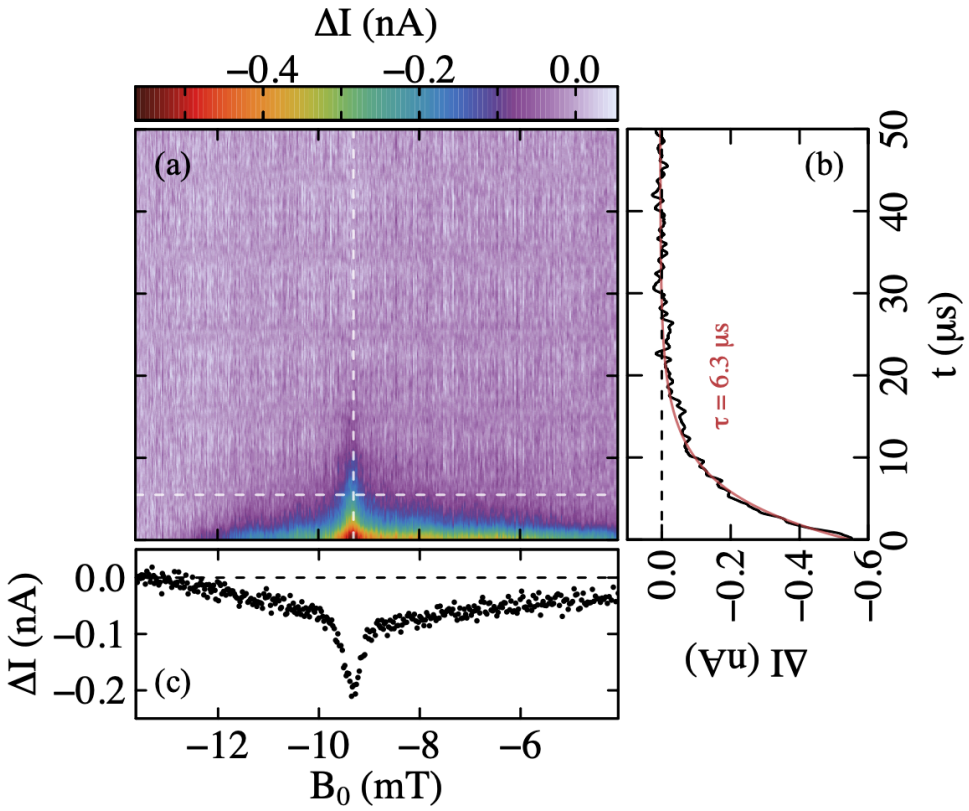

Fig. 7.4.: (a) Two-dimensional map of the current transient in response to a $P_{RF} = 950$ mW and $\tau_p = 4\mu s$ long RF pulse as a function of magnetic field after a background offset correction to remove any high power RF artefacts. (b) In resonance (vertical dotted white line), a current transient with a time constant of $\tau = 6.3\ \mu s$ is observed. (c) Time slice of the two-dimensional plot taken at $t = 5.5\ \mu s$ (horizontal dotted white line), revealing a quenching in the measured current in resonance at $B_0 = -9.31$ mT.

The pEDMR spectrum is consistent with the cwEDMR measurement taken in Fig. 5.6(b), but also highlights that a simple off-resonant background subtraction cannot entirely remove the non-resonant spin-mixing response in the measured spectrum. In the time-domain in Fig. 7.4(b), the current transient at resonance is described by a single exponential decay with a time constant of $t = 6.3\ \mu$s. The (negative) quenching current transient response measured corresponds to an increase in the singlet content and the number of recombination events in resonance, leading to a decrease in free charge carrier density and the measured overall device conductivity [137]. Additional spin-dependent transport pathways that can introduce (positive) enhancement current transient responses commonly found in organic semiconductors [223, 224, 236] were not observed, removing any potential integration window dependences when exploring pEDMR utilising lock-in detection.

A SNR of ~ 19 was found for the pEDMR measurement presented in Fig. 7.4 with signal averaging, which is mainly limited by low-frequency flicker noise [29]. As a result, no Rabi oscillations were observed with this particular experimental setup, a key pre-requisite for multi-pulse measurements. Lock-in detection was then implemented and the vast improvement in SNR can be clearly seen in Fig. 7.5(a) for a single pEDMR scan taking approximately 200 s. For this measurement, a shorter RF pulse length and higher RF power of $\tau_p = 60$ ns and $P_{RF} = 25$ W were used, respectively, and a SNR of ~ 23 was achieved. In addition, non-resonant background due to the hyperfine-induced spin-mixing effect was entirely removed, allowing detailed analysis of the spin resonance response. Further enhancement in the SNR was achieved after averaging over 750 individual magnetic field sweeps and the averaged pEDMR spectrum is shown in Fig. 7.5(b). The measured response is now expressed in terms of a change in the integrated charge ΔQ over a $10\,\mu$s integration window after the RF pulse, which reflects the relative change in singlet state density [137]. For this particular measurement, the average resonance peak amplitude is equal to around $\Delta Q = 3615$ charges, equivalent to the number of spin flips induced and measured during resonance. Off resonance, the noise floor corresponding to the detectable spin limit, is approximately 13 spins (SNR ~ 278). The current sensitivity achieved using lock-in detection shows promise in studying an even smaller ensemble of spin-

pairs through further optimisation and single spin readout may be possible using smaller device structures.

Focusing on the spin resonant signal at positive magnetic fields in the inset of Fig. 7.5(b), the signal was found to be best described by two Gaussians usually associated with an intermediate spin-pair system involving two spins coupled to different nuclear spin surroundings [227]. Following a resonant pulse excitation, either spin in the spin-pair coherently precesses in the B_1 excitation field, altering the permutation symmetry of the spin-pair that is electrically readout as a change in the device conductivity proportional to a change in the recombination rates. This is depicted in the cartoon illustration in the inset of Fig. 7.4(b), although we cannot definitely assign which electron spin in the spin-pair is associated to which Gaussian signal fitted. The

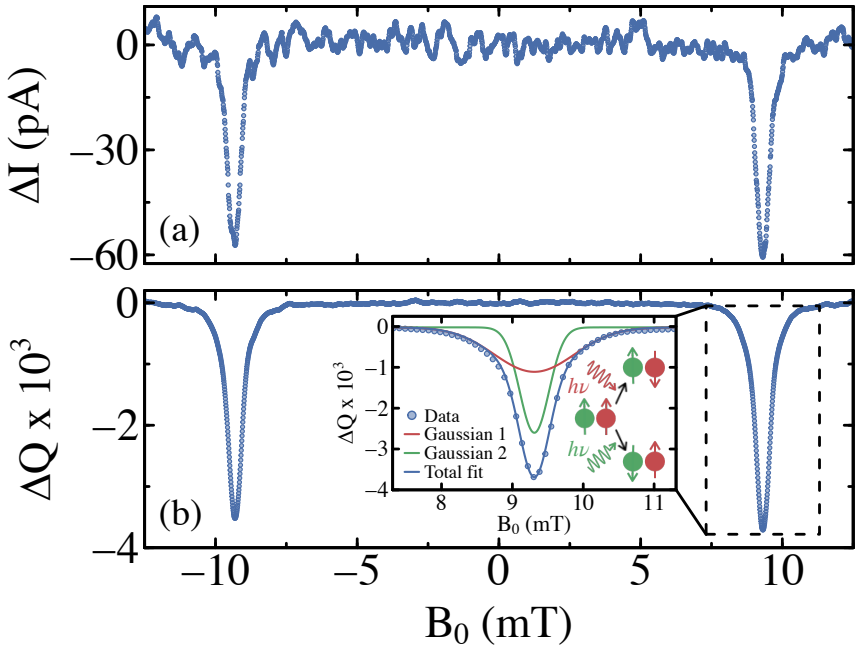

Fig. 7.5.: (a) Single scan pEDMR spectrum using lock-in detection for a RF pulse of $\tau_p = 60$ ns and $P_{RF} = 25$ W. (b) Averaged pEDMR spectrum of over 750 individual magnetic field sweeps and expressed in units of change in integrated charge. The standard deviation of the averaged spectrum noise floor corresponding to the detectable spin-pair limit is approximately 13. At resonance, around 3615 spin-pairs are addressed. A fit to the resonance signal at positive magnetic fields shown in the inset is best described by two Gaussians corresponding to the spin manipulation of each individual spin within the spin-pair, as depicted by the cartoon illustration.

Gaussian lineshape of the two deconvoluted resonance signals is a result of the inhomogeneously broadened Larmor distribution of each individual spin in the spin-pair within the ensemble as it experiences a slightly different hyperfine interaction from its spin partner. Physically, this inhomogeneous broadening can arise when the ensemble spin-pair is exposed to a non-uniform magnetic field due to local hyperfine interaction [227]. From the two Gaussian fits to the data, the linewidths proportional to the Larmor frequency distribution of the two electrons in the spin-pair are $\sigma_a = 0.207 \pm 0.001$ mT and $\sigma_b = 0.567 \pm 0.011$ mT. Inhomogeneous broadening is usually an undesired effect as it can result in the broadening of fine structure in the Rabi nutation [211], but is partially mitigated when operating at low magnetic fields [143].

7.5.1 Rabi oscillations

With the enhanced SNR observed in the pEDMR spectrum using lock-in detection, we now seek to observe coherent spin state manipulation of the spin-pair by monitoring the integrated charge as a function of the resonant pulse excitation duration, τ_p. Figure 7.6 shows the ensemble spin-pair spin state undergoing Rabi oscillations between singlet and triplet eigenstates at the fundamental Rabi frequency, Ω, and its second harmonic frequency, 2Ω. The overall oscillatory behaviour is well described by the fit in Fig. 7.6 (red curve) corresponding to the following equation [237]

$$\Delta Q(\tau_p) = [\Delta Q_1 T(\kappa_1 \gamma B_1 \tau_p) + \Delta Q_2 T(\kappa_2 \gamma B_1 \tau_p)] e^{-\tau_p / T^{\star}_{2,Rabi}} + \text{baseline}\,, \quad (7.3)$$

with $T(\alpha)$ defined in Eq. 3.114 and the displayed spectrum is corrected using a second-order polynomial baseline. The observed oscillation is sustained only over 4 cycles with the current experimental setup and parameters used and is heavily dampened by an exponential decay characterised by the $T^{\star}_{2,Rabi}$ spin dephasing time of 263 ± 13 ns. The $T^{\star}_{2,Rabi}$ spin dephasing time describes the duration in which triplet-singlet spin transitions in the spin-pair ensemble can be driven before the spin state of the spin-pair ensemble dephases into mixed states [151]. This process is mainly dominated by the B_1 field

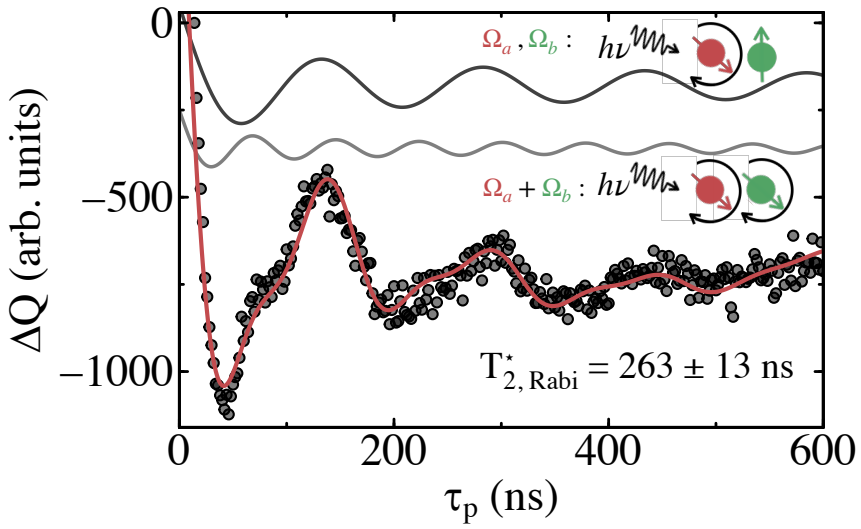

Fig. 7.6.: Electrically detected Rabi oscillations for $P_{RF} = 50$ W. The complex oscillatory behaviour of the integrated charge as a function of RF pulse length is a result of the spin-pair oscillating at its fundamental and its harmonic frequency due to spin-beating, as depicted by the cartoon illustration in the inset. Refer to the main text for more detail. A fit to the data following Eq. 7.3 (red curve) reveals $T^{\star}_{2,Rabi} = 263 \pm 13$ ns.

inhomogeneity over the device under test (DUT) and the inhomogeneous Larmor frequency distribution as described in the previous section.

A cartoon illustration of the deconstructed complex oscillation is sketched in the inset of Fig. 7.6, where the transient function oscillating at Ω describes only one electron spin in the spin-pair excited for weak B_1, whereas the transient function oscillating at 2Ω describes both spins oscillating simultaneously when the applied B_1 field strength is greater than the Larmor separation between the two spins, leading to a beating oscillation. Note that there is an apparent phase shift in the deconstructured transient function between the fundamental and harmonic component as the harmonic component oscillates slightly below twice the Rabi frequency. This will be discussed in more detail below and summarised in Fig. 7.7(c). The presence of both Ω and 2Ω in Fig. 7.6 for $P_{RF} = 50$ W is better highlighted in the FFT frequency domain in Fig. 7.7(a) along with four additional B_1 driving fields. Due to the short sampling duration and the strong exponential decaying envelope as a result of spin dephasing, the Fourier transform of the raw data (shaded symbols) is limited in frequency resolution, severely broadened,

and offset toward higher frequencies. Instead, the following analysis will be conducted using the Fourier components of the fits to the raw Rabi data following Eq. 7.3 without the exponential decay and polynomial baseline terms (red curves). This is required to clearly resolve the offset-free first and second harmonic components of the Rabi frequency. The corrected Fourier frequency components are plotted as a function of the B_1 driving field strength in Fig. 7.7(b). Estimations of B_1 for each RF power used were obtained from the Rabi frequencies of the fundamental Fourier component corresponding to spin nutation of a single $S = 1/2$ spin, which also follows

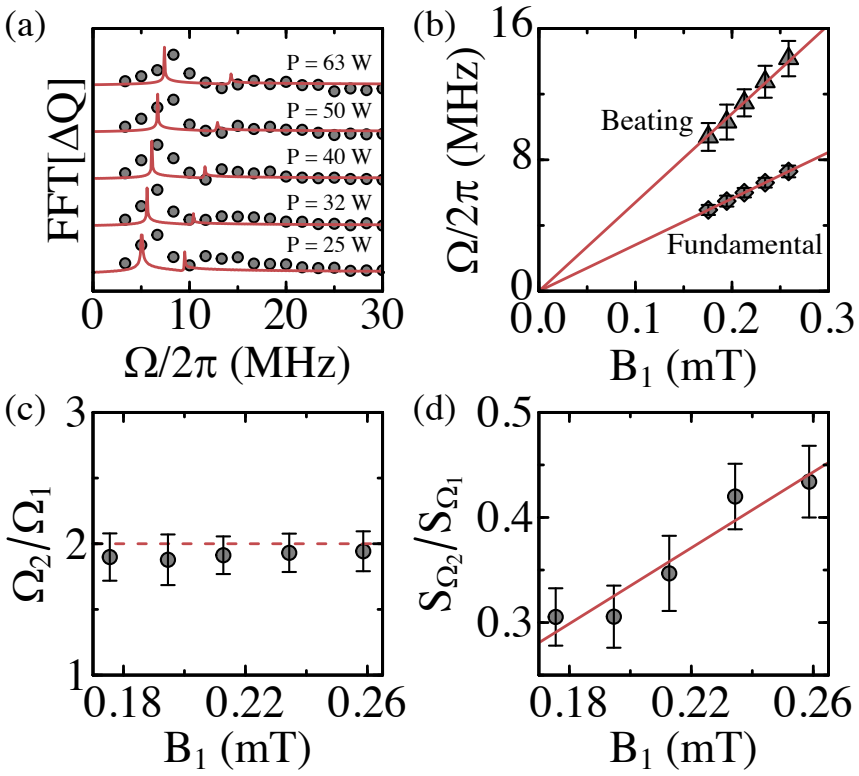

Fig. 7.7.: (a) FFT spectrum of the Rabi oscillations measured (shaded symbols) and fits to the data (red curves) for the five different RF powers indicated. (b) Plot of the two fitted frequency components in (a) as a function of B_1, both exhibiting the expected linear dependence. (c) Ratio between the beating (Ω_2) and fundamental (Ω_1) frequency component as a function of B_1. Within experimental error, the ratio is approximately equal to 2 independent of B_1, indicating the spin-pair measured is not strongly dipolar coupled. (d) Ratio between the beating and fundamental frequency component as a function of B_1. A linear dependence within experimental error and the low ratio below unity observed suggests the spin-pair measured is weakly exchanged coupled.

the expected $\sqrt{P_{RF}} \propto B_1$ dependence. Both the fundamental and harmonic frequency components increase linearly as a function of the B_1 driving field strength following Rabi's equation in Eq. 3.21 when in resonance, with a factor of ~ 2 difference between the slopes (red curves).

Upon closer inspection, the ratio between the beating and fundamental component is approximately 1.93 ± 0.15 and equal to 2 within experimental uncertainty regardless of B_1 driving field strength, as summarised in Fig. 7.7(c). This unambiguously rules out the presence of strong dipolar coupling within the spin-pair in which $\Omega_2/\Omega_1 = \sqrt{2} \sim 1.414$ is expected for $S = 1$ spin state [238]. However, we reiterate that small yet finite dipolar coupling is present as indicated by the presence of half-field transitions measured in the cwEDMR spectrum in Fig. 5.9. The presence of a 2Ω can arise either from non-selective excitation of a weakly-coupled spin-pair in which the amplitude of the spin-beating component is dependent on the B_1 driving field strength, or for a purely strongly exchanged coupled spin-pair with the 2Ω component independent of the B_1 driving field strength. Figure 7.7(d) plots the ratio between the amplitude of the 2Ω and Ω component as a function of B_1, suggesting a linear dependence. The consistently low amplitude ratio below unity and the linear dependence on B_1 suggest that the 2Ω component is a result of spin-beating from non-selective excitation of a weakly coupled spin-pair rather than a strongly exchanged coupled spin-pair. Following the procedure outlined by Lee et al. [228] for correlated Larmor frequency distributions between two electron spins, the spin-beating component is estimated to disappear when $B_1 < 0.146$ mT. This is yet to be confirmed experimentally as at such low B_1 magnetic field strengths, the Rabi frequency is comparable to $T^{\star}_{2,Rabi}$ such that no Rabi oscillations will be measurable with our current experimental setup.

To further demonstrate the compatibility of the lock-in protocol implemented, we employ the multi-pulse Ramsey protocol and characterise the spin dynamics of the ensemble spin-pair. For the following measurement presented, $B_1 = 0.259$ mT is used, corresponding to a π and $\pi/2$ pulse length of 68 ns and 34 ns, respectively.

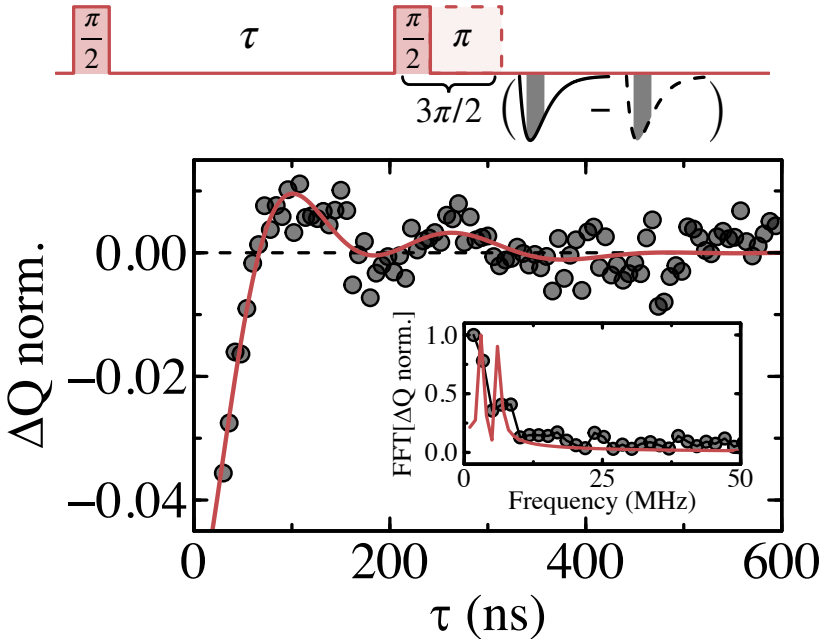

Fig. 7.8.: Normalised integrated charge in response to the Ramsey pulse sequence measured as a function of τ at 0.08 mT off resonance. The solid red line is a fit to the data following Eq. 7.4 and the FFT frequency spectrum is shown in the inset. Above the main figure, the Ramsey pulse sequence used is shown. Refer to the main text for more detail.

7.5.2 Free induction decay

Figure 7.8 shows experimental results of the Ramsey measurement slightly detuned off resonance by $B_{res} - B_0 = 0.080 \pm 0.008$ mT ($\sim 2.25 \pm 0.23$ MHz). The pulse sequence implemented is indicated above the main figure where phase cycling of the final spin projection pulse between $\pi/2$ and $3\pi/2$ is used. An oscillation in the integrated charge superimposed with a strong exponential decay envelope is observed and can be described by the following equation [152, 219]

$$\Delta Q(\tau) = A + B\tau + Ce^{(-\tau/T^{\star}_{2,FID})^n} \sum_{i=1}^{N} \cos(2\pi\delta_i\tau + \phi_i) \,, \tag{7.4}$$

where n is the stretched exponential parameter, δ_i are the detuning oscillation frequencies, ϕ_i are the phase shifts, and $A, B,$ and C are fitting parameters. The stretched exponential parameter takes on a value between 1 and 2 with

the limits corresponding to a purely Lorentzian and Gaussian resonance lineshape, respectively. When $1 < n < 2$, the resonance lineshape is described by a Voigt function. A better fit (red curve in Fig. 7.8) to the data is achieved when $n = 2$, corresponding to Gaussian broadening, with $T^{\star}_{2,FID} = 94.5 \pm 14.3$ ns. In the frequency domain shown in the inset of Fig. 7.8, two Fourier components at $\delta_1 = 2.27 \pm 0.16$ MHz and $\delta_2 = 5.26 \pm 0.18$ MHz were observed, corresponding to 0.081 ± 0.006 mT and 0.187 ± 0.006 mT in units of magnetic field detuned from resonance. The first oscillation frequency is consistent with the slight detuning off resonance used to perform the Ramsey measurement, whereas the second oscillation frequency describes the detuning off resonance for the second electron in the spin-pair, consistent with the previous model suggestive of a weakly coupled spin-pair non-selectively excited simultaneously.

The short $T^{\star}_{2,FID}$ spin dephasing time measured can arise due to several different mechanisms, including the randomly fluctuating nuclear spin bath and thermal fluctuations of the local field [239]. Despite the very fast exponential decay, Ramsey oscillations are still observable using the lock-in protocol implemented and longer oscillation cycles are expected for detuning further away from resonance. We note that the $T^{\star}_{2,Rabi}$ determined in Fig. 7.6 characterises the spin dephasing of the triplet-singlet spin state in the longitudinal plane on the Bloch sphere, whereas the $T^{\star}_{2,FID}$ measured from the Ramsey pulse sequence characterises the spin dephasing of the ensemble spin-pair in the transverse plane. Generally, $T^{\star}_{2,Rabi}$ is an upper limit estimation of $T^{\star}_{2}$ [240] and in this case $T^{\star}_{2,Rabi}$ is longer than $T^{\star}_{2,FID}$ by a factor of around 2.8. The spin dephasing time is closely related to the lineshape and the linewidth of the spin resonance signal [219]

$$T^{\star}_{2,FID} = \sqrt{\frac{2}{\sigma^2_{\omega}} + \frac{4}{\omega^2_1}}\,, \tag{7.5}$$

where σ^2_{ω} is the width of the Larmor frequency distribution related to the peak-to-peak linewidth of the spin resonance signal ($\Delta B_{pp} = 2\hbar\sigma_{\omega}/g\mu_B$). An expected peak-to-peak linewidth determined from $T^{\star}_{2,FID}$ using Eq. 7.5 is equal to $\Delta B^{FID}_{pp} = 0.185 \pm 0.035$ mT. From Fig. 5.9, the cwEDMR peak-to-peak linewidth of the spin resonance signal is $\Delta B^{cwEDMR}_{pp} = 0.219 \pm 0.008$ mT

for $B_1 = 0.063$ mT estimated from Rabi oscillation measurements extrapolated down to $P_{RF} = 950$ mW. Within experimental error, the spin resonance peak-to-peak linewidth estimated using $T^{\star}_{2,FID}$ and the experimentally measured linewidth using cwEDMR are in relatively good agreement, suggesting minimal to no power broadening at $P = 950$ mW, but also demonstrates the consistency between the different techniques. From Fig. 7.5(b), the pEDMR peak-to-peak linewidth for the main dominating spin resonance signal is $\Delta B_{pp}^{pEDMR} = 0.414 \pm 0.002$ mT for $B_1 = 0.176$ mT and $\tau_p = 60$ ns. The pEDMR linewidth measured approaches the inherent $T_2^{\star}$-limited inhomogeneous linewidth when $\tau_p \geq T_2^{\star}$ such that power broadening is effectively mitigated [241]. In this case however, $\tau_p < T^{\star}_{2,FID}$ and the measured pEDMR linewidth is severely power broadened.

7.5.3 Spin echo

After determining the $T_2^{\star}$ spin dephasing time using the Ramsey pulse sequence, we proceed to further explore the spin dynamics of the spin-pair system interrogated using the Hahn echo pulsing sequence. The individual raw integrated charge measured using a Hahn-echo pulse sequence utilising a $\pi/2$ (blue symbols) and $3\pi/2$ (red symbols) spin projection pulse for phase cycling is shown in Fig. 7.9(a) as a function of τ_2 with $\tau_1 = 300$ ns. A large background offset (black curve) determined by the average of the two traces is observed, covering the spin echo signal of interest. The spin echo signal is recovered when the two traces are subtracted from one another, as shown in Fig. 7.9(b) (black symbols), revealing a negative echo amplitude. For completeness, the individual spin echo traces after background offset subtraction are also shown. At $\tau_1 = \tau_2$, the pulse sequence forms an effective 2π and 3π spin nutation for the trace utilising a $\pi/2$ and $3\pi/2$ spin projection pulse, corresponding to a signal minimum ($+\Delta Q$) and maximum ($-\Delta Q$), respectively. This is in good agreement with the Rabi measurement in Fig. 7.6 and also demonstrates the effectiveness of phase cycling.

The spin echo amplitude is described by a Gaussian envelope in which, analogous to Eq. 7.5, the FWHM is related to the Larmor frequency distribution [219]

$$\mathrm{FWHM}_{\mathrm{echo}} = 2\sqrt{2\ln 2}\sqrt{\frac{2}{\sigma_\omega^2} + \frac{4}{\omega_1^2}}\,. \tag{7.6}$$

From the Gaussian fit to the data (black curve in Fig. 7.9(b)), the FWHM is equal to 125.2 ± 10.6 ns, corresponding to an estimated peak-to-peak linewidth of $\Delta B_{pp}^{echo} = 0.235 \pm 0.025$ mT. This value is consistent with the estimated peak-to-peak linewidth of the spin resonance signal ($\Delta B_{pp}^{FID} = 0.185 \pm 0.035$ mT) determined using $T_{2,FID}^{\star}$ within experimental error.

To determine the echo decay and spin decoherence of the spin system, the normalised spin echo amplitude is monitored as a function of $2\tau = \tau_1 + \tau_2$ with $\tau_1 = \tau_2$ in Fig. 7.10. The pulse sequence implemented is indicated above the main figure where phase cycling of the final spin projection pulse between

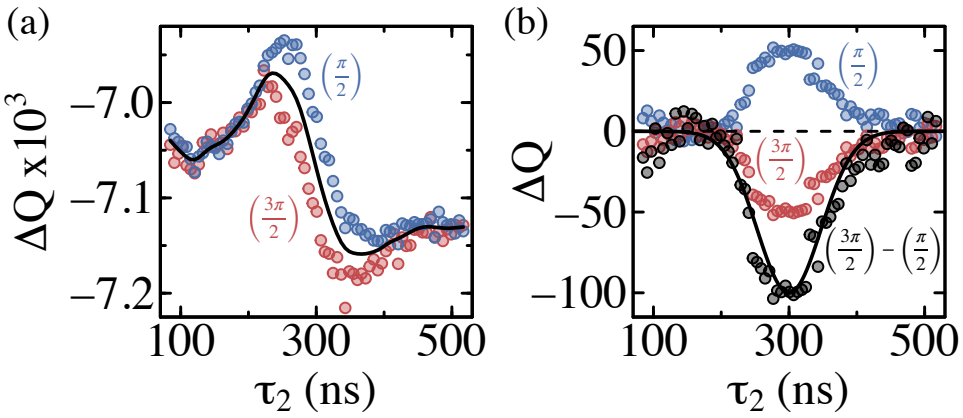

Fig. 7.9.: (a) Raw integrated charge in response to the Hahn-echo pulsing sequence as a function of τ_2 with $\tau_1 = 300$ ns from the $\pi/2$ (blue symbols) and $3\pi/2$ (red symbols) spin projection pulse. The background offset determined by the average of the two traces is also included (black curve). (b) Subtraction of the raw integrated charge between the two traces obtained from the $\pi/2$ and $3\pi/2$ spin projection pulse, revealing a spin echo response (black symbols) following a Gaussian distribution (black curve). The individual spin echo responses from the $\pi/2$ and $3\pi/2$ spin projection pulse after a background offset subtraction (black curve in (a)) are also shown for comparison.

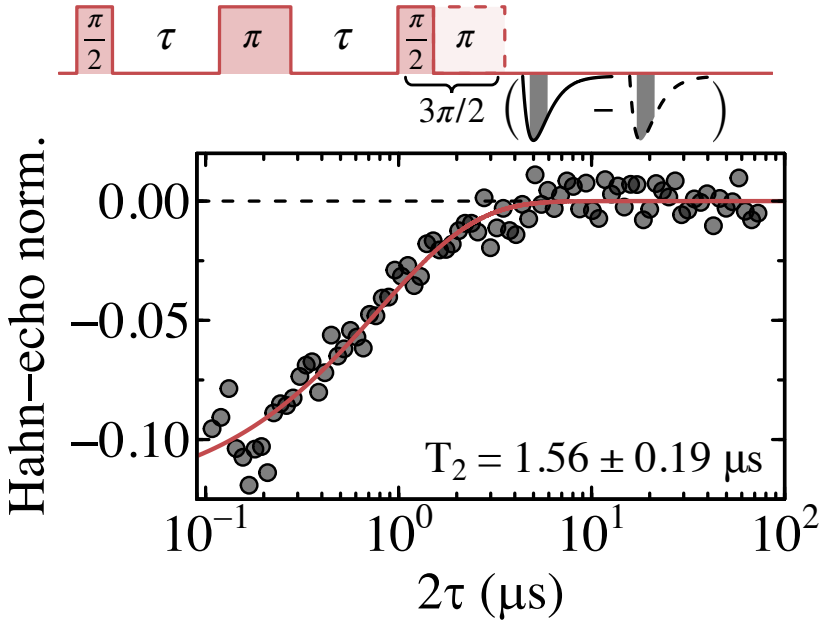

Fig. 7.10.: Coherence time measurement for the Hahn-echo pulse sequence with the normalised integrated charge measured as a function of 2τ. The solid red line is a stretched exponential decay fit to the data following Eq. 7.7. Above the main figure, the Hahn-echo pulse sequence used is shown. Refer to the main text for more detail.

$\pi/2$ and $3\pi/2$ is used. A decay in the normalised spin echo amplitude is observed following a stretched exponential of the following form

$$\Delta Q(\tau) = A \exp(-2\tau/T_2)^n \,, \tag{7.7}$$

with $T_2 = 1.56 \pm 0.19 \mu$s and $n = 0.85 \pm 0.11$ extrapolated from the fit. The stretched exponential parameter in a spin echo measurement describes the homogeneity of the ensemble spin-pair measured with each spin-pair in the ensemble having its own spin-spin coupling strength and recombination rate [150, 220, 242]. A value of $n = 0.85 \pm 0.11$ suggests a relatively uniform spin-pair ensemble distribution, where perfect homogeneity is achieved when $n = 1$ and the echo amplitude decay is described by a monoexponential.

Similar echo decay time constants have been observed for the ^{31}P-Pb quantum system at low temperature in Si [150, 221], whereas certain spin defects measured with pODMR in SiC can exhibit coherence times at least one order of magnitude longer at room temperature [38, 105]. On the other hand,

the spin coherence time measured here is much longer than the coherence times previously reported for organic semiconductor devices at room temperature and at cryogenic temperatures well below $1\ \mu s$ [226, 243, 244]. A summary of the spin relaxation times of organic semiconductor devices fabricated with different polymers can be found in Ref. [245]. Several processes can contribute to the observed decay in the spin echo amplitude, including coupling to the nuclear spin bath, finite singlet recombination rate, and the actual T_2 spin-spin relaxation process [150, 220, 221, 242]. Further studies under different experimental conditions, including temperature, magnetic field strength, pulsed excitation power and duration, and defect and isotopic concentrations will be required to resolve the contribution of each physical mechanism on the observed decay. For simplicity, here we will assume the echo decay is governed solely by T_2 rather than other processes possibly occurring on the same timescales. The ability to retain phase coherence on the μs timescale at room temperature demonstrates that SiC electronic devices are a promising and viable platform in exploring and applying quantum coherence effects, as evaluated in the following.

In the context of magnetometry, the magnetic field sensitivity utilising the Ramsey and Hahn-echo pulse protocol is limited by spin dephasing and spin decoherence, respectively. For a DC broadband Ramsey ensemble measurement, the shot noise and spin projection noise limited magnetic field sensitivity is

$$\eta_{Ramsey} = \frac{\delta B_{min}}{\sqrt{\Delta f}} \approx \frac{\hbar}{g\mu_B\sqrt{N\tau}} \frac{1}{e^{-(\tau/T^{\star}_{2,FID})^n}} \sqrt{1+\frac{1}{C^2 n_{avg}}} \sqrt{\frac{t_I+\tau+t_R}{\tau}}, \quad (7.8)$$

where $\hbar = h/2\pi$ is the reduced Planck constant, N the number of interrogated spins, C the signal contrast, $n_{avg} = (n_{ap}+n_p)/2$, and t_I and t_R the spin initialisation and readout times, respectively. Similarly, the shot noise and

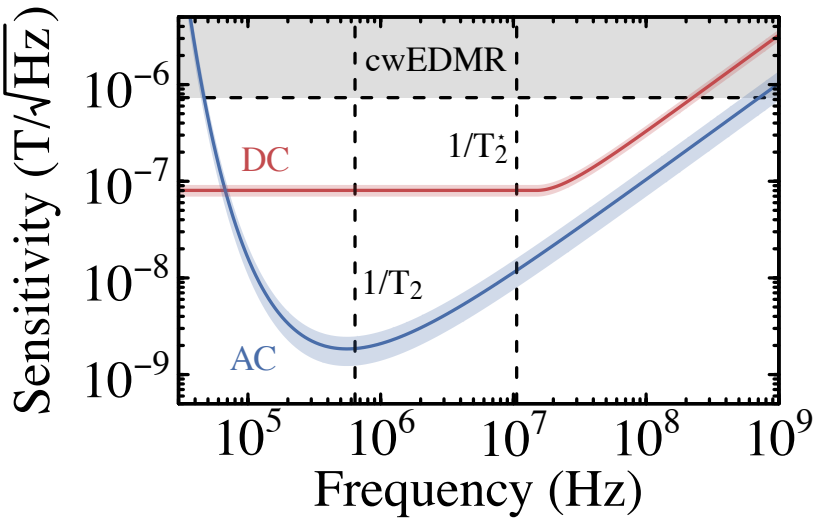

Fig. 7.11.: Magnetic field sensitivity as a function of signal frequency for DC broadband and AC narrowband detection utilising the Ramsey and Hahn-echo pulse protocol, respectively. The shaded colour regions are estimates of the uncertainty in the calculated sensitivity and the horizontal dashed line is the magnetic field sensitivity calculated in Chapter 5 using cwEDMR. Optimal DC and AC sensitivity is achieved when the signal frequency is $\sim 1/T_2^\star$ and $\sim 1/T_2$, respectively.

spin projection noise limited magnetic field sensitivity for a AC narrowband Hahn-echo ensemble measurement is

$$\eta_{Hahn} = \frac{\delta B_{min}}{\sqrt{\Delta f}} \approx \frac{\pi\hbar}{2g\mu_B\sqrt{N\tau}} \frac{1}{e^{-(\tau/T_2)^n}} \sqrt{1 + \frac{1}{C^2 n_{avg}}} \sqrt{\frac{t_I + \tau + t_R}{\tau}} \,. \tag{7.9}$$

The full derivation for Eqs. 7.8−7.9 can be found in Ref. [13] and were derived exclusively for NV centres in diamond detected with ODMR. Here, we generalise the equations for electrical readout where electrical shot noise in units of integrated charge is considered instead of photon shot noise for optical readout.

Ramsey magnetometry achieves the best DC magnetic field sensitivity over cwEDMR operation explored in Chapter 5 as the sensing interval τ between the two $\pi/2-$pulses in which the spin system undergoes spin precession does not suffer from interactions with the electric and RF driving field. The optimal Ramsey DC sensitivity is achieved when $\tau \sim T_2^\star$ [13, 246]. From

Eq. 7.8, it is evident that increasing the number of spins measured and the interrogation time enhances the sensitivity. However, the decay in the FID signal characterised by $T_2^\star$ leads to a decrease in sensitivity when $\tau > T_2^\star$, as indicated by the second term in Eq. 7.8. Figure 7.11 compares the Ramsey DC and Hahn-echo AC sensitivity as a function of the sample magnetic field frequency ($1/\tau$). For reference, the DC sensitivity ($\sim 730\ \mathrm{nT}/\sqrt{\mathrm{Hz}}$) determined in Chapter 5 under cwEDMR operation without common-mode rejection and photoexcitation is indicated by the horizontal dashed line. Utilising the values determined from Secs. 7.5.2–7.5.3, the optimal Ramsey DC and Hahn-echo AC sensitivity are $\eta_{Ramsey} = 80.4 \pm 11.1\ \mathrm{nT}/\sqrt{\mathrm{Hz}}$ and $\eta_{Hahn} = 1.84 \pm 0.62\ \mathrm{nT}/\sqrt{\mathrm{Hz}}$, respectively.

The additional $\pi-$pulse in the Hahn-echo sequence in comparison to the Ramsey sequence refocuses the dephasing of the spin ensemble, which effectively extends the sensing interval toward T_2. However, this comes at the cost of a reduced bandwidth, particularly at low frequencies below $1/T_2$, as shown in Fig. 7.11. As the spin decoherence time is typically much longer than the spin dephasing time ($T_2 \gg T_2^\star$), this corresponds to an increase in the sensing duration and magnetic field sensitivity. Similar to Ramsey magnetometry, the optimal Hahn-echo AC sensitivity is achieved when $\tau \sim T_2$, but additionally, τ must be an even multiple of the sample AC magnetic field period, T_{AC} [13, 246]. Thus, Hahn-echo AC magnetometry is most sensitive when $T_{AC} \sim T_2$, which in this case is approximately $1.56\ \mu\mathrm{s}$ (~ 640 kHz).

To put our results into perspective, the DC and AC sensitivity of a single NV center in a diamond sample limited by the dephasing due to naturally abundant ^{13}C with $T_2^\star \sim 1\ \mu\mathrm{s}$ and $T_2^\star \sim 300\ \mu\mathrm{s}$ are $\eta_{Ramsey} \sim 1\ \mu\mathrm{T}/\sqrt{\mathrm{Hz}}$ and $\eta_{Hahn} = 18\ \mathrm{nT}/\sqrt{\mathrm{Hz}}$, respectively [17]. On an ensemble level, a remarkable AC sensitivity of $\eta_{Hahn} = 0.9\ \mathrm{pT}/\sqrt{\mathrm{Hz}}$ has been previously achieved using an ensemble of $N \sim 10^{11}$ NV centres [18]. Currently, the small number of spins interrogated N during the measurement, on the order of several hundred estimated from the integrated charge signal, is one of the main limiting factors for the magnetic field sensitivity. The lack of knowledge on the atomic origin of the paramagnetic defect measured and how they can be created in a controllable manner means that the limits on N are presently unknown. Furthermore, in the high spin concentration limit where

the average separation between spin-pairs within the ensemble is reduced, increases in the spin-spin and hyperfine interaction may reduce the spin decoherence time, limiting the AC sensitivity of the magnetometer. This may be partially mitigated by implementing the Carr-Purcell-Meiboom-Gill (CPMG) [247] pulse sequence, which effectively extends T_2 by further decoupling the spins from magnetic noise and increasing the sensing interval at the expense of a reduced bandwidth. Reducing the spin initialisation and readout times (fourth term in Eqs. 7.8−7.9) can also enhance the sensitivity, but may reduce N and the signal contrast.

7.6 Summary and conclusion

In this chapter, we have experimentally demonstrated a lock-in detection scheme for pEDMR with enhanced SNR, which allowed us to explore more complex pulse sequences to characterise the spin dynamics of the ensemble spin-pair measured. The lock-in detection scheme was based on modulating the amplitude of the RF pulse sequence, in addition to modulating the device bias to induce SDR. Additional background subtraction was performed by subtracting the raw output measured at resonance and far off resonance and phase cycling between a $\pi/2$ and $3\pi/2$ spin projection pulse was used for multi-pulse measurements. While a direct comparison was not possible due to the slightly different experimental conditions used, an improvement in the SNR by a factor of ~ 14.6 was achieved, which was found to be crucial for extending the pEDMR technique utilising multi-pulse sequences.

The ensemble spin-pair system measured was able to be coherently driven between its singlet-triplet spin state up to $T^{\star}_{2,Rabi} = 263 \pm 13$ ns limited by B_1 inhomogeneity and the inhomogeneous Larmor frequency distribution as a result of hyperfine broadening. Analysis of the Rabi oscillations revealed the individual electron spins in the spin-pair within the ensemble are weakly coupled to each other, but are non-selectively driven simultaneously, resulting in the spin beating at twice the Rabi oscillation frequency. Next, electrically detected FID was measured slightly detuned off resonance, where oscillations are superimposed with an exponential decay with a characteristic time constant of $T^{\star}_{2,FID} = 94.5 \pm 14.3$ ns limited by hyperfine interactions with

surrounding nuclear spins. The measured FID is well described by a Gaussian broadened analytical model [219] and the expected natural linewidth calculated is consistent with previously measured linewidths using cwEDMR and pEDMR.

The Ramsey pulse sequence was then extended to measure the spin echo response. The linewidth of the spin echo measured when $\tau_1 = \tau_2$ is consistent with the expected natural linewidth calculated from the FID measurement. A decay in the spin echo amplitude characterised by a stretched exponential function is observed as a function of 2τ, with $T_2 = 1.56 \pm 0.19\ \mu\mathrm{s}$ and $n = 0.85 \pm 0.11$. With the spin dephasing and spin decoherence times measured, the theoretical shot noise and spin projection noise limited DC and AC magnetic field sensitivity were calculated to be $\eta_{Ramsey} = 80.4 \pm 11.1\,\mathrm{nT}/\sqrt{\mathrm{Hz}}$ and $\eta_{Hahn} = 1.84 \pm 0.62\,\mathrm{nT}/\sqrt{\mathrm{Hz}}$, respectively. These initial coherent spin measurements and calculations in the context of magnetometry will help to establish further research into pulse sequence-based electrically detected magnetometry, but also demonstrate that processing-induced paramagnetic defects in SiC are a potentially viable system to implement such quantum sensing protocols at room temperature.

Conclusions and Outlook 8

The studies conducted in this thesis aimed to advance our understanding on various aspects of electrically detected spin defects in SiC devices for quantum sensing applications. In particular, the characterisation and sensitivity enhancement of a SiC magnetometer, the zero-field spin-mixing response for temperature sensing capabilities, and coherent spin manipulation and detection for DC and AC magnetic field sensing were explored. Below, the key results from each experimental chapter and envisioned further works are summarised.

8.1 Absolute magnetometry based on spin defects in SiC

8.1.1 Summary and conclusions

As introduced in Chapter 5, a fabrication processing-induced spin defect in a 6H−SiC n^+p junction diode was found and characterised. Superhyperfine interaction and weak dipole-dipole coupling were observed. The device was then operated as a magnetometer and different methods in characterising its magnetic field sensitivity were then employed. Although the baseline magnetic field sensitivity of the 6H−SiC device measured was slightly less sensitive compared to a 4H−SiC device previously reported in the literature, two experimental methods were found to vastly improve the magnetic field sensitivity of the device measured.

Common mode rejection was implemented and was found to be effective at reducing common mode electrical noise arising from the detection electronics. In addition, excess charge carriers were optically injected with above bandgap photoexcitation to operate in the high-level injection regime such

that the recombination rate is significantly enhanced. These two experimental methods can be applied to any spin system utilising the SDR mechanism and it is envisioned that sub-nT$/\sqrt{\text{Hz}}$ EDMR-based magnetometers will be readily achieved in the near future.

8.1.2 Directions for future work

The main limiting factor on the magnetic field sensitivity is the spin defect concentration. Determining the atomic origin of the spin defect and the fabrication processing steps responsible for its creation will be of utmost importance. High-field EDMR measurements with finer spectral resolution can offer new insight on the spin defect, particularly when combined with angular dependent measurements to map out the defect symmetry characterised by its g$-$tensor and hyperfine tensor. Defect engineering techniques, such an particle irradiation, annealing, and isotopic enrichment may also be explored to further enhance the spin defect concentration.

As the device measured in Chapter 5 was not fabricated specifically for EDMR measurements and magnetometry, substantial device optimisation is yet to be explored. A series of systematic studies on how key parameters, such as device geometry, doping concentration, and polytype, may provide a simple method in enhancing the spin-mixing response. As highlighted by the additional measurements in Appendix A$-$C, the current device measured is also littered with additional non-paramagnetic defects. These unintentional non-paramagnetic defects may compete for free charge carriers required for the SDR process and have a significant impact on the EDMR response. Thus, this complex interaction must be explored in detail and methods in eliminating these non-paramagnetic defects must be determined.

8.2 Hyperfine-induced spin-mixing response

8.2.1 Summary and conclusions

A comprehensive study on how CP parameters and temperature affects the zero-field response in a commercial SiC power transistor device was

reported in Chapter 6. The observed dependences were explained in terms of standard CP theory where possible. Due to the incomplete ionization of N donors in the n-epilayer, CP results at low temperatures and at high frequencies were severely affected and may not be suitable operating conditions for applications utilising the zero-field response. The zero-field response for this particular commercial SiC power transistor device comprises of at least three individual components each with its unique dependence on electric field and temperature.

In particular, the linewidth of one of the Lorentzian components exhibited a linear dependence on temperature within a limited temperature range. This feature was tentatively assigned to the electron-nuclear dipole interaction, analogous to the electron-electron dipole interaction responsible for the temperature dependent zero-field splitting parameter found in some high spin manifold optical spin defects. The coupling coefficient and temperature sensitivity are comparable with values previously determined for an unidentified optical spin defect in SiC, showing promise for future thermometry applications.

8.2.2 Directions for future work

Due to the multiple overlapping features that make up the zero-field response, it is worth investigating the temperature dependence of the zero-field response in a simpler device structure under DC biasing, such as a junction diode device to simplify and deconvolute each contribution from the overall response. Higher doping concentrations may also be considered to avoid carrier freeze-out effects and investigate the zero-field response at lower temperatures. Improvements to the temperature controllable spectrometer utilised for this study can be implemented to include MW feed-through to the cryostat used to drive spin resonance and high temperature-compatible electrical contacts to further explore the temperature capabilities of SiC electronics at even more elevated temperatures.

Theoretical calculations using the stochastic Liouville equation in the steady-state may provide new insight on the zero-field response and its temperature dependence. In particular, the origin of the observed temperature-dependent

linewidth response must be resolved to fully utilise it for potential thermometry applications.

8.3 Coherent spin manipulation and detection

8.3.1 Summary and conclusions

In Chapter 7, we have outlined and successfully demonstrated a lock-in detection scheme for pEDMR that eliminates common issues associated with pEDMR measured in the time-domain. This allowed us to implement complex pulsing schemes developed for pESR to characterise various spin properties of the processing-induced spin defect introduced in Chapter 5. It was found that the two electron spins in the intermediate spin-pair are weakly coupled, but their Larmor separation is small such that the two electron spins are excited simultaneously, leading to Rabi spin beating. Additionally, the dependence of the Rabi spin beating on the B_1 driving field strength indicate the two electron spins exhibit weak exchange and dipole-dipole coupling.

The spin dephasing and spin relaxation times were then extracted and were found to be quite long compared to other spin systems at room temperature detected electrically. These characteristic time constants were then used to calculate the shot-noise and spin projection noise limited DC and AC sensitivity, respectively. The technique and methodology outlined in this chapter may also be applied to characterise and benchmark other spin and material systems.

8.3.2 Directions for future work

While a series of complex pulse sequences were successfully demonstrated, a non-negligible artificially-induced spin-dephasing due to B_1 inhomogeneity was present. This resulted in some measurements being performed under non-ideal conditions. For example, high RF powers near the maximum rating of the RF amplifier were required and it was only possible to generate and sustain 4 cycles of Rabi oscillations before it was heavily damped. Further

simulations and optimisation of the embedded antenna design may help alleviate this issue.

Ultimately, the DC and AC magnetic field sensitivity will be limited by the inherent spin dephasing and spin relaxation times of the spin system measured, respectively. The spin relaxation time can be experimentally extended by implementing the CPMG pulse sequence and will require additional I/Q modulator hardware to control the phase of each individual pulse in the pulse sequence. Other pulse sequences that were not pursued in this work may aid in the characterisation of the spin defect measured. Particularly, pulse sequences that address the electron-nuclear interaction, such as electron-nuclear double resonance (ENDOR) and electron spin echo envelope modulation (ESEEM), may supplement and reveal new insight on the zero-field spin-mixing response.

8.4 Final remarks

Quantum sensing based on electrically detected spin defects remains a field of research still in its infancy. As a result, there still exists a wide range of unanswered questions and unexplored topics. The results presented in this thesis demonstrate and provide the first steps toward the realisation of a fully fledged quantum sensor utilising process-induced spin defects in SiC, a promising quantum materials platform. As detailed by the CSIRO in its Growing Australia's Quantum Technology Industry report, quantum sensing alone in Australia is predicted to generate $\$\mathrm{AUD}\,0.9$ billion and 3000 jobs by 2040 [5], highlighting the ever-growing emergence and importance of quantum technology research. It remains to be seen how this exciting field of research evolves in the future and the novel ideas that will emerge. It is envisioned that SiC quantum devices, whether based on optical or electrical spin defects or even a hybrid approach, will have a crucial role in quantum sensing.

Appendices

Random telegraph signal

A

Presented here are random telegraph signal (RTS) results observed in the 6H−SiC n^+p junction diode device studied in Chapter 5. Noticeable fluctuations in the measured device current with increasing forward bias were observed. To explore this phenomenon in more detail, time traces of the

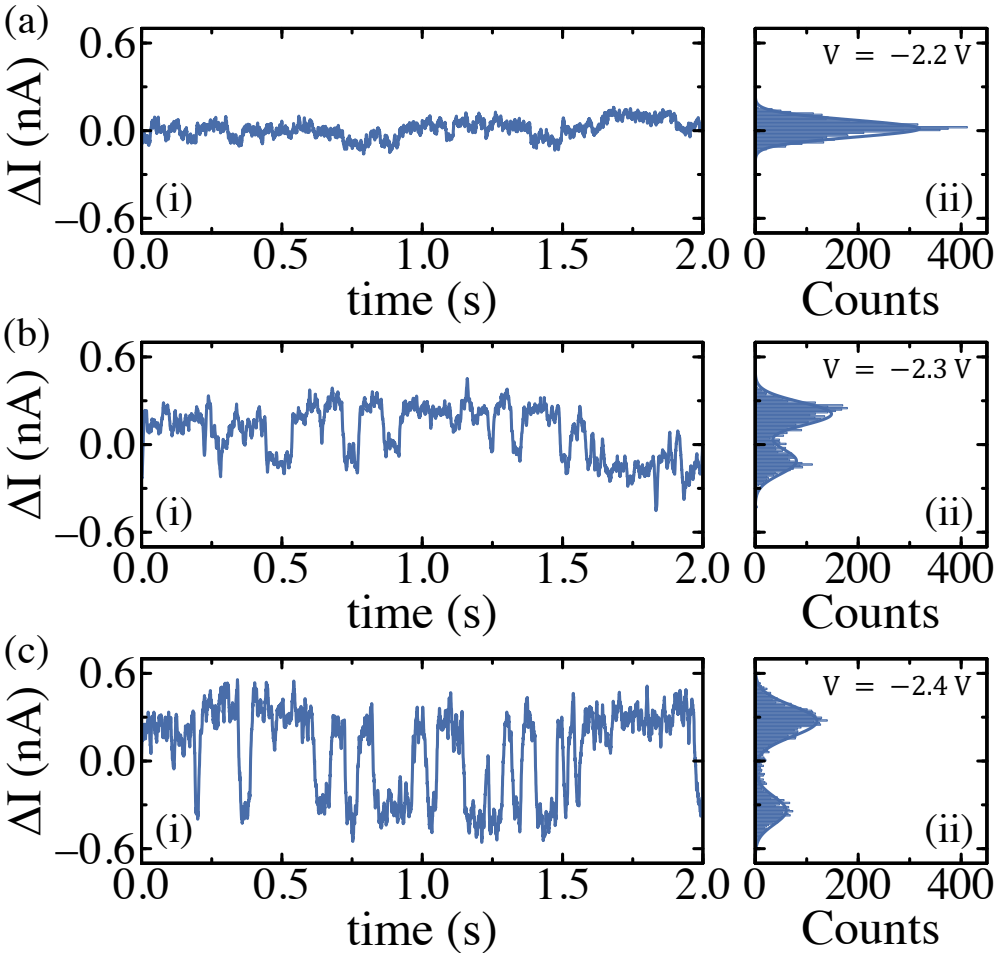

Fig. A.1.: Onset of the two-level random telegraph signal in the device current with increasing forward bias (i) recorded in the time-domain (ii) and its corresponding amplitude histogram at the indicated forward biases. Solid lines represent Gaussian fits to the amplitude histogram distribution.

device current with increasing forward bias were recorded, revealing the onset and increase in discrete jumps between two arbitrary current levels, as shown in Fig. A.1(a)-(c)(i). This phenomena is usually associated with RTS in small area transistors where individual charge carrier trapping and emission events due to interface defects are observed in the drain current [248].

Although a technologically-limiting effect that prevents the normal operation of devices, information gathered from RTS can be used to spectroscopically characterise the defect involved in the charge carrier trapping and emission process. For a forward-biased pn junction instead of a small area transistor where RTS is typically found, it has been previously proposed that RTS arises from the bistable fluctuation in the potential barrier of a single charge carrier trap in the depletion region as a single charge carrier is captured and emitted [249]. The capturing of a charge carrier leads to a local increase in the defect barrier height, reducing the flux of charge carriers passing through the barrier in the vicinity of the defect and can affect up to 2% of the total measured current [250].

The RTS is characterised by a well-defined current amplitude between the high and low level, ΔI_{HI-LO}, and the average times in the high and low levels following a Poissonian distribution. As the forward bias is increased, the separation between the high and low level becomes more resolved, as indicated by the amplitude histograms in Fig. A.1(a)-(c)(ii). Gaussian fits to the amplitude histograms (solid lines) can be used to determine ΔI_{HI-LO}, which is equal to zero for V $= -2.2$ V and increases to approximately 0.61 nA for V $= -2.4$ V. During hole capture by a defect, the reduction in free charge carriers gives rise to a decrease in the device current. Thus, the pulse time in the high level state corresponds to hole capture, whereas the pulse time in the low level state corresponds to hole emission. Interestingly from the amplitude histogram, there seems to exist a preferential bias toward the device existing in the high level state, corresponding to more hole capture events than hole emission events.

The distribution of pulse times in the high and low level from a 20 s time trace for V $= -2.4$ V is shown in Fig. A.2(a) and (b), respectively, exhibiting an exponentially decaying distribution following Poissonian statistics expected for charge trapping and emission. From the distributions, an exponential

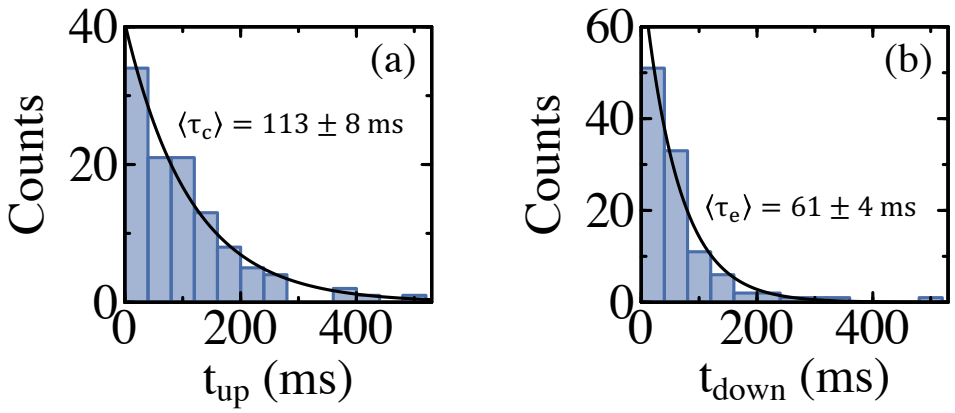

Fig. A.2.: Distribution of pulse times in the (a) high and (b) low level in the random telegraph signal at V $= -2.4$ V, both exhibiting an exponential decaying distribution following Poissonian statistics. Solid lines represents exponential decay fits to the pulse time distributions to extract average capture and emission times.

fit to the data reveals an average capture and emission time constant of 113 ± 8 and 61 ± 4 ms, respectively. Given the relatively long time constants extracted, a longer sampling interval may be required to increase the number of counts for a more accurate determination of the time constants.

Spectroscopic information about the defect responsible for the observed RTS is usually extracted by observing the dependence of the capture and emission time constants on temperature. The temperature-dependent emission time constant follows an Arrhenius relation and the trap energy level and capture cross-section can be determined, similar to a deep level transient spectroscopy (DLTS) analysis. Additional temperature-dependent RTS measurements will be required to spectroscopically characterise this specific defect.

In the context of EDMR, random fluctuations in the device current due to RTS can reduce the signal-to-noise ratio (SNR). While the random fluctuations may be partially mitigated and averaged out by signal averaging over several hundred individual EDMR scans, the acquisition time is increased. Furthermore, for single-shot EDMR measurements where signal averaging is not possible, such as in real-time magnetometry operation, larger forward biases where RTS dominates must be avoided. Thus, the EDMR operating voltage above V $= -2.30$ V is avoided for this particular device.

Electroluminescence

B

The onset of RTS with increasing forward bias is accompanied by the onset of electroluminescence (EL), which will be examined here. An EL peak situated at approximately 555 nm is observed and shown in Fig. B.1(a) for V $= -2.35$ V. This EL feature was previously labelled as the D_1 luminescence line and is attributed to a neutral Si antisite (Si_C) hole trap situated $\sim 0.3-0.4$ eV above the valence band edge [251, 252]. The neutral Si antisite is formed as a result of implantation-induced damage, surviving high temperature anneals typically employed during SiC device fabrication [44]. Visually, the D_1 appears as a background luminescence in the vicinity of the implanted region, as shown in the optical micrograph of the device operated at V $= -2.35$ V in the inset of Fig. B.1(a). The Si antisite is an extremely stable defect and can persist up to $1700°$C [252]. Currently, it is unclear whether the D_1 EL is of the same origin as the RTS described in Appendix A.

The D_1 EL intensity voltage dependence is shown in Fig. B.1(b) where EL is detectable above a threshold voltage of approximately -2.1 V using a single

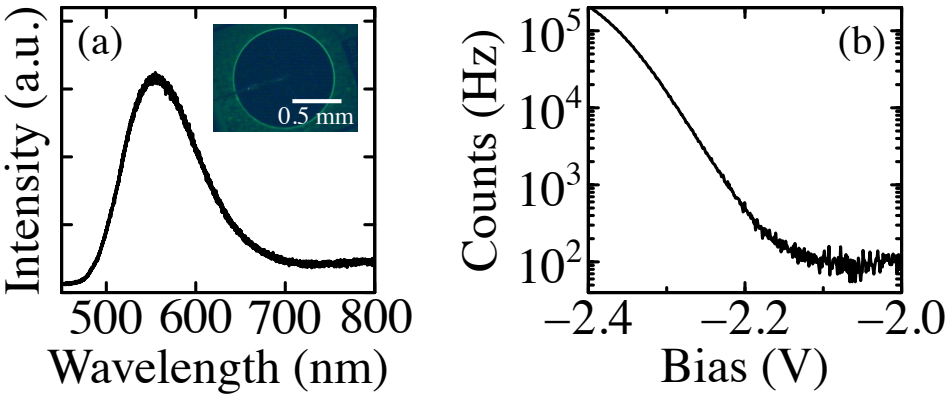

Fig. B.1.: (a) Room temperature EL spectrum showing the D_1 centre phonon side-band with a peak intensity around 555 nm. An optical micrograph of the device operated at V $= -2.35$ V is shown in the inset where EL from the D_1 centre is clearly visible with the naked eye. (b) EL intensity of the D_1 centre as a function of forward bias.

photon counter (PerkinElmer SPCM-AQR-16) and monotonically increases with increasing forward bias. On application of an external magnetic field and resonant electromagnetic excitation, the D_1 EL did not exhibit any spin dependence (not shown), corroborating with previous calculations that the neutral Si antisite is a fully occupied double degenerate level [252]. In the context of an EDMR measurement, it is speculated that the D_1 defect centre may instead provide an alternative recombination pathway and compete with the spin defect measured in Chapter 5 for free charge carriers, reducing the EDMR signal contrast [253], as indicated by the vastly different voltage dependence of the D_1 EL intensity in Fig. B.1(b) and the spin resonance response in Fig. 5.8(b).

C

Deep level transient spectroscopy

Supplementary DLTS measurements were carried out to gain further insight on electrically-active defects present in the 6H−SiC n^+p junction diode device studied in Chapter 5. The theory of operation of the DLTS technique can be found elsewhere in Ref. [254] and DLTS measurement were carried out using an in-house custom-built spectrometer described in Ref. [255]. A representative DLTS spectrum of the 6H−SiC n^+p junction diode is shown in Fig. C.1 measured using a rate window of 63 ms.

For a n^+p diode device, the majority of the depletion region extends far into the p-epilayer region and hole traps are probed under reverse biasing condition. A dominating peak occurring at approximately 168 K was observed along with a broad shoulder feature at elevated temperatures above room temperature.

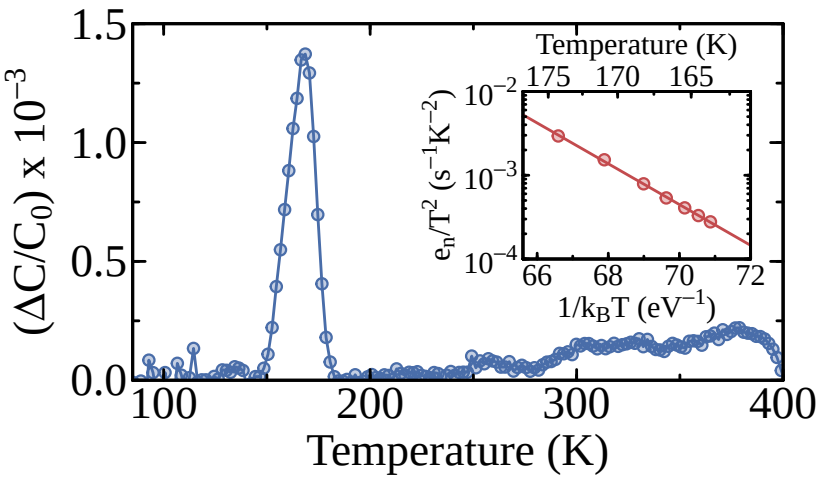

Fig. C.1.: DLTS spectrum of the 6H−SiC n^+p junction diode measured with a rate window of 63 ms, revealing one dominating peak at around 168 K. A $t_p = 25$ ms filling pulse with a quiescent reverse bias of$V_r = 8$ V and a filling pulse height of $V_p = -7.5$ V was applied at a period of 250 ms. The inset shows the corresponding Arrhenius plot for the dominating peak in the main plot. Error bars are smaller than symbols and omitted for clarity.

Broad features in a DLTS spectrum are usually associated with extended defects characterised by a broad density of states in the bandgap formed during high temperature heat treatments [256, 257]. Arrhenius analysis for the broad shoulder feature was avoided due to its poor SNR. The Arrhenius plot for the main dominating peak is shown in the inset of Fig. C.1, where a trap activation energy of $E_V + E_T = 0.560 \pm 0.012$ eV was extracted. An additional depth profiling measurement was performed by measuring a series of capacitance transients at 168 K with increasing filling pulse height. Within the experimental range considered, a maximum concentration of approximately 1.5×10^{13} cm^{-3} was found situated approximately $2.25\ \mu$m away from the junction, as shown in Fig. C.2.

Several defects have been previously identified in p$-$type 6H $-$SiC with activation energies near $E_V + E_T = 0.560$ eV, including a boron-related hole trap [258, 259], an electron-irradiation induced deep level defect [260], and a secondary defect formed after a $900°$C anneal [261]. A definitive defect assignment of the measured DLTS signal will likely require a dedicated DLTS study beyond the scope of this work following its thermal stability for example. Regardless, several properties of the defect can still be inferred from the current results. The defect distribution profile in Fig. C.2 is indicative of end-of-range defects formed by ion implantation as compared to a uniform trap distribution that may arise from defects introduced during the SiC growth process. A peak in the trap concentration is expected to appear if the mea-

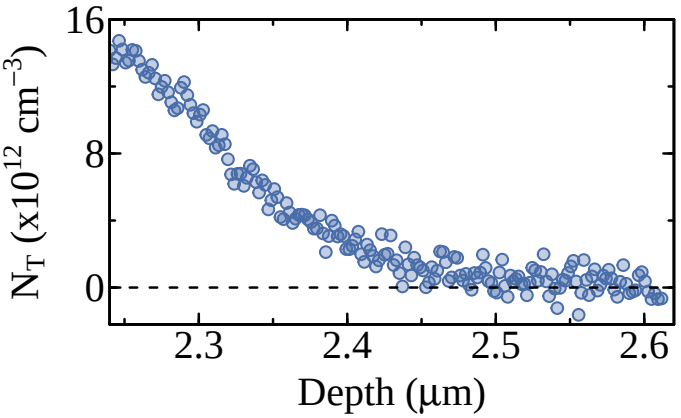

Fig. C.2.: Trap concentration depth profile of the defect identified in Fig. C.1, revealing a maximum concentration situated of approximately 1.5×10^{13} cm^{-3} within the experimental range considered.

surement range is extended toward the junction, which is yet to be confirmed. When the Arrhenius relationship calculated from the DLTS measurement in the inset of Fig. C.1 is extrapolated out to room temperature, the trap emission rate does not match the average trap emission time constant determined for the RTS in Fig. A.2(b). This suggests that the two measurement techniques are addressing two different types of defects. In total, at least three different types of non-paramagnetic defects have been observed by various techniques outlined in the Appendix.

Bibliography

[1] Bruce E Kane. “A silicon-based nuclear spin quantum computer”. *Nature* 393.6681 (1998), p. 133.

[2] David P DiVincenzo. “The physical implementation of quantum computation”. *Fortschritte der Physik: Progress of Physics* 48.9-11 (2000), pp. 771–783.

[3] C. H. Bennett and G. Brassard. “Quantum cryptography: Public key distribution and coin tossing”. *In Proceedings of IEEE International Conference on Computers, Systems and Signal Processing,* 175.8 (1984).

[4] Christian L Degen, F Reinhard, and Paola Cappellaro. “Quantum sensing”. *Reviews of modern physics* 89.3 (2017), p. 035002.

[5] CSIRO. *Growing Australia’s Quantum Technology Industry*. 2020.

[6] Hiroyuki Matsunami. “Technological breakthroughs in growth control of silicon carbide for high power electronic devices”. *Japanese journal of applied physics* 43.10R (2004), p. 6835.

[7] Pavel Hazdra and Stanislav Popelka. “Displacement damage and total ionisation dose effects on 4H-SiC power devices”. *IET Power Electronics* 12.15 (2019), pp. 3910–3918.

[8] Stefania Castelletto and Alberto Boretti. “Silicon carbide color centers for quantum applications”. *Journal of Physics: Photonics* 2.2 (2020), p. 022001.

[9] Corey J Cochrane, Jordana Blacksberg, Mark A Anders, and Patrick M Lenahan. “Vectorized magnetometer for space applications using electrical readout of atomic scale defects in silicon carbide”. *Scientific reports* 6 (2016), p. 37077.

[10] Corey J Cochrane, Hannes Kraus, Philip G Neudeck, et al. “Magnetic Field Sensing with 4H SiC Diodes: N vs P Implantation”. *Materials Science Forum*. Vol. 924. Trans Tech Publ. 2018, pp. 988–992.

[11] Jean-Philippe Tetienne, Nikolai Dontschuk, David A Broadway, et al. “Quantum imaging of current flow in graphene”. *Science advances* 3.4 (2017), e1602429.

[12] Julia M McCoey, Mirai Matsuoka, Robert W de Gille, et al. “Quantum Magnetic Imaging of Iron Biomineralization in Teeth of the Chiton Acanthopleura hirtosa”. *Small Methods* 4.3 (2020), p. 1900754.

[13] John F Barry, Jennifer M Schloss, Erik Bauch, et al. “Sensitivity optimization for NV-diamond magnetometry”. *Reviews of Modern Physics* 92.1 (2020), p. 015004.

[14] Gopalakrishnan Balasubramanian, Philipp Neumann, Daniel Twitchen, et al. “Ultralong spin coherence time in isotopically engineered diamond”. *Nature materials* 8.5 (2009), pp. 383–387.

[15] Hannah Clevenson, Matthew E Trusheim, Carson Teale, et al. “Broadband magnetometry and temperature sensing with a light-trapping diamond waveguide”. *Nature Physics* 11.5 (2015), pp. 393–397.

[16] Jeronimo R Maze, Paul L Stanwix, James S Hodges, et al. “Nanoscale magnetic sensing with an individual electronic spin in diamond”. *Nature* 455.7213 (2008), pp. 644–647.

[17] JM Taylor, Paola Cappellaro, L Childress, et al. “High-sensitivity diamond magnetometer with nanoscale resolution”. *Nature Physics* 4.10 (2008), pp. 810–816.

[18] Thomas Wolf, Philipp Neumann, Kazuo Nakamura, et al. “Subpicotesla diamond magnetometry”. *Physical Review X* 5.4 (2015), p. 041001.

[19] D Simin, VA Soltamov, AV Poshakinskiy, et al. “All-optical dc nanotesla magnetometry using silicon vacancy fine structure in isotopically purified silicon carbide”. *Physical Review X* 6.3 (2016), p. 031014.

[20] Anasua Chatterjee, Paul Stevenson, Silvano De Franceschi, et al. “Semiconductor qubits in practice”. *Nature Reviews Physics* 3.3 (2021), pp. 157–177.

[21] D Kaplan, I Solomon, and NF Mott. “Explanation of the large spin-dependent recombination effect in semiconductors”. *Journal de Physique Lettres* 39.4 (1978), pp. 51–54.

[22] WJ Baker, K Ambal, DP Waters, et al. “Robust absolute magnetometry with organic thin-film devices”. *Nature communications* 3.1 (2012), pp. 1–7.

[23] CJ Cochrane and Patrick M Lenahan. “Zero-field detection of spin dependent recombination with direct observation of electron nuclear hyperfine interactions in the absence of an oscillating electromagnetic field”. *Journal of Applied Physics* 112.12 (2012), p. 123714.

[24] Philippe Klemm, Sebastian Bange, Agnes Pöllmann, Christoph Boehme, and John M Lupton. “Nanotesla magnetoresistance in π-conjugated polymer devices”. *Physical Review B* 95.24 (2017), p. 241407.

[25] FL Bloom, W Wagemans, M Kemerink, and B Koopmans. “Correspondence of the sign change in organic magnetoresistance with the onset of bipolar charge transport”. *Applied Physics Letters* 93.26 (2008), p. 449.

[26] AJ Schellekens, Wiebe Wagemans, SP Kersten, PA Bobbert, and Bert Koopmans. “Microscopic modeling of magnetic-field effects on charge transport in organic semiconductors”. *Physical Review B* 84.7 (2011), p. 075204.

[27] Tho D Nguyen, Golda Hukic-Markosian, Fujian Wang, et al. “Isotope effect in spin response of π-conjugated polymer films and devices”. *Nature materials* 9.4 (2010), pp. 345–352.

[28] Christoph Boehme and Klaus Lips. “Time domain measurement of spin-dependent recombination”. *Applied Physics Letters* 79.26 (2001), pp. 4363–4365.

[29] Felix Hoehne, Lukas Dreher, Jan Behrends, et al. “Lock-in detection for pulsed electrically detected magnetic resonance”. *Review of Scientific Instruments* 83.4 (2012), p. 043907.

[30] Phila Rembold, Nimba Oshnik, Matthias M Müller, et al. “Introduction to quantum optimal control for quantum sensing with nitrogen-vacancy centers in diamond”. *AVS Quantum Science* 2.2 (2020), p. 024701.

[31] R.F. Davis. “Silicon Carbide”. *Reference Module in Materials Science and Materials Engineering*. Elsevier, 2017.

[32] Alberto Boretti. “Silicon carbide’s quantum aspects”. *Nature Photonics* 8.2 (2014), pp. 88–90.

[33] Tsunenobu Kimoto and James A Cooper. *Fundamentals of Silicon Carbide Technology: Growth, Characterization, Devices and Applications*. John Wiley & Sons, 2014.

[34] JB Casady and R Wayne Johnson. “Status of silicon carbide (SiC) as a wide-bandgap semiconductor for high-temperature applications: A review”. *Solid-State Electronics* 39.10 (1996), pp. 1409–1422.

[35] Lynnette D Madsen. “Formation of ohmic contacts to α-SiC and their impact on devices”. *Journal of electronic materials* 30.10 (2001), pp. 1353–1360.

[36] Robert J Trew, J-B Yan, and Philip M Mock. “The potential of diamond and SiC electronic devices for microwave and millimeter-wave power applications”. *Proceedings of the IEEE* 79.5 (1991), pp. 598–620.

[37] D Riedel, F Fuchs, H Kraus, et al. “Resonant addressing and manipulation of silicon vacancy qubits in silicon carbide”. *Physical review letters* 109.22 (2012), p. 226402.

[38] SG Carter, ÖO Soykal, Pratibha Dev, Sophia E Economou, and ER Glaser. “Spin coherence and echo modulation of the silicon vacancy in 4 H- SiC at room temperature”. *Physical Review B* 92.16 (2015), p. 161202.

[39] N Mizuochi, S Yamasaki, H Takizawa, et al. “Continuous-wave and pulsed EPR study of the negatively charged silicon vacancy with S= 3 2 and C 3 v symmetry in n-type 4 H- SiC”. *Physical Review B* 66.23 (2002), p. 235202.

[40] Alexandre Bourassa, Christopher P Anderson, Kevin C Miao, et al. “Entanglement and control of single nuclear spins in isotopically engineered silicon carbide”. *Nature Materials* 19.12 (2020), pp. 1319–1325.

[41] David J Christle, Abram L Falk, Paolo Andrich, et al. “Isolated electron spins in silicon carbide with millisecond coherence times”. *Nature materials* 14.2 (2015), pp. 160–163.

[42] Alexander Lohrmann, Timothy James Karle, Vikas Kanayalal Sewani, et al. “Integration of single-photon emitters into 3C-SiC microdisk resonators”. *ACS Photonics* 4.3 (2017), pp. 462–468.

[43] Bennett B Goldberg, SB Ippolito, Lukas Novotny, Zhiheng Liu, and MS Unlu. “Immersion lens microscopy of photonic nanostructures and quantum dots”. *IEEE Journal of Selected Topics in Quantum Electronics* 8.5 (2002), pp. 1051–1059.

[44] A Lohrmann, N Iwamoto, Z Bodrog, et al. “Single-photon emitting diode in silicon carbide”. *Nature communications* 6 (2015), p. 7783.

[45] Alexander Lohrmann, BC Johnson, JC McCallum, and Stefania Castelletto. “A review on single photon sources in silicon carbide”. *Reports on Progress in Physics* 80.3 (2017), p. 034502.

[46] Brett C Johnson, Judith Wörle, Daniel Haasmann, et al. “Optically Active Defects at the Si C/Si O 2 Interface”. *Physical Review Applied* 12.4 (2019), p. 044024.

[47] GR Fisher and P Barnes. “Towards a unified view of polytypism in silicon carbide”. *Philosophical Magazine B* 61.2 (1990), pp. 217–236.

[48] Simon M Sze and Kwok K Ng. *Physics of semiconductor devices*. John wiley & sons, 2006.

[49] Chris JH Wort and Richard S Balmer. “Diamond as an electronic material”. *Materials today* 11.1-2 (2008), pp. 22–28.

[50] Anke Krueger. *Carbon materials and nanotechnology*. John Wiley & Sons, 2010.

[51] Lewis S Ramsdell. “Studies on silicon carbide”. *American Mineralogist: Journal of Earth and Planetary Materials* 32.1-2 (1947), pp. 64–82.

[52] M Ikeda, H Matsunami, and T Tanaka. “Site effect on the impurity levels in 4 H, 6 H, and 1 5 R SiC”. *Physical Review B* 22.6 (1980), p. 2842.

[53] DJ Larkin. “SiC dopant incorporation control using site-competition CVD”. *physica status solidi (b)* 202.1 (1997), pp. 305–320.

[54] Evgeniy N Mokhov. “Doping of SiC crystals during sublimation growth and diffusion”. *Crystal Growth*. IntechOpen, 2018.

[55] T Troffer, M Schadt, T Frank, et al. “Doping of SiC by implantation of boron and aluminum”. *physica status solidi (a)* 162.1 (1997), pp. 277–298.

[56] Mulpuri V Rao. “Maturing ion-implantation technology and its device applications in SiC”. *Solid-State Electronics* 47.2 (2003), pp. 213–222.

[57] MA Capano, S Ryu, MR Melloch, JA Cooper, and MR Buss. “Dopant activation and surface morphology of ion implanted 4H-and 6H-silicon carbide”. *Journal of Electronic Materials* 27.4 (1998), pp. 370–376.

[58] XD Chen, CC Ling, S Fung, et al. “Beryllium implantation induced deep level defects in p-type 6H–silicon carbide”. *Journal of applied physics* 93.5 (2003), pp. 3117–3119.

[59] Dai Okamoto, Hiroshi Yano, Yuki Oshiro, et al. “Investigation of near-interface traps generated by NO direct oxidation in C-face 4H-SiC metal–oxide–semiconductor structures”. *Applied physics express* 2.2 (2009), p. 021201.

[60] Hiroshi Yano, Yuki Oshiro, Dai Okamoto, Tomoaki Hatayama, and Takashi Fuyuki. “Instability of 4H-SiC MOSFET characteristics due to interface traps with long time constants”. *Materials Science Forum*. Vol. 679. Trans Tech Publ. 2011, pp. 603–606.

[61] VV Afanasev, M Bassler, G Pensl, and M Schulz. “Intrinsic SiC/SiO2 interface states”. *physica status solidi (a)* 162.1 (1997), pp. 321–337.

[62] Daniel M Fleetwood and Ronald D Schrimpf. *Defects in microelectronic materials and devices*. CRC press, 2008.

[63] Edward H Nicollian and John R Brews. *MOS (metal oxide semiconductor) physics and technology*. Vol. 1987. Wiley New York, 1982.

[64] EH Poindexter, GJ Gerardi, M-E Rueckel, et al. “Electronic traps and P b centers at the Si/SiO2 interface: Band-gap energy distribution”. *Journal of Applied Physics* 56.10 (1984), pp. 2844–2849.

[65] Gary J Gerardi, Edward H Poindexter, Philip J Caplan, and Noble M Johnson. “Interface traps and P b centers in oxidized (100) silicon wafers”. *Applied Physics Letters* 49.6 (1986), pp. 348–350.

[66] Peyush Pande, Daniel Haasmann, Jisheng Han, et al. “Electrical characterization of SiC MOS capacitors: A critical review”. *Microelectronics Reliability* 112 (2020), p. 113790.

[67] Jan M Knaup, Peter Deák, Thomas Frauenheim, et al. “Theoretical study of the mechanism of dry oxidation of 4 H-SiC”. *Physical Review B* 71.23 (2005), p. 235321.

[68] Fabien Devynck, Audrius Alkauskas, Peter Broqvist, and Alfredo Pasquarello. “Charge transition levels of carbon-, oxygen-, and hydrogen-related defects at the SiC/SiO 2 interface through hybrid functionals”. *Physical Review B* 84.23 (2011), p. 235320.

[69] S Dhar, XD Chen, PM Mooney, JR Williams, and Leonard C Feldman. “Ultrashallow defect states at Si O 2/ 4 H–Si C interfaces”. *Applied Physics Letters* 92.10 (2008), p. 102112.

[70] Halldór Örn Ólafsson, Einar Ö Sveinbjörnsson, TE Rudenko, et al. “A study of the shallow electron traps at the 4H-SiC/SiO2 interface”. *Materials Science Forum*. Vol. 433. Trans Tech Publ. 2003, pp. 547–550.

[71] Naoya Iwamoto and Bengt G Svensson. “Point defects in silicon carbide”. *Semiconductors and Semimetals*. Vol. 91. Elsevier, 2015, pp. 369–407.

[72] C Kasper, D Klenkert, Z Shang, et al. “Influence of irradiation on defect spin coherence in silicon carbide”. *Physical Review Applied* 13.4 (2020), p. 044054.

[73] Takahide Umeda, Mitsuo Okamoto, Hironori Yoshioka, et al. “Interface Defects in C-face 4H-SiC MOSFETs: An Electrically-Detected-Magnetic-Resonance Study”. *ECS Transactions* 80.1 (2017), p. 147.

[74] Ryan J Waskiewicz, Mark A Anders, Patrick M Lenahan, and Aivars J Lelis. “Ionizing radiation effects in 4H-SiC nMOSFETs studied with electrically detected magnetic resonance”. *IEEE Transactions on Nuclear Science* 64.1 (2016), pp. 197–203.

[75] Stefania Castelletto, Ahmed Fahad M Almutairi, K Kumagai, et al. “Photoluminescence in hexagonal silicon carbide by direct femtosecond laser writing”. *Optics letters* 43.24 (2018), pp. 6077–6080.

[76] Cheng-Tyng Yen, Chien-Chung Hung, Hsiang-Ting Hung, et al. “Negative bias temperature instability of SiC MOSFET induced by interface trap assisted hole trapping”. *Applied Physics Letters* 108.1 (2016), p. 012106.

[77] T Wimbauer, BK Meyer, A Hofstaetter, A Scharmann, and H Overhof. “Negatively charged Si vacancy in 4 H SiC: A comparison between theory and experiment”. *Physical Review B* 56.12 (1997), p. 7384.

[78] Nguyen Tien Son, Pontus Stenberg, Valdas Jokubavicius, et al. “Ligand hyperfine interactions at silicon vacancies in 4H-SiC”. *Journal of Physics: Condensed Matter* 31.19 (2019), p. 195501.

[79] NT Son, Patrick Carlsson, J Ul Hassan, et al. “Divacancy in 4H-SiC”. *Physical review letters* 96.5 (2006), p. 055501.

[80] K Maier, J Schneider, W Wilkening, S Leibenzeder, and R Stein. “Electron spin resonance studies of transition metal deep level impurities in SiC”. *Materials Science and Engineering: B* 11.1-4 (1992), pp. 27–30.

[81] J Baur, M Kunzer, and J Schneider. “Transition metals in SiC polytypes, as studied by magnetic resonance techniques”. *physica status solidi (a)* 162.1 (1997), pp. 153–172.

[82] U Gerstmann, E Rauls, Th Frauenheim, and H Overhof. “Formation and annealing of nitrogen-related complexes in SiC”. *Physical Review B* 67.20 (2003), p. 205202.

[83] A Csóré, HJ Von Bardeleben, JL Cantin, and A Gali. “Characterization and formation of NV centers in 3 C, 4 H, and 6 H SiC: An ab initio study”. *Physical Review B* 96.8 (2017), p. 085204.

[84] HJ Von Bardeleben, JL Cantin, A Csóré, et al. “NV centers in 3 C, 4 H, and 6 H silicon carbide: A variable platform for solid-state qubits and nanosensors”. *Physical Review B* 94.12 (2016), p. 121202.

[85] HJ Von Bardeleben, JL Cantin, E Rauls, and U Gerstmann. “Identification and magneto-optical properties of the NV center in 4 H- SiC”. *Physical Review B* 92.6 (2015), p. 064104.

[86] CJ Cochrane, Patrick M Lenahan, and AJ Lelis. “Identification of a silicon vacancy as an important defect in 4H SiC metal oxide semiconducting field effect transistor using spin dependent recombination”. *Applied Physics Letters* 100.2 (2012), p. 023509.

[87] MA Anders, Patrick M Lenahan, and AJ Lelis. “Multi-resonance frequency spin dependent charge pumping and spin dependent recombination-applied to the 4H-SiC/SiO2 interface”. *Journal of Applied Physics* 122.23 (2017), p. 234503.

[88] Mark A Anders, Patrick M Lenahan, Nicholas J Harmon, and Michael E Flatté. “A technique to measure spin-dependent trapping events at the metal–oxide–semiconductor field-effect transistor interface: Near zero field spin-dependent charge pumping”. *Journal of Applied Physics* 128.24 (2020), p. 244501.

[89] T Umeda, T Kobayashi, M Sometani, et al. “Carbon dangling-bond center (carbon P b center) at 4H-SiC (0001)/SiO2 interface”. *Applied Physics Letters* 116.7 (2020), p. 071604.

[90] T Umeda, G-W Kim, T Okuda, et al. “Interface carbon defects at 4H-SiC (0001)/SiO2 interfaces studied by electron-spin-resonance spectroscopy”. *Applied Physics Letters* 113.6 (2018), p. 061605.

[91] T Umeda, Y Nakano, E Higa, et al. “Electron-spin-resonance and electrically detected-magnetic-resonance characterization on P bC center in various 4H-SiC (0001)/SiO2 interfaces”. *Journal of Applied Physics* 127.14 (2020), p. 145301.

[92] Hisayoshi Itoh, Masahito Yoshikawa, Isamu Nashiyama, et al. “Radiation induced defects in CVD-grown 3C-SiC”. *IEEE Transactions on nuclear science* 37.6 (1990), pp. 1732–1738.

[93] E Sörman, NT Son, WM Chen, et al. “Silicon vacancy related defect in 4H and 6H SiC”. *Physical Review B* 61.4 (2000), p. 2613.

[94] Matthias Niethammer, Matthias Widmann, Torsten Rendler, et al. “Coherent electrical readout of defect spins in silicon carbide by photo-ionization at ambient conditions”. *Nature communications* 10.1 (2019), pp. 1–8.

[95] MA Anders, PM Lenahan, and AJ Lelis. “Are dangling bond centers important interface traps in 4H-SiC metal oxide semiconductor field effect transistors?” *Applied Physics Letters* 109.14 (2016), p. 142106.

[96] Gernot Gruber, Jonathon Cottom, Robert Meszaros, et al. “Electrically detected magnetic resonance of carbon dangling bonds at the Si-face 4H-SiC/SiO2 interface”. *Journal of Applied Physics* 123.16 (2018), p. 161514.

[97] J Cottom, G Gruber, G Pobegen, T Aichinger, and AL Shluger. “Recombination defects at the 4H-SiC/SiO2 interface investigated with electrically detected magnetic resonance and ab initio calculations”. *Journal of Applied Physics* 124.4 (2018), p. 045302.

[98] Jean-Louis Cantin, HJ Von Bardeleben, Y Shishkin, et al. “Identification of the Carbon Dangling Bond Center at the 4 H- S i C/S i O 2 Interface by an EPR Study in Oxidized Porous SiC”. *Physical review letters* 92.1 (2004), p. 015502.

[99] T Umeda, Y Kagoyama, K Tomita, et al. “Electrically detected-magnetic-resonance identifications of defects at 4H-SiC (000 1¯)/SiO2 interfaces with wet oxidation”. *Applied Physics Letters* 115.15 (2019), p. 151602.

[100] Takahide Umeda, Mitsuo Okamoto, Hironori Yoshioka, et al. “Interface Defects in C-face 4H-SiC MOSFETs: An Electrically-Detected-Magnetic-Resonance Study”. *ECS Transactions* 80.1 (2017), p. 147.

[101] Y Kagoyama, M Okamoto, T Yamasaki, et al. “Anomalous carbon clusters in 4H-SiC/SiO2 interfaces”. *Journal of Applied Physics* 125.6 (2019), p. 065302.

[102] T Umeda, J Ishoya, T Ohshima, et al. “Identification of positively charged carbon antisite-vacancy pairs in 4 H- Si C”. *Physical Review B* 75.24 (2007), p. 245202.

[103] T Umeda, NT Son, Janzen Isoya, et al. “Identification of the carbon antisite-vacancy pair in 4 H-SiC”. *Physical review letters* 96.14 (2006), p. 145501.

[104] JW Steeds. “Photoluminescence study of the carbon antisite-vacancy pair in 4 H-and 6 H-SiC”. *Physical Review B* 80.24 (2009), p. 245202.

[105] William F Koehl, Bob B Buckley, F Joseph Heremans, Greg Calusine, and David D Awschalom. “Room temperature coherent control of defect spin qubits in silicon carbide”. *Nature* 479.7371 (2011), pp. 84–87.

[106] Stefania Castelletto, BC Johnson, Viktor Ivády, et al. “A silicon carbide room-temperature single-photon source”. *Nature materials* 13.2 (2014), pp. 151–156.

[107] Y Abe, T Umeda, M Okamoto, et al. “Single photon sources in 4H-SiC metal-oxide-semiconductor field-effect transistors”. *Applied Physics Letters* 112.3 (2018), p. 031105.

[108] Thomas Aichinger, Patrick M Lenahan, Blair R Tuttle, and Dethard Peters. “A nitrogen-related deep level defect in ion implanted 4H-SiC pn junctions—A spin dependent recombination study”. *Applied Physics Letters* 100.11 (2012), p. 112113.

[109] J Cottom, Gernot Gruber, P Hadley, et al. “Recombination centers in 4H-SiC investigated by electrically detected magnetic resonance and ab initio modeling”. *Journal of Applied Physics* 119.18 (2016), p. 181507.

[110] Jun-Feng Wang, Fei-Fei Yan, Qiang Li, et al. “Coherent control of nitrogen-vacancy center spins in silicon carbide at room temperature”. *Physical review letters* 124.22 (2020), p. 223601.

[111] Pieter Zeeman. “On the Influence of Magnetism on the Nature of the Light Emitted by a Substance.” *The Astrophysical Journal* 5 (1897), p. 332.

[112] Peter J Mohr, David B Newell, and Barry N Taylor. “CODATA recommended values of the fundamental physical constants: 2014”. *Journal of Physical and Chemical Reference Data* 45.4 (2016), p. 043102.

[113] Gareth R Eaton, Sandra S Eaton, David P Barr, and Ralph T Weber. *Quantitative Epr*. Springer Science & Business Media, 2010.

[114] Felix Bloch. “Nuclear induction”. *Physical review* 70.7-8 (1946), p. 460.

[115] Harry M Assenheim. *Introduction to electron spin resonance*. Springer, 2014.

[116] G Feher. “Sensitivity considerations in microwave paramagnetic resonance absorption techniques”. *Bell System Technical Journal* 36.2 (1957), pp. 449–484.

[117] Julian Schwinger. “On quantum-electrodynamics and the magnetic moment of the electron”. *Physical Review* 73.4 (1948), p. 416.

[118] MHL Pryce. “A modified perturbation procedure for a problem in paramagnetism”. *Proceedings of the Physical Society. Section A* 63.1 (1950), p. 25.

[119] Matthias Widmann, Sang-Yun Lee, Torsten Rendler, et al. “Coherent control of single spins in silicon carbide at room temperature”. *Nature materials* 14.2 (2015), pp. 164–168.

[120] Marina Bennati. “EPR Interactions–Hyperfine Couplings”. *Emagres* (2007), pp. 271–282.

[121] Manfred Bucher. “The electron inside the nucleus: An almost classical derivation of the isotropic hyperfine interaction”. *European Journal of Physics* 21.1 (2000), p. 19.

[122] VR Kortan, C Şahin, and ME Flatté. “Nanometer-scale exchange interactions between spin centers in diamond”. *Physical Review B* 93.22 (2016), p. 220402.

[123] DR McCamey, H Huebl, MS Brandt, et al. “Electrically detected magnetic resonance in ion-implanted Si: P nanostructures”. *Applied Physics Letters* 89.18 (2006), p. 182115.

[124] Andrea Morello, Jarryd J Pla, Floris A Zwanenburg, et al. “Single-shot readout of an electron spin in silicon”. *Nature* 467.7316 (2010), pp. 687–691.

[125] J Schmidt and I Solomon. “Modulation de la photoconductivité dans le silicium à basse température par résonance magnétique électronique des impuretés peu profondes”. *COMPTES RENDUS HEBDOMADAIRES DES SEANCES DE L ACADEMIE DES SCIENCES SERIE B* 263.2 (1966), p. 169.

[126] Andre R Stegner, Christoph Boehme, Hans Huebl, et al. “Electrical detection of coherent 31 P spin quantum states”. *Nature Physics* 2.12 (2006), pp. 835–838.

[127] JT Ryan, Patrick M Lenahan, AT Krishnan, and S Krishnan. “Spin dependent tunneling spectroscopy in 1.2 nm dielectrics”. *Journal of Applied Physics* 108.6 (2010), p. 064511.

[128] MC Chen and DV Lang. “Observation of spin-dependent thermal emission from deep levels in semiconductors”. *Physical review letters* 51.5 (1983), p. 427.

[129] DD Thornton and A Honig. “Shallow-donor negative ions and spin-polarized electron transport in silicon”. *Physical Review Letters* 30.19 (1973), p. 909.

[130] Cheuk C Lo, J Bokor, T Schenkel, AM Tyryshkin, and SA Lyon. “Spin-dependent scattering off neutral antimony donors in Si 28 field-effect transistors”. *Applied Physics Letters* 91.24 (2007), p. 242106.

[131] LH Willems van Beveren, H Huebl, DR McCamey, et al. “Broadband electrically detected magnetic resonance of phosphorus donors in a silicon field-effect transistor”. *Applied Physics Letters* 93.7 (2008), p. 072102.

[132] Genshiro Kawachi, Carlos FO Graeff, Martin S Brandt, and Martin Stutzmann. “Carrier transport in amorphous silicon-based thin-film transistors studied by spin-dependent transport”. *Physical Review B* 54.11 (1996), p. 7957.

[133] AR Stegner, RN Pereira, K Klein, et al. “Electronic transport in phosphorus-doped silicon nanocrystal networks”. *Physical review letters* 100.2 (2008), p. 026803.

[134] Daniel J Lepine. “Spin-dependent recombination on silicon surface”. *Physical Review B* 6.2 (1972), p. 436.

[135] Jun John Sakurai and Eugene D Commins. *Modern quantum mechanics, revised edition*. 1995.

[136] Stefan Stoll and Arthur Schweiger. “EasySpin, a comprehensive software package for spectral simulation and analysis in EPR”. *Journal of magnetic resonance* 178.1 (2006), pp. 42–55.

[137] Christoph Boehme and Klaus Lips. “Theory of time-domain measurement of spin-dependent recombination with pulsed electrically detected magnetic resonance”. *Physical Review B* 68.24 (2003), p. 245105.

[138] R Haberkorn and W Dietz. “Theory of spin-dependent recombination in semiconductors”. *Solid State Communications* 35.6 (1980), pp. 505–508.

[139] AV Barabanov, OV Tretiak, and VA L’vov. “Complete theoretical analysis of the Kaplan-Solomon-Mott mechanism of spin-dependent recombination in semiconductors”. *Physical Review B* 54.4 (1996), p. 2571.

[140] AG Redfield. “IBM J. Res. De V elop. 1957, 1, 19”. *Adv. Magn. Reson* 1 (1965), p. 1.

[141] F Klotz, H Huebl, D Heiss, et al. “Coplanar stripline antenna design for optically detected magnetic resonance on semiconductor quantum dots”. *Review of Scientific Instruments* 82.7 (2011), p. 074707.

[142] Andreas Bogner, Carsten Steiner, Stefanie Walter, et al. “Planar microstrip ring resonators for microwave-based gas sensing: Design aspects and initial transducers for humidity and ammonia sensing”. *Sensors* 17.10 (2017), p. 2422.

[143] Gajadhar Joshi, Richards Miller, Lillie Ogden, et al. “Separating hyperfine from spin-orbit interactions in organic semiconductors by multi-octave magnetic resonance using coplanar waveguide microresonators”. *Applied Physics Letters* 109.10 (2016), p. 103303.

[144] Stefan Machlup. “Noise in semiconductors: spectrum of a two-parameter random signal”. *Journal of Applied Physics* 25.3 (1954), pp. 341–343.

[145] Douglas MG Leite, Augusto Batagin-Neto, Oswaldo Nunes-Neto, Jorge A Gómez, and Carlos FO Graeff. “Electrically detected magnetic resonance modeling and fitting: An equivalent circuit approach”. *Journal of Applied Physics* 115.3 (2014), p. 034510.

[146] CJ Cochrane. “On the performance enhancement of adaptive signal averaging: A means for improving the sensitivity and rate of data acquisition in magnetic resonance and other analytical measurements”. *Review of Scientific Instruments* 83.10 (2012), p. 105108.

[147] CJ Cochrane and PM Lenahan. “Real time exponentially weighted recursive least squares adaptive signal averaging for enhancing the sensitivity of continuous wave magnetic resonance”. *Journal of Magnetic Resonance* 195.1 (2008), pp. 17–22.

[148] Christopher G Brinton and Donald J Hirsh. “Note: Sensitivity enhancement in continuous-wave electron paramagnetic resonance: Adaptive signal averaging versus a moving average”. *Review of Scientific Instruments* 81.2 (2010), p. 026102.

[149] Christoph Boehme and Klaus Lips. “The ultra-sensitive electrical detection of spin-Rabi oscillation at paramagnetic defects”. *Physica B: Condensed Matter* 376 (2006), pp. 930–935.

[150] S-Y Paik, S-Y Lee, WJ Baker, DR McCamey, and C Boehme. “T 1 and T 2 spin relaxation time limitations of phosphorous donor electrons near crystalline silicon to silicon dioxide interface defects”. *Physical Review B* 81.7 (2010), p. 075214.

[151] Vikas K Sewani, Hyma H Vallabhapurapu, Yang Yang, et al. “Coherent control of NV- centers in diamond in a quantum teaching lab”. *American Journal of Physics* 88.12 (2020), pp. 1156–1169.

[152] Michal Gulka, Emilie Bourgeois, Jaroslav Hruby, et al. “Pulsed photoelectric coherent manipulation and detection of N- V center spins in diamond”. *Physical Review Applied* 7.4 (2017), p. 044032.

[153] CH Wu, MH Hsu, KL Chen, et al. “A highly sensitive YBCO serial SQUID magnetometer with a flux focuser”. *Superconductor Science and Technology* 19.5 (2006), S246.

[154] F Baudenbacher, LE Fong, JR Holzer, and M Radparvar. “Monolithic low-transition-temperature superconducting magnetometers for high resolution imaging magnetic fields of room temperature samples”. *Applied Physics Letters* 82.20 (2003), pp. 3487–3489.

[155] JR Kirtley, MB Ketchen, KG Stawiasz, et al. “High-resolution scanning SQUID microscope”. *Applied Physics Letters* 66.9 (1995), pp. 1138–1140.

[156] Adarsh Sandhu, Kouichi Kurosawa, Munir Dede, and Ahmet Oral. “50 nm Hall sensors for room temperature scanning Hall probe microscopy”. *Japanese journal of applied physics* 43.2R (2004), p. 777.

[157] Y Sugiyama and S Kataoka. “S/N study of micro-Hall sensors made of single crystal InSb and GaAs”. *Sensors and Actuators* 8.1 (1985), pp. 29–38.

[158] Adarsh Sandhu, Hiroshi Masuda, Ahmet Oral, and Simon J Bending. “Room temperature magnetic imaging of magnetic storage media and garnet epilayers in the presence of external magnetic fields using a sub-micron GaAs SHPM”. *Journal of crystal growth* 227 (2001), pp. 899–905.

[159] Balazs Janossy, Youcef Haddab, Jean-Michel Villiot, and Rade S Popovic. “Hot carrier Hall devices in CMOS technology”. *Sensors and Actuators A: Physical* 71.3 (1998), pp. 172–178.

[160] Vishal Shah, Svenja Knappe, Peter DD Schwindt, and John Kitching. “Sub-picotesla atomic magnetometry with a microfabricated vapour cell”. *Nature Photonics* 1.11 (2007), pp. 649–652.

[161] IK Kominis, TW Kornack, JC Allred, and Michael V Romalis. “A subfemtotesla multichannel atomic magnetometer”. *Nature* 422.6932 (2003), pp. 596–599.

[162] C Hinnrichs, C Pels, and M Schilling. “Noise and linearity of a fluxgate magnetometer in racetrack geometry”. *Journal of Applied Physics* 87.9 (2000), pp. 7085–7087.

[163] Chih-Cheng Lu, Jeff Huang, Po-Kai Chiu, Shih-Liang Chiu, and Jen-Tzong Jeng. “High-sensitivity low-noise miniature fluxgate magnetometers using a flip chip conceptual design”. *Sensors* 14.8 (2014), pp. 13815–13829.

[164] F Primdahl, P Ripka, JR Petersen, and OV Nielsen. “The sensitivity parameters of the short-circuited fluxgate”. *Measurement Science and Technology* 2.11 (1991), p. 1039.

[165] Jennifer M Schloss, John F Barry, Matthew J Turner, and Ronald L Walsworth. “Simultaneous broadband vector magnetometry using solid-state spins”. *Physical Review Applied* 10.3 (2018), p. 034044.

[166] Huijie Zheng, Zhiyin Sun, Georgios Chatzidrosos, et al. “Microwave-free vector magnetometry with nitrogen-vacancy centers along a single axis in diamond”. *Physical Review Applied* 13.4 (2020), p. 044023.

[167] Huijie Zheng, Jingyan Xu, Geoffrey Z Iwata, et al. “Zero-field magnetometry based on nitrogen-vacancy ensembles in diamond”. *Physical Review Applied* 11.6 (2019), p. 064068.

[168] Sepehr Ahmadi, Haitham AR El-Ella, Jørn OB Hansen, Alexander Huck, and Ulrik L Andersen. “Pump-enhanced continuous-wave magnetometry using nitrogen-vacancy ensembles”. *Physical Review Applied* 8.3 (2017), p. 034001.

[169] Matthias Niethammer, Matthias Widmann, Sang-Yun Lee, et al. “Vector Magnetometry Using Silicon Vacancies in 4 H-SiC Under Ambient Conditions”. *Physical Review Applied* 6.3 (2016), p. 034001.

[170] John BS Abraham, Cameron Gutgsell, Dalibor Todorovski, et al. “nanoTesla magnetometry with the silicon vacancy in silicon carbide”. *Physical Review Applied* 15.6 (2021), p. 064022.

[171] Albrecht Jander and Pallavi Dhagat. “Sensitivity analysis of magnetic field sensors utilizing spin-dependent recombination in silicon diodes”. *Solid-state electronics* 54.11 (2010), pp. 1479–1484.

[172] Donggyu Kim, Mohamed I Ibrahim, Christopher Foy, et al. “A CMOS-integrated quantum sensor based on nitrogen–vacancy centres”. *Nature Electronics* 2.7 (2019), pp. 284–289.

[173] James Lenz and S Edelstein. “Magnetic sensors and their applications”. *IEEE Sensors journal* 6.3 (2006), pp. 631–649.

[174] Didier Robbes. “Highly sensitive magnetometers—a review”. *Sensors and Actuators A: Physical* 129.1-2 (2006), pp. 86–93.

[175] Stefan Forstner, Joachim Knittel, Eoin Sheridan, et al. “Sensitivity and performance of cavity optomechanical field sensors”. *Photonic Sensors* 2.3 (2012), pp. 259–270.

[176] FC Rong, GJ Gerardi, WR Buchwald, et al. “Electrically detected magnetic resonance of a transition metal related recombination center in Si p–n diodes”. *Applied physics letters* 60.5 (1992), pp. 610–612.

[177] B Stich, S Gruelich-Weber, J-M Spaeth, and H Overhof. “Electrically detected electron paramagnetic resonance of a deep recombination centre in a silicon diode”. *Semiconductor science and technology* 8.7 (1993), p. 1385.

[178] Takeshi Ohshima and Shinobu Onodaa. “Radiation Resistance of Semiconductors”. *Radiation Applications*. Springer, 2018, pp. 81–116.

[179] Ben G Streetman and Sanjay Banerjee. *Solid state electronic devices*. Prentice-Hall of india, 2001.

[180] Gerhard Heinzel, Albrecht Rüdiger, and Roland Schilling. “Spectrum and spectral density estimation by the Discrete Fourier transform (DFT), including a comprehensive list of window functions and some new at-top windows” (2002).

[181] Harry Nyquist. “Certain topics in telegraph transmission theory”. *Transactions of the American Institute of Electrical Engineers* 47.2 (1928), pp. 617–644.

[182] James F Ziegler, JP Biersack, and U Littmark. “The stopping and range of ions in matter, Vol. 1”. *1, Pergamon Press, New York* (1985).

[183] Y Negoro, K Katsumoto, T Kimoto, and H Matsunami. “Electronic behaviors of high-dose phosphorus-ion implanted 4H–SiC (0001)”. *Journal of Applied Physics* 96.1 (2004), pp. 224–228.

[184] Yoshiaki Kamigaki, Takao Miyazaki, Naotsugu Yoshihiro, Kikuo Watanabe, and Ken'etsu Yokogawa. "Two signals in electrically detected magnetic resonance of platinum-doped silicon p–n junctions". *Journal of applied physics* 84.4 (1998), pp. 2193–2198.

[185] Z Xiong and DJ Miller. "Detailed investigation of a nonradiative recombination center in Si by electrically detected magnetic resonance". *Journal of applied physics* 77.10 (1995), pp. 5201–5207.

[186] CJ Cochrane and PM Lenahan. "Detection of interfacial Pb centers in Si/SiO2 metal-oxide-semiconducting field-effect transistors via zero-field spin dependent recombination with observation of precursor pair spin-spin interactions". *Applied Physics Letters* 103.5 (2013), p. 053506.

[187] Sandra S Eaton, Kundalika M More, Bhimrao M Sawant, and Gareth R Eaton. "Use of the ESR half-field transition to determine the interspin distance and the orientation of the interspin vector in systems with two unpaired electrons". *Journal of the American Chemical Society* 105.22 (1983), pp. 6560–6567.

[188] Corey J Cochrane and Patrick M Lenahan. "Spin counting in electrically detected magnetic resonance via low-field defect state mixing". *Applied Physics Letters* 104.9 (2014), p. 093503.

[189] Gregory Breit and II Rabi. "Measurement of nuclear spin". *Physical Review* 38.11 (1931), p. 2082.

[190] Takashi Takiya and Tsuyoshi Uchiyama. "Common-mode magnetic field rejection-type magneto-impedance gradiometer". *Journal of International Council on Electrical Engineering* 7.1 (2017), pp. 1–6.

[191] Franck HL Koppens, Joshua A Folk, Jeroen M Elzerman, et al. "Control and detection of singlet-triplet mixing in a random nuclear field". *Science* 309.5739 (2005), pp. 1346–1350.

[192] Frank HL Koppens, Christo Buizert, Klaas-Jan Tielrooij, et al. "Driven coherent oscillations of a single electron spin in a quantum dot". *Nature* 442.7104 (2006), pp. 766–771.

[193] VN Prigodin, JD Bergeson, DM Lincoln, and AJ Epstein. "Anomalous room temperature magnetoresistance in organic semiconductors". *Synthetic Metals* 156.9-10 (2006), pp. 757–761.

[194] Robert L White. "Giant magnetoresistance materials and their potential as read head sensors". *IEEE transactions on magnetics* 30.2 (1994), pp. 346–352.

[195] Yifei Wang, Kevser Sahin-Tiras, Nicholas J Harmon, Markus Wohlgenannt, and Michael E Flatté. “Immense magnetic response of exciplex light emission due to correlated spin-charge dynamics”. *Physical Review X* 6.1 (2016), p. 011011.

[196] Elias B Frantz, Nicholas J Harmon, Stephen R McMillan, et al. “Extraction of isotropic electron-nuclear hyperfine coupling constants of paramagnetic point defects from near-zero field magnetoresistance spectra via least squares fitting to models developed from the stochastic quantum Liouville equation”. *Journal of Applied Physics* 128.12 (2020), p. 124504.

[197] Elias B Frantz, David J Michalak, Nicholas J Harmon, et al. “Electrically detected magnetic resonance and near-zero field magnetoresistance in 28Si/28SiO2”. *Journal of Applied Physics* 130.6 (2021), p. 065701.

[198] Elias B Frantz, David J Michalak, Nicholas J Harmon, et al. “Effects of 29Si and 1H on the near-zero field magnetoresistance response of Si/SiO2 interface states: Implications for oxide tunneling currents”. *Applied Physics Letters* 119.18 (2021), p. 184101.

[199] Thomas Aichinger and Patrick M Lenahan. “Giant amplification of spin dependent recombination at heterojunctions through a gate controlled bipolar effect”. *Applied Physics Letters* 101.8 (2012), p. 083504.

[200] BC Bittel, Patrick M Lenahan, Jason T Ryan, Jody Fronheiser, and AJ Lelis. “Spin dependent charge pumping in SiC metal-oxide-semiconductor field-effect-transistors”. *Applied Physics Letters* 99.8 (2011), p. 083504.

[201] Predrag Habas, Zoran Prijic, Dragan Pantiċ, and Ninoslav D Stojadinoviċ. “Charge-pumping characterization of SiO/sub 2//Si interface in virgin and irradiated power VDMOSFETs”. *IEEE transactions on electron devices* 43.12 (1996), pp. 2197–2209.

[202] Petar M Igic. “Determination of the surface states trap density in power VDMOSFETs using charge pumping technique”. *Proceedings of International Conference on Microelectronics*. Vol. 1. IEEE. 1995, pp. 255–258.

[203] G Prevost, P Augier, and J-M Palau. “The use of charge-pumping for characterizing irradiated power MOSFETs”. *IEEE Transactions on Nuclear Science* 43.3 (1996), pp. 858–864.

[204] Xintian Zhou, Hongyuan Su, Ruifeng Yue, et al. “A deep insight into the degradation of 1.2-kV 4H-SiC MOSFETs under repetitive unclamped inductive switching stresses”. *IEEE Transactions on Power Electronics* 33.6 (2017), pp. 5251–5261.

[205] SC Witczak, KF Galloway, RD Schrimpf, et al. “The determination of Si-SiO/sub 2/interface trap density in irradiated four-terminal VDMOSFETs using charge pumping”. *IEEE Transactions on Nuclear Science* 43.6 (1996), pp. 2558–2564.

[206] J Stephen Brugler and Paul GA Jespers. “Charge pumping in MOS devices”. *IEEE Transactions on Electron Devices* 16.3 (1969), pp. 297–302.

[207] Guido Groeseneken, Herman E Maes, Nicolas Beltran, and Roger F De Keersmaecker. “A reliable approach to charge-pumping measurements in MOS transistors”. *IEEE Transactions on Electron Devices* 31.1 (1984), pp. 42–53.

[208] Dai Okamoto, Hiroshi Yano, Tomoaki Hatayama, Yukiharu Uraoka, and Takashi Fuyuki. “Analysis of anomalous charge-pumping characteristics on 4H-SiC MOSFETs”. *IEEE transactions on electron devices* 55.8 (2008), pp. 2013–2020.

[209] Masahiro Hori, Toshiaki Tsuchiya, and Yukinori Ono. “Improvement of charge-pumping electrically detected magnetic resonance and its application to silicon metal–oxide–semiconductor field-effect transistor”. *Applied Physics Express* 10.1 (2016), p. 015701.

[210] LJ Passmore, K Sarpatwari, SA Suliman, et al. “Modified three terminal charge pumping technique applied to vertical transistor structures”. *Journal of Vacuum Science & Technology B: Microelectronics and Nanometer Structures Processing, Measurement, and Phenomena* 23.5 (2005), pp. 2189–2193.

[211] Kipp J Van Schooten, Douglas L Baird, Mark E Limes, John M Lupton, and Christoph Boehme. “Probing long-range carrier-pair spin–spin interactions in a conjugated polymer by detuning of electrically detected spin beating”. *Nature communications* 6.1 (2015), pp. 1–9.

[212] Nazareno Donato and Florin Udrea. “Static and dynamic effects of the incomplete ionization in superjunction devices”. *IEEE Transactions on Electron Devices* 65.10 (2018), pp. 4469–4475.

[213] Andrei V Los and Michael S Mazzola. “Influence of carrier freeze-out on SiC Schottky junction admittance”. *Journal of electronic materials* 30.3 (2001), pp. 235–241.

[214] Victor M Acosta, Erik Bauch, Micah P Ledbetter, et al. “Temperature dependence of the nitrogen-vacancy magnetic resonance in diamond”. *Physical review letters* 104.7 (2010), p. 070801.

[215] X-D Chen, C-H Dong, F-W Sun, et al. “Temperature dependent energy level shifts of nitrogen-vacancy centers in diamond”. *Applied Physics Letters* 99.16 (2011), p. 161903.

[216] H Kraus, VA Soltamov, F Fuchs, et al. “Magnetic field and temperature sensing with atomic-scale spin defects in silicon carbide”. *Scientific reports* 4.1 (2014), pp. 1–8.

[217] Andreas Gottscholl, Matthias Diez, Victor Soltamov, et al. “Spin defects in hBN as promising temperature, pressure and magnetic field quantum sensors”. *Nature Communications* 12.1 (2021), pp. 1–8.

[218] Kan Hayashi, Yuichiro Matsuzaki, Takashi Taniguchi, et al. “Optimization of temperature sensitivity using the optically detected magnetic-resonance spectrum of a nitrogen-vacancy center ensemble”. *Physical Review Applied* 10.3 (2018), p. 034009.

[219] Jinming Lu, Felix Hoehne, Andre R Stegner, et al. “High-resolution electrical detection of free induction decay and Hahn echoes in phosphorus-doped silicon”. *Physical Review B* 83.23 (2011), p. 235201.

[220] L Dreher, F Hoehne, H Morishita, et al. “Pulsed low-field electrically detected magnetic resonance”. *Physical Review B* 91.7 (2015), p. 075314.

[221] Hans Huebl, Felix Hoehne, Benno Grolik, et al. “Spin echoes in the charge transport through phosphorus donors in silicon”. *Physical review letters* 100.17 (2008), p. 177602.

[222] Christoph Meier, Christian Teutloff, Jan Behrends, et al. “Triplet excitons as sensitive spin probes for structure analysis of extended defects in microcrystalline silicon”. *Physical Review B* 94.4 (2016), p. 045302.

[223] Felix Kraffert, Robert Steyrleuthner, Christoph Meier, Robert Bittl, and Jan Behrends. “Transient electrically detected magnetic resonance spectroscopy applied to organic solar cells”. *Applied Physics Letters* 107.4 (2015), 72_1.

[224] DR McCamey, HA Seipel, S-Y Paik, et al. “Spin Rabi flopping in the photocurrent of a polymer light-emitting diode”. *Nature materials* 7.9 (2008), pp. 723–728.

[225] H Morishita, WJ Baker, DP Waters, et al. “Mechanisms of spin-dependent dark conductivity in films of a soluble fullerene derivative under bipolar injection”. *Physical Review B* 89.12 (2014), p. 125311.

[226] MY Teferi, J Ogle, G Joshi, et al. “Tuning effective hyperfine fields in PEDOT: PSS thin films by doping”. *Physical Review B* 98.24 (2018), p. 241201.

[227] DR McCamey, KJ Van Schooten, WJ Baker, et al. “Hyperfine-field-mediated spin beating in electrostatically bound charge carrier pairs”. *Physical review letters* 104.1 (2010), p. 017601.

[228] Sang-Yun Lee, Seo-Young Paik, Dane R McCamey, et al. “Tuning hyperfine fields in conjugated polymers for coherent organic spintronics”. *Journal of the American Chemical Society* 133.7 (2011), pp. 2019–2021.

[229] Roland Nagy, Matthias Niethammer, Matthias Widmann, et al. “High-fidelity spin and optical control of single silicon-vacancy centres in silicon carbide”. *Nature communications* 10.1 (2019), pp. 1–8.

[230] Fei-Fei Yan, Jun-Feng Wang, Qiang Li, et al. “Coherent control of defect spins in silicon carbide above 550 K”. *Physical Review Applied* 10.4 (2018), p. 044042.

[231] David J Christle, Paul V Klimov, F Charles, et al. “Isolated spin qubits in SiC with a high-fidelity infrared spin-to-photon interface”. *Physical Review X* 7.2 (2017), p. 021046.

[232] T Murooka, M Shiigai, Y Hironaka, et al. “Photoelectrical detection of nitrogen-vacancy centers by utilizing diamond lateral p–i–n diodes”. *Applied Physics Letters* 118.25 (2021), p. 253502.

[233] Florian M Hrubesch, Georg Braunbeck, Martin Stutzmann, Friedemann Reinhard, and Martin S Brandt. “Efficient electrical spin readout of NV- centers in diamond”. *Physical review letters* 118.3 (2017), p. 037601.

[234] FM Hrubesch, G Braunbeck, A Voss, M Stutzmann, and MS Brandt. “Broadband electrically detected magnetic resonance using adiabatic pulses”. *Journal of Magnetic Resonance* 254 (2015), pp. 62–69.

[235] Alexander J Kupijai, Konstantin M Behringer, Florian G Schaeble, et al. “Bipolar polaron pair recombination in polymer/fullerene solar cells”. *Physical Review B* 92.24 (2015), p. 245203.

[236] Sebastian Schaefer, Kati Huebener, Wolfgang Harneit, et al. “Thin film engineering for N@ C60 quantum computers: Spin detection and device patterning approaches”. *Solid state sciences* 10.10 (2008), pp. 1314–1321.

[237] Xiaojie Liu, Henna Popli, Ohyun Kwon, et al. “Isotope Effect in the Magneto-Optoelectronic Response of Organic Light-Emitting Diodes Based on Donor–Acceptor Exciplexes”. *Advanced Materials* 32.48 (2020), p. 2004421.

[238] K Lips, C Boehme, and T Ehara. “The impact of the electron spin on charge carrier recombination–the example of amorphous silicon”. *Journal of Optoelectronics and Advanced Materials* 7.1 (2005), pp. 13–24.

[239] Gang-Qin Liu, Xin-Yu Pan, Zhan-Feng Jiang, Nan Zhao, and Ren-Bao Liu. "Controllable effects of quantum fluctuations on spin free-induction decay at room temperature". *Scientific reports* 2.1 (2012), pp. 1–5.

[240] Andreas Gottscholl, Matthias Diez, Victor Soltamov, et al. "Room temperature coherent control of spin defects in hexagonal boron nitride". *Science Advances* 7.14 (2021), eabf3630.

[241] A Dréau, M Lesik, L Rondin, et al. "Avoiding power broadening in optically detected magnetic resonance of single NV defects for enhanced dc magnetic field sensitivity". *Physical Review B* 84.19 (2011), p. 195204.

[242] David P Franke, Felix Hoehne, Leonid S Vlasenko, Kohei M Itoh, and Martin S Brandt. "Spin-dependent recombination involving oxygen-vacancy complexes in silicon". *Physical Review B* 89.19 (2014), p. 195207.

[243] WJ Baker, TL Keevers, JM Lupton, DR McCamey, and C Boehme. "Slow hopping and spin dephasing of Coulombically bound polaron pairs in an organic semiconductor at room temperature". *Physical review letters* 108.26 (2012), p. 267601.

[244] Richards Miller, KJ Van Schooten, H Malissa, et al. "Morphology effects on spin-dependent transport and recombination in polyfluorene thin films". *Physical Review B* 94.21 (2016), p. 214202.

[245] Matthew Groesbeck, Haoliang Liu, Marzieh Kavand, et al. "Separation of spin and charge transport in pristine π-conjugated polymers". *Physical review letters* 124.6 (2020), p. 067702.

[246] Edlyn V Levine, Matthew J Turner, Pauli Kehayias, et al. "Principles and techniques of the quantum diamond microscope". *Nanophotonics* 8.11 (2019), pp. 1945–1973.

[247] Saul Meiboom and David Gill. "Modified spin-echo method for measuring nuclear relaxation times". *Review of scientific instruments* 29.8 (1958), pp. 688–691.

[248] Kwok K Hung, Ping K Ko, Chenming Hu, and Yiu Chung Cheng. "Random telegraph noise of deep-submicrometer MOSFETs". *IEEE electron device letters* 11.2 (1990), pp. 90–92.

[249] ST Hsu. "Bistable noise in pn junctions". *Solid-State Electronics* 14.6 (1971), pp. 487–497.

[250] ST Hsu, RJ Whittier, and CA Mead. "Physical model for burst noise in semiconductor devices". *Solid-State Electronics* 13.7 (1970), pp. 1055–1071.

[251] TAG Eberlein, R Jones, Sven Öberg, and PR Briddon. “Density functional theory calculation of the D I optical center in SiC”. *Physical Review B* 74.14 (2006), p. 144106.

[252] Adam Gali, P Deák, E Rauls, et al. “Correlation between the antisite pair and the D I center in SiC”. *Physical Review B* 67.15 (2003), p. 155203.

[253] NT Son, E Sörman, WM Chen, et al. “Dominant recombination center in electron-irradiated 3 C SiC”. *Journal of applied physics* 79.7 (1996), pp. 3784–3786.

[254] D. V. Lang. “Deep-level transient spectroscopy: A new method to characterize traps in semiconductors”. *J. Appl. Phys.* 45.7 (1974), pp. 3023–3032.

[255] CT-K Lew, BC Johnson, and JC McCallum. “Deep level transient spectroscopy study of heavy ion implantation induced defects in silicon”. *Journal of Applied Physics* 124.12 (2018), p. 125701.

[256] PK Giri and YN Mohapatra. “Thermal stability of defect complexes due to high dose MeV implantation in silicon”. *Materials Science and Engineering: B* 71.1-3 (2000), pp. 327–332.

[257] PK Giri and YN Mohapatra. “Electrical characterization of MeV heavy-ion-induced damage in silicon: Evidence for defect migration and clustering”. *Journal of applied physics* 84.4 (1998), pp. 1901–1912.

[258] Michael S Mazzola, Stephen E Saddow, Philip G Neudeck, VK Lakdawala, and Susan We. “Observation of the D-center in 6 H-SiC p-n diodes grown by chemical vapor deposition”. *Applied physics letters* 64.20 (1994), pp. 2730–2732.

[259] G Alfieri and T Kimoto. “Thermal stability of defects in p-type as-grown 6H-SiC”. *Journal of Physics: Condensed Matter* 19.30 (2007), p. 306204.

[260] M Gong, S Fung, CD Beling, and Zhipu You. “A deep level transient spectroscopy study of electron irradiation induced deep levels in p-type 6H–SiC”. *Journal of applied physics* 85.10 (1999), pp. 7120–7122.

[261] JM Luo, ZQ Zhong, M Gong, S Fung, and CC Ling. “Isochronal annealing study of low energy electron irradiated Al-doped p-type 6H silicon carbide with deep level transient spectroscopy”. *Journal of Applied Physics* 105.6 (2009), p. 063711.